University at Buffalo
The State University of New York

Earthquake-Simulator Experiments of a Model of a Seismically-Isolated, Fluoride-Salt Cooled High-Temperature Reactor

by

Faizan Ul Haq Mir, Kaivalya M. Lal, Benjamin D. Kosbab, Nam Nguyen, Brian Song, Matthew Clavelli, Kaniel Z. Tilow and Andrew S. Whittaker

Technical Report MCEER-22-0004

October 24, 2022

NOTICE

This report was prepared by the University at Buffalo, State University of New York, as a result of research sponsored by the Advanced Research Projects Agency - Energy (ARPA-E) under award number DE-AR0000978. Neither MCEER, associates of MCEER, its sponsors, University at Buffalo, State University of New York, nor any person acting on their behalf:

a. makes any warranty, express or implied, with respect to the use of any information, apparatus, method, or process disclosed in this report or that such use may not infringe upon privately owned rights; or

b. assumes any liabilities of whatsoever kind with respect to the use of, or the damage resulting from the use of, any information, apparatus, method, or process disclosed in this report.

Any opinions, findings, and conclusions or recommendations expressed in this publication are those of the author(s) and do not necessarily reflect the views of MCEER, the Advanced Research Projects Agency, or other sponsors.

University at Buffalo
The State University of New York

Earthquake-Simulator Experiments of a Model of a Seismically-Isolated, Fluoride-Salt Cooled High-Temperature Reactor

by

Faizan Ul Haq Mir,[1] Kaivalya M. Lal,[1] Benjamin D. Kosbab,[2] Nam Nguyen,[3] Brian Song,[4] Matthew Clavelli,[5] Kaniel Z. Tilow[6] and Andrew S. Whittaker[7]

Publication Date: October 24, 2022
Submittal Date: October 4, 2022

Technical Report MCEER-22-0004

Advanced Research Projects Agency – Energy
Award Number DE-AR0000978

1. Graduate Student, Department of Civil, Structural and Environmental Engineering, University at Buffalo, The State University of New York
2 Principal, Simpson Gumpertz & Heger, Atlanta, GA
3 Senior Structural Engineer, Kairos Power, Alameda, CA
4 Manager, Civil Structures, Kairos Power, Alameda, CA
5 Mechanical Engineer, Kairos Power, Alameda, CA
6 Consulting Engineer, Simpson Gumpertz & Heger, Atlanta, GA
7 SUNY Distinguished Professor, Department of Civil, Structural and Environmental Engineering, University at Buffalo, The State University of New York

MCEER: Earthquake Engineering to Extreme Events
University at Buffalo, The State University of New York
212 Ketter Hall, Buffalo, NY 14260
buffalo.edu/mceer

Preface

MCEER was originally established by the National Science Foundation in 1986 at the University at Buffalo, The State University of New York, as the first National Center for Earthquake Engineering Research (NCEER). In 1998, it became known as the Multidisciplinary Center for Earthquake Engineering Research (MCEER), from which the current name, MCEER, evolved.

Comprising a consortium of researchers and industry partners from numerous disciplines and institutions throughout the United States, MCEER's mission expanded in the early 2000s from its original focus on earthquake engineering to one which addresses the technical and socioeconomic impacts of a variety of hazards, both natural and man-made, on critical infrastructure, facilities, and society.

This report describes earthquake-simulator experiments of a scaled model of a prototype fluoride-salt cooled high-temperature nuclear reactor. The components of the prototype reactor addressed in the experiments include an outer vessel, a concentric core barrel, positively buoyant reflector blocks that act as a moderator, positively-buoyant spherical fuel pebbles, and a molten-salt coolant. A detailed scaling analysis was carried out to support the design of the test specimen. Multi-component seismic inputs were used for testing. Two types of friction pendulum seismic isolation bearings were utilized for the experiments: Single concave Friction Pendulum (SFP) and Triple Friction Pendulum (TFP). The earthquake response of such a reactor model involves multiple non-linear interactions, and the physical test results described in this report provided valuable insights into these behaviors and enabled formulation of analysis and modelling recommendations.

ABSTRACT

Kairos Power is developing an advanced reactor that uses a fluoride salt as a coolant, graphite reflector blocks as a moderator, and circulating buoyant TRISO pebbles as nuclear fuel. To characterize the behavior of reactor components under earthquake shaking, validate numerical models for seismic analysis, and develop recommendations for seismic design, a set of earthquake-simulator experiments on a scaled model of the reactor vessel and internals was executed on a six-degree-of-freedom earthquake simulator. The model was seismically isolated at its base using two types of spherical sliding bearings. The scaled model involved representations of prototype reactor vessel, core barrel, reflector blocks, coolant, and spherical fuel pebbles. The material and geometric properties of different test components were selected based on a dynamic similitude scaling analysis and an approximate length scale of 2.5. Three recorded earthquake motions and one synthetically generated motion, all triplets, were used as inputs for testing. The recorded earthquake motions were time scaled for consistency with the chosen length scale of the model. Instrumentation on the test specimen was focused on recording dynamic responses of the outer vessel, core barrel, and reflector-block assembly, hydrodynamic responses (sloshing and hydrodynamic pressure) of the liquid coolant, pebble consolidation under earthquake shaking, and the behavior of the isolation systems. Test results and numerical studies, building on the data generated in the tests and leading to recommendations for analysis and modelling, are presented in this report.

ACKNOWLEDGMENTS

The work presented in this report was funded by the Advanced Research Projects Agency – Energy (ARPA-E), US Department of Energy, under Award Number DE-AR0000978. Kairos Power contributed knowledge and hardware for the experiments described herein. The financial support provided by ARPA-E and the technical support provided by Kairos Power is gratefully acknowledged. The views and opinions of the authors expressed herein do not necessarily state or reflect those of the US Government or any agency thereof, or Kairos Power.

The experiments described in this report were conducted at the Structural Engineering and Earthquake Simulation Laboratory (SEESL) at the University at Buffalo. The authors appreciate the technical support provided by the laboratory staff, including Messrs. Mark Pitman, Scot Weinreber, Robert Staniszewski, Christopher Budden, Michael Branch, Jeffrey Cizdziel, and Louis Moretta. The valuable assistance provided by Mr. Elliot Whittaker in assembling the test specimen is highly appreciated.

The authors thank Professor Mettupalayam Sivaselvan, Professor Michael Constantinou, and Dr. Ching-Ching Yu of the University at Buffalo for providing input and ideas over the course of this research project. The authors gratefully acknowledge the support of Earthquake Protection Systems, Vallejo, CA who provided the friction pendulum bearings used for the testing program at no cost to the project. Computers and Structures Inc. (CSI) provided a SAP2000 license to support remotely-executed numerical studies presented in Section 6 of this report. This support is gratefully acknowledged. The authors also thank Ms. Heather Kosbab who provided a fabric net for use in the experiments at a very short notice.

TABLE OF CONTENTS

TABLE OF CONTENTS (CONT'D)

TABLE OF CONTENTS (CONT'D)

TABLE OF CONTENTS (CONT'D)

LIST OF FIGURES

LIST OF FIGURES (CONT'D)

LIST OF FIGURES (CONT'D)

LIST OF FIGURES (CONT'D)

LIST OF FIGURES (CONT'D)

LIST OF FIGURES (CONT'D)

LIST OF FIGURES (CONT'D)

LIST OF FIGURES (CONT'D)

LIST OF FIGURES (CONT'D)

LIST OF FIGURES (CONT'D)

LIST OF TABLES

LIST OF TABLES (CONT'D)

SECTION 1
INTRODUCTION

1.1 Introduction

Kairos Power (https://kairospower.com/) is developing an advanced (Generation IV) reactor: the Kairos Power Fluoride salt-cooled High temperature Reactor (KP-FHR). The KP-FHR uses a low-pressure, fluoride salt as the coolant, positively buoyant graphite reflector blocks as the moderator, and circulating (positively buoyant) graphite pebbles filled with TRISO (DOE 2019) particles as fuel. The use of a low-pressure, molten salt coolant avoids the need for specialized, high-pressure vessels and piping systems. The molten salt coolant is also advantageous owing to its high volumetric heat capacity and low chemical reactivity (Bardet and Peterson 2008).

Seismic isolation is a design solution for the KP-FHR. Recent studies have shown that seismic isolation can significantly reduce the overnight capital cost of advanced reactors and support deployment of standardized reactor designs at sites of varying seismicity (Lal *et al.* 2022; Parsi *et al.* 2022).

Kairos Power has adopted an iterative approach of rapid development and testing to build an operating power reactor, including the construction and operation of a non-power test reactor named Hermes (NRC 2021). The earthquake-simulator experiments described in this report will inform the seismic design of this molten salt reactor (MSR).

The components of the prototype reactor addressed in the experiments described in this report include an outer vessel, a concentric core barrel, positively-buoyant reflector blocks that act as a moderator, positively-buoyant spherical fuel pebbles, and molten-salt coolant.[1] Figure 1.1 presents the tested components at the model scale. In operation (and for testing), the fuel pebbles are buoyant and not supported at the base of the vessel. The reflector-block assembly comprises stacked individual blocks connected using shear pins and keys. Two types of spherical sliding bearings were utilized to base isolate the vessel in the experiments: Single concave Friction Pendulum (SFP) bearings and Triple Friction Pendulum (TFP) bearings. The bearings were installed below the base of the vessel and separate tests were performed for each bearing type. The dynamic response of such a reactor model involves multiple non-linear interactions, and the physical test results provide valuable insights into these behaviors.

[1]Head mounted equipment in the prototype reactor (e.g., pumps, pebble circulation equipment, and control rod drive mechanism housings) were also tested in a separate test program. Some details are available in Mir *et al.* (2022a).

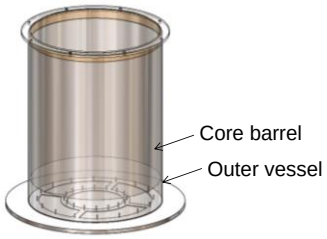

a. outer vessel and concentric core barrel

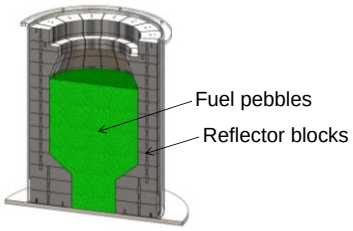

b. reflector blocks and fuel pebbles (green), cutaway view, before the addition of coolant

Figure 1.1. Test components

1.2 Overview of related past work available in literature

Although the KP-FHR is a novel design, some of the reactor's components are similar to those used in other designs. As an example, many high temperature gas-cooled reactor (HTGR) designs use graphite reflector block assemblies similar to KP-FHR; the difference being that in KP-FHR, the blocks float in the liquid coolant.

Experimental studies on the seismic behavior of graphite reflector blocks, block-type fuel assemblies, and their supporting structures in HTGRs have been published, although none at the scale and level of complexity described in this report. Most of the studies focused on generation of test data that could be used to describe impact phenomenon in analytical models and to characterize the seismic integrity of the connections between blocks.

The Japan Atomic Energy Research Institute (JAERI) studied the seismic response of graphite reflector blocks and fuel block assembly (core) in an HTGR (Ikushima *et al.* 1982). The experimental part of the study involved impact tests using two graphite blocks followed by seismic tests of a single column of blocks, seven columns (one core region) of blocks, a two-dimensional vertical core section, and a two-dimensional horizontal core section; see Figure 1.2. The goals of the tests included determining the coefficient of restitution and impact duration (for impact between reflector blocks), generation of data on block rocking and impact characteristics, column displacement, and connecting pin (dowel pin) forces. The data generated from the tests were used for correlation studies with analytical models (Ikushima 1982a; Ikushima and Honma 1989; Ikushima and Nakazawa 1979) and for validation studies in a companion software development program (Ikushima 1982b; Ikushima 1990). In the numerical models, the blocks

were treated as rigid bodies with block-to-block interactions modelled using springs and dashpots, as shown in Figure 1.3.

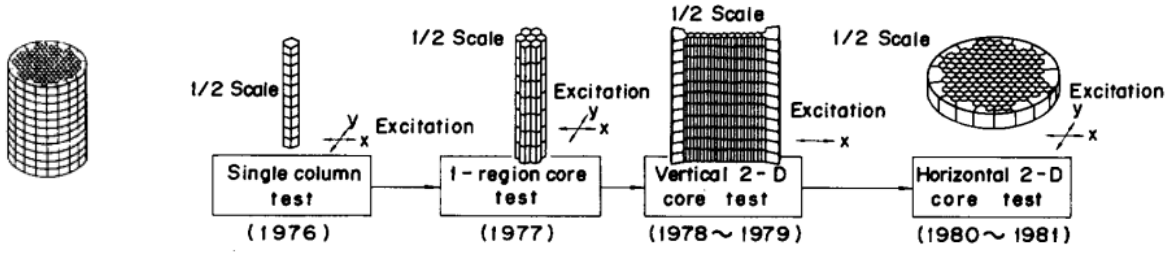

Figure 1.2. Seismic tests on reflector-block assembly (core) in a HTGR, adapted from Fig 2 in Ikushima *et al.* (1982)

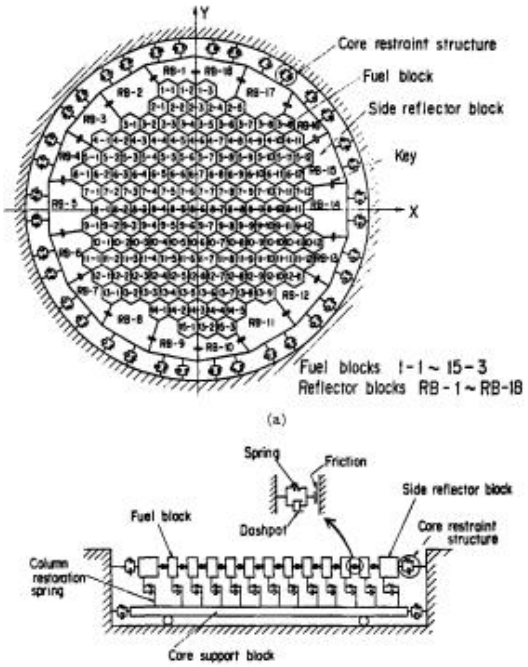

Figure 1.3. Analytical model of a two-dimensional horizontal core, adapted from Fig 1 in Ikushima and Honma (1989)

Experimental studies on the seismic response of graphite blocks in HTGRs continued at JAERI in the 1990s (Iyoku *et al.* 1994; Iyoku *et al.* 1992a; Iyoku *et al.* 1992b). The studies included seismic tests on a half-scale vertical section model, a full-scale seven-column model of the core graphite block, and a one-fifth and a one-third scale-model of core bottom structures. A summary of the studies can be found in Iyoku *et al.* (2004).

Olsen *et al.* (1976) describes one-dimensional earthquake simulator tests of a one-fifth scale, horizontal array of HTGR graphite reflector blocks, as shown in Figure 1.4. The tests were conducted using two different lateral core support designs (lateral support springs with *small* and *large* stiffnesses of 800 lb/in and 100,000 lb/in, respectively). Core dynamic characteristics, in terms of frequency of vibration and equivalent viscous damping, were investigated and support (reaction) and in-core forces for different levels of input acceleration were generated. The core damping was greater than 30% of critical. The use of lateral support springs with small stiffness expectedly resulted in small support forces and large core displacements. The support forces generated in the tests were used for a correlation study using the computer code CRUNCH (Rickard 1977).

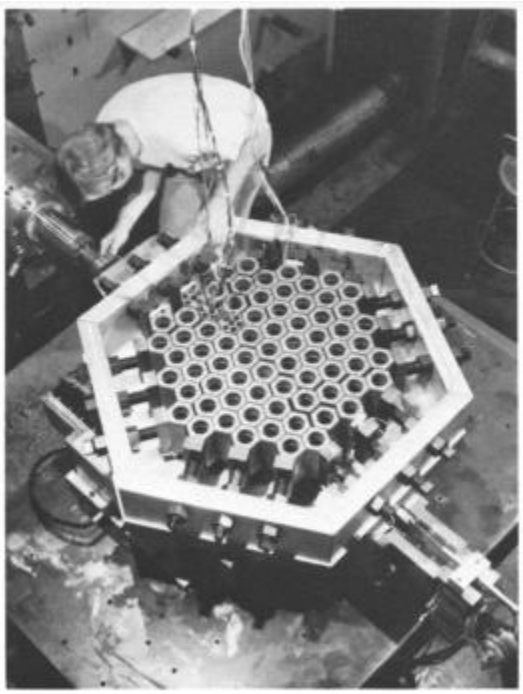

Figure 1.4. One-fifth scale horizontal array test, adapted from Fig. 3 in Olsen *et al.* (1976)

Dove *et al.* (1981) describes a study of the seismic response of a core in a large gas-cooled reactor. The authors tested a one-dimensional, four-block system of reflector blocks and a two-dimensional, 4 × 4 block vertical array on an earthquake simulator at the White Sands Missile Range in New Mexico, using sinusoidal inputs. The models are shown in Figure 1.5 (note the two fixed blocks and columns at the extremes in Figure 1.5a and Figure 1.5b, respectively). Separate models were constructed based on two governing scaling laws: one preserving gravitational effects (body forces) and the other utilizing prototype

materials at model scale. A study of the changes in shear pin or side support forces with varying clearances between shear pins and sockets and between blocks and side supports was presented.

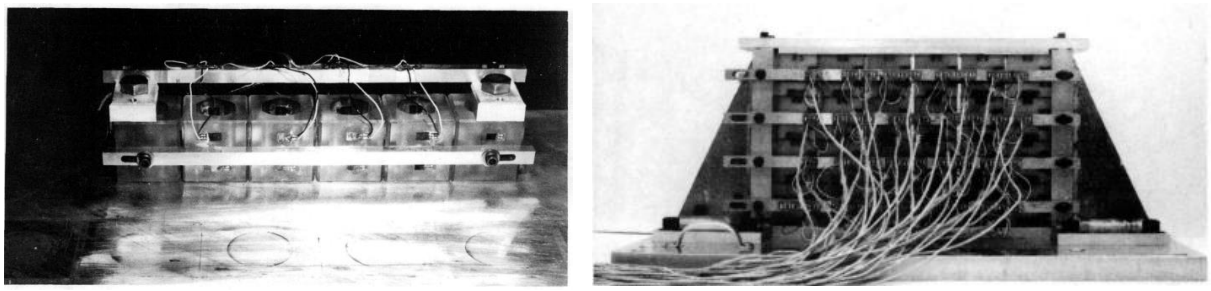

a. one-dimensional, four-block system b. two-dimensional, 4 × 4 block vertical array

Figure 1.5. Reflector blocks tested for seismic behavior, adapted from Fig. 3 and Fig. 9 in Dove *et al.* (1981)

Theymann *et al.* (1989) presents an overview of studies performed in Germany to support the development of a high temperature gas-cooled reactor. The core of the reactor comprised a loose bed of spherical fuel elements (pebbles) enclosed in a structure of graphite reflector blocks. The graphite structure was composed of a side reflector, a top reflector, and a bottom reflector. The side reflector blocks were supported by radially-oriented, prestressed springs. The experiments included tests focused on behavior of the pebble bed, the side reflector (see Figure 1.6), and the impact behavior of the top reflector blocks. *Minor* compaction of the pebble bed was observed. The damping effects in the pebble bed core were found to be high (damping > 15% of critical) and the pebble bed did not behave like a liquid and slosh, even under high accelerations. Opening of gaps between the reflector blocks was not observed in the earthquake-simulator experiments.

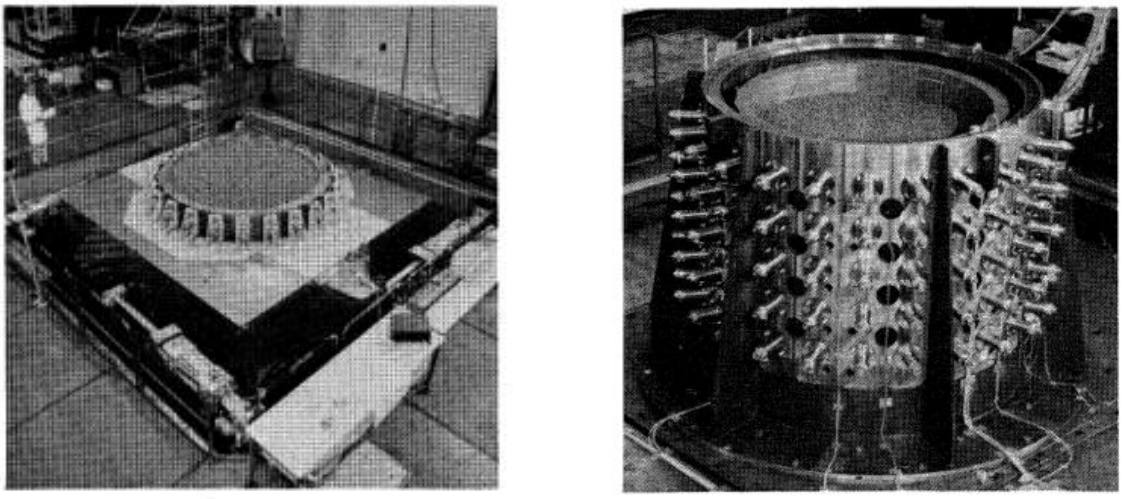

a. 2D ring model b. 3D cylindrical model

Figure 1.6. Models of the side reflector blocks with the pebble bed, adapted from Fig. 4 and Fig. 5 in Theymann *et al.* (1989)

Ichikawa *et al.* (2003) describes seismic tests of a model of a neutron reflector assembly of an advanced pressurized water reactor. The prototype reflector assembly comprised a stack of eight octagonal ring-blocks (see Figure 1.7a), tightened and secured to a lower core plate using eight long bolts (tie rods). The assembly was separated from the core barrel by a narrow gap. In the test, four cylindrical blocks, tightened using eight bolts, were tested along with an enclosure simulating the core barrel and the gap in between them (see Figure 1.7b). The enclosure was filled with water. The in-air natural frequency and damping of the assembly were 64.5 Hz and 1.25%, respectively. The corresponding values in-water were dependent on the amplitude of vibration: the frequency ranged between 12 Hz and 13 Hz and decreased with increasing vibration amplitude, and the damping ranged from a little less than 5% to values greater than 15%. The damping ratio tended to increase with vibration amplitude. The study also investigated the effect of vertical vibrations, tie-rod tightening forces, gap size, and friction at the bottom (supporting) surface. The vertical displacement response of the assembly under seismic excitations decreased with tie-rod tightening forces. The horizontal displacement response of the assembly tended to increase as the gap widened and decrease as the friction increased. The described test is different from the other studies described above as the reflector-block assembly was tested in a submerged state.

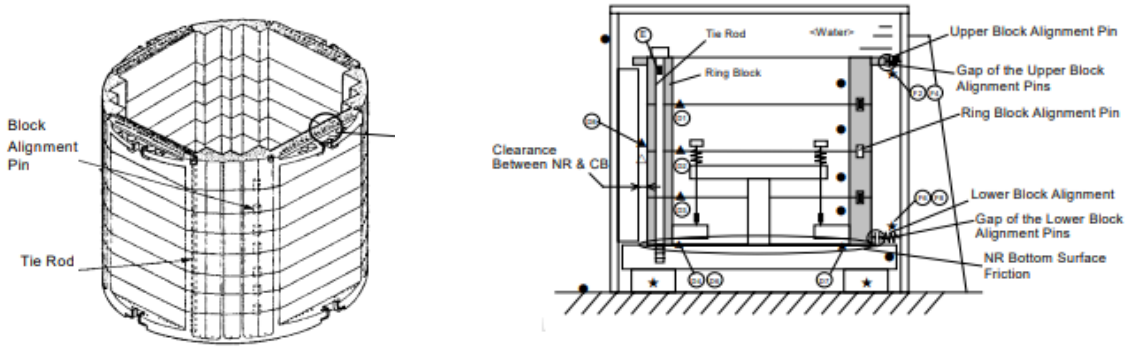

a. neutron reflector in an advanced pressurized water reactor

b. four-block reflector model for tests

Figure 1.7. Tests of a neutron reflector assembly in an advanced pressurized water reactor, adapted from Fig.1 and Fig.2 in Ichikawa *et al.* (2003)

Sun *et al.* (2012) describe seismic tests on a half-scale, double-layer graphite core model executed on the six degrees-of-freedom earthquake simulator at the China Academy of Building Research. The model (see Figure 1.8) was tested with different gaps (1.6 mm, 3.0 mm, and 5.0 mm) between the blocks. The model with a 5 mm gap between the blocks was tested with and without hold-down plates to simulate core-structure conditions expected at different stages of operation. The tests were carried out in support of the design of the graphite reflector assembly for a high temperature gas-cooled reactor in China. White noise excitations in the two horizontal directions with amplitudes between 0.1g and 0.5g, sine sweeps, and three directional seismic excitations[2] were used for testing. Acceleration and displacement sensors were used at multiple locations on the specimen and pressure films were used around keys and dowels connecting the blocks. The natural frequency of the test specimen could not be identified from the test data. The authors reported that the assembly remained intact under all excitations although some graphite blocks were damaged. No pattern of damage or cause were reported. The measured pressure on the surface of some of the dowels exceeded 10 MPa, which was the upper limit on the film. Amplification of accelerations was found to be greatest in the model with the greatest gap size between blocks.

[2] The amplitude of the seismic excitations used in Sun *et al.* (2012) is unclear. Table 4 in Sun *et al.* (2012) presents the specifications of the earthquake simulator, mentioning maximum acceleration capacities of ±1.5g, ±1 g, and ±0.8g in the X, Y, and Z directions, respectively. (X, Y, and Z denote the two horizontal directions and the vertical direction, respectively.) However, on page 4 of the study, where seismic excitations used in the tests are discussed, a significantly greater acceleration amplitude of 7.4g is mentioned.

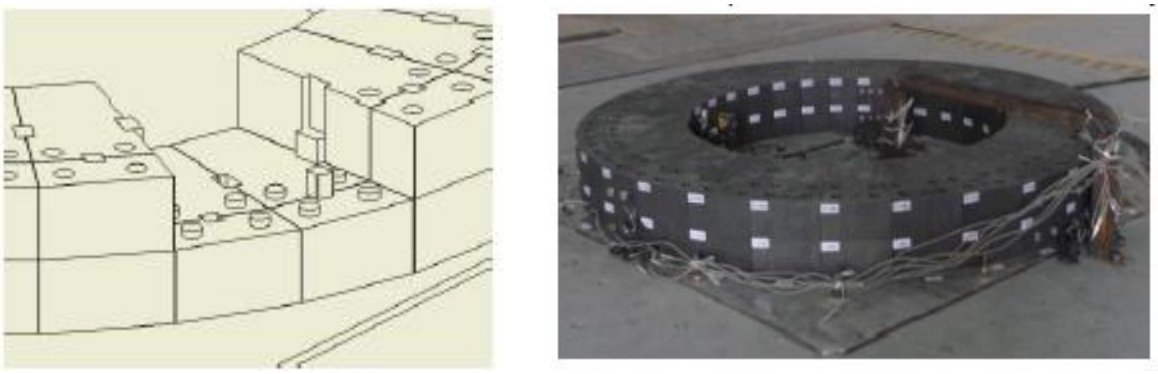

a. CAD model of the double-layer core model, connection details

b. double-layer core model on earthquake simulator

Figure 1.8. Double-layer graphite core model, adapted from Figure 1 in Sun *et al.* (2012)

Jin *et al.* (2014) describe impact experiments using two graphite blocks of a planned HTGR. Two types of collisions were investigated: flat and oblique; see Figure 1.9. The contact time of the colliding blocks was found to decrease and the coefficient of restitution was found to increase with contact speed. The authors note that it was challenging to achieve a *normal* collision, wherein the colliding faces of the two blocks come in contact across their whole areas. They observed that the dimensions of the blocks and collision angles may be more important to the collision process than material properties.

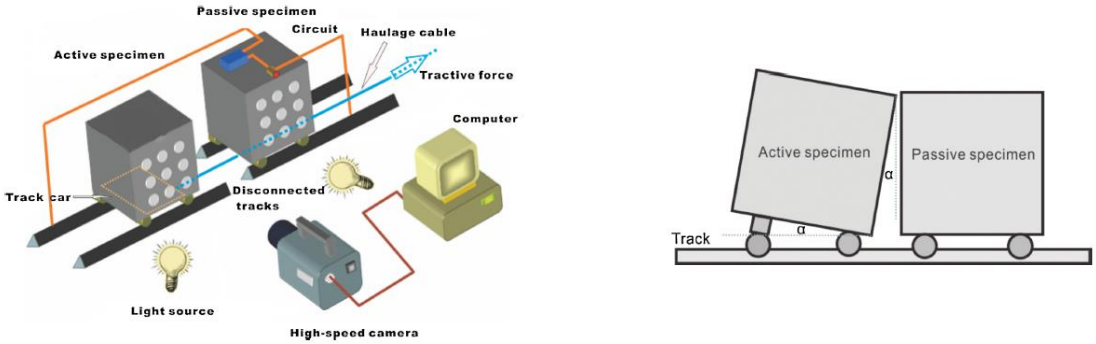

a. experimental setup

b. oblique collision

Figure 1.9. Experiment for characterizing collisions between reflector blocks, adapted from Fig. 1 and Fig. 7 in Jin *et al.* (2014)

Cai *et al.* (2018) present a numerical study on the seismic response of submerged graphite reflector blocks in a Thorium-based Molten Salt Reactor (TMSR). The study uses a simplified approach to model individual reflector blocks by considering a lumped mass at the center of gravity of a block and using rigid beams to

outline the profile of a block (see Figure 1.10). The fluid was modeled as an additional lumped mass. The block-to-block interactions in the model of the complete reflector-block assembly were simulated using springs, dashpots, and gap elements, the properties of which were calibrated using a more detailed finite element model of two impacting blocks as a reference. The reference finite element model was neither verified nor validated and thus the results of the seismic analyses are of questionable value.

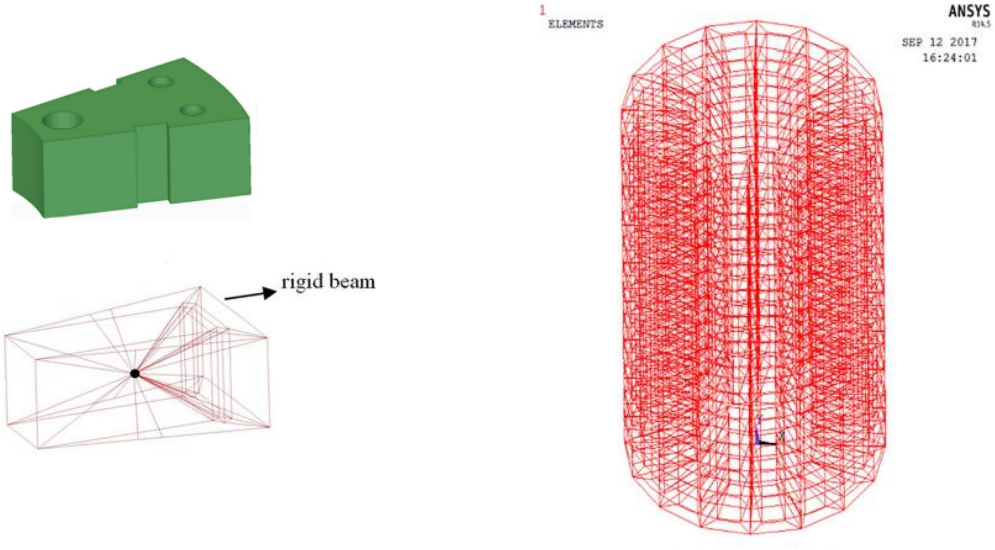

a. reflector block and simplified lumped mass model

b. model of the reflector-block assembly

Figure 1.10. Modelling of reflector-block assembly using lumped masses and rigid beams, adapted from Fig. 3 and Fig. 9 in Cai *et al.* (2018)

A few studies on the behavior of pebble beds (as shown in Figure 1.1b) under seismic excitations are available in the literature. During shaking, the packing fraction (i.e., ratio of volume of pebbles to the summation of the volume of pebbles and voids) of the pebble bed could increase, which could lead to an increase in core reactivity (and power output from the reactor core) and changes in coolant flow through the pebble bed. Both the distribution of packing fraction in a pebble bed and the average packing fraction depend on how the pebbles are loaded or placed. Existing literature suggests that the packing fraction varies between 0.609 and 0.625 for spheres poured into a bed and between 0.625 and 0.641 for a vibrated bed (Dullien 1992). A recent study (Satvat *et al.* 2021) involved a sensitivity analysis of a core reactivity model performed by varying the pebble packing fraction from 0.57 to 0.63. The resulting change in core reactivity was small. Another study (Auwerda 2014) suggests that small changes in core reactivity due to earthquake shaking can be easily countered by control mechanisms (e.g., small movements of control rods).

Nonetheless, information on the expected change in packing fraction in design basis shaking is important. A study at the Shanghai Institute of Applied Physics (Chen *et al.* 2017; Chen *et al.* 2018) investigated the effect of earthquake shaking on a pebble bed in a one-fourth scale model of a Thorium Molten Salt Reactor (TMSR); see Figure 1.11a. The model included nearly ten thousand polypropylene spheres (pebbles). Flow velocities of 0.015 m/s, 0.03 m/s, 0.045 m/s, and 0.06 m/s through the pebble bed were used during the shaking tests. The model was vibrated using sinusoidal excitations at frequencies of 20 Hz and 10 Hz. The latter resulted in strong vibrations in the model vessel. The time-variation of the packing fraction for different flow velocities under sustained strong vibrations (lasting for over an hour) at 10 Hz frequency is shown in Figure 1.11b. The packing fraction changed significantly in the initial 10 minutes of shaking for low flow velocities. At high flow velocities through the pebble bed, the changes in packing fraction were minimal, pointing to the possible stabilizing effect of high flow velocities. The results from the study might be helpful for design of pebble bed reactors although the long-duration, sinusoidal excitations used in the experiment are not representative of recorded earthquakes.

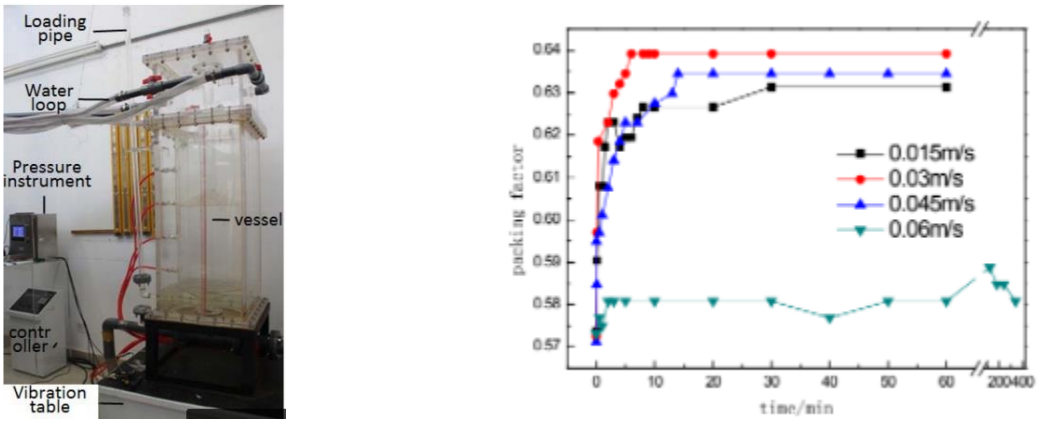

a. one-fourth scale model on vibration table

b. packing fraction (factor) for different flow velocities through the pebble bed undue strong shaking

Figure 1.11. Set up and results of a study on effect of earthquake shaking on pebble bed packing fraction, adapted from Fig. 1 and Fig. 7 in Chen *et al.* 2017

1.3 Objectives of the report

There is a body of research on the seismic responses of reflector block cores and pebble beds but it is not sufficient for informing the design of an integrated system (such as the one shown in Figure 1.1) comprising a base-isolated reactor vessel, a core barrel, a reflector-block assembly with complex block geometries,

pebbles, and coolant. The goals of the research program described in this report were to gain a better understanding of the dynamic behavior of such an integrated system, formulate recommendations for its seismic analysis (numerical or analytical), and experimentally demonstrate the benefits of seismically isolating equipment in a nuclear power plant. These goals are achieved by meeting the following objectives:

1. Designing a scale model of an FHR for earthquake-simulator experiments considering aspects of the KP-FHR as the prototype.
2. Generating experimental data for dynamic responses of model-scale coolant, reflector-block assembly, pebble bed, core barrel, and vessel for multi-directional seismic inputs and two isolation systems, curating the data and archiving it for use by others.
3. Analyzing the experimental data for assessing system behavior and formulating recommendations for seismic analysis and design suitable for use by designers and regulators.

1.4 Organization of this report

This report is organized into seven sections, a list of references, and an appendix, as follows:

Section 2 presents a dimensional analysis for a generic coupled fluid-solid problem and presents scaling analyses for different components of the model used in the experiments.

Section 3 describes the model geometry and the used friction pendulum bearings.

Details of instrumentation, seismic inputs, and the test plan are presented in Section 4.

Key results from the experiments are presented in Section 5. Sloshing of the fluid (representing coolant), amplification of accelerations along the height of the vessel, behavior of the reflector-block assembly and challenges in assembling it, change in pebble packing fraction due to shaking, and benefits of seismic isolation are explored.

Section 6 provides recommendations and examples for simplified numerical analysis of components of the reactor vessel, based on results presented in Section 5.

Section 7 summarizes the work and presents conclusions.

A list of references is provided after Section 7 and is followed by an appendix describing the characterization tests for the friction pendulum bearings used for the experiments.

SECTION 2
SCALING ANALYSES

2.1 Introduction

This section presents scaling analyses guiding the design of a scale model of the Fluoride salt-cooled High temperature Reactor introduced in Section 1. As discussed in Section 1, the scale model involved representations of an outer vessel, a concentric core barrel, positively-buoyant reflector blocks that act as a moderator, positively-buoyant spherical fuel pebbles, and molten-salt coolant (see Figure 1.1). The geometries of prototype components correspond to the hot condition in normal operation. Different physical phenomena govern the scaling of these test components for earthquake-simulator experiments. As an example, scaling buoyant effects is critical for proper scaling of reflector block behavior, but not for the core barrel or the outer vessel. Accordingly, different scaling approaches were used for different components. The following sub-sections summarize a dimensional analysis for a generic coupled fluid-solid problem and present scaling analyses for different components in the scale model. The inlet and outlet temperatures in the prototype reactor vessel are 550 °C and 650 °C, respectively. For the scaling analyses that follow, the mechanical properties of prototype components at the average of the inlet and outlet temperatures (i.e., 600 °C) are used and the variability in properties over the temperature range is noted.

2.2 Dimensional analysis for a coupled fluid-solid problem

The discussion below is based on the presentation of DeLangre (2020). The physical quantities that can be used to define a general coupled fluid-solid problem are listed in Table 2.1.

Table 2.1. Quantities considered for defining the coupled fluid-solid problem

Fluid	Solid
Coordinates, X	Coordinates, X
Time, t	Time, t
Velocity field, U	Displacement field, ξ
Viscosity, μ	Stiffness, E
Size, L	Size, L
Gravity, g	Gravity, g
Density, ρ	Density, ρ_s
Velocity data, U_o	Displacement data, ξ_o

Some of the quantities listed in Table 2.1 are specific to the fluid or solid domain (e.g., μ and E) whereas some are common to both (e.g., g and t). Considering U (or ξ) as the variable of interest, the coupled fluid-solid problem can be expressed by a dimensionally homogeneous equation involving the remaining eleven ($n = 11$) variables listed in Table 2.1, as noted below:

$$Q(U, x, t, \mu, \rho, U_o, L, g, E, \rho_s, \xi_o) = 0 \tag{2-1}$$

The dimensional matrix (of exponents in terms of fundamental quantities: length, mass and time) can be formed as:

$$\begin{array}{c} \\ L \\ M \\ T \end{array} \begin{array}{c} \begin{array}{cccccccccccc} U & x & t & \mu & \rho & U_o & L & g & E & \rho_s & \xi_o \end{array} \\ \begin{bmatrix} 1 & 1 & 0 & -1 & -3 & 1 & 1 & 1 & -1 & -3 & 1 \\ 0 & 0 & 0 & 1 & 1 & 0 & 0 & 0 & 1 & 1 & 0 \\ -1 & 0 & 1 & -1 & 0 & -1 & 0 & -2 & -2 & 0 & 0 \end{bmatrix} \end{array}$$

The rank, r, of this matrix is 3. Invoking Buckingham's Pi theorem (Buckingham 1914), equation (2-1) can be expressed in an equivalent form (2-2), where eight ($n - r = 8$) dimensionless products are used to describe the phenomenon:

$$F(\pi_1, \pi_2 ..... \pi_8) = 0 \tag{2-2}$$

The independent dimensionless products are formed by inspection and appropriate grouping of variables, and are presented below. Products π_1 through π_5 are related to the fluid domain and are similar to what would be obtained for a fluid-only case. Similarly, π_6 and π_7 are related to the solid domain. The product π_8 involves quantities from both domains (fluid and solid) indicating its importance for coupled problems. Three possible choices for π_8 are presented here: mass number denoting the ratio of fluid density to solid density, reduced velocity number denoting the ratio of fluid velocity to velocity of elastic waves in the solid, and Cauchy number denoting the ratio of fluid loading (quantified by dynamic pressure) to the stiffness of the solid (quantified by E). The choice of π_8 should be made in accordance with the nature of fluid-solid coupling at hand. For example, if buoyancy effects are important, mass number should be chosen. Similarly, if the deformations of the solid under fluid loading are important, Cauchy number should be chosen.

$$\pi_1 = \frac{U}{U_o};\ \pi_2 = \frac{x}{L};\ \pi_3 = \frac{U_o t}{L};\ \pi_4 = \frac{\rho U_o L}{\mu};\ \pi_5 = \frac{U_o}{\sqrt{gL}}$$

$$\pi_6 = \frac{\xi_o}{L};\ \pi_7 = \frac{\rho_s g L}{E}$$

$$\pi_8 = \begin{cases} \dfrac{\rho}{\rho_s} & \text{(Mass number)} \\ \dfrac{U_o}{\sqrt{E/\rho_s}} & \text{(Reduced velocity)} \\ \dfrac{\rho U_o^2}{E} & \text{(Cauchy number)} \end{cases}$$

2.3 Scaling of pebble dynamics: fluid and pebbles

In the prototype, the spherical fuel pebbles are randomly packed in the reactor core and float in the molten salt (Flibe). The molten slat flows through the gaps between pebbles and extracts heat. Thus, buoyancy and drag forces dominate the dynamic behavior of pebbles in the prototype. Laufer (2013) showed that for proper scaling of pebble dynamics, three dimensionless numbers should be matched for model and prototype: π_4, π_5 and π_8. Since buoyancy is important here, mass number is chosen for π_8. A description of each term is provided here:

a. π_4 (Reynolds number): The ratio of viscous and inertial forces in the model and prototype should be the same, so that drag forces (on the pebbles, particularly) scale properly. That is:

$$\frac{U_m L_m}{U_p L_p} = \frac{\nu_m}{\nu_p} \tag{2-3}$$

where U, L and ν are the flow velocity, characteristic length, and kinematic viscosity respectively. The subscripts m and p denote model and prototype, respectively.

b. π_5 (Froude number): The ratio of inertial force to gravitational force in the model and the prototype should be the same. This is important in case a free surface exists or in case an active pump is used to circulate the fluid through the core. The condition is:

$$\frac{U_m}{\sqrt{gL_m}} = \frac{U_p}{\sqrt{gL_p}}$$

or

$$\frac{U_m}{U_p} = \left(\frac{L_m}{L_p}\right)^{1/2} \tag{2-4}$$

c. π_8 (Mass number): The ratio of the density of fuel pebbles to the surrounding fluid must be the same in the model and the prototype to correctly simulate buoyancy effects. This was nearly achieved by using polypropylene (PP) spheres to represent fuel pebbles, as shown in Table 2.2.

Table 2.2. Scaling analysis, PP spheres for modeling fuel pebbles

	Prototype at 600 °C	Model
Fuel pebble density, ρ_{sf}	1785 kg/m^3 (1740 kg/m^3 – 1830 kg/m^3) †	880 kg/m^3
Fluid density, ρ	1986 kg/m^3 (2011 kg/m^3 – 1962 kg/m^3) ††	998 kg/m^3
Mass number, ρ / ρ_{sf}	1.11	1.13

†The fuel pebbles have a nominal (as fabricated) density of 1740 kg/m^3 which can change under neutron flux to about 1830 kg/m^3. The average value is used here.

††Values in parenthesis indicate range over 550 °C – 650 °C

Combining equations (2-3) and (2-4):

$$\frac{L_m}{L_p} = \left(\frac{\nu_m}{\nu_p} \right)^{2/3} \tag{2-5}$$

The kinematic viscosity of water (ν_m) at 20 °C is 10^{-6} m^2/s and that of Flibe (ν_p) at a temperature of 600 °C is 4.3×10^{-6} m^2/s, leading to a required length scale ratio (The kinematic viscosity of Flibe is 5.46×10^{-6} m^2/s and 3.45×10^{-6} m^2/s at temperatures of 550 °C and 650 °C, respectively.):

$$S_L = \frac{L_m}{L_p} = 0.38$$

Using equation (2-4), the required flow scale ratio, $S_U = \frac{U_m}{U_p} = 0.62$.

An available outer vessel (see Mir *et al.* (2021)) was used for the model, the use of which resulted in a nearly equal length scale $S_L = 0.39$.

2.4 Scaling of reflector blocks

Reflector blocks in the prototype float in the coolant and function as a moderator in an operating reactor. To represent them at the model scale, density scaling was considered primary. Dynamic effects (related to stiffness and inertia) may also be important given that the blocks form a significant fraction of the specimen mass and it was of interest to investigate gap openings between adjacent blocks. So π_7 and π_8 (mass number) were considered for scaling analysis. A model material with a density of approximately 870 kg/m^3 and an elastic modulus of 1.85 GPa would be ideal for modeling the reflector blocks, but such a material does not exist to the knowledge of the authors. The used material at the model scale, polypropylene, has physical and mechanical properties close to what were required per scaling: density of 900 kg/m^3 and an

average elastic modulus of 1.3 GPa (Material Properties 2022) . Table 2.3 lists the relevant values and scale factors. The density and elastic modulus of graphite are essentially constant over the temperature range of 550 °C - 650 °C.

Table 2.3. Scaling analysis, polypropylene for modeling reflector blocks

	Prototype at 600 °C†	Model	Scale factor
Fluid density, ρ	1986 kg/m^3 (2011 kg/m^3 – 1962 kg/m^3)	998 kg/m^3	$S_\rho = 0.50$
Reflector density, ρ_{sr}	1739 kg/m^3	900 kg/m^3	$S_{\rho_{sr}} = 0.52$
Mass number, ρ / ρ_{sr}	1.14	1.10	-
Elastic modulus of reflector	9.5 GPa	1.3 GPa	$S_E = 0.14$
Size (generalized), L	-	-	$S_L = 0.39$

†Values in parenthesis indicate range over 550 °C - 650 °C

For the listed values, the ratio of π_8 (mass number) for the model and the prototype is 0.96. For π_7, the ratio is 1.45. The departures of these values from unity represents distortion in the model. The distortion in mass number π_8 was minimized by creating voids (hollow spaces) in some of the polypropylene reflector blocks such that an equivalent density of 850 kg/m^3 was achieved for the reflector-block assembly, resulting in a mass number ratio for model and prototype of 1.02.

2.5 Scaling of core barrel

The primary function of the core barrel in the prototype is to channel the inflow of the coolant down in the annular space between that separates it from the outer vessel (see Figure 1.1) (The coolant flows bottom-up through the pebble bed for heat extraction.). For simulating fluid-structure interaction (FSI) effects at the core barrel-fluid interface and the dynamic effects (related to stiffness and inertia of the core barrel), it is sufficient to match π_7 and π_8 for the model and the prototype. For π_8, it could be argued that preserving the Cauchy number is critical. (The Cauchy number, as defined in section 2.2, is the ratio of the fluid loading quantified by the dynamic pressure, ρU^2, to the stiffness of the structure characterized here by elastic modulus, E.)

Scaling of FSI effects was considered primary, so π_8 was considered first. The expression for π_8 is re-written here:

$$\pi_8 = \frac{\rho U^2}{E} \tag{2-6}$$

The dimesnionless product, π_8, was derived using the same length scale factor for all dimensions (height, diameter, and thickness). Since it may be valuable to use a different scale factor for thickness, the above dimensionless product is modified to:

$$\tilde{\pi}_8 = \frac{\rho U^2 L}{Eh} \tag{2-7}$$

where h is the thickness of the core barrel and L is any other dimension (e.g., radius, or height of fluid). This modification is not arbitrary, as explained below.

The condition for scaling that is obtained from (2-7) can be written as follows (subscripts m and p denote model and prototype, respectively; and S denotes a scale factor):

$$\tilde{\pi}_m = \tilde{\pi}_p$$

$$\text{or} \qquad \frac{S_\rho S_U^2 S_L}{S_E S_h} = 1 \tag{2-8}$$

Now consider the following equation for the impulsive period of a flexible tank (Malhotra *et al.* 2000):

$$T_{imp} = C_i \frac{H\sqrt{\rho}}{\sqrt{h/R}\sqrt{E}} \tag{2-9}$$

where T_{imp} is the impulsive period, H is the fluid height, ρ is the fluid density, R is the radius of the tank, C_i is a factor that depends on the ratio of fluid height-to-tank radius, and E is the modulus of elasticity of the tank material. Equation (2-9) can be written separately for the model and the prototype. The two equations can then be combined to give the following relationship for the scale factor for impulsive period, S_T:

$$S_T = \frac{S_L\sqrt{S_\rho}}{\sqrt{S_h/S_L}\sqrt{S_E}} \tag{2-10}$$

Equation (2-10) can be re-written as:

$$1 = \frac{\left(S_L/S_T\right)\sqrt{S_\rho}}{\sqrt{S_h/S_L}\sqrt{S_E}} = \frac{S_U\sqrt{S_\rho}}{\sqrt{S_h/S_L}\sqrt{S_E}}$$

$$\text{or} \qquad \frac{S_\rho S_U^2 S_L}{S_E S_h} = 1 \tag{2-11}$$

which is identical to (2-8) and hence the modification from (2-6) to (2-7) is justified.

Using either equation (2-11) or (2-8), the information in Table 2.4 below and considering aluminum as the model scale material, the scale factor for thickness, S_h, was calculated as 0.16, which is less than the (general) scale factor for length, $S_L = 0.39$.

Table 2.4. Scaling analysis, aluminum as core-barrel material

	Prototype at 600°C†	Model	Scale factor
Fluid density, ρ	1986 kg/m^3 (2011 kg/m^3 – 1962 kg/m^3)	998 kg/m^3	$S_\rho = 0.50$
Elastic modulus, core barrel, E	148 GPa (155 GPa – 148 GPa)	70 GPa	$S_E = 0.47$
Mass density, core barrel, ρ_{sc}	7709 kg/m^3 (7731 kg/m^3 – 7688 kg/m^3)	2700 kg/m^3	$S_{\rho_{sc}} = 0.35$
Size (generalized), L	-	-	$S_L = 0.39$
Velocity (flow), U	-	-	$S_U = 0.62$

†Values in parenthesis indicate range over 550 °C - 650 °C

Using aluminum for the core barrel and the derived scale factor for thickness led to proper scaling of FSI effects, and enabled rolling of available sheet, fabrication, and welding. However, a check on the ratio of π_7 at the model and prototype scales indicated that the ratio was not unity, indicating a distortion:

$$\frac{S_{\rho_{sc}} S_L}{S_E} = 0.29 \tag{2-12}$$

The thickness scale factor does not appear in (2-12) because π_7 is a ratio of inertial and elastic forces for the core barrel alone and the thickness term cancels. Mass could have been added to the aluminum core barrel to achieve a ratio of π_7 at the model and prototype scales equal to unity, but there was insufficient space in the model to do so. Importantly, earthquake-induced strains in the prototype core barrel due to inertial loadings were expected to be small due to its high stiffness and relatively low mass. Accordingly, the ratio of 0.29 for the model and prototype scale core barrel was not considered problematic, which was confirmed in the experiments.

2.6 Scaling of outer vessel

An approach similar to that presented in section 2.5 for the core barrel should ideally be used for scaling FSI and dynamic effects for the outer vessel as well. However, as mentioned in 2.3, an existing steel vessel with a wall thickness of 7.9 mm was used. Considering steel as the model material for the outer vessel, relevant quantities for scaling are listed in Table 2.5.

Table 2.5. Scaling analysis, steel as outer vessel material

	Prototype at 600°C†	Model	Scale factor
Fluid density, ρ	1986 kg/m^3 (2011 kg/m^3 – 1962 kg/m^3)	998 kg/m^3	$S_\rho = 0.50$
Elastic modulus, outer vessel, E	148 GPa (155 GPa – 148 GPa)	200 GPa	$S_E = 1.35$
Mass density, outer vessel, ρ_{sv}	7709 kg/m^3 (7731 kg/m^3 – 7688 kg/m^3)	7800 kg/m^3	$S_{\rho_{sv}} = 1.01$
Size (generalized), L	-	-	$S_L = 0.39$
Thickness, h	60 mm	7.9 mm	$S_h = 0.13$
Velocity (flow), U	-	-	$S_U = 0.62$

†Values in parenthesis indicate range over 550 °C - 650 °C

Using the values in Table 2.5, it can be shown that the ratio of π_7 or $\tilde{\pi}_8$ for the model and the prototype is not equal to one as noted below, indicating distortion:

$$\frac{\pi_{7,m}}{\pi_{7,p}} = 0.29 \quad \text{and} \quad \frac{\tilde{\pi}_{8,m}}{\tilde{\pi}_{8,p}} = 0.43$$

The distortion in the force response of the vessel was inevitable, unless artificial masses could be added. However, the distortion in terms of FSI effects was ignored since the vessel was practically rigid at both the model and prototype scales.

2.7 Summary

This section presented scaling analyses for different test components of a model FHR for earthquake simulator testing. A length scale of 0.39 was selected except for thickness of the core barrel, for which a length scale of 0.16 was used. Model components were scaled per different governing scaling laws. There were practical limits, in terms of available materials and space, on ideal scaling of all components and desired behaviors, and compromises were inevitable. Possible compromises were identified in terms of

importance to the test goals and made such that important behaviors (e.g., buoyancy in the reflector blocks, fluid-structure interaction in the core barrel) were simulated as best as possible at the model scale. Table 2.6 summarizes the analyses for different components. The presented information was used to design the scale model, the geometry of which is described in detail in the next section.

Table 2.6. Summary of scaling analysis

Component	Governing behavior or property for scaling analysis	Material	
		Prototype scale	Model Scale
Outer vessel	Interaction with coolant	Stainless steel	Carbon steel
Core barrel	Interaction with coolant	Stainless steel	Aluminum
Fuel pebbles	Buoyancy and flow behavior	Graphite pebbles filled with TRISO particles	Polypropylene
Reflector blocks	Buoyancy and stiffness	Graphite	Polypropylene
Coolant	Buoyancy of submerged components (fuel pebbles and reflector blocks)	Molten salt (Flibe: a LiF/BeF_2 mixture)	Water

SECTION 3
MODEL DESCRIPTION AND BUILD

3.1 Introduction

The scaling analyses presented in Section 2 informed the design of a scale model of a Fluoride salt-cooled High temperature Reactor (FHR) for earthquake-simulator testing. The tested model included representations of a reactor vessel, core barrel, graphite reflector blocks, TRISO fuel pebbles, and molten salt coolant. Section 3.2 describes the geometry of the model components and the sequence of assembling the model. Challenges, associated with tight tolerances in the model components, were encountered during the model build, and those are discussed in section 3.2.1.1. The properties of the friction pendulum bearings used to seismically isolate the model are described in 3.3.

3.2 Model geometry and build

A schematic of the model on the earthquake simulator is shown in Figure 3.1. The primary components of the model included a base plate, a cylindrical outer vessel (OV) and a cylindrical core barrel (CB) each provided with a flange, a double ring with vertical pins at the base of the vessel, polypropylene *reflector-block assembly*, top ring with pins, head, and polypropylene (PP) pebbles. A flexible tube for instrumentation was inserted through the top of the head and the reflector-block assembly, as shown in Figure 3.1. The vessel base was supported on four load cells (introduced later) in the fixed-base tests and on four bearings in the isolated configuration. A description of the model components is provided in this sub-section.

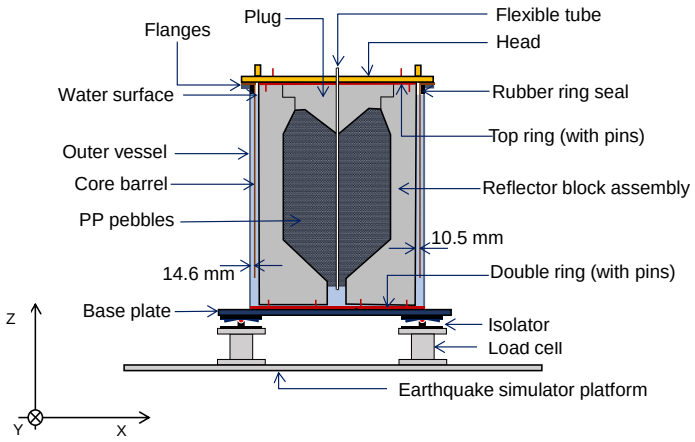

Figure 3.1. Schematic of the model on the earthquake-simulator platform, base-isolated configuration

The cylindrical outer vessel had a height of 2 m, an outer diameter of 1.524 m, and a wall thickness of 7.9 mm. The vessel was welded to a 95 mm thick base plate with plan dimensions of 2 m × 2 m. A 76.2 mm

wide, 25.4 mm thick flange was welded to the top of the vessel. The outer vessel, base plate, and the flange were fabricated using carbon steel.

The aluminum core barrel had a height of 1.778 m, an outer diameter of 1.479 m, and a wall thickness of 2 mm. A 98.4 mm wide, 12.7 mm thick (aluminum) flange was welded at its top. The core barrel was placed concentrically within the vessel such that its flange rested on the flange of the outer vessel (see Figure 3.1). A nominal radial gap (*annulus*) of 14.6 mm separated the outer surface of the core barrel and the inner surface of the outer vessel. The core barrel was provided with twenty-four tabs (*spacers*) in arrays of eight at three heights (see Figure 3.2a). Each tab was 50.8 mm long, 9.5 mm wide, and 3.1 mm thick. The tabs were welded to the core barrel such that their width (9.5 mm) was oriented radially, as shown in Figure 3.2a. A fill level (water) of 1.93 m was used for testing. The space above the free surface of water, between the outer vessel and the core barrel, was filled with rubber, as shown in Figure 3.2b, such that sloshing of water in this space was prevented, consistent with the prototype boundary condition of this annulus not having a free surface.

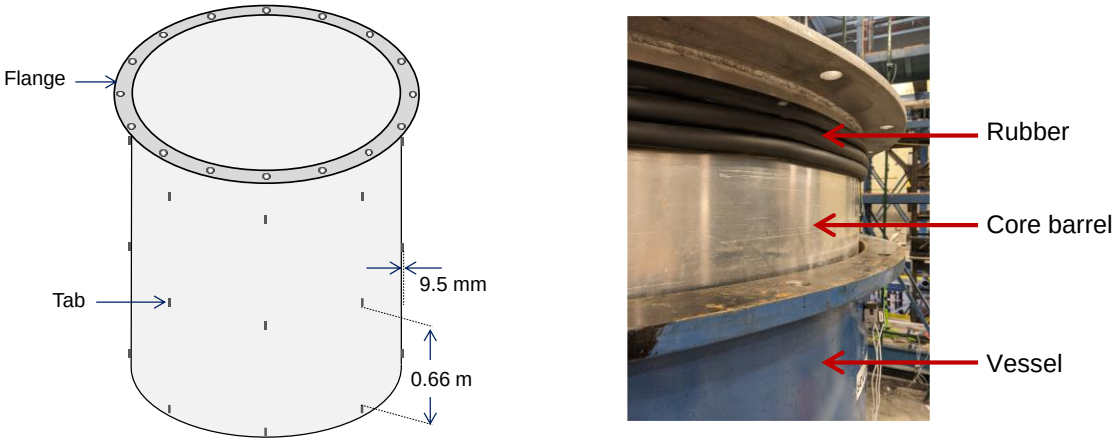

a. schematic b. rubber ring seal between vessel and core barrel

Figure 3.2. Core barrel, schematic and placement

A 12.7 mm thick steel *double ring* (see Figure 3.1) was welded to the base of the vessel, as shown in Figure 3.3. The ring was provided with thirty-two vertically oriented pins (see Figure 3.3), arranged in two arrays of sixteen pins, along circles of diameters 0.71 m and 1.32 m. Each pin had a diameter of 12.7 mm and protruded 50.8 mm above the upper face of the ring. These pins were provided to ensure proper positioning of the reflector-block assembly during installation and when afloat.

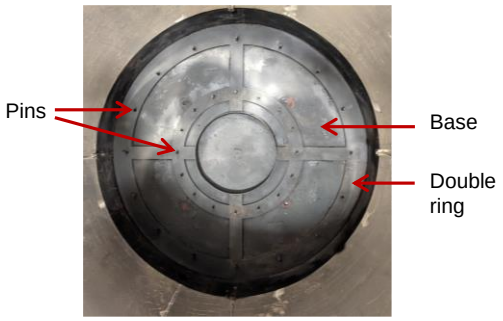

Figure 3.3. Double ring at the base of the vessel

Figure 3.4 presents a cutaway view of the reflector-block assembly. The assembly comprised sixteen vertical columns and a top block referred to hereafter as the *plug*. Each of the sixteen vertical columns comprised a stack of fourteen blocks, denoted RB-1 through RB-14. Blocks RB-1 and RB-14 denote the lower most and the upper most blocks in a column, respectively. Air voids (hollow spaces) with a net volume of 0.141 m^3 were provided in blocks RB-1, RB-2, RB-3, RB-5, RB-6, RB-7, RB-8, RB-9, RB-10 to reduce the equivalent density of the reflector-block assembly as a whole, as explained in section 2.4. The air voids can be seen in the cutaway view presented in Figure 3.4. A nominal gap (*annulus*) of 10.5 mm separated the outer surface of the reflector-block assembly and the inner face of the core barrel (see Figure 3.1). The fluid in in this gap was free to slosh under seismic excitations.

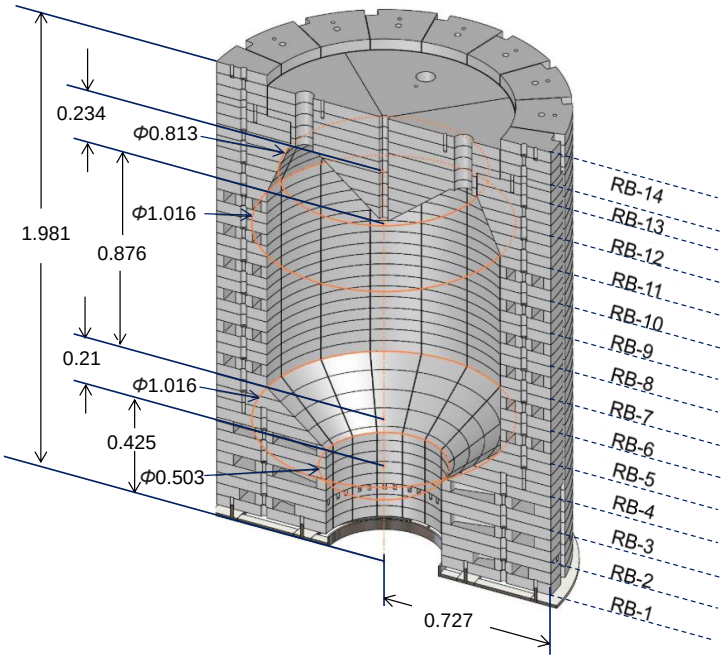

Figure 3.4. Reflector-block assembly, cutaway view, dimensions in m

Drawings of the fourteen blocks and the plug are shown in Figure 3.5 (Blocks RB-5 through RB-10 were of a similar geometry). The blocks were fabricated by gluing machined sheets of polypropylene which were cut to specific shapes using a waterjet. Three sheets were used for each block, except for RB-13, for which two sheets were used.

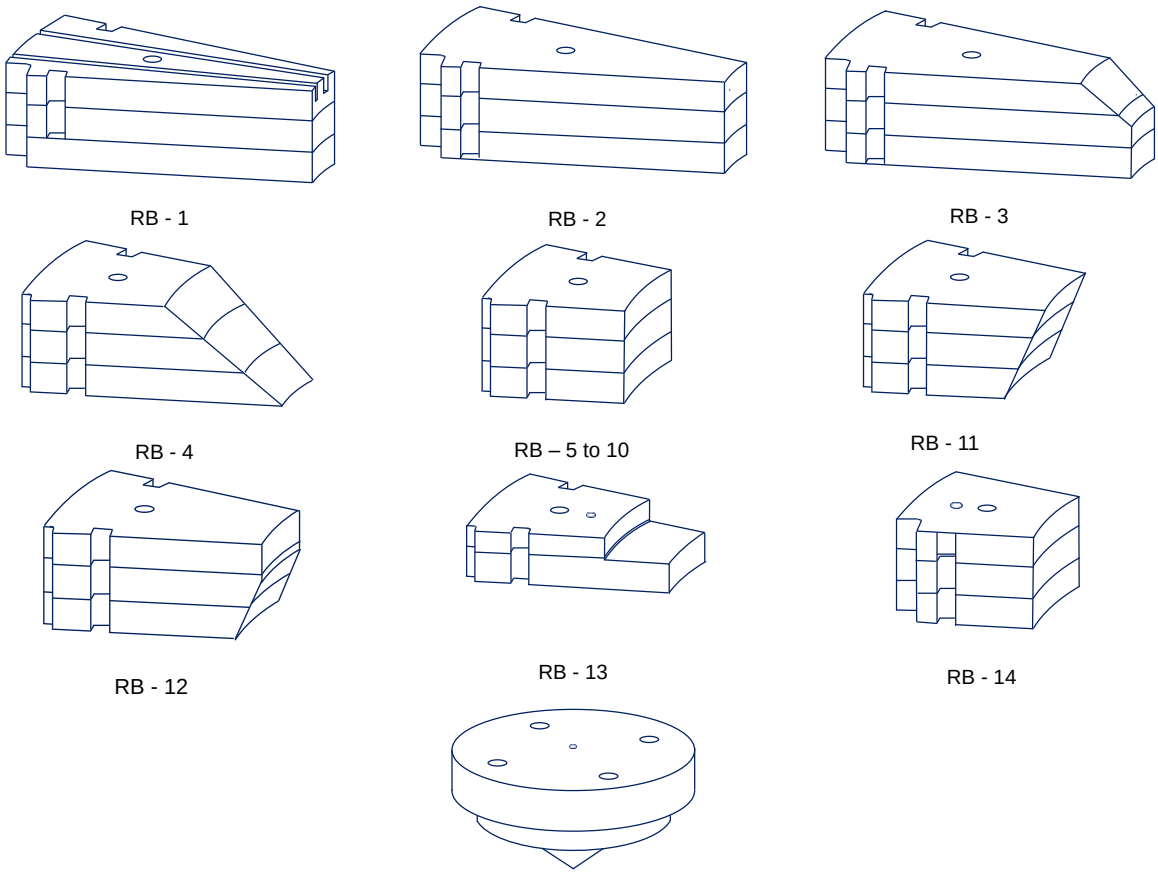

Figure 3.5. Reflector blocks

Blocks in a column were connected by polypropylene shear pins, 12.7 mm in diameter. Circular, partial-depth slots of 15.2 mm diameter were provided in the blocks to accommodate these pins. The underside of RB-1 was provided with two circular slots to interface with the steel pins protruding above the double ring (see Figure 3.4). Blocks in adjacent columns were connected by polypropylene shear keys, rectangular in cross section. The shear keys had cross sectional dimensions of 25.4 mm × 50.8 mm. The corresponding slot for a shear key formed by two adjacent blocks (of two adjacent vertical columns) had cross sectional dimensions of 27.9 mm × 55.9 mm. A slot was also provided at the periphery of each block for

instrumentation wires. Figure 3.6 shows the slots for the shear key, shear pin, and instrumentation wires in one block. Similar slots were provided in other blocks, as presented in Figure 3.5.

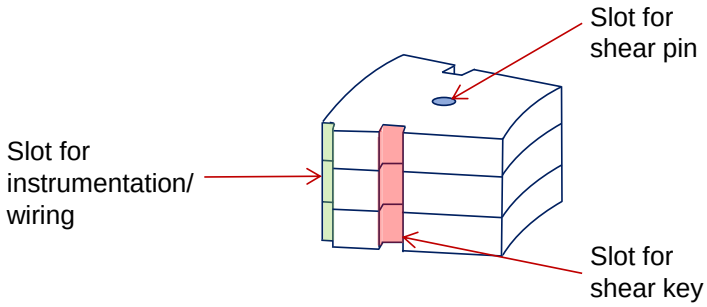

Figure 3.6. Slots in RB-5 to 10

A 12.7 mm thick, steel *top-ring* with inner and outer diameters of 1.22 m and 1.37 m, respectively, and sixteen and four steel pins on the lower and upper faces, respectively, as shown in Figure 3.7, was used to interface between the reflector-block assembly and the head of the vessel (described below). The pins were 12.7 mm in diameter. The four pins on the upper face were fabricated from threaded rod. The pins on the lower face fitted into slots in the top-most blocks of the sixteen reflector block columns and the threaded pins on the upper face (referred as top-ring threaded pins hereafter) protruded through slots in the head.

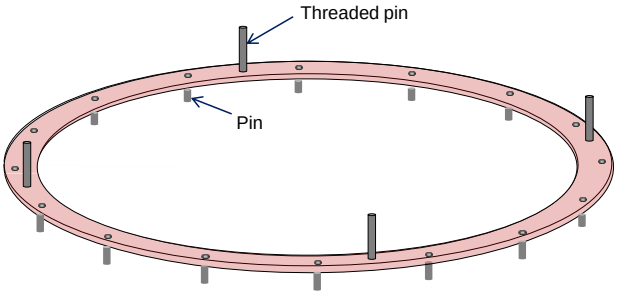

Figure 3.7. Top ring

The head of the assembly was a 38.1 mm thick circular plate, as shown in Figure 3.8a. The plate was provided with *through holes* for bolts and slots for instrumentation wires, top-ring threaded pins, and pebble loading and viewing as indicated in the figure. In the assembled condition, the top-ring threaded pins were secured to the head using nuts and washers, as presented in Figure 3.8b. The head and the flanges of the core barrel and the outer vessel were connected using sixteen 25.4 mm diameter bolts.

The pebbles used in the experiments were 15.87 mm diameter PP spheres as presented in Figure 3.9. A total of 285,000 pebbles were used. The nominal density of the spheres, as specified by the manufacturer, was 880 kg/m^3.

Coolant flow through the fuel pebbles in the core of the reactor vessel was not simulated.

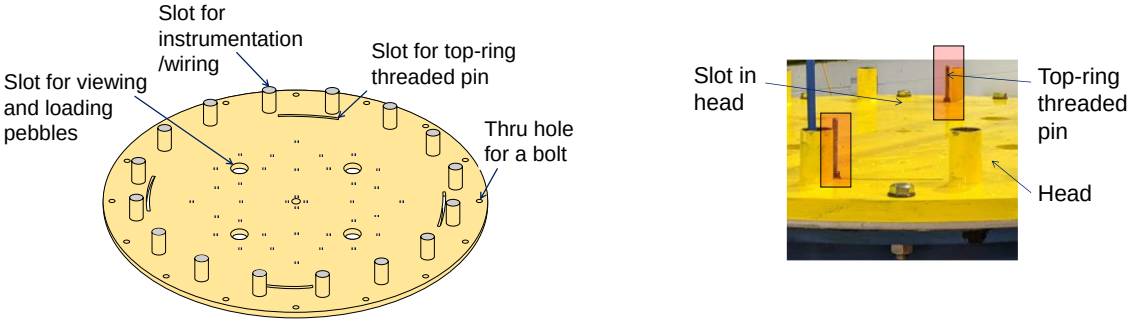

a. slots in head

b. top-ring threaded pins secured to head

Figure 3.8. Head of the vessel

Figure 3.9. A pebble used in the experiments

3.2.1 Assembly sequence and challenges

This sub-section describes the sequence in which the model was assembled. (The sequence described here does not include the installation of the load cells or the bearings under the base of the vessel.) The double-ring was welded to the base of the vessel first. This was followed by placement of the rubber ring on the core barrel and lowering the core barrel (see Figure 3.2b) inside the outer vessel using an overhead crane. The reflector blocks were manually placed inside the vessel, one block at a time (see Figure 3.10b). After the first (of fourteen) layer of reflector blocks had been positioned (see Figure 3.10c), shear keys and shear pins were installed, as shown in Figure 3.10d and Figure 3.10e. The shear keys connected adjacent blocks in a layer and the shear pins interfaced with the next layer. This procedure of placing blocks, shear keys, and shear pins was repeated until all fourteen layers of the assembly had been assembled inside the vessel

(see Figure 3.10f). The top ring was then placed atop the fourteenth layer, as shown in Figure 3.10g and Figure 3.10h, using an overhead crane. Figure 3.11 presents pictures taken at different stages of the assembly.

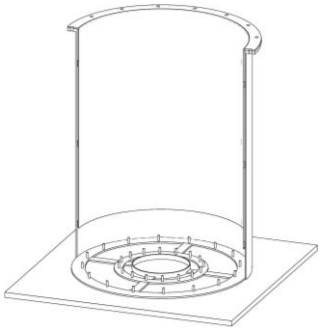

a. double ring and core barrel in place

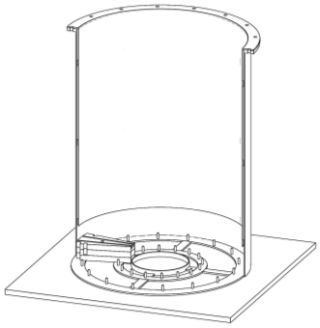

b. one RB-1 in place

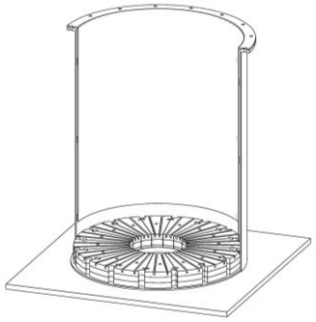

c. sixteen RB-1 blocks in place (first of fourteen layers)

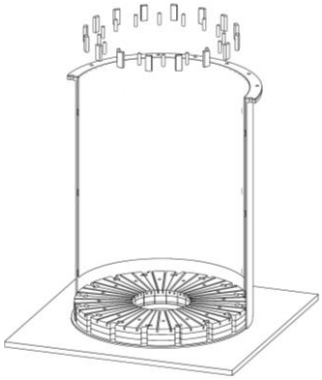

d. shear keys and pins above first layer

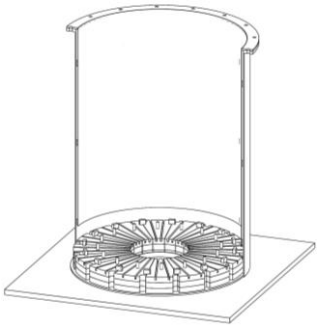

e. shear keys and pins above first layer in place

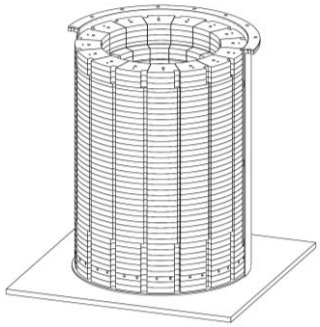

f. reflector-block assembly, except plug, in place

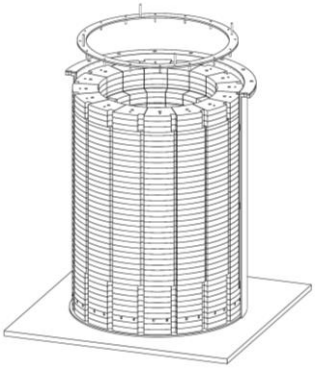

g. placement of the top ring

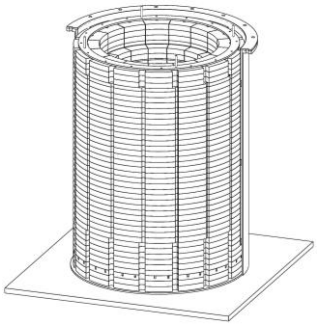

h. top ring in place

Figure 3.10. Assembly sequence, cutaway views of outer vessel and core barrel shown

a. three layers of reflector blocks installed

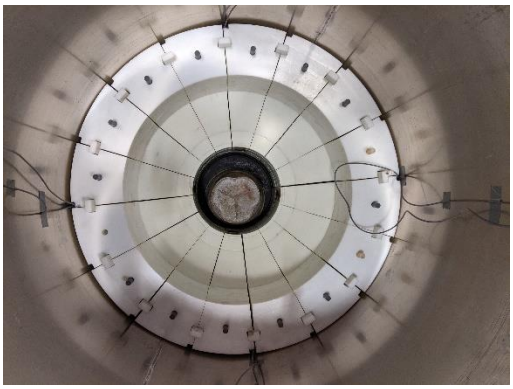

b. six layers of reflector blocks installed

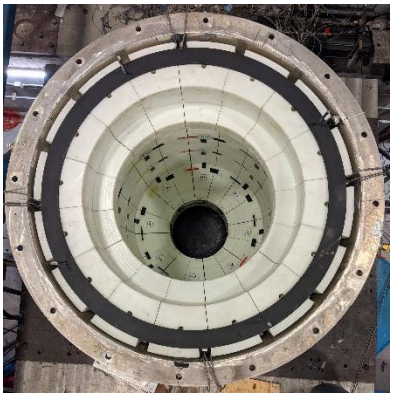

c. fourteen layers of reflector blocks and the top ring in place

Figure 3.11. Different stages of building the reflector-block assembly

The reflector-block assembly was completed by placing the plug in position using an overhead crane, as shown in Figure 3.12. The head was also positioned using an overhead crane, as shown in Figure 3.13. Water was filled through an inlet provided in the vessel wall, as indicated in Figure 3.13. A slot was cut in the rubber ring (between the outer vessel and the core barrel) at the location of the inlet such that water could flow down the annulus between the core barrel and the outer vessel. An air outlet, with arrangement similar to the inlet, was provided in the outer vessel at a location diametrically opposite to the inlet. The air outlet was provided to ensure an exit path for air leaving the annulus between the outer vessel and the core barrel during filling with water. (This air outlet proved to be unnecessary because the flange of the core barrel did not have an air-tight fit with the flange of the outer vessel in the bolted condition.)

a. positioning the plug using an overhead crane

b. completed reflector-block assembly

Figure 3.12. Placement of plug

Figure 3.13. Placement of head

Pebbles were manually loaded into the vessel through the four large-sized holes in the head (see Figure 3.8a). During the loading process, the flow of water into and out of the vessel was controlled such that the underside of the pebble bed stayed above the bottom layer of reflector blocks and the reflector-block assembly floated at all times. A borescope (Make: DEPSTECH) was inserted into the interior of the reflector-block assembly (core) through the hollow tube shown in Figure 3.1 and used to monitor the location of the underside of the pebble bed and the lowermost layer of reflector blocks during loading.

3.2.1.1 Challenges

Listed below are some challenges encountered during the assembly of the model for earthquake-simulator testing. These were associated with tight design tolerances.

1. The outer radius of the double ring was 1.6 mm smaller than the inner radius of the vessel. Lowering the double-ring assembly into the vessel (using an overhead crane) such that it laid flat (horizontal) on the base of the vessel was challenging because of small fabrication-related shape distortions in the outer vessel and the ring (see Figure 3.14). Multiple regions along the periphery of the double ring were machined on-site using an angle grinder to ensure proper placement of the ring.

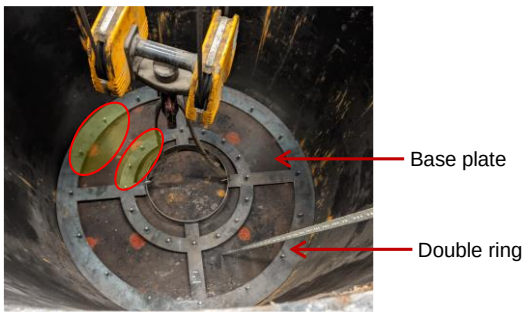

Figure 3.14. Vertical gaps (highlighted) between the double ring and the base of the vessel

2. The underside of each block in the first layer (RB-1) of the reflector-block assembly was provided with two circular slots to interface with the 50.8 mm long steel pins projecting above the double ring. The circular slots and pins had diameters of 15.2 mm and 12.7 mm, respectively. In the water-filled condition, the reflector-block assembly was designed to float 25.4 mm above the double ring such that the pins stayed engaged with the slots over a length of 25.4 mm. However, the designed difference in the diameters of the pins and the slots was small and practically insufficient to allow all columns of the reflector-block assembly to float freely. To allow free vertical movement of the reflector-block assembly, the slots sizes in the lower layer of blocks were increased to a diameter of 17.1 mm (using a 43/64-inch drill bit).

3. The design gap between the lateral surface of the reflector-block assembly and the inside of the core barrel was 10.5 mm. Measurements taken after the reflector-block assembly was built and before placement of the head indicated that the gap size varied along the circumference. Figure 3.15 presents measurements of the gap taken at eight locations. The size varied between 9.5 mm and 15.1 mm. Measurements of gap size could not be taken after placement of the head.

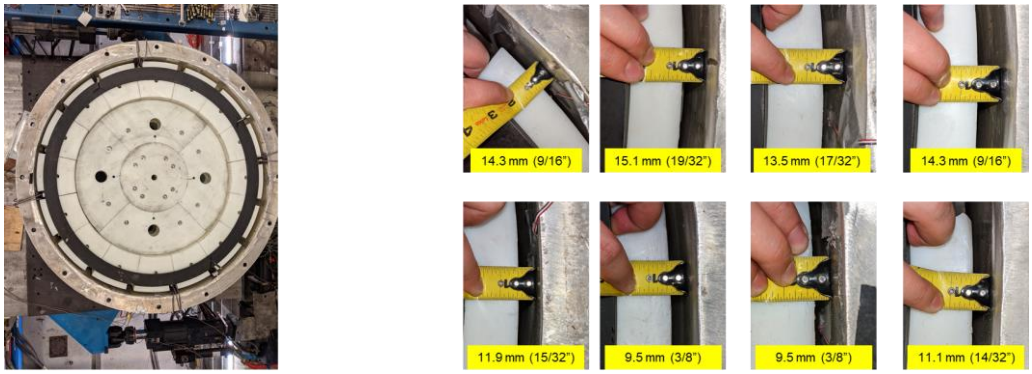

a. completed reflector-block assembly

b. gap at eight locations, inch-tape

Figure 3.15. Gap between reflector-block assembly and core barrel

4. The placement of the head using an overhead crane, as shown in Figure 3.13, such that the four top-ring threaded pins engaged the four slots in the head was challenging and required manual adjustment. At the prototype scale, such a manual intervention may not be practical.

5. The designed gap between adjacent reflector blocks in a layer was 2.8 mm, as indicated in Figure 3.16a. In the fully-assembled and water-filled condition, the gaps between blocks in a layer coalesced at a few locations creating gaps large enough to accommodate the 15.87-mm diameter pebbles (see Figure 3.16b). To prevent pebbles from entering such large gaps between columns of reflector blocks, a fabric net was subsequently installed inside the reflector-block assembly, as shown in Figure 3.16c.

a. designed gap of 2.8 mm between adjacent blocks in a layer

b. pebbles in gap between adjacent columns of blocks

c. fabric net installed on inside the reflector-block assembly

Figure 3.16. Gap between adjacent blocks and installed fabric net

3.3 Friction pendulum bearings

Two types of friction pendulum (FP) bearings were used to base-isolate the model described above: 1) Single concave Friction Pendulum (SFP) bearings, and 2) Triple Friction Pendulum (TFP) bearings. Four bearings of a type (SFP or TFP) were installed under the base of the vessel for tests in the isolated configurations, as presented in Figure 3.1. The bearings were tested individually to characterize their force-displacement behavior in the horizontal and vertical directions. The characterization tests for the bearings are summarized below and described in detail in Appendix A.

3.3.1 SFP isolators

The four SFP bearings used for testing are identified here as SFP1, SFP2, SFP3, and SFP4. Each bearing consists of a sliding surface (concave plate), a housing plate, and a slider that is coated with a PTFE-type composite, as shown in Figure 3.17. Figure 3.18 presents the fabrication drawings of the bearings, as provided by the manufacturer, Earthquake Protection Systems. The bearings had a sliding period of 1.38 seconds (where period is a function of the radius of curvature of the sliding surface) and a displacement capacity of approximately 9 cm. The idealized force-displacement behavior of an SFP isolator in the horizontal directions is characterized by the radius of curvature of the sliding surface (R) and the coefficient of friction (μ) at the sliding surface (see Figure 3.19). The coefficient of friction is a function of axial load on the bearing, sliding velocity, and temperature of the sliding surface. An increase in axial load leads to a reduction in the coefficient of friction. The coefficient of friction at near zero sliding velocity is referred to as the breakaway friction. As the sliding velocity increases, the coefficient of friction drops to a minimum value ($\mu_{\min}$) at a small sliding velocity before attaining a maximum value ($\mu_{\max}$) at a higher velocity. In general, for a fixed value of axial load, the relationship between the coefficient of friction and the sliding velocity (V) can be described by (Constantinou *et al.* 2007):

$$\mu = \mu_{\max} - (\mu_{\max} - \mu_{\min})e^{-aV} \tag{3-1}$$

where a is a rate parameter. The coefficient of friction reduces with an increase in temperature of the sliding surface.

The behavior of an SFP bearing in the vertical direction is characterized by stiffness under a specified (compressive) axial load (the stiffness in tension is zero). Figure 3.20 shows a representative axial force-axial displacement behavior of a friction pendulum bearing. The axial stiffness is small at low axial load and increases with axial load.

Figure 3.17. Components of an SFP isolator

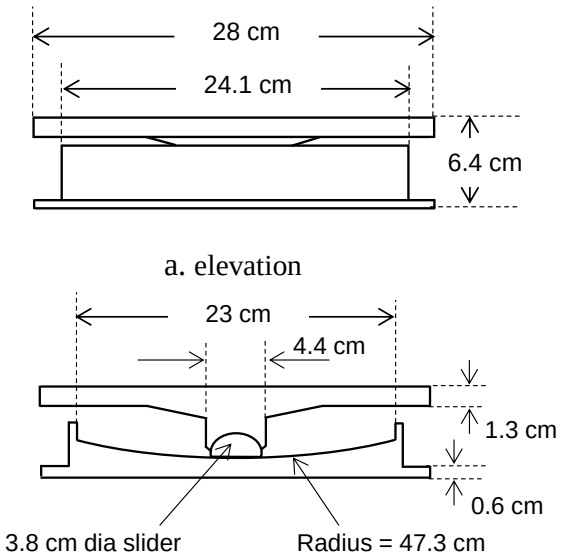

a. elevation

b. cross-section

Figure 3.18. Fabrication drawings of SFP isolators (provided by Earthquake Protection Systems)

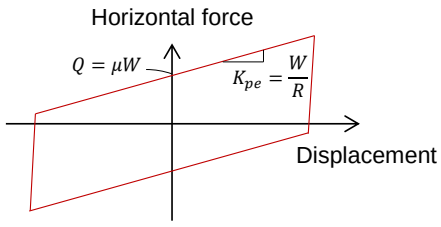

Figure 3.19. Force-displacement behavior of an SFP isolator

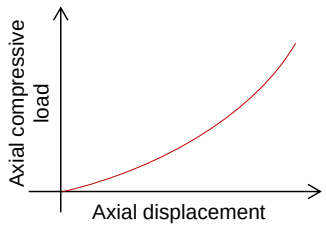

Figure 3.20. Representative behavior of a friction pendulum bearing in compression

The behavior of the four SFP bearings under horizontal and vertical loads was characterized at an axial load of 20 kN (4.5 kips), which was approximately equal to the expected load per bearing in the earthquake-simulator tests. Behavior under horizontal loads was characterized by estimating slow and fast coefficients of friction using a bearing testing machine (BTM) (Warn and Whittaker 2006). The radius of the sliding surface is a known geometric quantity. The velocity dependence of the coefficient of friction for each bearing was characterized by a rate parameter (see equation (3-1)). The behavior under vertical load was established by estimating the vertical stiffness of each bearing at an axial load of 20 kN using a tension-compression machine. Table 3.1 summarizes results of characterization tests for the four SFP bearings.

Table 3.1. Summary of characterization tests for SFP bearings, axial load = 20 kN

Bearing	Friction coefficient (slow), μ_{min} (%)	Friction coefficient (fast), μ_{max} (%)	Rate parameter (s/cm)	Axial stiffness ($\times 10^5$ kN/m)
SFP1	3.7	12.5	0.39	1.08
SFP2	2.3	7.5	0.67	0.96
SFP3	2.6	10.5	0.35	1.07
SFP4	2.4	10.1	0.35	1.20
Average	2.8	10.2	0.44	1.07

3.3.2 TFP isolators

The four TFP bearings used in tests are identified here as TFP1, TFP2, TFP3, and TFP4. A TFP bearing comprises two concave plates (top and bottom) and a slider assembly, as shown in Figure 3.21. Two concave plates separated by a rigid slider and enclosed in a rubber seal form the slider assembly. The surfaces of the slider assembly in contact with the top and bottom concave plates and the surfaces of the rigid slider in contact with the concave plates of the slider assembly are coated with a PTFE-type material.

Figure 3.22 presents the construction of the TFP bearings. The four surfaces on which sliding is permitted are marked 1 through 4 in Figure 3.22b. The bearings had a sliding period (for sliding on the outer concave surfaces) of 1.96 seconds (frequency of 0.51 Hz) and a displacement capacity of about 16 cm.

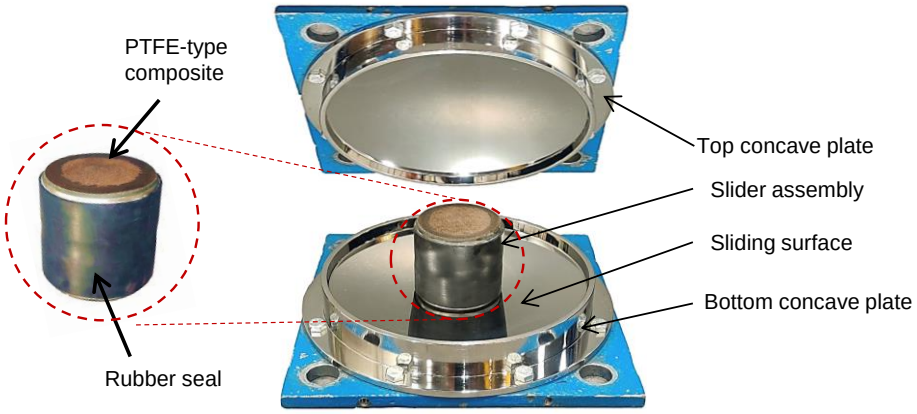

Figure 3.21. Components of a TFP isolator

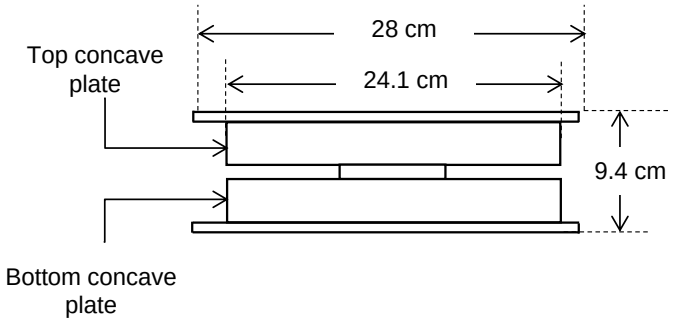

a. elevation

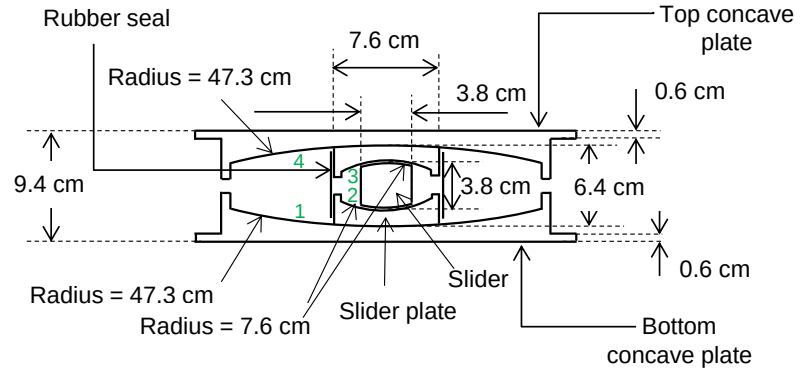

b. cross-section, sliding surfaces numbered 1 through 4 in green

Figure 3.22. Fabrication drawings of TFP isolators (provided by Earthquake Protection Systems)

Figure 3.23 presents the horizontal force-displacement behavior of a TFP bearing. The force-displacement relationship in a TFP bearing is displacement dependent and differs depending on which of the four sliding surfaces accommodate bearing displacements. Accordingly, (sliding) Regimes I through V are identified in Figure 3.23. A detailed discussion of the force-displacement relationships of a TFP bearing in different *sliding* regimes is presented in Section 4 of Fenz and Constantinou (2008) and not reproduced here. The relationships are characterized by the radii of curvature of the sliding surfaces and the coefficients of friction at the four sliding surfaces. The radii of curvature of the surfaces are known geometric quantities (see Figure 3.22b). The coefficients of friction of the four surfaces were determined from tests in the BTM and were such that $\mu_1 = \mu_4 > \mu_2 = \mu_3$, where μ_i denotes the coefficient of friction at sliding surface i. Such a relationship between coefficients of friction is common in practice. The minimum and maximum values of $\mu_1 (= \mu_4)$ (outer surface friction) at slow and fast sliding velocities, respectively, was determined from the characterization tests. The velocity dependence of friction at sliding surface 1 (or 4) was characterized by a rate parameter, as introduced in equation (3-1).

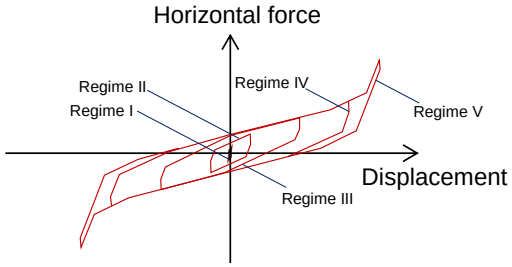

Figure 3.23. Force-displacement behavior of a TFP bearing

Achieving high sliding velocities at the inner surfaces (2 and 3) in tests is difficult. Thus, only the minimum value of $\mu_2 (= \mu_3)$ (inner surface friction) was determined in the tests. The maximum value of $\mu_2 (= \mu_3)$ was assumed to be equal to the product of the estimated minimum value and the ratio of the maximum and minimum values of $\mu_1 (= \mu_4)$. The rate parameter characterizing the velocity dependance of μ_2 (or μ_3) was assumed to be identical to that for μ_1 (or μ_4). These assumptions regarding friction on the inner surface are insignificant because the behavior of a TFP bearing is primarily governed by sliding on the outer surfaces (McVitty and Constantinou 2015).

The behavior of the TFP bearings in the vertical direction was characterized by estimation of vertical stiffness at a specified axial load (20 kN here), as explained previously for SFP bearings.

Table 3.2 summarizes results of characterization tests for the four TFP bearings.

Table 3.2. Summary of characterization tests for TFP bearings, axial load = 20 kN

Bearing	Friction coefficients				Rate parameter (s/cm)	Axial stiffness ($\times 10^5$ kN/m)
	$\mu_2 = \mu_3$ (%)		$\mu_1 = \mu_4$ (%)			
	Minimum (slow)	Maximum (fast)	Minimum (slow)	Maximum (fast)		
TFP1	2.1	4.7	7.0	15.5	0.28	1.08
TFP2	2.2	5.0	6.0	13.6	0.47	1.10
TFP3	2.1	5.6	5.2	13.8	0.47	1.03
TFP4	2.3	5.0	6.6	14.3	0.47	1.00
Average	2.2	5.1	6.2	14.3	0.42	1.05

The variability in the estimated parameters for the SFP and TFP bearings, evident in Table 3.1 and Table 3.2, is typical for friction pendulum bearings at both model and prototype scales (e.g., see Sarlis *et al.* (2013) and McVitty and Constantinou (2015)).

3.4 Summary

A scale model of an FHR reactor was designed per scaling analyses presented in Section 2. The geometries of the different components of the scale model were described in this section. The sequence of assembling the components and the challenges encountered therein were discussed. Two types of friction pendulum bearings were used to seismically isolate the scale model at its base: Single concave Friction Pendulum bearings and Triple Friction Pendulum bearings. The properties used to characterize the behavior of the bearings were described.

SECTION 4
INSTRUMENTATION, SEISMIC INPUTS, AND TEST PLAN

4.1 Introduction

This section presents the instrumentation and test plan for the earthquake-simulator testing of the Fluoride salt-cooled High temperature Reactor (FHR) model described in section 3. The responses measured in the experiments included the dynamic response of the fluid (hydrodynamic pressure and sloshing displacements), base reactions, dynamic responses of the vessel, core barrel, and reflector blocks, reflector block attachment performance, and pebble bed compaction under shaking. Section 4.2 describes the instrumentation used to record these responses. Unidirectional, bidirectional, and three directional seismic motions were used as inputs to the specimen, as described in section 4.3. Section 4.4 introduces the three test series focused on different behaviors of the test components.

4.2 Instrumentation

The instrumentation plan described below accommodates the conventional and isolated configurations and was designed to capture the responses identified above. Figure 4.1 presents the cartesian (x, y, and z) and cylindrical (r, θ, z) coordinate systems used in the presentation that follows.

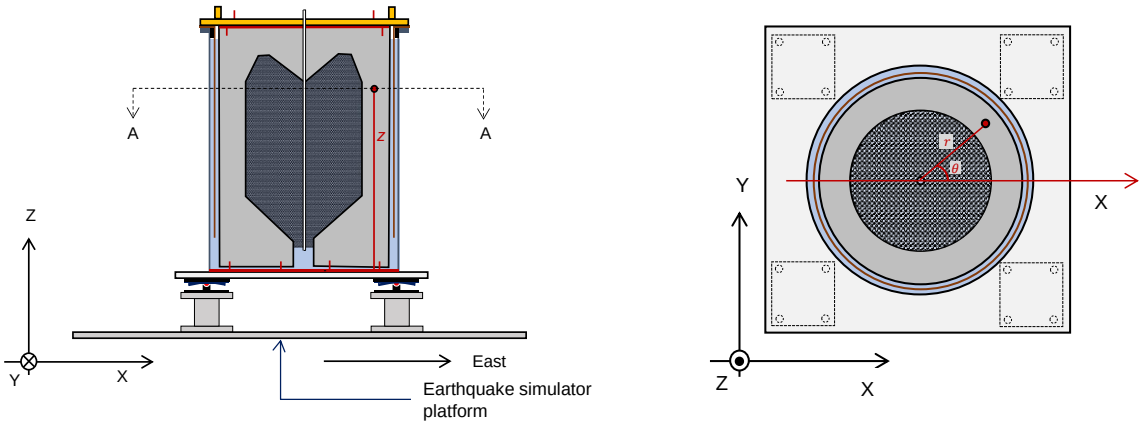

a. elevation b. section A-A, earthquake simulator not shown

Figure 4.1. Coordinate systems

Three-directional accelerations were recorded at the center of the earthquake-simulator platform at the location indicated by a green solid triangle in Figure 4.2a and 4.2b. Four vertically-oriented accelerometers were installed on the earthquake-simulator platform to record rocking accelerations of the simulator about

the two horizontal axes (*x* and *y*). The locations of these vertically-oriented accelerometers are indicated by red solid triangles in Figure 4.2b.

Four load cells were installed under the base of the vessel and used to measure reactions (shear forces and normal forces); see Figure 4.2a and 4.2c. The load cells were built at the University at Buffalo. A NIST (National Institute of Standards and Technology) traceable reference load cell was used to calibrate the load cells in a tension-compression machine (Tinius Olsen Testing Machine Co.) prior to earthquake-simulator testing; see Appendix A of Mir *et al.* (2022b) for details. The load cells were named LNE, LNW, LSE, and LSW, denoting the load cells at the north-eastern, north-western, south-eastern, and south-western corners, respectively, as shown in Figure 4.2c.

Three-directional acceleration responses were measured above the four load cells, on the base of the vessel (above the isolators), and near the top of the vessel, at the locations indicated by green solid triangles in Figure 4.2c, Figure 4.2d, and Figure 4.2f, respectively. Rocking accelerations above the isolation system (on the base of the vessel) were measured using four vertically-oriented accelerometers (in addition to the tri-axial accelerometers), as indicated by red solid triangles in Figure 4.2d.

Horizontal displacements of the isolators were measured using eight string potentiometers: four installed above the load cells and four above the isolators (on the base plate). The locations of the string potentiometers are indicated by solid yellow circles in Figure 4.2.

Twelve pressure gages, arranged in arrays of four at three heights (0.15 m, 0.914 m, and 1.524 m) above the base of the vessel, were used to measure hydrodynamic pressure on the wall of the outer vessel; see Figure 4.2a and 4.2e.

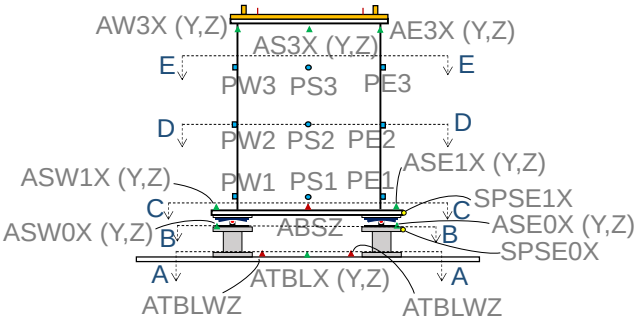

a. elevation

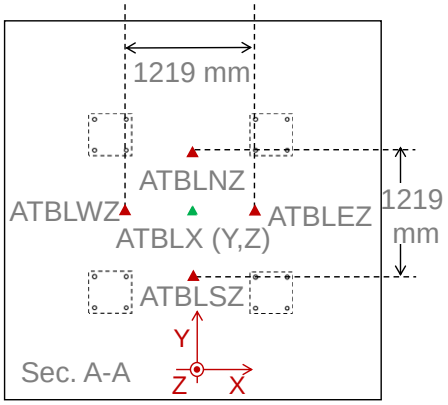

b. section A-A, earthquake simulator

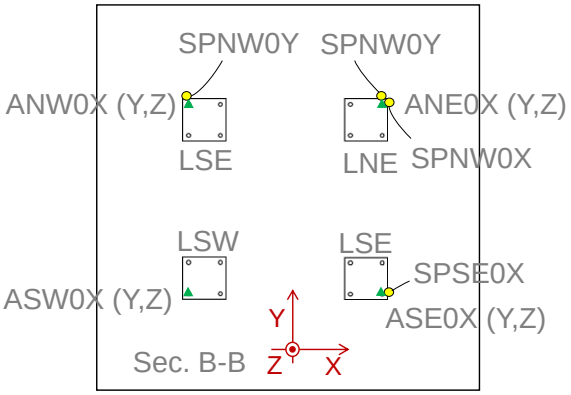

c. section B-B, above load cells

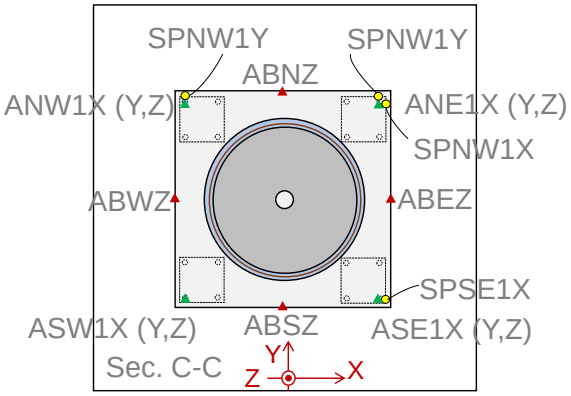

d. section C-C, above base plate

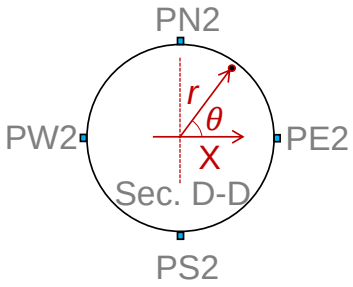

e. section D-D, pressure gages near mid-height of vessel

Figure 4.2. Instrumentation on outer vessel, base plate and earthquake simulator; accelerometer, string potentiometer and pressure gage names begin with ‘A’, ‘SP’, and ‘P’, respectively

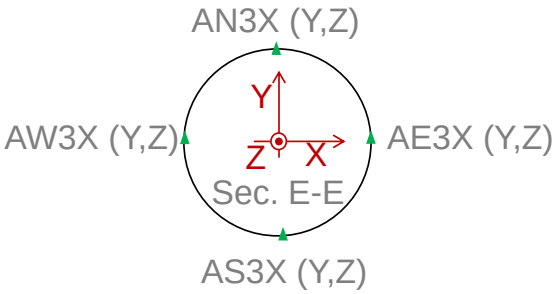

f. section E-E, top of the outer vessel

Figure 4.2. Instrumentation on outer vessel, base plate and earthquake simulator; accelerometer, string potentiometer and pressure gage names begin with 'A', 'SP' and 'P', respectively (cont.)

The acceleration and strain response of the core barrel was measured using four unidirectional accelerometers, waterproofed using an epoxy compound, and four strain gages as shown in Figure 4.3. The accelerometers were installed on the inner face of the core barrel. Slots were machined in the reflector blocks to accommodate these accelerometers and their wiring, as explained in section 3.2. The accelerometers were oriented at an angle of 9.5° to directions *x* and *y*, as indicated in Figure 4.3b.

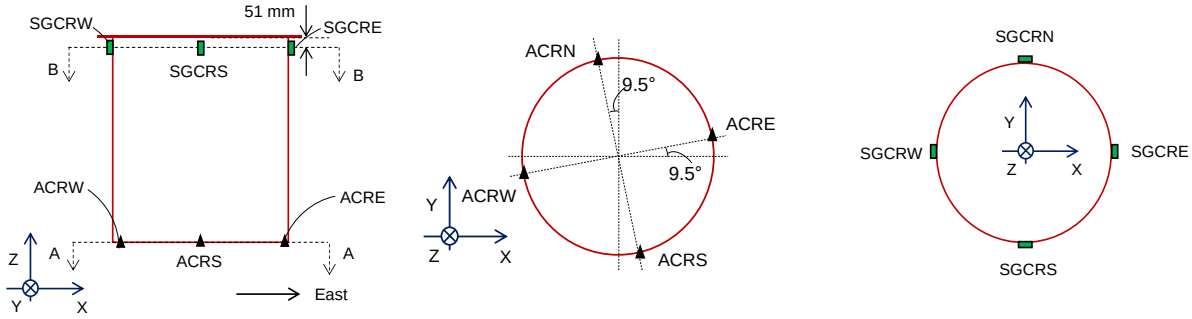

a. elevation b. section A-A, accelerometers c. section B-B, strain gages

Figure 4.3. Instrumentation on core barrel, accelerometer and strain gage names begin with 'ACR' and 'SGCR', respectively; angles not shown at scale

The vertical and lateral acceleration response of the reflector blocks was measured at four locations at the top of the blocks and four locations at the bottom of the blocks, as shown in Figure 4.4b. Similar to the accelerometers on the core barrel, the accelerometers on the reflector-block assembly were oriented at an angle of 9.5° to directions *x* and *y*, as indicated in Figure 4.4b.

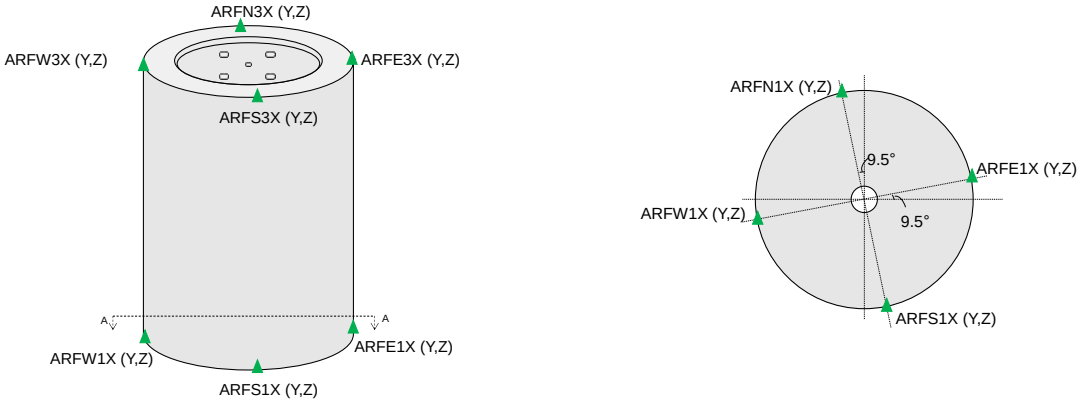

a. isometric view b. section A-A, angles not shown at scale

Figure 4.4. Instrumentation on reflector-block assembly, accelerometer names begin with 'ARF'

To evaluate the seismic behavior of the reflector blocks and the reflector-block assembly, *paper* markers were used on four blocks each in eight out of the sixteen vertical reflector-block assembly columns. (The four selected blocks were RB-4, RB-7, RB-9, and RB-11 per Figure 3.4 and Figure 3.5.) The selected eight vertical columns were denoted A through H and the selected four blocks in a column were denoted 1 through 4 such that the individual blocks were identified as A1, A2, A3, A4, B1, B2 and so on, as shown in Figure 4.5. Two markers, made of parchment paper (shown in black in Figure 4.5), were used on each selected block: one connecting the selected block to another block in an adjacent column and the other connecting it to a block above or below. The ends of the tape markers were secured to the blocks using adhesive tape. A borescope (Make: DEPSTECH; Model: 8.0MP WiFi Endoscope) was used to check for damaged markers after an earthquake simulator test. (The tests to evaluate the attachment performance were carried out prior to the installation of pebbles.)

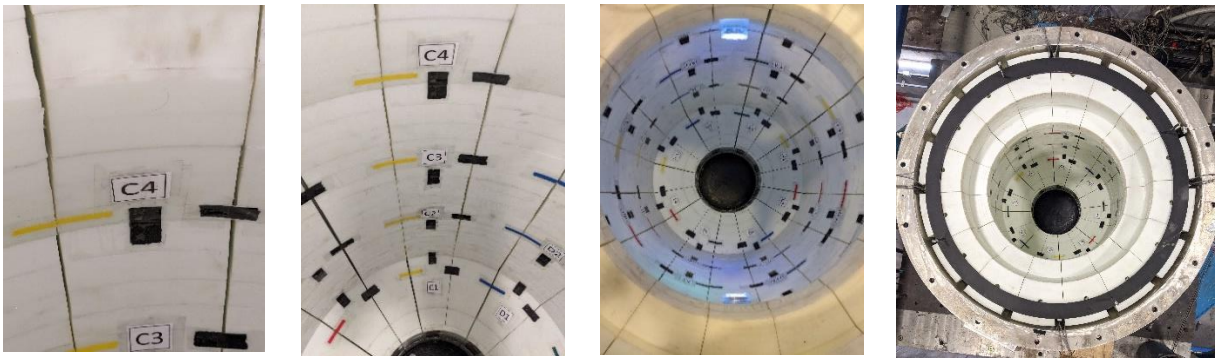

a. two black markers on block C4 b. markers on reflector-block assembly, different views

Figure 4.5. Markers for assessing attachment performance of reflector blocks

Visual scales were installed on blocks RB-2 and RB-3 of eight vertical columns of reflector blocks, as shown in Figure 4.6a, to assess compaction of the pebble bed. A visual scale comprised twenty bands with each band having a distinct color or pattern and a depth of 10 mm, as shown in Figure 4.6b. A borescope inserted through the tube shown in Figure 3.1 was used to capture images of the underside of the pebble bed against the visual scales before and after an earthquake simulator test. One such image is presented in Figure 4.6c. The vertical displacement of the underside of the pebble bed was used to calculate changes in pebble packing fraction.

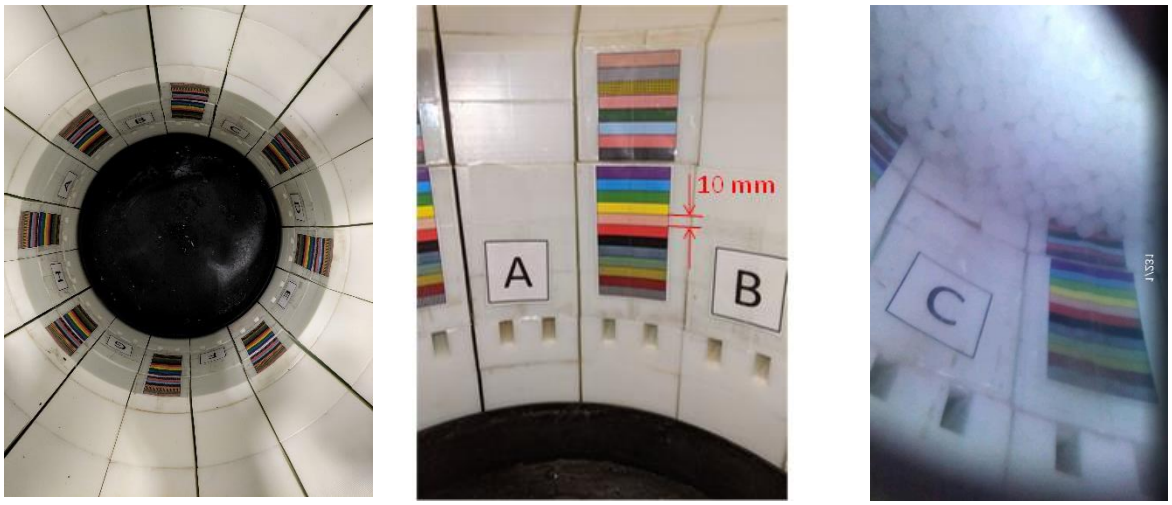

a. eight visual scales b. twenty bands of a visual scale c. picture of the underside of the pebble bed

Figure 4.6. Colored markers for assessing pebble consolidation

The sloshing displacements of water in the annular space between the reflector blocks and the core barrel were measured using two bespoke float-and-Temposonic sensors. Each sensor comprised a float attached to a lightweight tube mounted on to the waveguide of a Temposonic, as presented in Figure 4.7a. A magnet was attached to the top of the tube as shown in Figure 4.7a and the Temposonic recorded the vertical motion of the magnet, which was driven by the motion of the float. A discussion on the performance of this sensor is presented in Section B.6 of Mir *et al.* (2022b). The two sensors were installed above the head of the vessel on an overhead frame as shown in Figure 4.7b. The locations of the sensors in the $r-\theta$ plane (per Figure 4.1b) were $(r,\theta)=(0.7,-0.072\pi)$ and $(r,\theta)=(0.7,1.052\pi)$, and were denoted TE and TW, respectively, as indicated in Figure 4.7b.

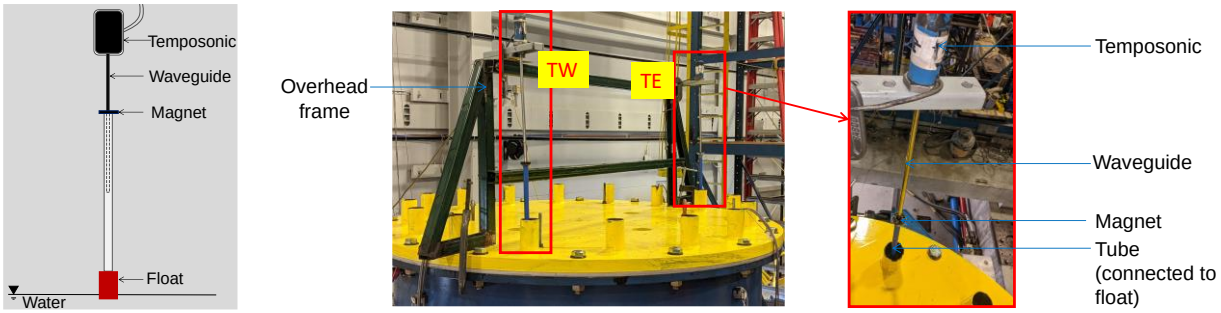

a. sensor, schematic b. TE and TW installed on an overhead frame

Figure 4.7. Float-and-Temposonic sensors for recording sloshing displacements

4.3 Seismic inputs

Four sets of three-component motions, including three recorded triplets, and one synthetic triplet were used for testing. The recorded ground motions were from the 1999 Chi-Chi Earthquake, the 1940 Imperial Valley earthquake, and the 1952 Kern County earthquake, and were extracted from PEER Ground Motion Database (http://ngawest2.berkeley.edu). The recorded motions were time-scaled to be consistent with the assumed length scale of test specimen: the time-axis was compressed by a factor of 1.6 ($=\sqrt{1/S_L}$, where $S_L = 0.39$ per section 2). The synthetic triplet had frequency contents that spanned a broad range (< 50 Hz) and is referred to as the broad-band motion (BBM) hereafter. The peak accelerations of the three components of the different inputs were selected to ensure that the displacement capacities of the earthquake simulator's actuators or the friction pendulum bearings were not exceeded. Table 4.1 presents information on the earthquake simulator inputs and Figure 4.8 presents the response spectra for the time-scaled inputs used in the experiments. The chosen ground motions envelop a wide frequency range: the horizontal components of Chi-Chi earthquake have a dominant low-frequency content whereas those of the Imperial Valley and Kern County earthquakes have a dominant high-frequency content.

Table 4.1. Earthquake-simulator inputs used for testing

Motion	Event	Recording station	Time scale compression	Peak accel. (g)		
				x	*y*	*z*
CCE	Chi-Chi earthquake, 1999	TCU052	1.6	0.4	0.19	0.14
ECE	Imperial Valley earthquake, 1940	El Centro Array #9	1.6	0.4	0.3	0.25
KCE	Kern County earthquake, 1952	Taft Lincoln School, 21	1.6	0.57	0.65	0.39
BBM	-	-	-	0.37	0.22	0.23

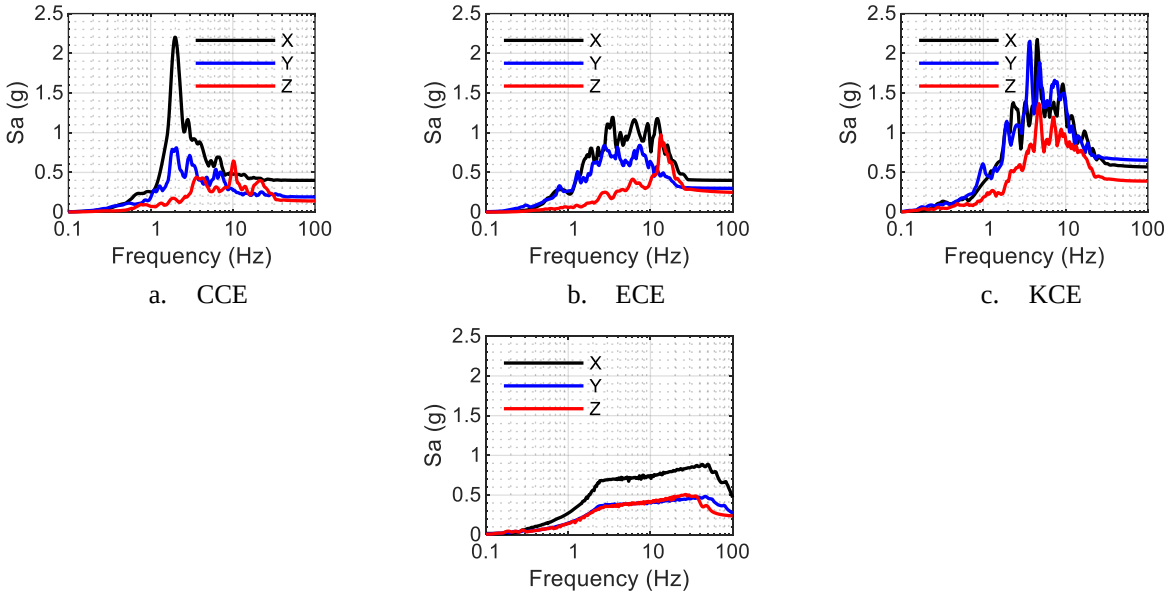

a. CCE b. ECE c. KCE

d. BBM

Figure 4.8. Response spectra of used earthquake simulator inputs, damping ratio of 5%

4.4 Test series

The earthquake-simulator tests of the test specimen were grouped into three series based on the previously defined objectives. Test series 1 through 3 are described below.

4.4.1 Test series 1

The primary objective of test series 1 was to assess the buoyant behavior and attachment performance of the reflector blocks. A secondary objective of the test series was to characterize the assembly comprising the vessel, the core barrel, the reflector blocks, and water. Accordingly, the *paper* markers and

accelerometers on the reflector blocks were the key instruments for this test series. Instrumentation on the outer vessel, core barrel, and the float-and-Temposonic sensors described in section 4.2, were also active. Pebbles were not placed for this test series. White noise excitations in the three directions, horizontal sinusoidal excitations of different frequencies, and one-directional (*x*) and three-directional (*x*, *y*, and *z*) inputs listed in Table 4.1 were used for testing. The input motions used for test series 1 are listed in Table 4.2.

Table 4.2. Input motions for test series 1

Number	Motion	*x*-direction PGA (g)	*y*-direction PGA (g)	*z*-direction PGA (g)
1	White noise, *x*	0.2	-	-
2	White noise, *y*	-	0.2	-
3	White noise, *z*	-	-	0.2
4	Sine sweep, *z*	-	-	0.15
5	Sine wave (0.5 Hz)	0.14	-	-
6	Sine wave (0.6 Hz)	0.16	-	-
7	Sine wave (0.7 Hz)	0.2	-	-
8	Sine wave (0.8 Hz)	0.18	-	-
9	Sine wave (1 Hz)	0.19	-	-
10	Sine wave (5 Hz)	0.43	-	-
11	CCE	0.4	-	-
12	ECE	0.4	-	-
13	KCE	0.57	-	-
14	BBM	0.37	-	-
15	CCE	0.4	0.19	0.14
16	ECE	0.4	0.3	0.25
17	KCE	0.57	0.65	0.39
18	BBM	0.37	0.22	0.23

4.4.2 Test series 2

Test series 2 involved earthquake-simulator tests of the complete assembly, including the pebbles. Tests were conducted in the fixed base configuration and two base-isolated configurations utilizing the Single

concave Friction Pendulum (SFP) bearings and Triple Friction Pendulum (TFP) bearings described in Section 3. Test configurations were grouped into sub-series 2-FB (fixed base), 2-SFP (base-isolated with Single concave Friction Pendulum bearings), and 2-TFP (base-isolated with Triple Friction Pendulum bearings). The input motions used for 2-FB, 2-SFP, and 2-TFP are listed in Table 4.3, Table 4.4, and Table 4.5, respectively. The peak accelerations of the CCE motion in 2-SFP and 2-TFP were reduced to 80% of the values listed in Table 4.1 because the isolation-system displacements in the full-scale CCE motion were close to the capacity of the bearings and an earthquake-simulator-control related amplification in the input acceleration could lead to the bearing displacement capacities being exceeded. Sloshing displacements, hydrodynamic pressure on the vessel wall, force response of the test assembly, dynamic responses of the core barrel and reflector blocks were of interest in test series 2. These responses were recorded using the instrumentation described previously.

Table 4.3. Input motions for test series 2-FB

Number	Motion	*x*-direction PGA (g)	*y*-direction PGA (g)	*z*-direction PGA (g)
1	White noise, *x*	0.2	-	-
2	White noise, *y*	-	0.2	-
3	White noise, *z*	-	-	0.2
4	Sine sweep, *z*	-	-	0.15
5	Sine wave (0.5 Hz)	0.1	-	-
6	Sine wave (0.6 Hz)	0.15	-	-
7	Sine wave (0.7 Hz)	0.17	-	-
8	Sine wave (0.8 Hz)	0.17	-	-
9	Sine wave (1 Hz)	0.18	-	-
10	Sine wave (5 Hz)	0.32	-	-
11	CCE	0.4	-	-
12	ECE	0.4	-	-
13	KCE	0.57	-	-
14	BBM	0.37	-	-
15	CCE	0.4	0.19	0.14
16	ECE	0.4	0.3	0.25
17	KCE	0.57	0.65	0.39
18	BBM	0.37	0.22	0.23

Table 4.4. Input motions for test series 2-SFP

Number	Motion	Peak accel. (g)		
		x	*y*	*z*
1	CCE	0.32	-	-
2	KCE	0.57	-	-
3	CCE	0.32	0.152	0.112
4	ECE	0.4	0.3	0.25
5	KCE	0.57	0.65	0.39
6	BBM	0.37	0.22	0.23

Table 4.5. Input motions for test series 2-TFP

Number	Motion	Peak accel. (g)		
		x	*y*	*z*
1	CCE	0.32	-	-
2	KCE	0.57	-	-
3	CCE	0.32	0.152	0.112
4	ECE	0.4	0.3	0.25
5	KCE	0.57	0.65	0.39
6	BBM	0.37	0.22	0.23

4.4.3 Test series 3

The focus of test series 3 was on assessing the impact of strong earthquake shaking on the packing fraction of the pebble bed. The three-directional KCE motion with peak accelerations per Table 4.1 was selected as the strong earthquake input for this test series. The motion was run repeatedly and the compaction of the pebble bed was assessed using a borescope to capture images of the underside of the pebble bed before and after each run. Tests were conducted in the fixed base and the two base-isolated configurations. The pebbles were un-loaded and re-loaded into the vessel after each set of runs.

SECTION 5
TEST RESULTS

5.1 Introduction

This section presents results from earthquake-simulator tests of the scaled model of the Fluoride salt-cooled High temperature Reactor (FHR) described in Section 3. The tests were conducted on a six-degrees-of-freedom earthquake simulator and utilized the three-directional seismic inputs introduced in section 4.3. Section 5.2.2 through section 5.2.6 below discuss the behavior of individual model components: the outer vessel, the core barrel, the reflector-block assembly, the fluid, and the pebble bed. Test results from base-isolated configurations utilizing Single concave Friction Pendulum bearings and Triple Friction Pendulum bearings, introduced in section 3.3, are presented in section 5.3. The conclusions drawn in this section are used in Section 6 to formulate recommendations for seismic analysis and modelling of FHR components.

5.2 Component behaviors

5.2.1 Introduction

Conclusions are drawn from results of test series 1 through 3, introduced in Section 4, in the following sub-sections on the behavior of different model components. A discussion on the *additional* rocking inputs, observed in the experiments, is presented first.

The seismic inputs introduced in Section 4 do not include rocking about the two horizontal axes of the earthquake simulator. However, rocking of the platform was observed in tests due to compliance between the simulator's horizontal and vertical actuators. These accelerations impacted certain component behaviors as discussed below. Rocking accelerations (in rad/sec^2) at the base of the vessel about the *x*- and *y*-axes, denoted r_x and r_y, respectively, were determined using recordings from the four vertically-oriented accelerometers presented in Figure 4.2d as follows:

$$r_x = (ABNZ - ABSZ) / L \tag{5-1}$$

$$r_y = (ABWZ - ABEZ) / L \tag{5-2}$$

where *ABNZ*, *ABSZ*, *ABWZ*, and *ABEZ* are the vertical acceleration histories (in m/sec^2) at the north, east, south, and west sides of the base plate, respectively (see Figure 4.2d), and L (= 2 m) is the size of the square base plate (the four vertically-oriented accelerometers were installed on the edges of the 2 m × 2 m square base plate).

5.2.2 Outer vessel

The response spectra of the horizontal acceleration responses at the base and the top of the outer vessel are presented in Figure 5.1 through Figure 5.5 for the 1D and 3D earthquake inputs of Table 4.3. The accelerations at the base of the vessel along the *x* and *y* directions, denoted $a_{b,x}$ and $a_{b,y}$, respectively, were calculated as:

$$a_{b,x} = (ANE1X + ANW1X + ASE1X + ASW1X)/4 \tag{5-3}$$

$$a_{b,y} = (ANE1Y + ANW1Y + ASE1Y + ASW1Y)/4 \tag{5-4}$$

where *ANE1X (Y)*, *ANW1X (Y)*, *ASE1X (Y)*, and *ASW1X (Y)* are the acceleration histories recorded above the base of the vessel by identically-named accelerometers per Figure 4.2d. The accelerations at the top of the vessel along the *x* and *y* directions, denoted $a_{t,x}$ and $a_{t,y}$, respectively, were calculated as:

$$a_{t,x} = (AN3X + AS3X + AE3X + AW3X)/4 \tag{5-5}$$

$$a_{t,y} = (AN3Y + AS3Y + AE3Y + AW3Y)/4 \tag{5-6}$$

where *AN3X (Y)*, *AS3X (Y)*, *AE3X (Y)*, and *AW3X (Y)* are the acceleration histories recorded by accelerometers at the top of the vessel per the instrumentation layout in Figure 4.2a and f.[3]

Figure 5.1 through Figure 5.5 also include spectral accelerations at the top of the vessel calculated assuming the outer vessel to be rigid (dashed lines). That is, the acceleration at the top was calculated as a summation of the acceleration at the base and the horizontal acceleration at the top due to rocking at the base. Accordingly, the accelerations at the top of the vessel along the *x* and *y* directions, calculated using a *rigid-vessel* assumption, were $(a_{b,x} + r_y H)$ and $(a_{b,y} - r_x H)$, respectively, where H (= 2 m) is the height of the vessel.

The response spectra of the recorded accelerations at the top of the vessel (calculated per equations (5-5) and (5-6)) and the accelerations calculated using a *rigid-vessel* assumption are virtually identical, as seen in Figure 5.1 through Figure 5.5, indicating that: (a) any amplification in accelerations along the height of the outer vessel is due to rocking inputs only, and as a consequence, (b) the outer vessel is effectively rigid.

[3] Equations (5-3) through (5-6) involve averaging the accelerations recorded by four accelerometers. The recordings from the four accelerometers were similar in each case and the averaging is done for the purpose of completeness in presentation.

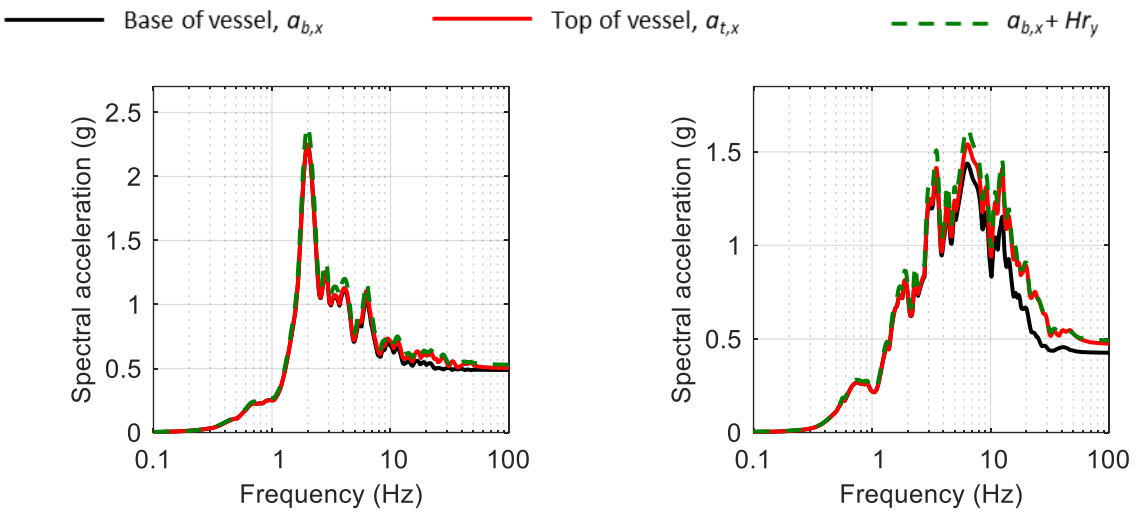

a. 1D CCE, motion #11 in Table 4.3

b. 1D ECE, motion #12 in Table 4.3

c. 1D KCE, motion #13 in Table 4.3

d. 1D BBM, motion #14 in Table 4.3

Figure 5.1. Amplification in acceleration along the height of the vessel due to rocking inputs, *x* direction, spectra for 5% damping

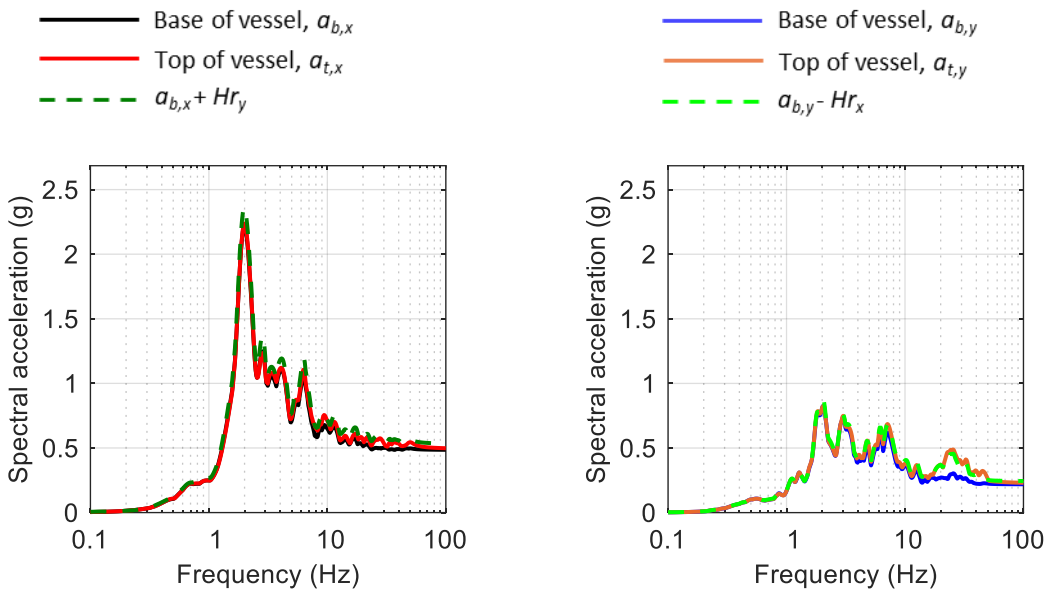

a. *x* direction b. *y* direction

Figure 5.2. Amplification in accelerations along the height of the vessel due to rocking inputs, 3D CCE input, motion #15 in Table 4.3, spectra for 5% damping

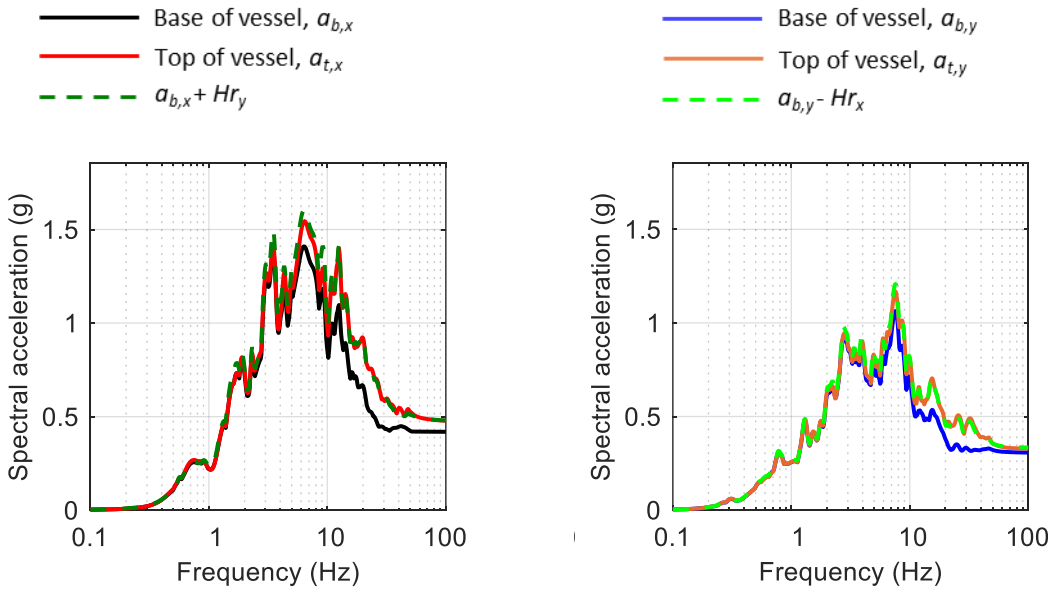

a. *x* direction b. *y* direction

Figure 5.3. Amplification in accelerations along the height of the vessel due to rocking inputs, 3D ECE input, motion #16 in Table 4.3, spectra for 5% damping

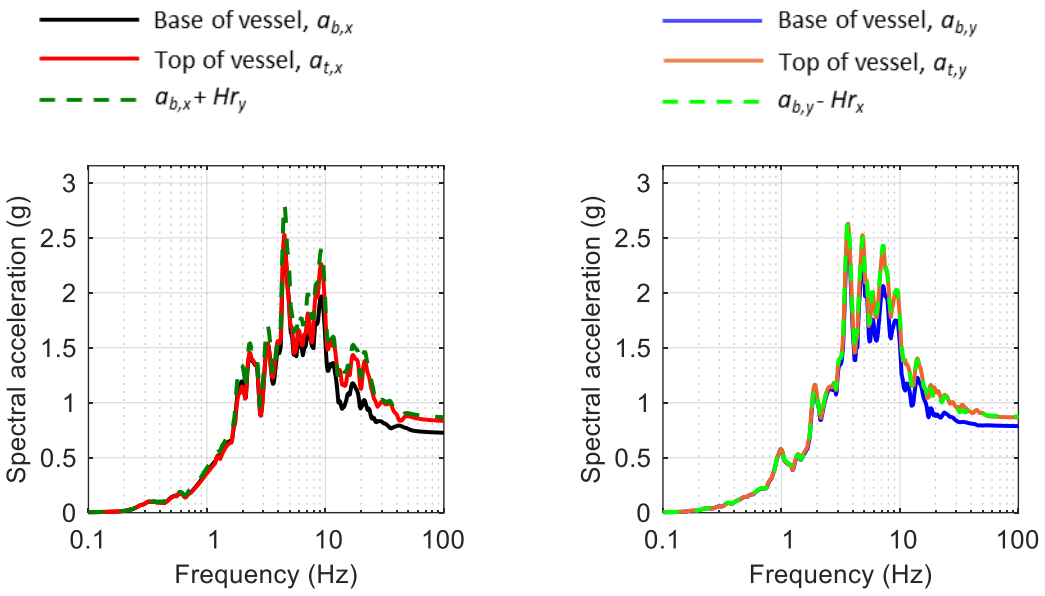

a. *x* direction b. *y* direction

Figure 5.4. Amplification in accelerations along the height of the vessel due to rocking inputs, 3D KCE input, motion #17 in Table 4.3, spectra for 5% damping

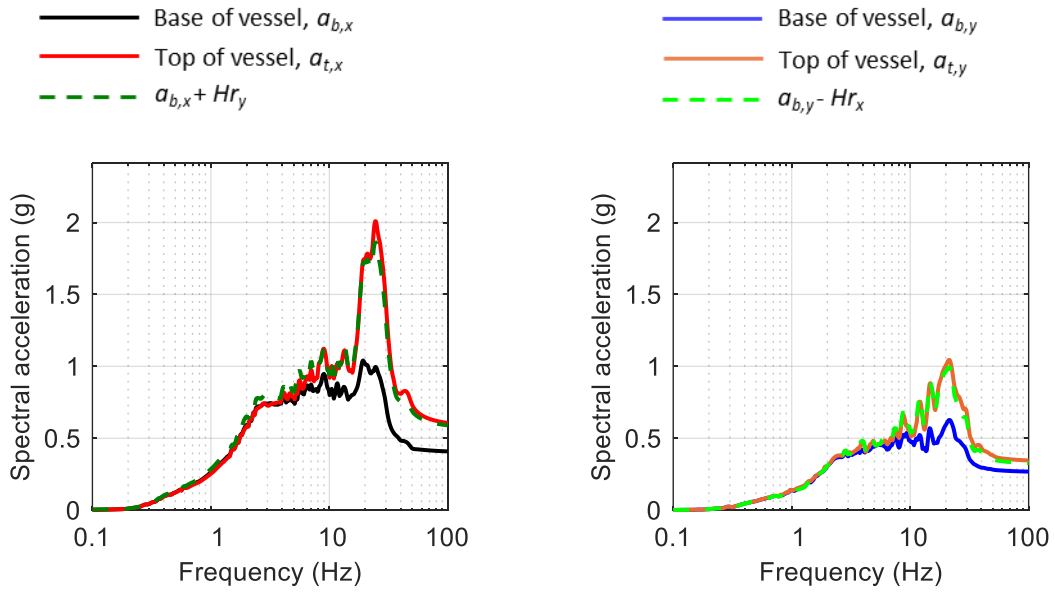

a. *x* direction b. *y* direction

Figure 5.5. Amplification in accelerations along the height of the vessel due to rocking inputs, 3D BBM input, motion #18 in Table 4.3, spectra for 5% damping

Reaction force time series recorded under the base of the vessel for the 1D and 3D earthquake inputs per Table 4.3 (fixed-base configuration) are presented in Figure 5.7 through Figure 5.11. For the 1D inputs, only the shear force in *x* direction is presented. For the 3D inputs, shear forces in the two horizontal directions and the normal force are presented. Reaction force time series calculated considering a lumped-mass approach are also plotted to enable a comparison. For the lumped-mass calculation, denoted Calculation in the figures, the mass of the test specimen is lumped at its center of mass, as presented in Figure 5.6, and the forces in the *x*, *y*, and *z* directions, denoted F_x, F_y, and F_z, respectively, are calculated as:

$$F_x = M(a_{b,x} + r_y h_{CM}) \tag{5-7}$$

$$F_y = M(a_{b,y} - r_x h_{CM}) \tag{5-8}$$

$$F_z = Ma_{b,z} \tag{5-9}$$

where M is the mass of the specimen (= 7700 kg), h_{CM} (= 0.76 m) is the height of the center of mass of the test specimen, as indicated in Figure 5.6, and $a_{b,z}$ is the vertical acceleration recorded at the base of the vessel calculated per Figure 4.2d as:

$$a_{b,z} = (ANE1Z + ANW1Z + ASE1Z + ASW1Z)/4 \tag{5-10}$$

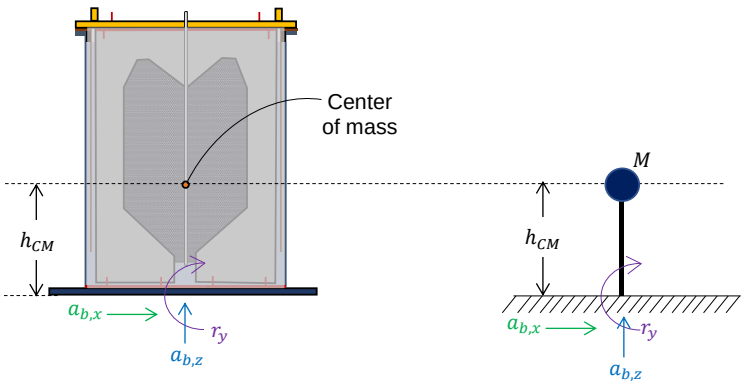

Figure 5.6. Lumped mass approximation of the test specimen

The insets in the panels of Figure 5.7 through Figure 5.11 present measured (experiment) and calculated (lumped mass) reaction histories around the time of peak response to aid the interpretation of results.

The experimental and calculated histories of base reactions correlate well, as can be seen in Figure 5.7 through Figure 5.11: the measured time series are recovered reasonably well using the lumped-mass

approach. Table 5.1 presents the percentage differences in absolute maximum values of the measured and calculated base reactions for the 1D and 3D earthquake inputs in test series 2. The absolute values of the percentage differences in the case of test series 2-FB (fixed-base configuration), 2-SFP (base-isolated with SFP bearings), and 2-TFP (base-isolated with TFP bearings) range between 0% and 17%, indicating that the lumped-mass approach can be used to calculate support reactions with sufficient accuracy for design.

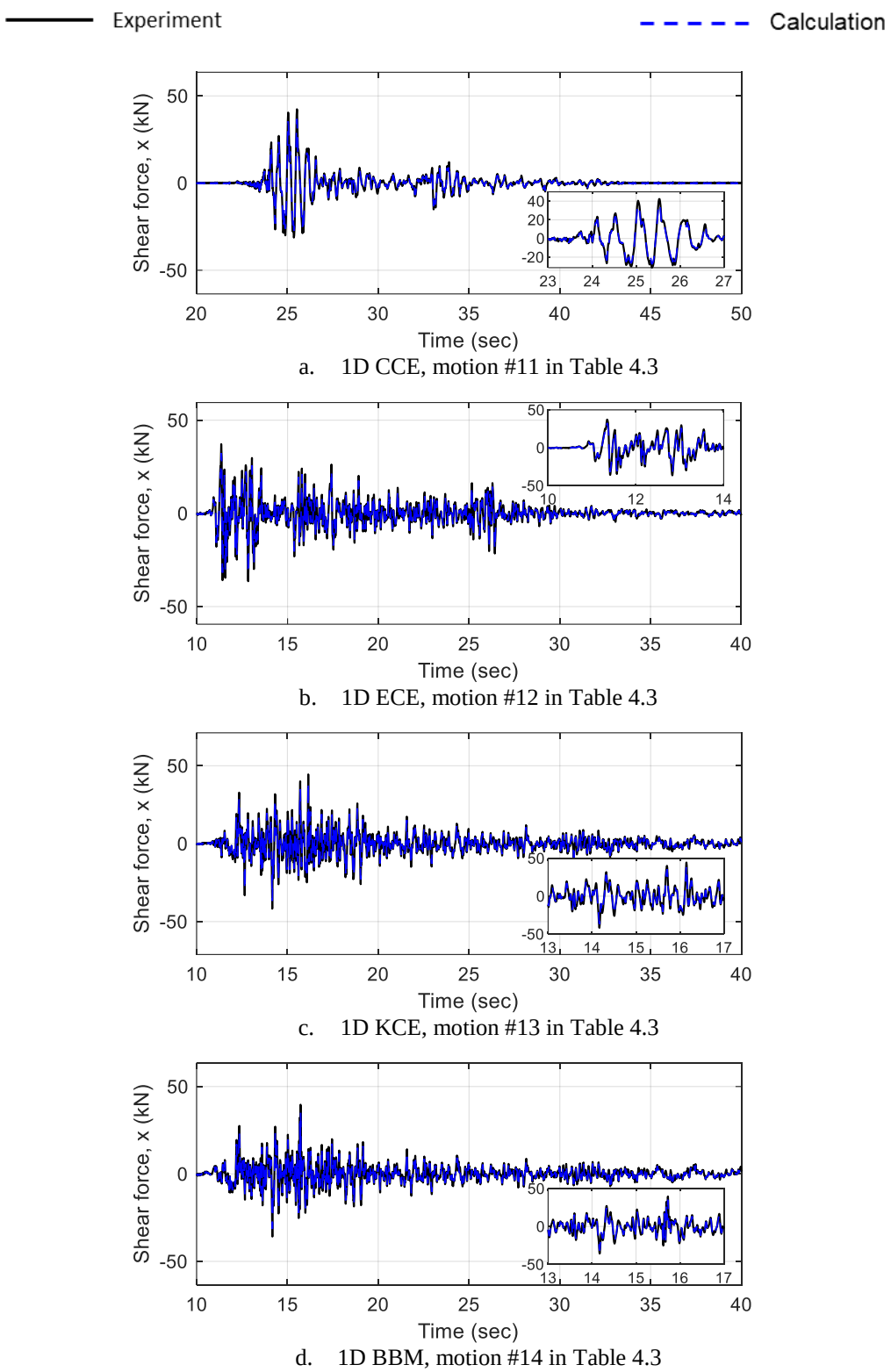

a. 1D CCE, motion #11 in Table 4.3

b. 1D ECE, motion #12 in Table 4.3

c. 1D KCE, motion #13 in Table 4.3

d. 1D BBM, motion #14 in Table 4.3

Figure 5.7. Comparison of experimental and calculated time series of shear force in the *x* direction, 1D inputs

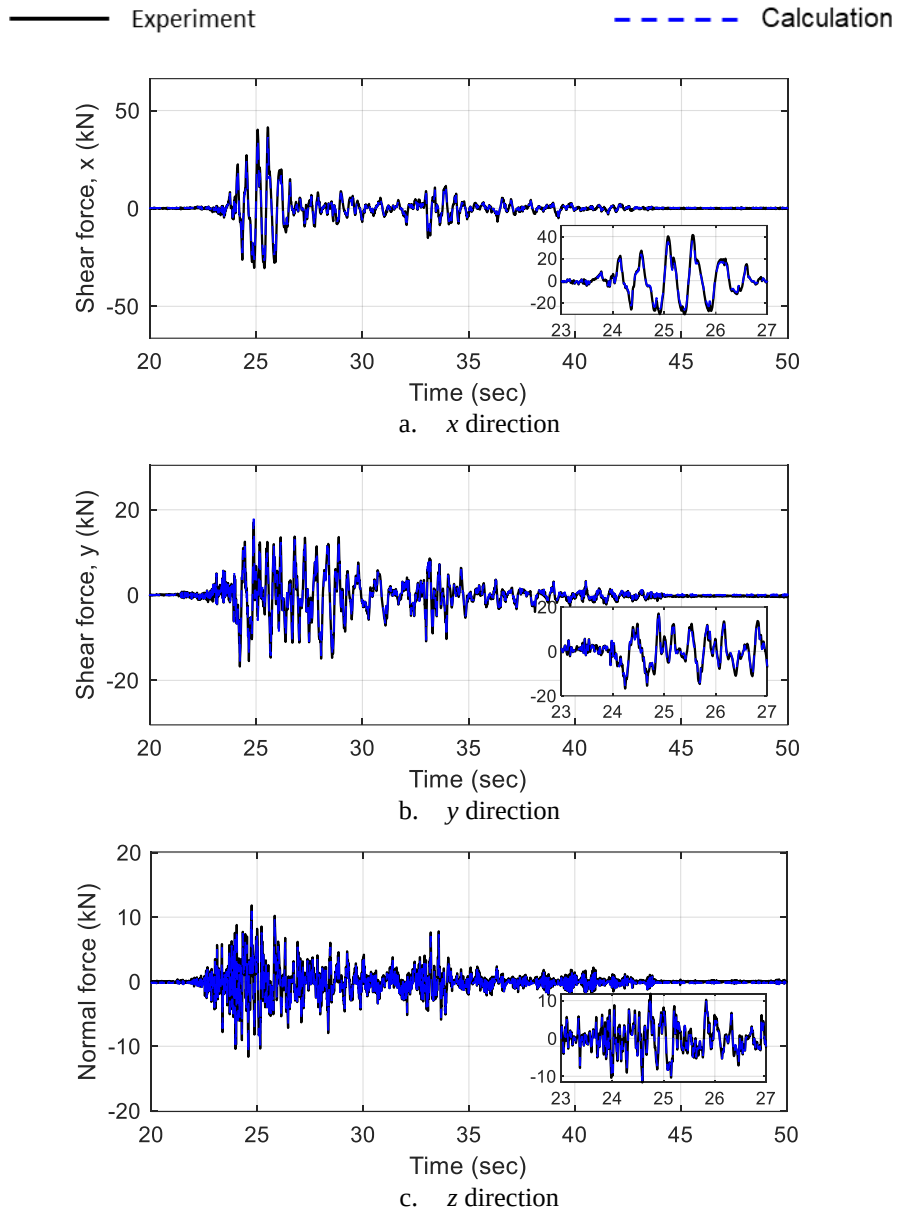

a. *x* direction

b. *y* direction

c. *z* direction

Figure 5.8. Comparison of experimental and calculated time series of base reactions, 3D CCE input, motion #15 in Table 4.3

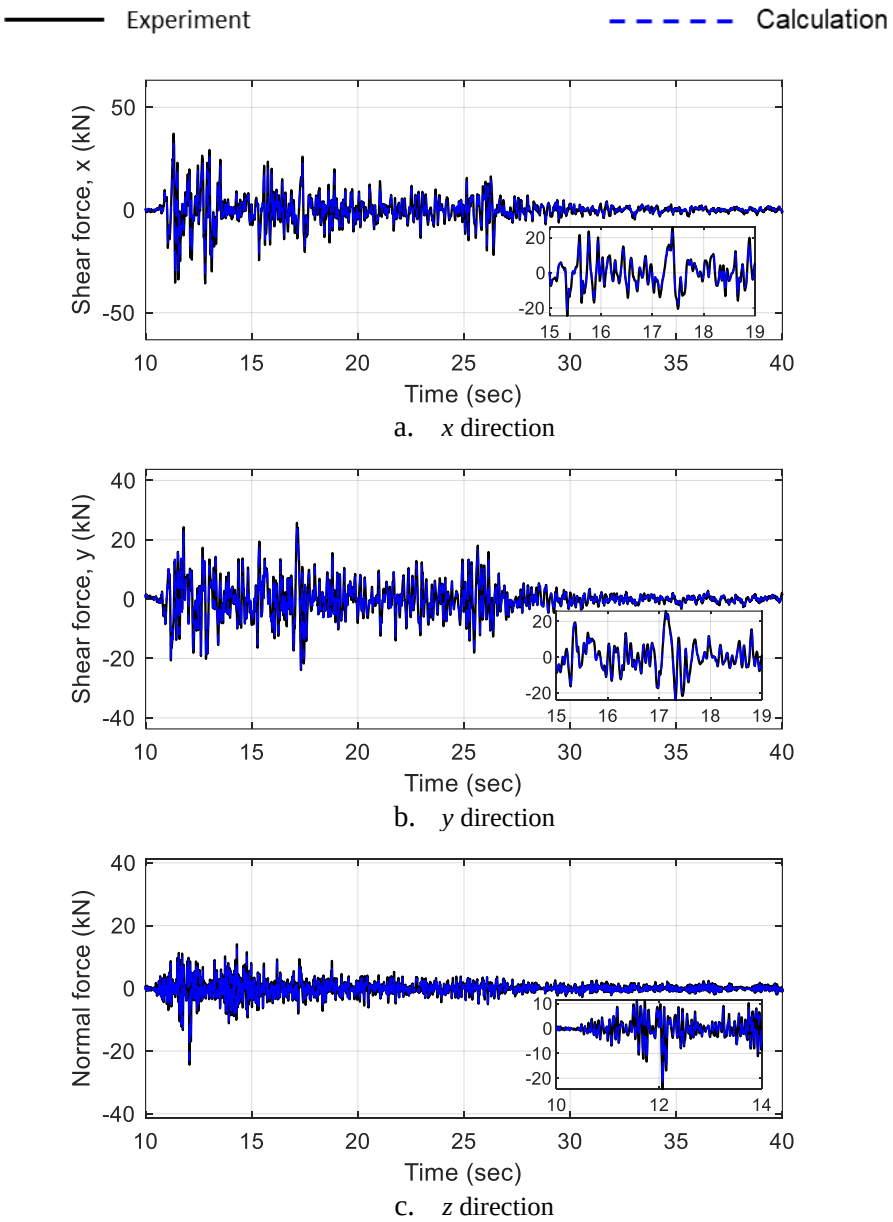

a. *x* direction

b. *y* direction

c. *z* direction

Figure 5.9. Comparison of experimental and calculated time series of base reactions, 3D ECE input, motion #16 in Table 4.3

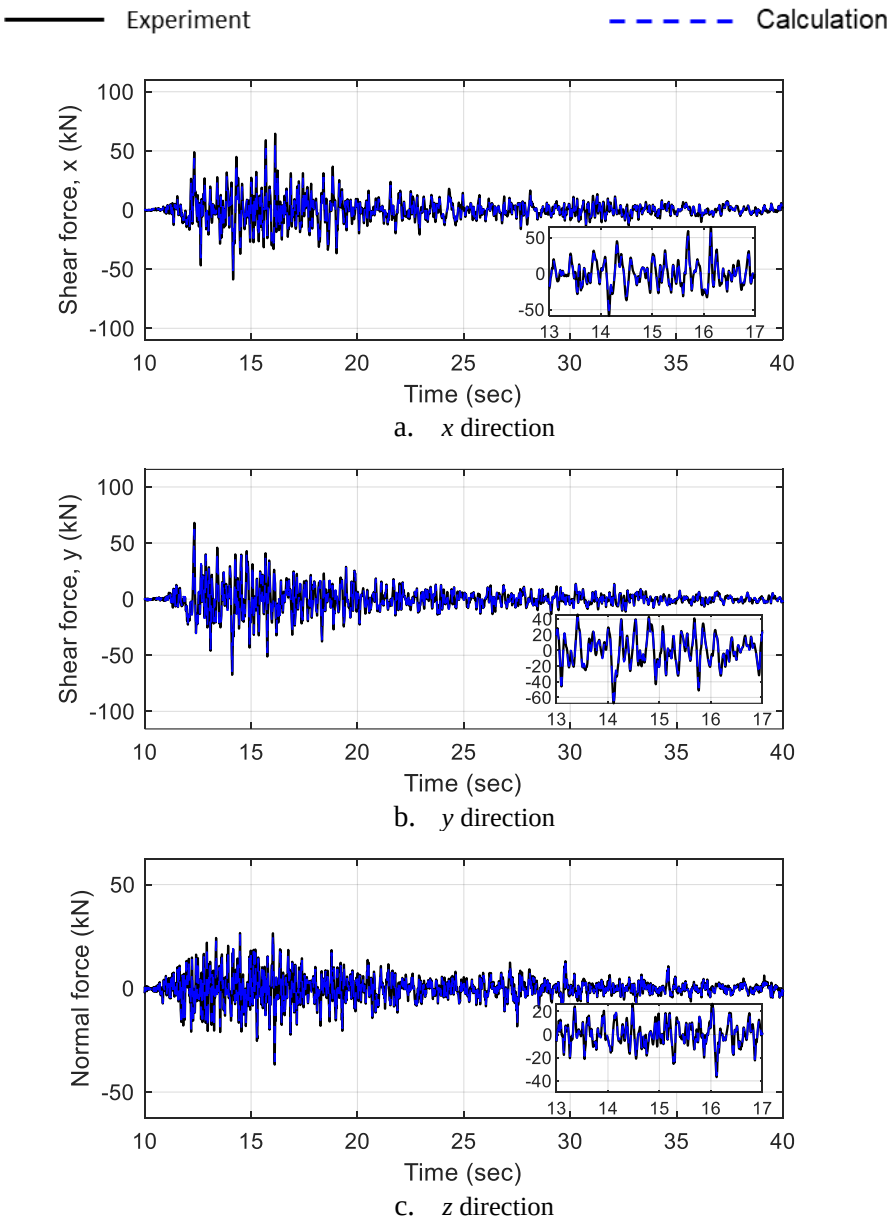

a. *x* direction

b. *y* direction

c. *z* direction

Figure 5.10. Comparison of experimental and calculated time series of base reactions, 3D KCE input, motion #17 in Table 4.3

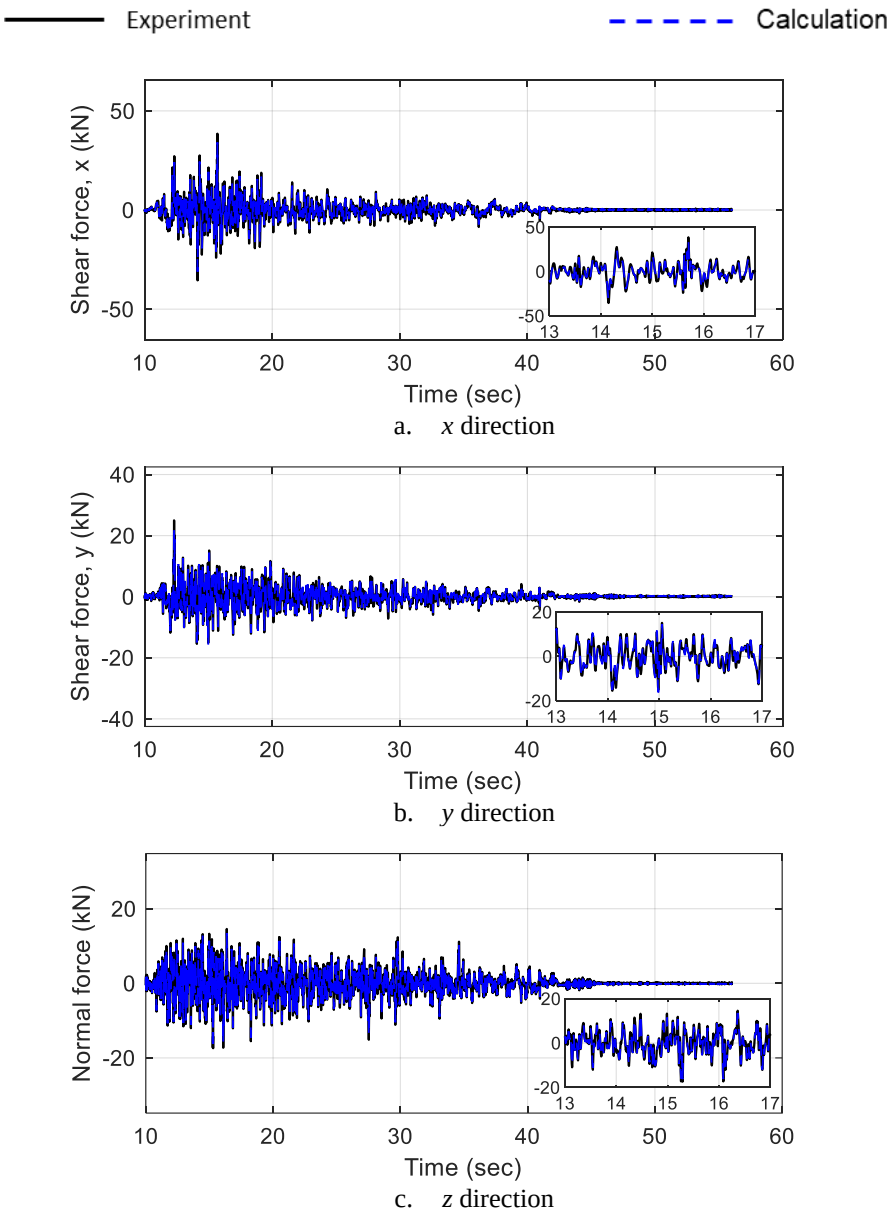

a. *x* direction

b. *y* direction

c. *z* direction

Figure 5.11. Comparison of experimental and calculated time series of base reactions, 3D BBM input, motion #18 in Table 4.3

Table 5.1. Percentage differences between absolute maximum values of experimental and calculated base reactions[†]

Test series	Input motion[††]	*x* direction	*y* direction	*z* direction
2-FB	1D CCE (#11)	15	-	-
	1D ECE (#12)	15	-	-
	1D KCE (#13)	14	-	-
	1D BBM (#14)	13	-	-
	3D CCE (#15)	14	-4	6
	3D ECE (#16)	14	4	6
	3D KCE (#17)	14	5	4
	3D BBM (#18)	13	9	7
2-SFP	1D CCE (#1)	7	-	-
	1D KCE (#2)	13	-	-
	3D CCE (#3)	9	5	13
	3D ECE (#4)	17	3	6
	3D KCE (#5)	10	-3	11
	3D BBM (#6)	7	4	14
2-TFP	1D CCE (#1)	1	-	-
	1D KCE (#2)	7	-	-
	3D CCE (#3)	1	-1	10
	3D ECE (#4)	11	-3	11
	3D KCE (#5)	5	0	10
	3D BBM (#6)	2	0	8

[†]The differences are calculated as: (experimental value – calculated value)/calculated value ×100

[††]Number in parenthesis are motion numbers per Table 4.3, Table 4.4, and Table 4.5 for test series 2-FB, 2-SFP, and 2-TFP, respectively.

5.2.3 Core barrel

The acceleration response of the core barrel, obtained from accelerometers per Figure 4.3, is compared with the input acceleration at the base of the vessel in this sub-section. Since the accelerometers near the bottom of the core barrel were not aligned with the defined *x* and *y* axes, the horizontal accelerations at the base of the vessel were transformed to align with transformed axes $\hat{x}$ and $\hat{y}$ per Figure 5.12. The transformed horizontal accelerations along axes $\hat{x}$ and $\hat{y}$, denoted $a_{b,\hat{x}}$ and $a_{b,\hat{y}}$, respectively, were calculated as:

$$a_{b,\hat{x}} = a_{b,x}\cos(9.5°) + a_{b,y}\sin(9.5°) \tag{5-11}$$

$$a_{b,\hat{y}} = -a_{b,x}\sin(9.5°) + a_{b,y}\cos(9.5°) \tag{5-12}$$

Figure 5.13 through Figure 5.17 enable a comparison of response spectra of accelerations recorded on the base of the vessel (input to the superstructure/specimen) and on the core barrel in tests using the 1D and 3D earthquake inputs of Table 4.3.

The acceleration response spectra on the base of the vessel and on the core barrel are virtually identical for all input motions considered here, except for minor differences at high frequencies, particularly in case of the 1D and 3D BBM motions (see Figure 5.13d and Figure 5.17), which were not characterized.

It is challenging to numerically or analytically characterize these minor differences in the high-frequency acceleration responses of the core barrel because the core barrel was not a perfect cylinder. Specifically, some of the tabs on the core barrel (introduced in section 3.2) were in contact with the inner surface of the vessel during testing and two thick welds (see Figure 5.18) ran along the height of the cylindrical core barrel at two locations.

The strain response of the core barrel, recorded using strain gages *SGCRN*, *SGCRS*, and *SGCRW* per Figure 4.3[4] was insignificant. The peak strains recorded in motions #11 through #18 per Table 4.3 were smaller than 40 microstrain (40×10^{-6}): less than 1% of the yield strain of aluminum. Figure 5.19 presents the strain histories recorded in motion #17, which was the most intense earthquake input used for testing (in terms of peak accelerations).

Inertial effects on the core barrel at the model scale were distorted, as noted in section 2.5, and forces would have been 3.5 times greater if the ratio of π_7 at model and prototype scales had equaled 1.0 and not 0.29.

[4]The fourth strain gage on the core barrel, SGCRE, malfunctioned during tests and is not included in the discussion here.

However, the corresponding maximum strain in the core barrel would have been less than 5% of the yield value. Accordingly, because the acceleration response spectra computed on the core barrel and at the base of the vessel are similar, and the strains in the core barrel are very small, it is concluded that the core barrel and outer vessel respond as a unit.

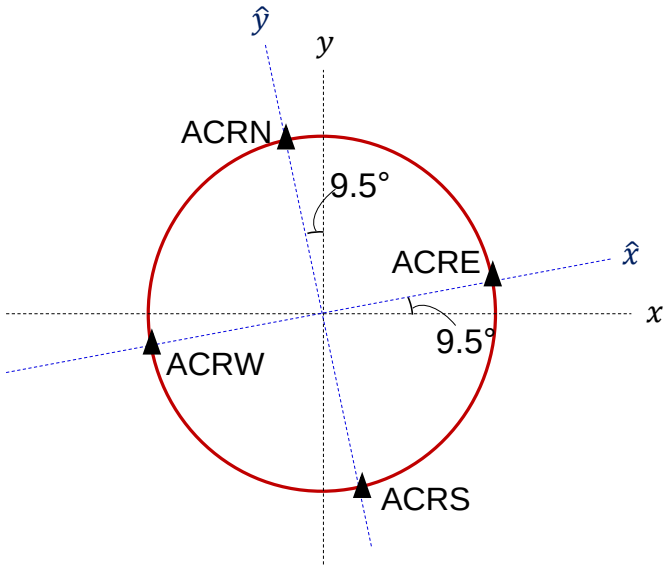

Figure 5.12. Accelerometers near the lower end of the core barrel and transformed axes $\hat{x}$ and $\hat{y}$

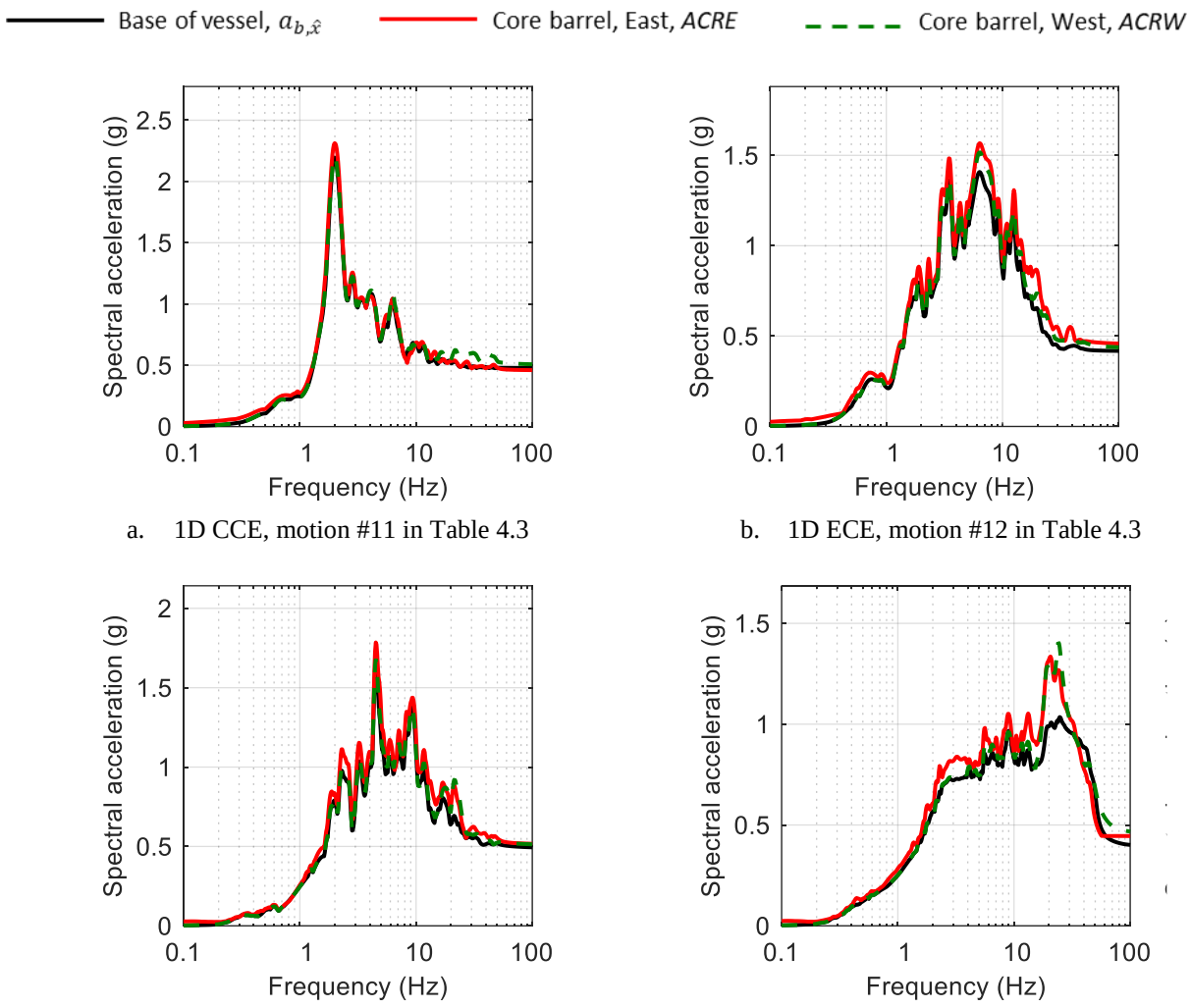

a. 1D CCE, motion #11 in Table 4.3

b. 1D ECE, motion #12 in Table 4.3

c. 1D KCE, motion #13 in Table 4.3

d. 1D BBM, motion #14 in Table 4.3

Figure 5.13. Acceleration response spectra of the core barrel, $\hat{x}$ direction, 5% damping

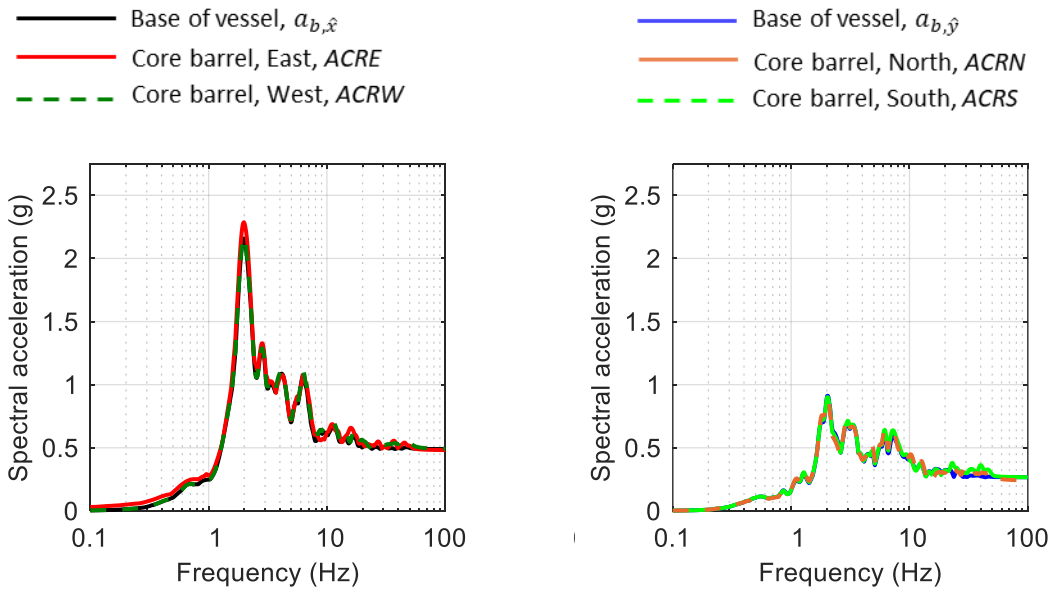

a. $\hat{x}$ direction b. $\hat{y}$ direction

Figure 5.14. Acceleration response spectra of the core barrel, 3D CCE input, motion #15 in Table 4.3, 5% damping

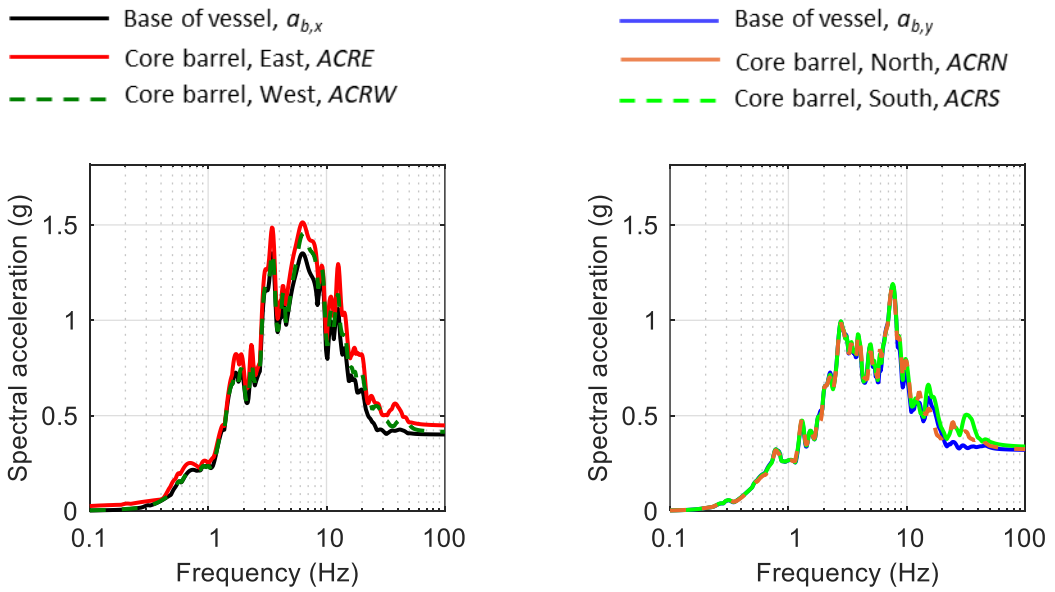

a. $\hat{x}$ direction b. $\hat{y}$ direction

Figure 5.15. Acceleration response spectra of the core barrel, 3D ECE input, motion #16 in Table 4.3, 5% damping

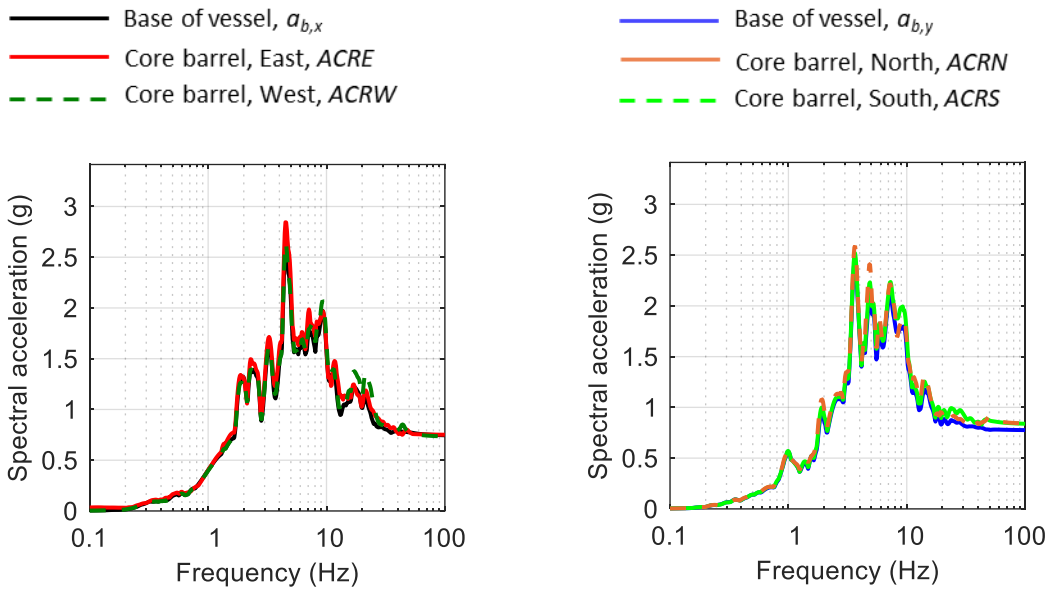

a. $\hat{x}$ direction b. $\hat{y}$ direction

Figure 5.16. Acceleration response spectra of the core barrel, 3D KCE input, motion #17 in Table 4.3, 5% damping

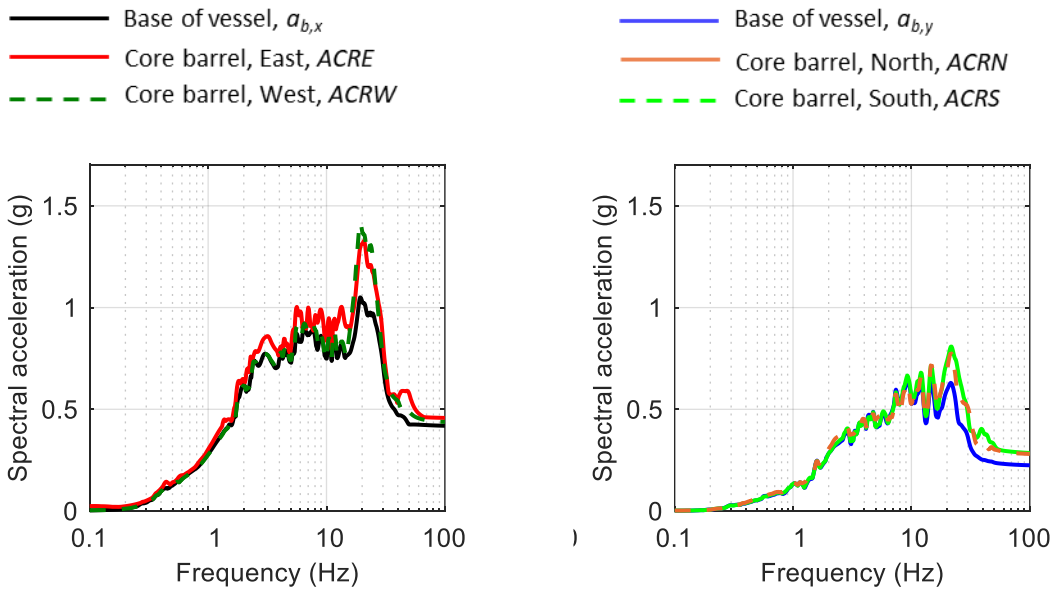

a. $\hat{x}$ direction b. $\hat{y}$ direction

Figure 5.17. Acceleration response spectra of the core barrel, 3D BBM input, motion #18 in Table 4.3, 5% damping

Figure 5.18. Weld on the core barrel

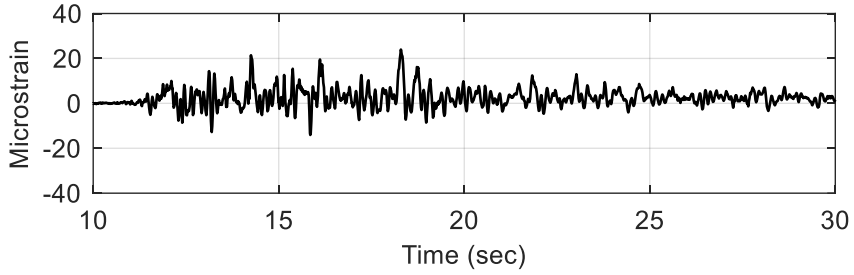

a. SGCRW

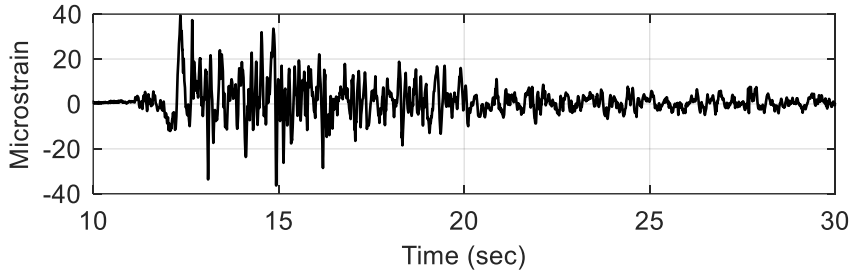

b. SGCRN

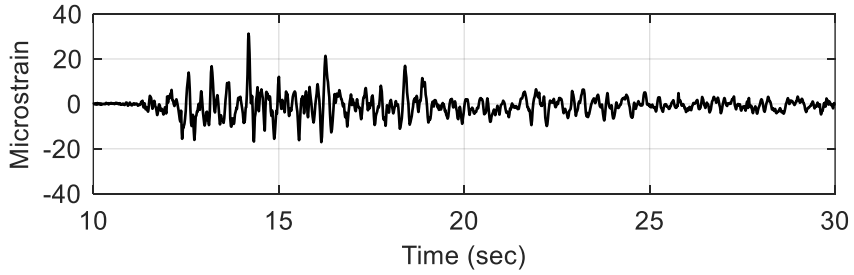

c. SGCRS

Figure 5.19. Strain response of the aluminum core barrel, 3D KCE input, motion #17 in Table 4.3, yield strain = 4000 Microstrain

5.2.4 Reflector-block assembly

A borescope, inserted into the core of the specimen through the head, was used in test series 1 to check that all reflector block columns were afloat to confirm the buoyant behavior of the reflector-block assembly.

The potential for movement between reflector blocks was assessed by running motion #17 (3D KCE) at 25%, 50%, 75%, and 100% of the full intensity followed by motion #15, #16, and #18 per Table 4.2. The paper markers on the reflector blocks, introduced in section 4.2, were checked using a borescope after each run. Figure 5.20 presents pictures of a few markers taken (in the submerged state) after these tests. None of the tape markers were damaged during shaking with the 3D inputs, indicating the gaps between the blocks did not change significantly with shaking.

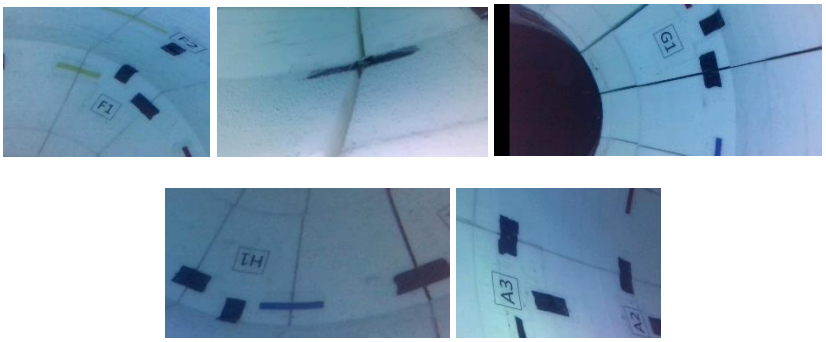

Figure 5.20. Paper markers after tests for attachment performance

The three-directional acceleration responses at the bottom (top) of the reflector-block assembly, recorded by accelerometers per Figure 4.4, and the acceleration responses at the base (top) of the vessel are presented in Figure 5.21 through Figure 5.24 (Figure 5.25 through Figure 5.28)[5]. Data are presented for the three-directional earthquake motions #15 through #18 per Table 4.3. The acceleration response spectra at the north, south, east, and west ends of the reflector-block assembly are essentially identical for frequencies less than 20 Hz, both at the top and bottom of the assembly, indicating that the assembly responded as a rigid unit. The minor differences in responses at high frequencies are not well-characterized but are likely due to impacts of the blocks, shear keys, and shear pins.

[5]The tri-axial accelerometer *ARFN1X (Y, Z)*, located near the northern end at the bottom of the reflector-block assembly per Figure 4.4, did not function during these tests. Response spectra for the *north* accelerometer time series are not presented in Figure 5.21 through Figure 5.24.

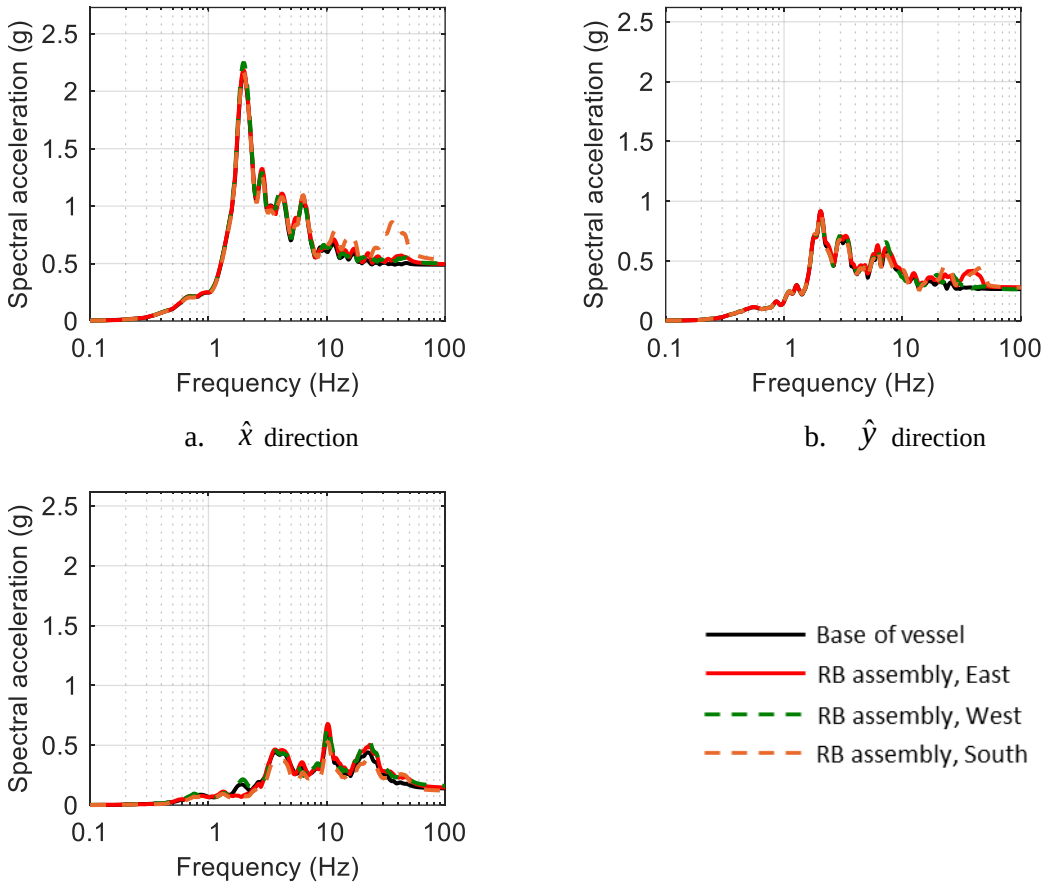

a. $\hat{x}$ direction

b. $\hat{y}$ direction

c. z direction

Figure 5.21. Acceleration response spectra at the bottom of the reflector block (RB) assembly, 3D CCE input, motion #15 in Table 4.3, 5% damping

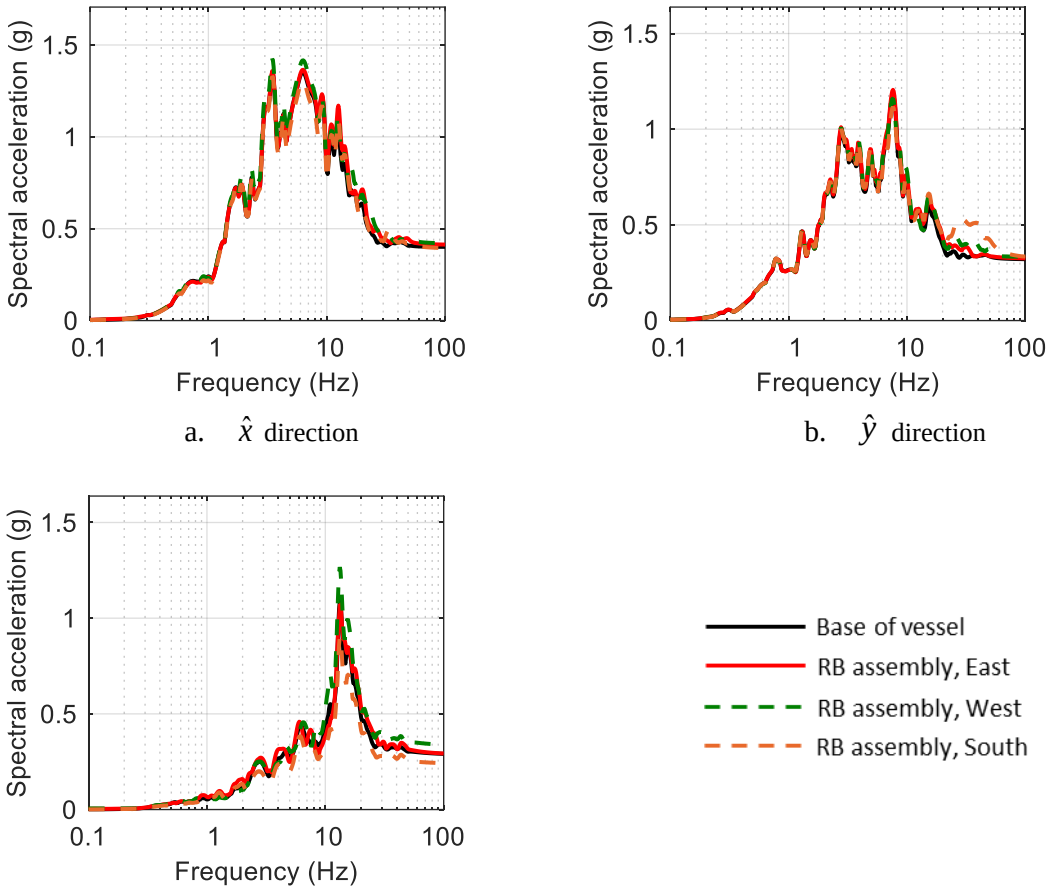

a. $\hat{x}$ direction

b. $\hat{y}$ direction

c. z direction

Figure 5.22. Acceleration response spectra at the bottom of the reflector block (RB) assembly, 3D ECE input, motion #16 in Table 4.3, 5% damping

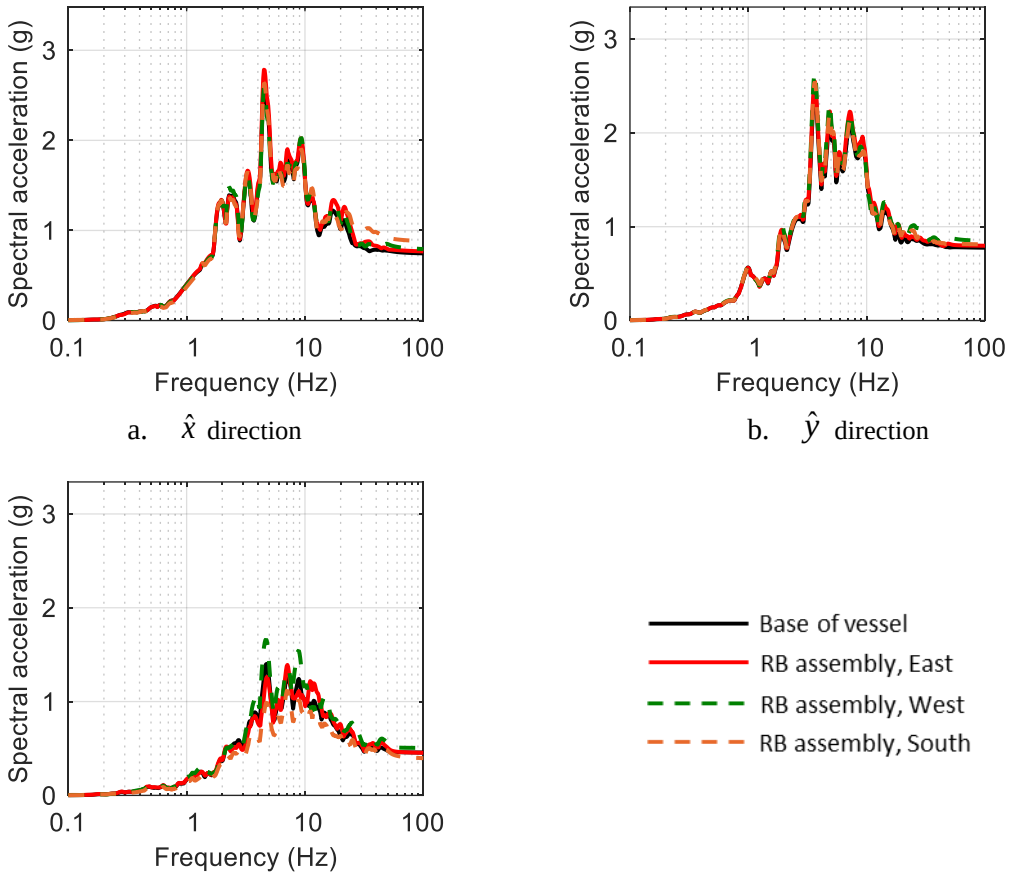

a. $\hat{x}$ direction

b. $\hat{y}$ direction

c. z direction

Figure 5.23. Acceleration response spectra at the bottom of the reflector block (RB) assembly, 3D KCE input, motion #17 in Table 4.3, 5% damping

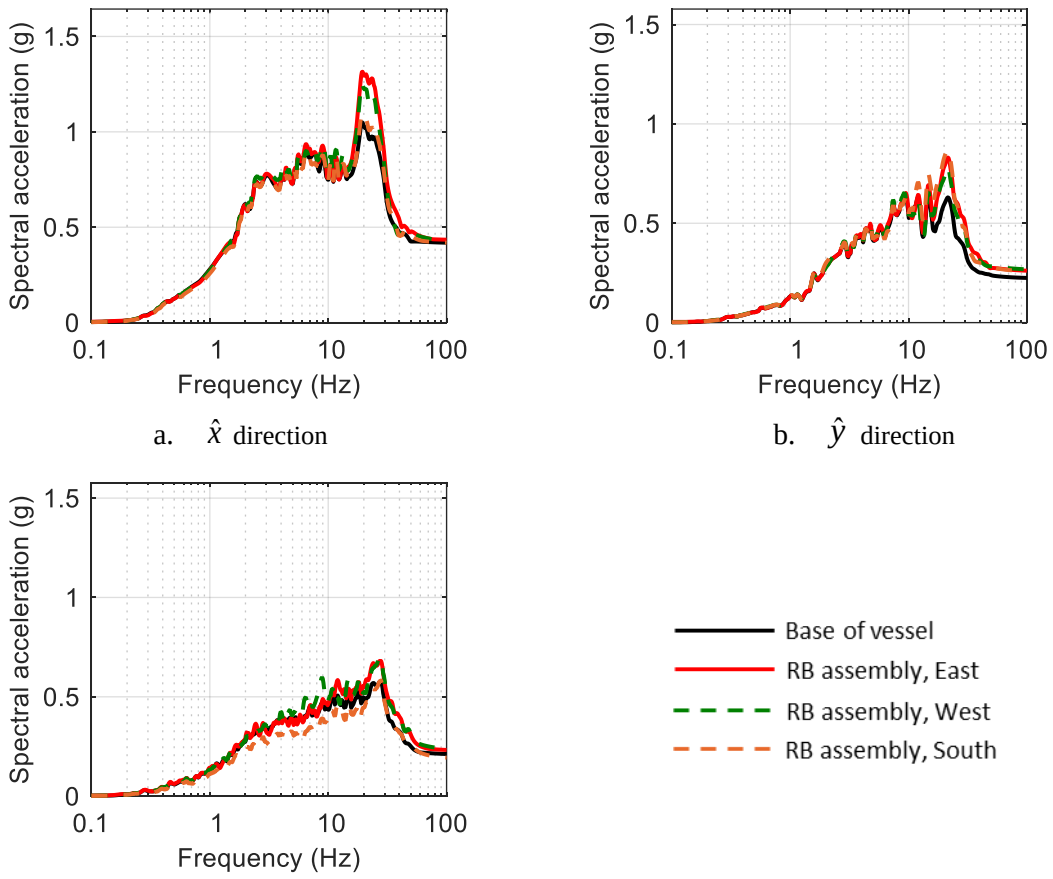

a. $\hat{x}$ direction

b. $\hat{y}$ direction

c. z direction

Figure 5.24. Acceleration response spectra at the bottom of the reflector block (RB) assembly, 3D BBM input, motion #18 in Table 4.3, 5% damping

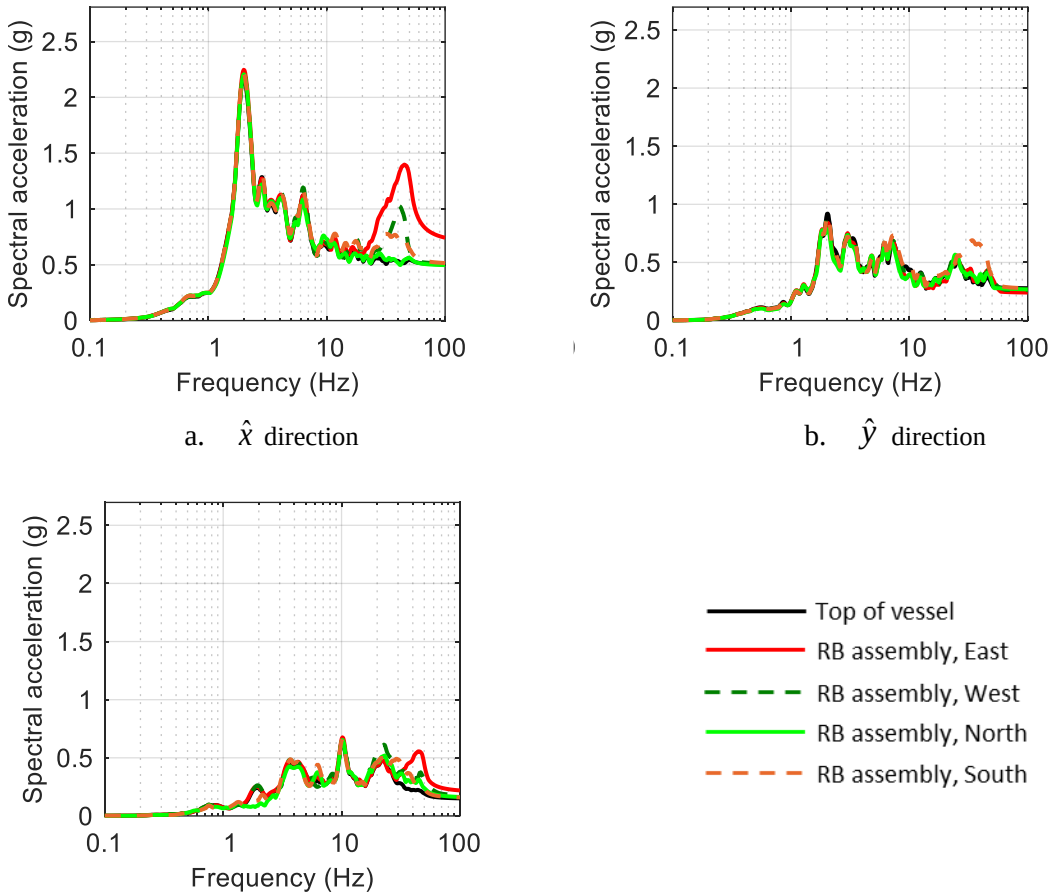

a. $\hat{x}$ direction

b. $\hat{y}$ direction

c. z direction

Figure 5.25. Acceleration response spectra at the top of the reflector block (RB) assembly, 3D CCE input, motion #15 in Table 4.3, 5% damping

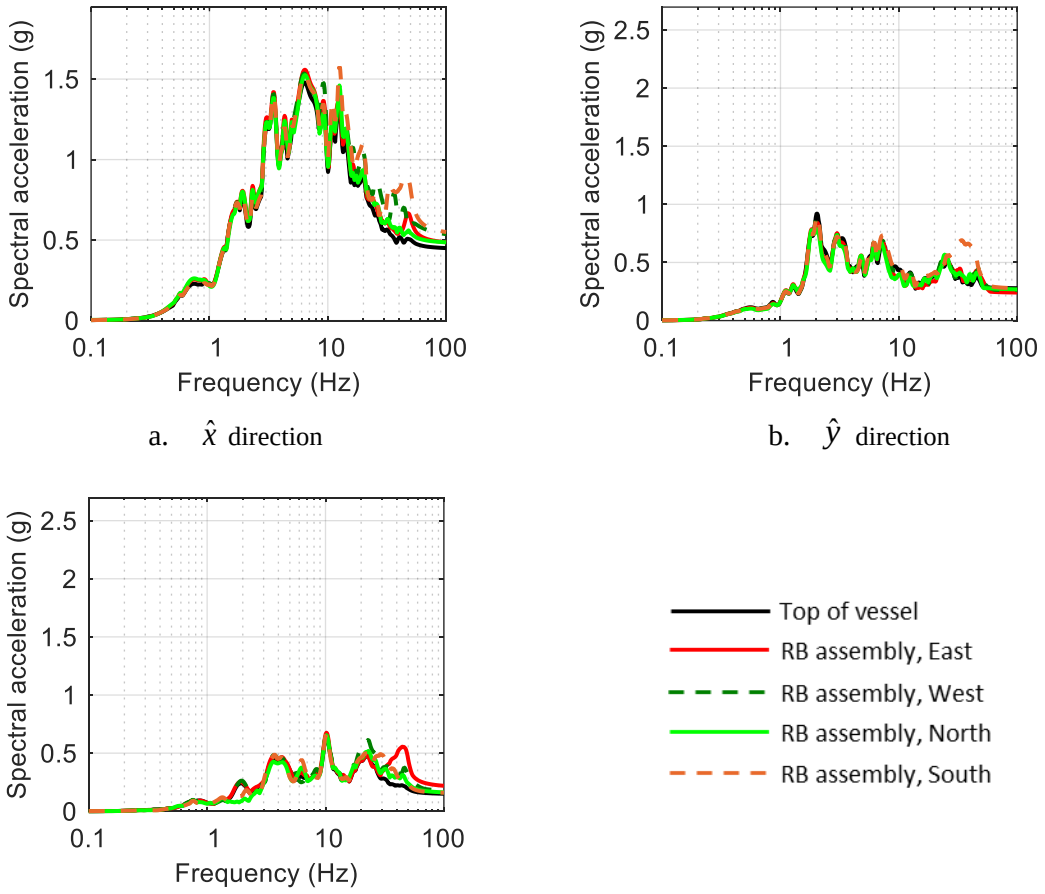

a. $\hat{x}$ direction

b. $\hat{y}$ direction

c. z direction

Figure 5.26. Acceleration response spectra at the top of the reflector block (RB) assembly, 3D ECE input, motion #16 in Table 4.3, 5% damping

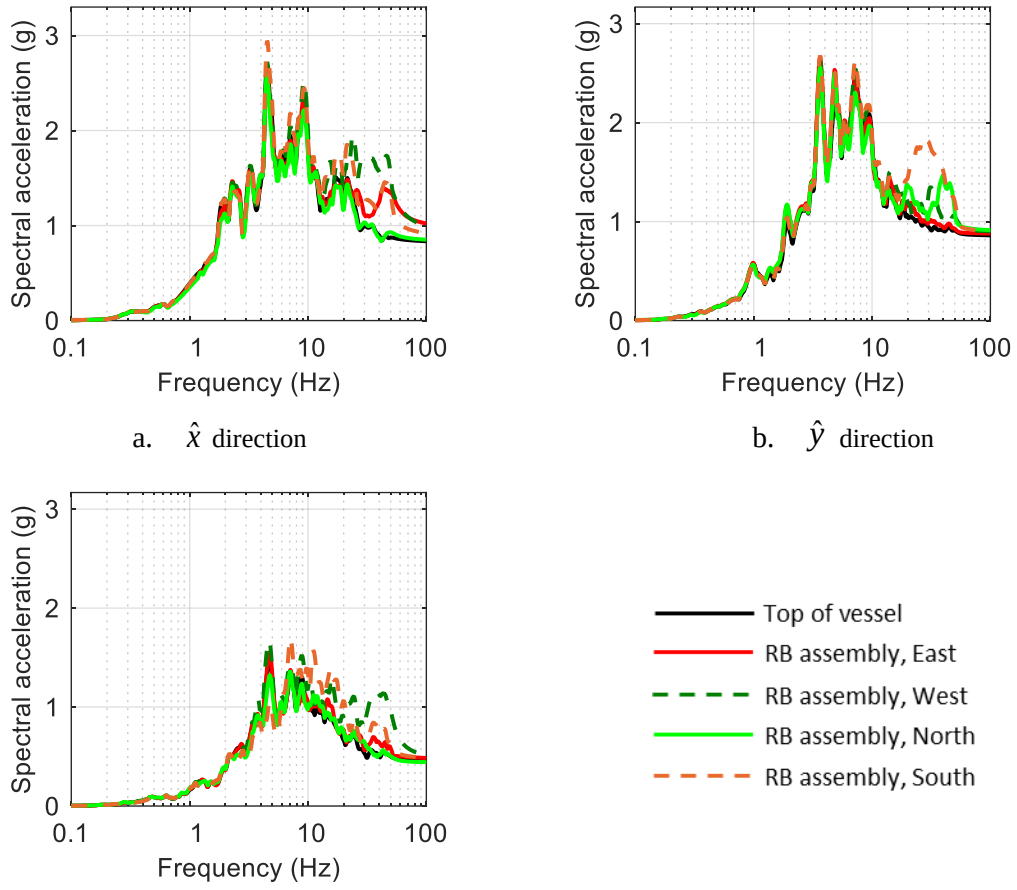

a. $\hat{x}$ direction

b. $\hat{y}$ direction

c. z direction

Figure 5.27. Acceleration response spectra at the top of the reflector block (RB) assembly, 3D KCE input, motion #17 in Table 4.3, 5% damping

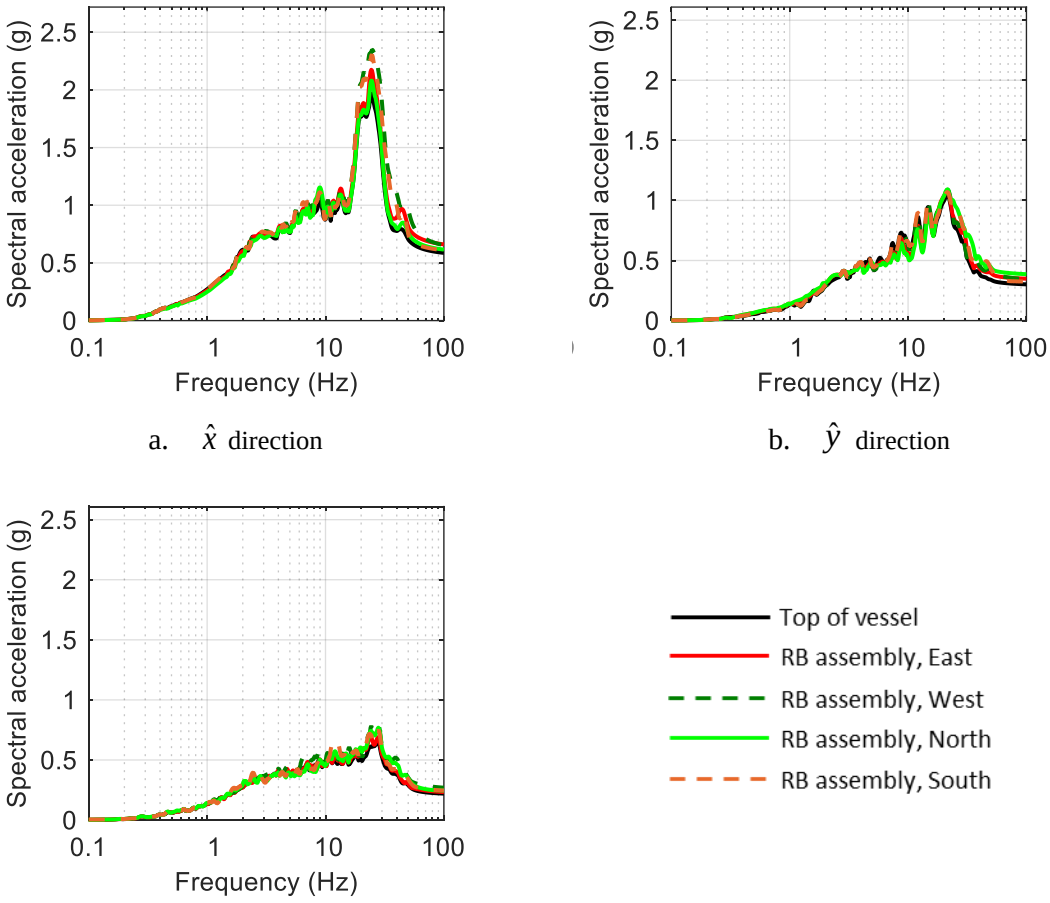

a. $\hat{x}$ direction

b. $\hat{y}$ direction

c. z direction

Figure 5.28. Acceleration response spectra at the top of the reflector block (RB) assembly, 3D BBM input, motion #18 in Table 4.3, 5% damping

5.2.5 Fluid

The sloshing behavior of the fluid in the annular space between the core barrel and the reflector blocks was studied using time series of wave heights recorded by the float-and-Temposonic transducers introduced in Figure 4.7.

Figure 5.29 presents the normalized power spectral density (PSD) plots of the wave-height time series recorded by the two wave-height transducers for the fixed-base specimen excited by white noise excitation in the *x* direction. For reference, the analytically-evaluated, first-mode sloshing frequencies of fluid-filled tanks with two geometries are also indicated on the plots in Figure 5.29: (1) an annular cylindrical tank with outer and inner radii of 0.748 m and 0.732 m, respectively, and a fluid height of 1.93 m, frequency = 0.6 Hz, and (2) a cylindrical tank with an outer radius of 0.748 m and a fluid height of 0.04 m, frequency = 0.25 Hz. The two geometries, depicted in Figure 5.30, represent simplifications of the fluid-domain geometry in the test specimen that could enable use of existing analytical solutions for assessment of the seismic response of the fluid. The analytical solutions by Tang *et al.* (2010) and Veletsos (1984) for seismic (hydrodynamic) responses of fluid in annular and *regular* cylindrical tanks, respectively, were used to calculate the indicated frequencies.

The angular frequency $\omega_{annular,1}$ of the first sloshing mode in an annular tank with outer radius and fluid height of a and H, respectively, is given by the following expression (Tang *et al.* 2010):

$$\omega_{annular,1}^2 = g\frac{\alpha_1}{a}\tanh\left(\frac{\alpha_1 H}{a}\right) \tag{5-13}$$

where α_1 (=1.01 here) depends on the ratio of inner and outer tank radii. For outer and inner radii of 0.748 m and 0.732 m, respectively, and a fluid height of 1.93 m, $\omega_{annular,1} = 3.77$ rad/s (frequency = 0.6 Hz).

For a *regular* cylindrical tank with radius and fluid height of a and H, respectively, the angular frequency of the first sloshing mode, $\omega_{regular,1}$, is given by (Veletsos 1984):

$$\omega_{regular,1}^2 = g\frac{\lambda_1}{a}\tanh\left(\frac{\lambda_1 H}{a}\right) \tag{5-14}$$

where $\lambda_1 = 1.841$. For a tank with an outer radius of 0.748 m and a fluid height of 0.04 m, which is the clearance between the underside of the reflector-block assembly and the base of the vessel, $\omega_{regular,1} = 1.57$ rad/s (frequency = 0.25 Hz).

The peak amplitude in each PSD plot in Figure 5.29 is at a frequency of 0.4 Hz. Smaller peaks are observed at other frequencies, including at 0.25 Hz and at a frequency of approximately 0.6 Hz. This range of frequencies observed in the PSD plots indicates that idealizing the fluid-domain geometry as an annular or a *regular* tank, as discussed below, would at best, result in approximate estimates of responses.

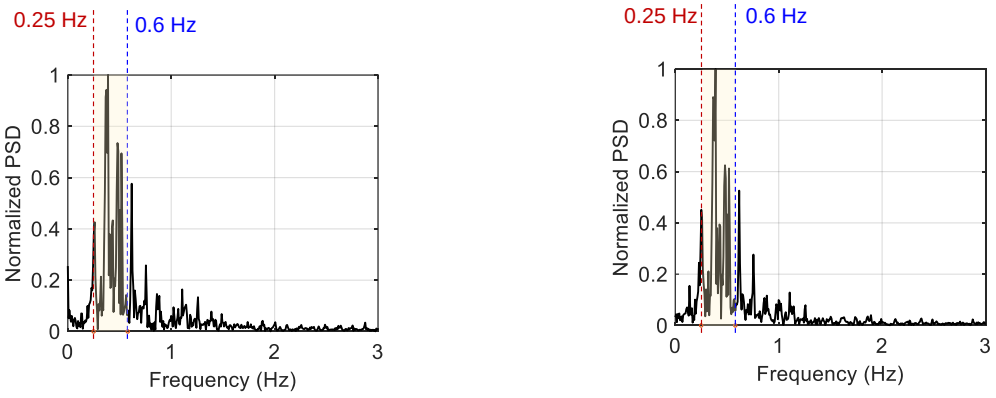

a. transducer TE b. transducer TW

Figure 5.29. Normalized PSD plot for wave height, white noise excitation in the *x* direction

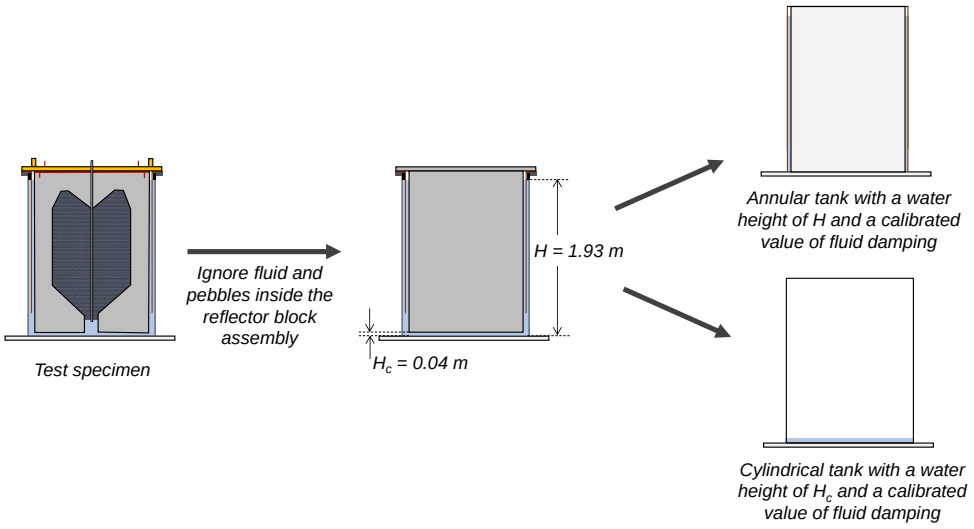

Figure 5.30. Simplification of fluid-domain geometry for application of existing analytical solutions

The sloshing response of the fluid in the experiments was heavily damped and ceased as soon as the input motion stopped. As an illustration of the heavily-damped response of the fluid, Figure 5.31 through Figure 5.34 present time series of four unidirectional input accelerations ($a_{b,x}$) and the corresponding wave height responses recorded by TE: there was no free vibration response of the fluid.

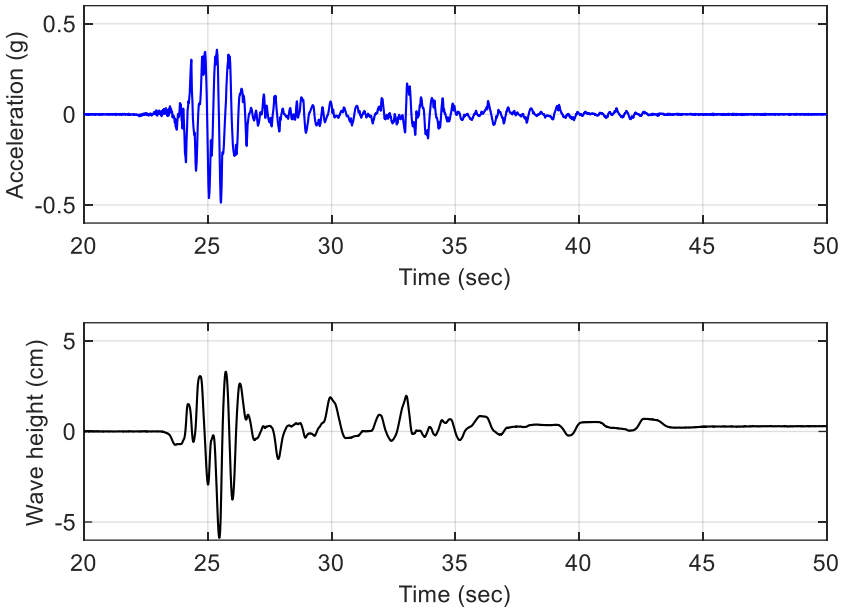

Figure 5.31. Input acceleration at base and wave height response recorded by TE, 1D CCE input, motion #11 per Table 4.3

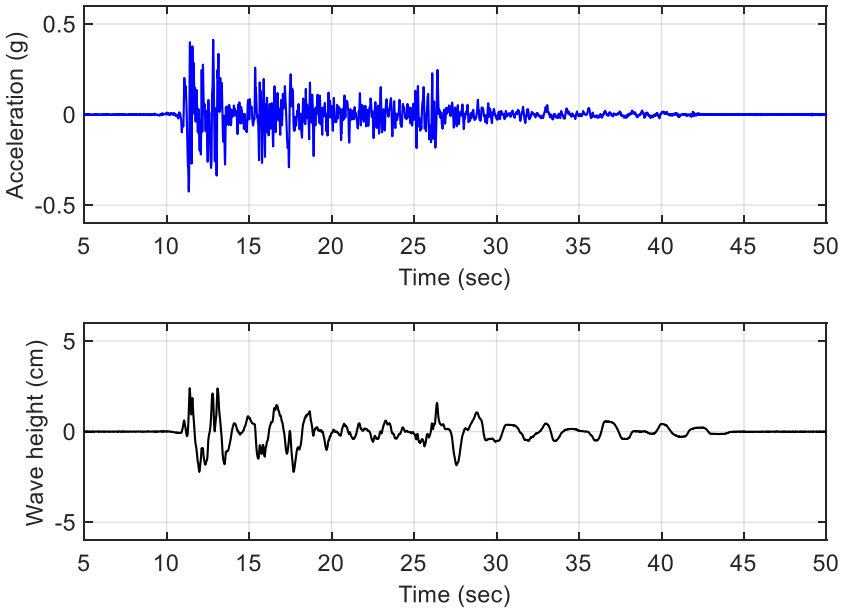

Figure 5.32. Input acceleration at base and wave height response recorded by TE, 1D ECE input, motion #12 per Table 4.3

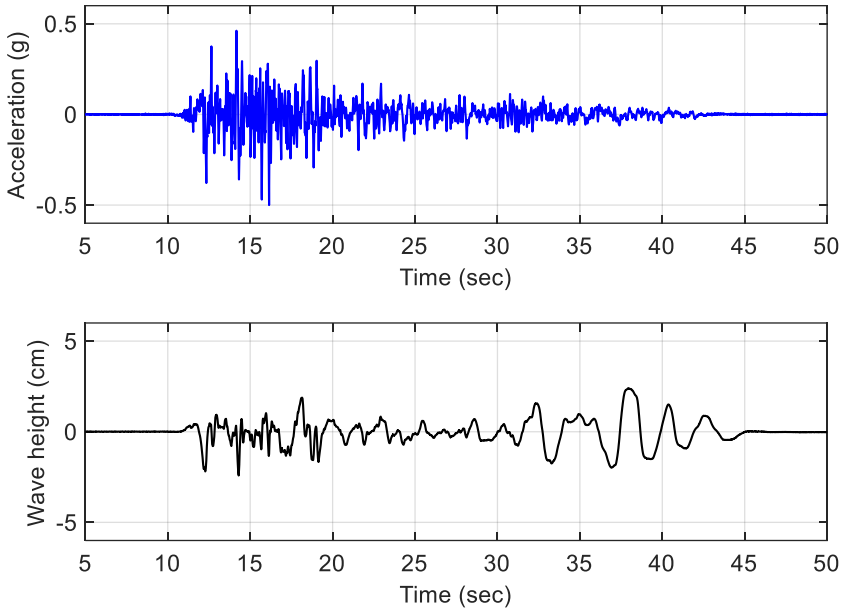

Figure 5.33. Input acceleration at base and wave height response recorded by TE, 1D KCE input, motion #13 per Table 4.3

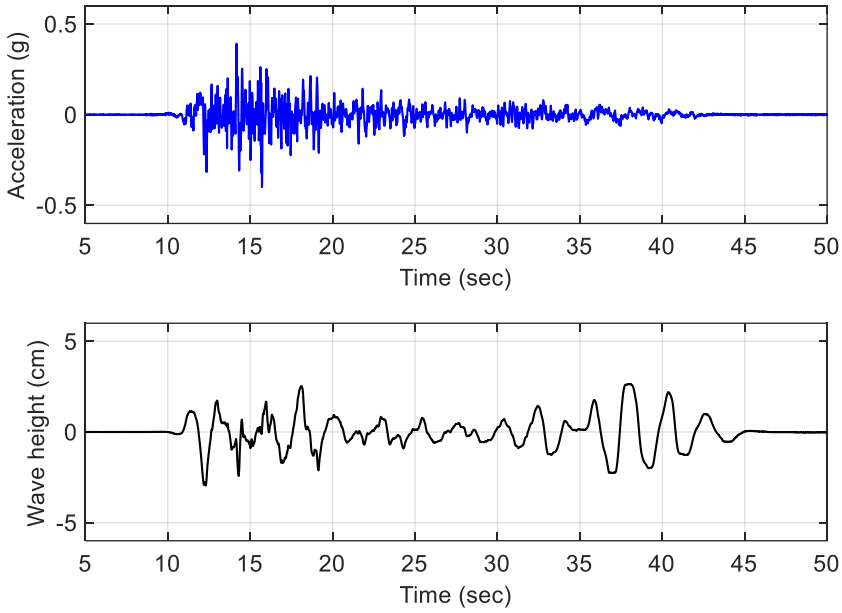

Figure 5.34. Input acceleration at base and wave height response recorded by TE, 1D BBM input, motion #14 per Table 4.3

The wave height responses recorded in experiments with those evaluated analytically using the *regular* tank approximation per Figure 5.30, and the Veletsos solution, are presented in Figure 5.35 through Figure 5.37 for unidirectional earthquake inputs in tests series 2-FB, 2-SFP, and 2-TFP, respectively. A damping ratio of 30% of critical was used in the analysis based on a sensitivity study[6]. Peak values of experimentally and analytically evaluated wave height responses and their percentage differences are presented in Table 5.2. The percentage differences vary between 2% and 49% and the match between the time series of experimental and analytical responses is judged to be satisfactory.

[6] Damping ratios between 0.5% and 75% of critical were considered for the sensitivity analysis. For each value of damping ratio, wave-height responses were calculated for eight unidirectional inputs: motions #11 through #14 in Table 4.3, motions #1 and #2 in Table 4.4, and motions #1 and #2 in Table 4.5. Differences in the calculated and measured peak responses for each value of damping were arranged as an 8×1 vector. The Euclidean norm (2-norm) of the vector was minimized at a damping ratio equal to 30%.

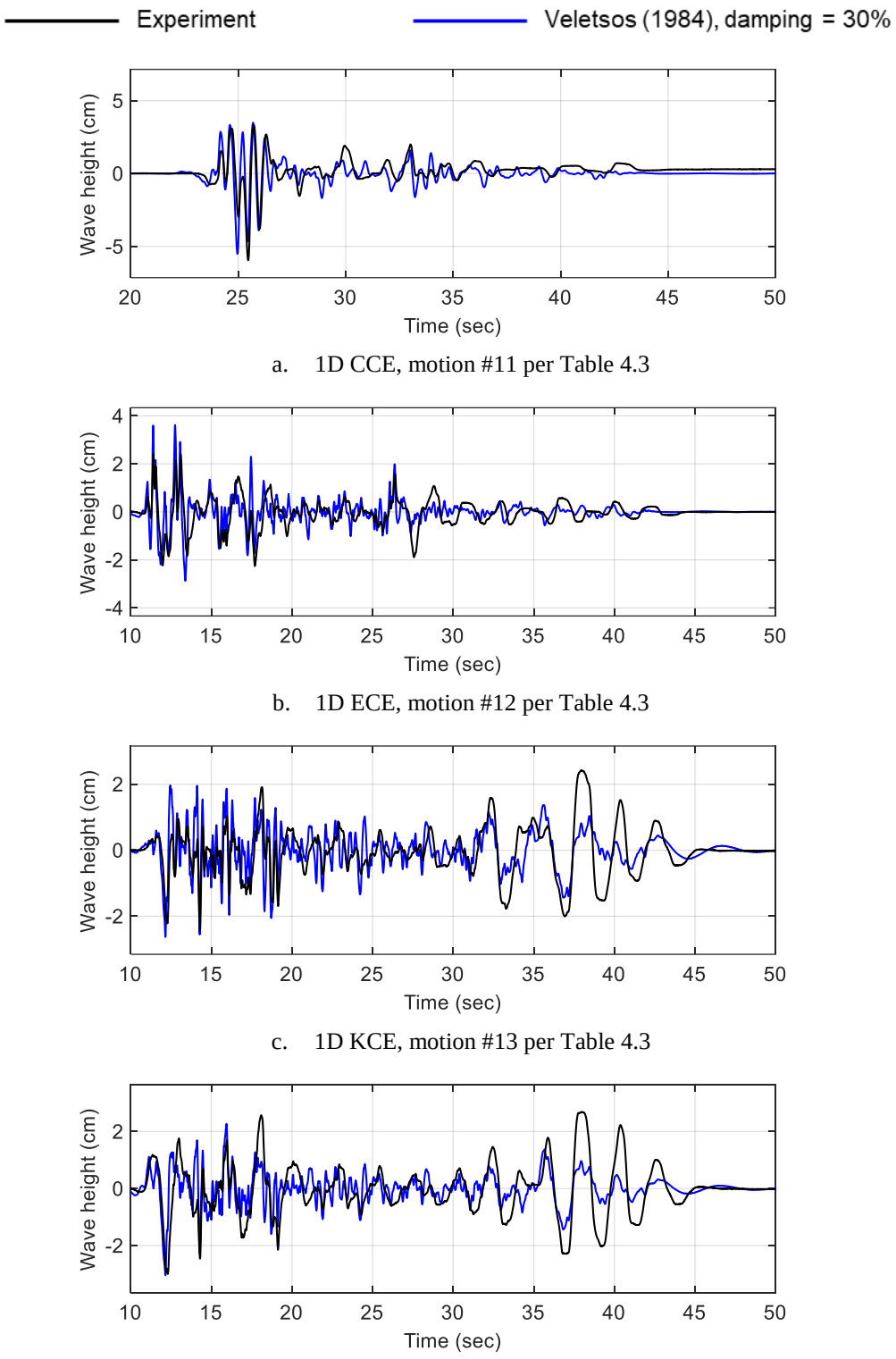

a. 1D CCE, motion #11 per Table 4.3

b. 1D ECE, motion #12 per Table 4.3

c. 1D KCE, motion #13 per Table 4.3

d. 1D BBM, motion #14 per Table 4.3

Figure 5.35. Wave height time series calculated using a *regular tank approximation* per Figure 5.30 and experimental results recorded by TE, tests series 2-FB

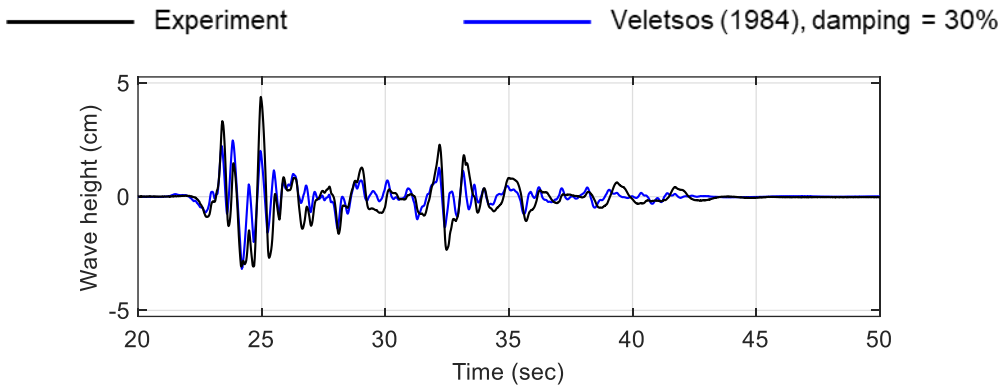

a. 1D CCE, motion #1 per Table 4.4

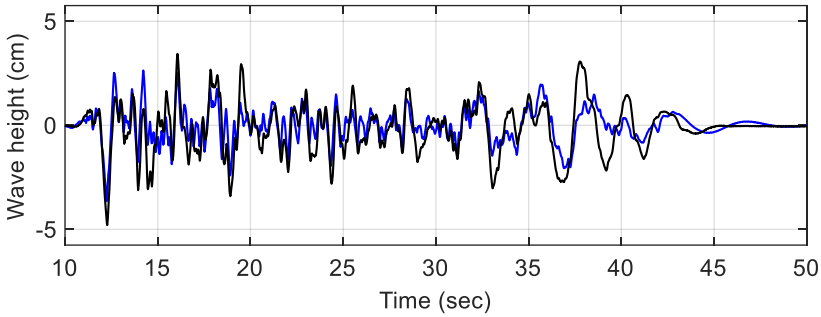

b. 1D KCE, motion #2 per Table 4.4

Figure 5.36. Wave height time series calculated using a *regular tank approximation* per Figure 5.30 and experimental results recorded by TE, tests series 2-SFP

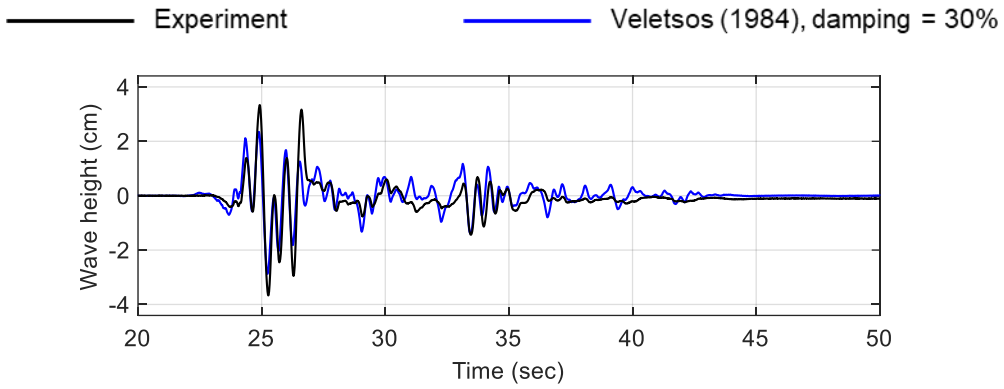

a. 1D CCE, motion #1 per Table 4.5

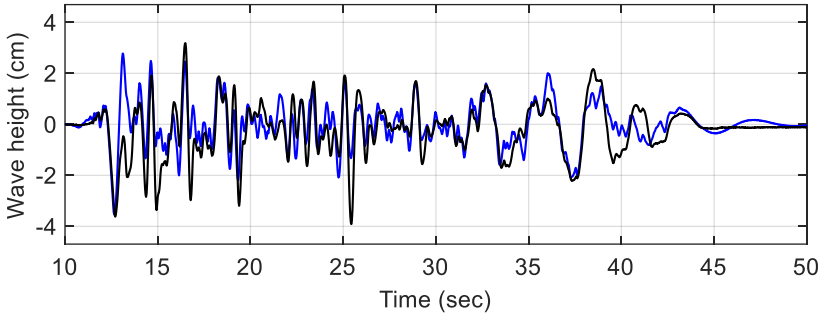

b. 1D KCE, motion #2 per Table 4.5

Figure 5.37. Wave height time series calculated using a *regular tank approximation* per Figure 5.30 and experimental results recorded by TE, tests series 2-TFP

Table 5.2. Peak experimental and analytical[†] wave height responses and percentage differences

Motion, test series	Experimental (cm)	Analytical (cm)	Difference (%)
1D CCE, 2-FB	6.0	5.5	-7
1D ECE, 2-FB	2.4	3.6	49
1D KCE, 2-FB	2.4	2.6	7
1D BBM, 2-FB	3.0	3.0	2
1D CCE, 2-SFP	4.4	3.2	-28
1D KCE, 2-SFP	4.8	3.6	-24
1D CCE, 2-TFP	3.7	2.9	-22
1D KCE, 2-TFP	3.9	3.5	-10

[†]Analytical wave height responses evaluated using Veletsos (1984).

Responses calculated using the *annular tank approximation* per Figure 5.30 and the Tang solution were significantly greater than those measured in the experiments. Figure 5.38 presents wave height responses calculated using the *annular tank approximation* and experimental results for two earthquake inputs. No value of damping ratio provided satisfactory results in this case. This indicates that of the two approximations, the *regular tank approximation* is better suited for analyzing the sloshing response of the fluid in the test specimen.

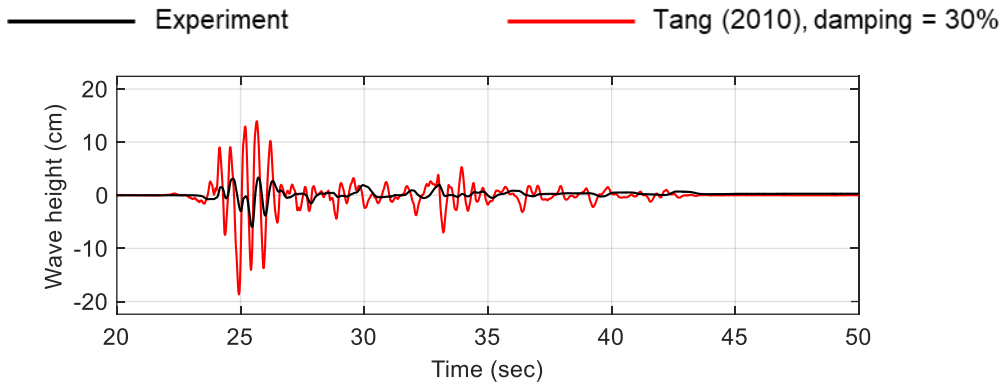

a. 1D CCE, motion #11 per Table 4.3

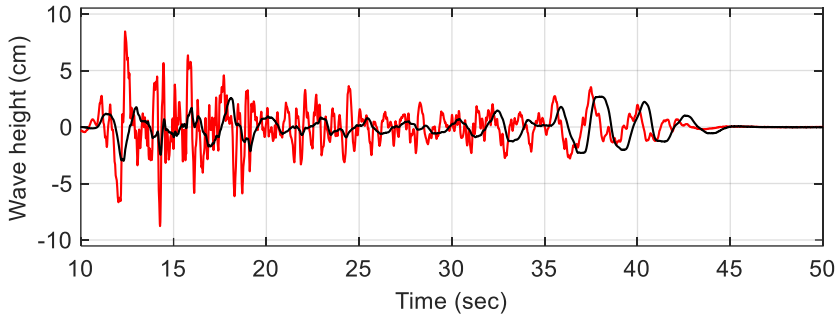

b. 1D ECE, motion #13 per Table 4.3

Figure 5.38. Wave height time series calculated using an *annular tank approximation* per Figure 5.30 and experimental results recorded by TE, tests series 2-FB

5.2.6 Pebble bed

Compaction of the pebble bed under earthquake shaking was studied in test series 3. The visual scales introduced in Figure 4.6 were used to monitor and estimate the displacement of the underside of the pebble bed and to calculate changes in packing fraction. As discussed in section 4.4.3, the 3D KCE motion with peak accelerations of 0.57g, 0.65g, and 0.39g in the *x*, *y*, and *z* directions, respectively, was run repeatedly and the packing fraction calculated after each run. The three components had *significant shaking* durations of 19.2 s, 18.0 s, and 19.7 s, as indicated in Figure 5.39, where significant shaking duration is defined as the time interval bracketing 90% of the Arias intensity (I_A) (Arias 1970) of the acceleration time series[7].

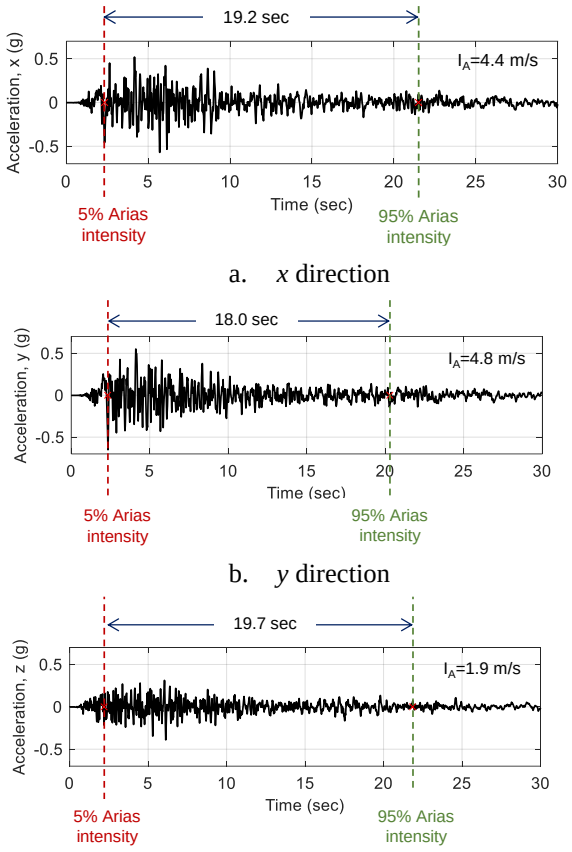

Figure 5.39. Significant shaking duration of the three components of 3D KCE motion used for assessing pebble compaction

[7]The Arias intensity I_A of an acceleration time series is defined as $I_A = \frac{\pi}{2g}\int_0^{T_d} a(t)^2\,dt$ where, where $a(t)$ is the acceleration time (t) series and T_d is the duration of the time series.

Tests were run in the fixed-base (FB) configuration, and two base-isolated configurations using Single concave Friction Pendulum (SFP) bearings and Triple Friction Pendulum (TFP) bearings. The height of the underside of the pebble bed was measured using the visual scales before and after each run of the 3D KCE motion. Figure 5.40 presents pictures of the underside of the pebble bed taken before and after tests with the 3D KCE input in different test configurations. Since the pebbles were loaded manually, a constant initial packing fraction was not achieved in the different configurations.

Figure 5.41 presents the change in packing fraction with duration of significant shaking in the different configurations. One run of the 3D KCE motion is considered to correspond to a significant shaking duration of 19.0 s, which is the average of the significant shaking duration in the three directions; see Figure 5.39. For the TFP-isolated configuration, two rounds of tests were conducted (round 1 and round 2 in Figure 5.41) because the initial packing fraction in round 1 (= 0.622) was greater than that achieved in the prior two configurations (=0.613 in both the fixed base and the SFP isolated configurations). The initial packing fraction in all tested configurations was greater than that expected in the prototype reactor vessel (= 0.6) where the pebbles are loaded using a different approach: introduced one by one near the base of the vessel such that they rise through the Flibe.

The maximum change in packing fraction in all tested configurations after 150+ seconds of significant shaking was of the order of 3%. The percentage change in packing fraction in a particular configuration depended on the initial packing fraction. The greatest packing fraction after shaking in all tested configurations was 0.628, which was within the expected range (0.625 to 0.641) for a vibrated bed of spheres per Dullien (1992).

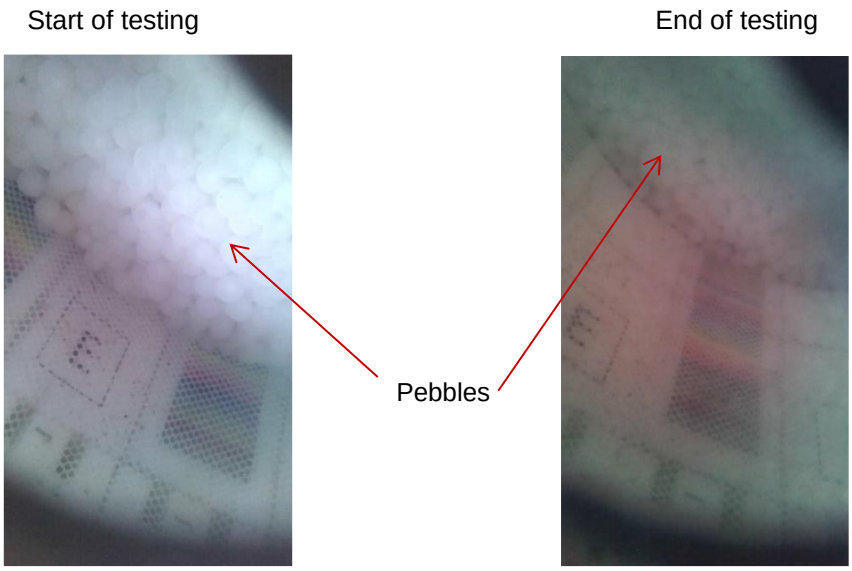

a. fixed base configuration

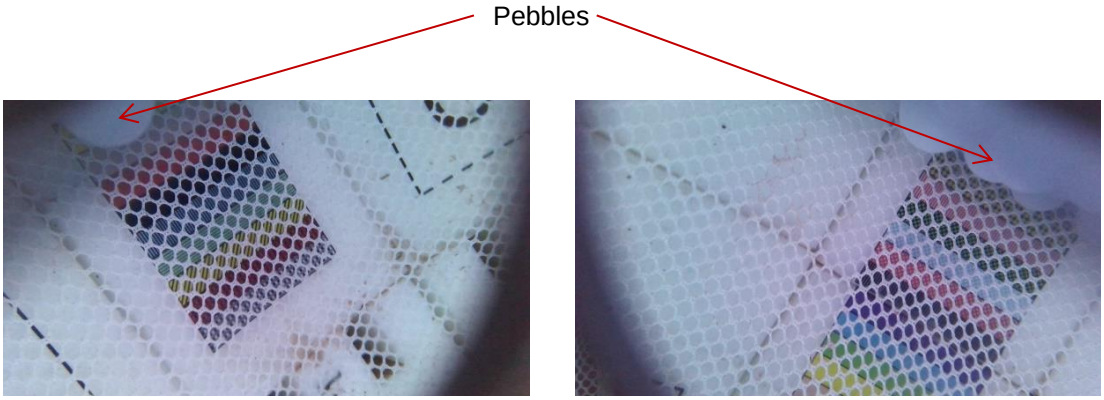

b. SFP-isolated configuration

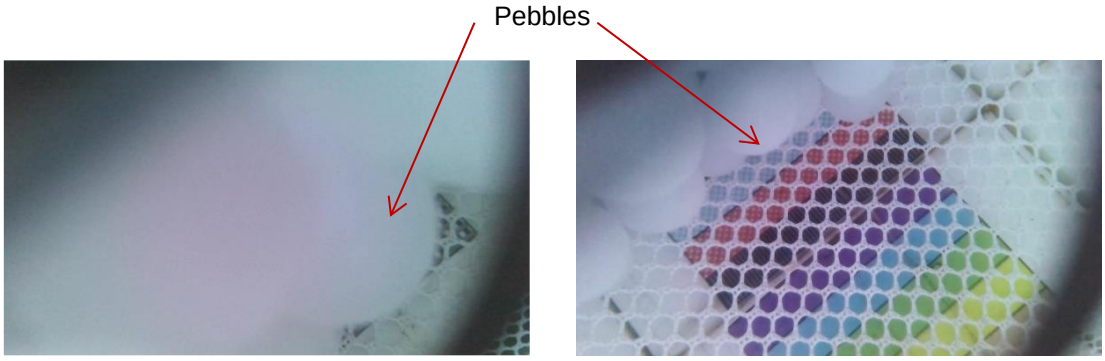

c. TFP-isolated configuration, round 2

Figure 5.40. Pictures of the underside of the pebble bed taken at the start and end of testing (refer to the visual scales presented in Figure 4.6)

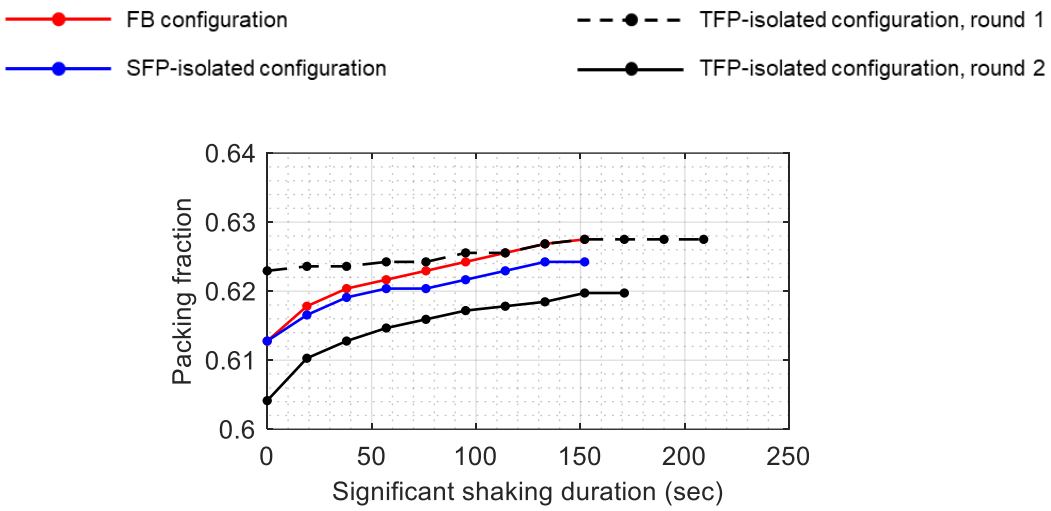

Figure 5.41. Change in packing fraction with significant shaking duration

5.3 Key responses in isolated configurations

Key test results from test series 2-SFP and 2-TFP per section 4.4.2 are presented in this sub-section. Table 5.3 presents information on the acceleration time series used to compare response spectra at different locations in the test specimen. Response spectra of accelerations recorded below the isolation interface and at multiple locations above the isolation interface in tests of 2-SFP and 2-TFP are presented in Figure 5.42 through Figure 5.53.

Table 5.3. Calculation of key acceleration responses† from test data for comparison

Location and direction		Expression† used for calculation
Below isolation interface (see Figure 4.2)	*x* direction (m/s^2)	$(ANE0X + ANW0X + ASE0X + ASW0X)/4$
	y direction (m/s^2)	$(ANE0Y + ANW0Y + ASE0Y + ASW0Y)/4$
	z direction (m/s^2)	$(ANE0Z + ANW0Z + ASE0Z + ASW0Z)/4$
	Rocking about *x* direction (rad/s^2)	$(ATBLNZ - ATBLSZ)/1.219\,\text{m}$
	Rocking about *y* direction (rad/s^2)	$(ATBLWZ - ATBLEZ)/1.219\,\text{m}$
Above isolation interface (see Figure 4.2)	*x* direction (m/s^2)	$(ANE1X + ANW1X + ASE1X + ASW1X)/4$
	y direction (m/s^2)	$(ANE1Y + ANW1Y + ASE1Y + ASW1Y)/4$
	z direction (m/s^2)	$(ANE1Z + ANW1Z + ASE1Z + ASW1Z)/4$
	Rocking about *x* direction (rad/s^2)	$(ABNZ - ABSZ)/2\,\text{m}$
	Rocking about *y* direction (rad/s^2)	$(ABWZ - ABEZ)/2\,\text{m}$
Bottom of core barrel†† (see Figure 4.3)	$\hat{x}$ direction (m/s^2)	$(ACRE + ACRW)/2$
	$\hat{y}$ direction (m/s^2)	$(ACRN + ACRS)/2$
Top of reflector-block assembly†† (see Figure 4.4)	$\hat{x}$ direction (m/s^2)	$(ARFN3X + ARFS3X + ARFE3X + ARFW3X)/4$
	$\hat{y}$ direction (m/s^2)	$(ARFN3Y + ARFS3Y + ARFE3Y + ARFW3Y)/4$
	z direction (m/s^2)	$(ARFN3Z + ARFS3Z + ARFE3Z + ARFW3Z)/4$

† All acceleration time series were filtered using a 0.05 Hz – 50 Hz *bandpass* filter.

† Accelerometer names per section 4.2 are used here to denote recorded acceleration time series in units of m/s^2.

†† The acceleration responses along $\hat{x}$ and $\hat{y}$ directions were transformed for comparison with *x* and *y* direction responses above and below the isolation interface.

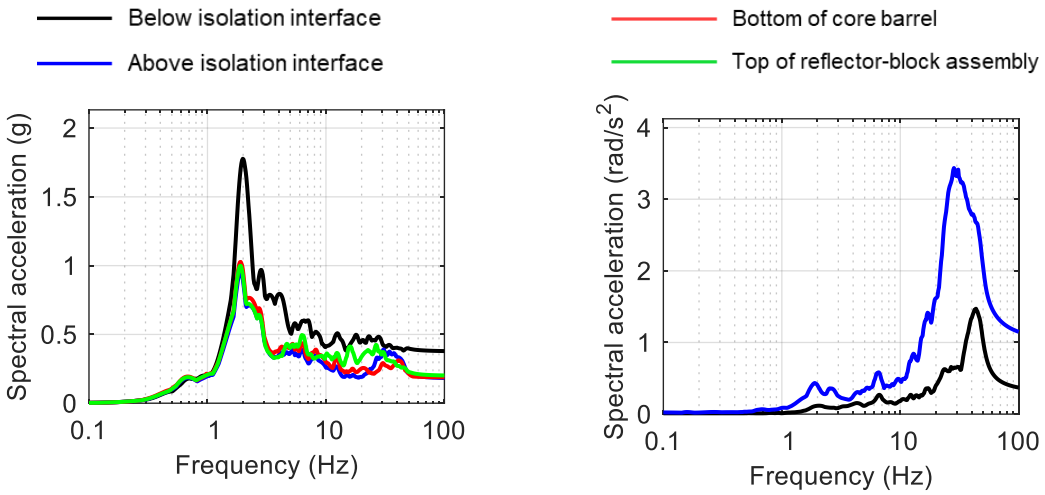

a. *x* direction b. rocking about *y* direction

Figure 5.42. Acceleration spectra in SFP-isolated configuration, motion #1 per Table 4.4 (1D CCE), 5% damping

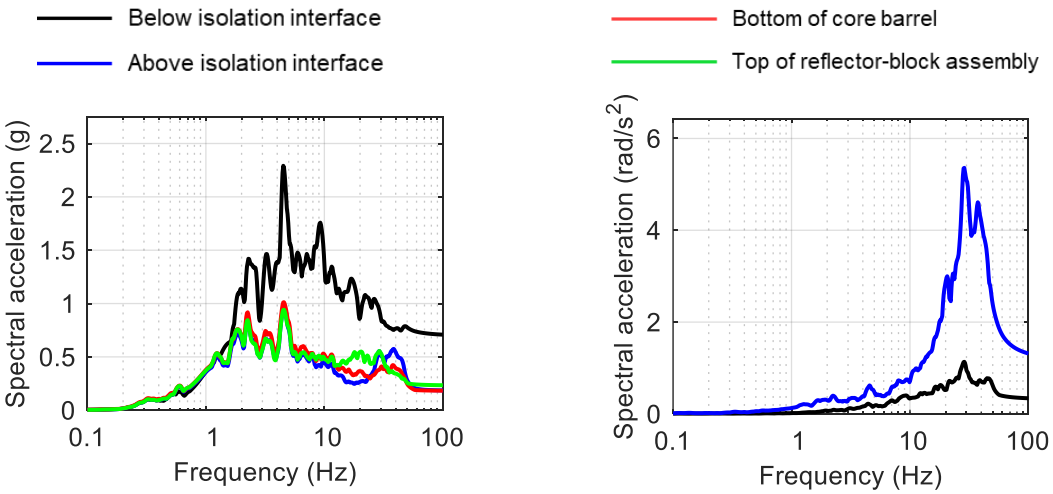

a. *x* direction b. rocking about *y* direction

Figure 5.43. Acceleration spectra in SFP-isolated configuration, motion #2 per Table 4.4 (1D KCE), 5% damping

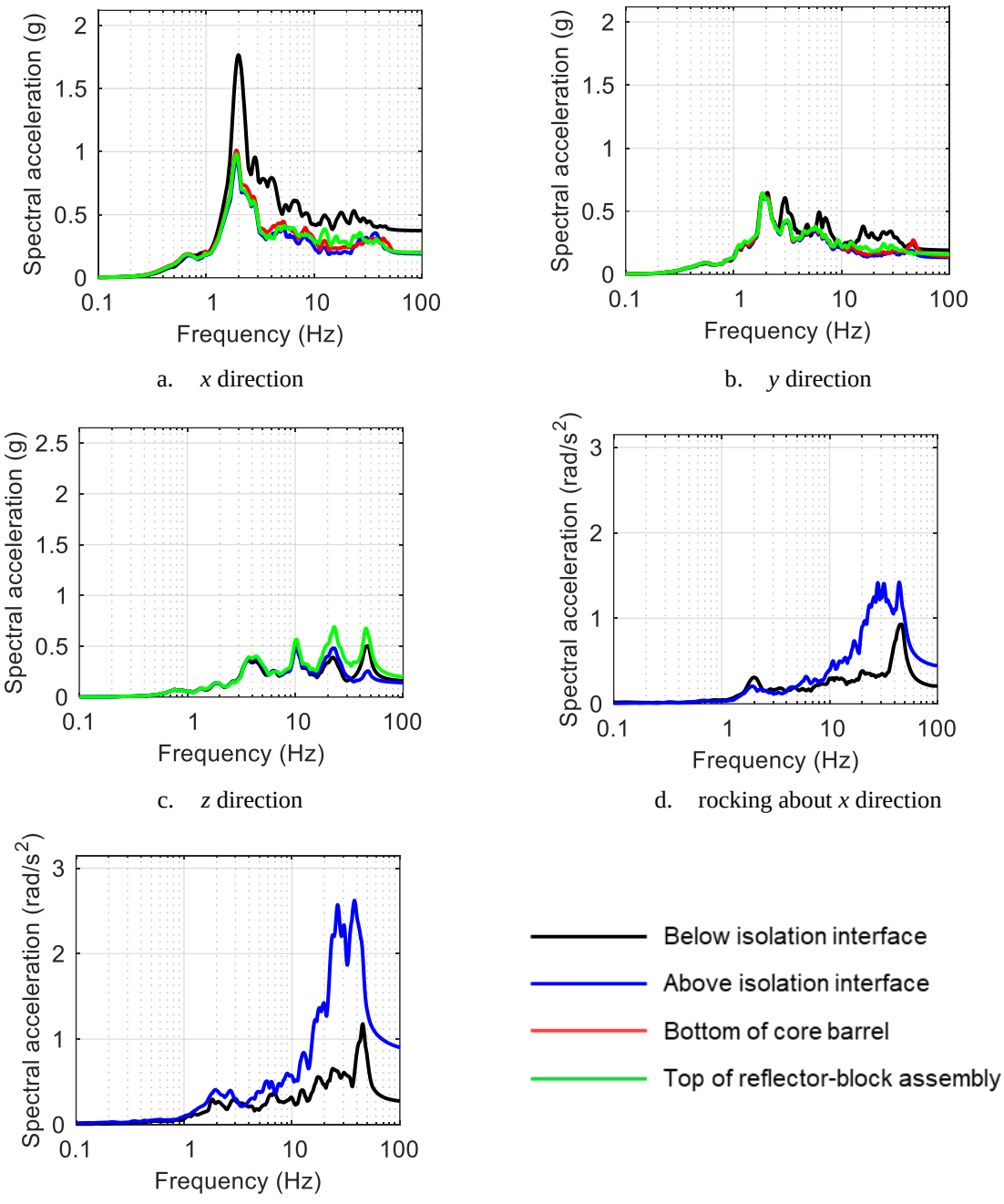

a. *x* direction

b. *y* direction

c. *z* direction

d. rocking about *x* direction

e. rocking about *y* direction

Figure 5.44. Acceleration spectra in SFP-isolated configuration, motion #3 per Table 4.4 (3D CCE), 5% damping

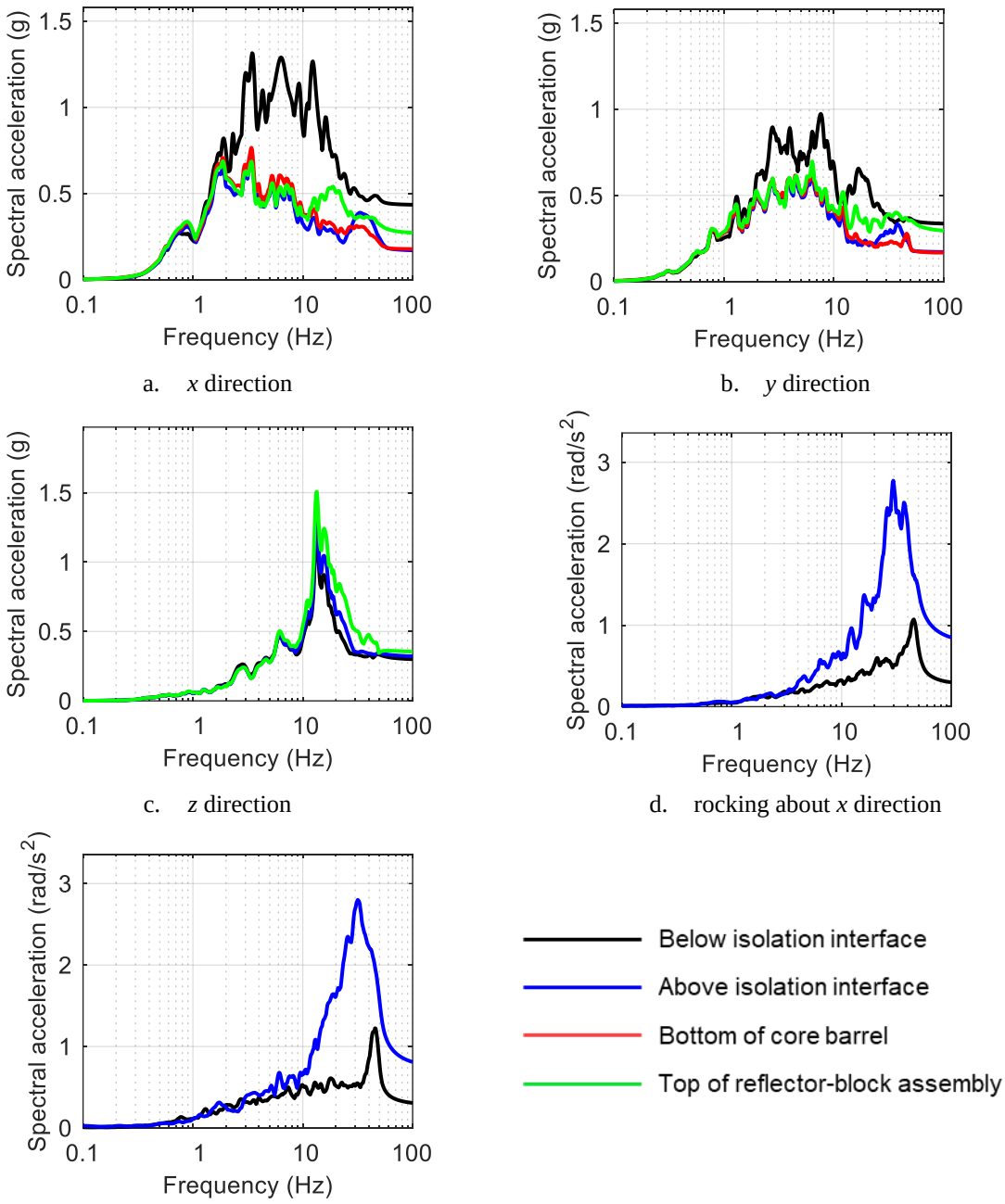

a. *x* direction

b. *y* direction

c. *z* direction

d. rocking about *x* direction

e. rocking about *y* direction

Figure 5.45. Acceleration spectra in SFP-isolated configuration, motion #4 per Table 4.4 (3D ECE), 5% damping

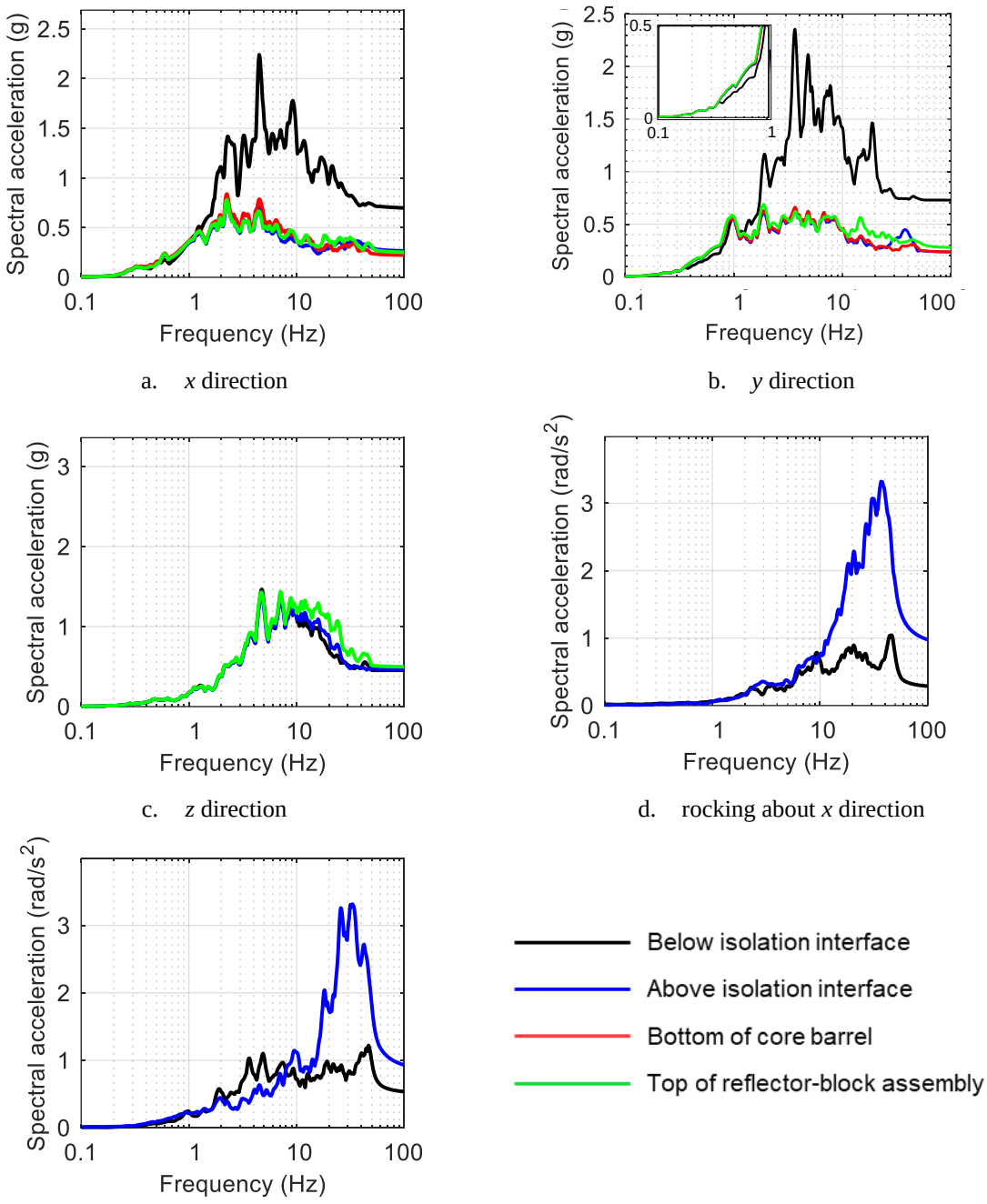

a. *x* direction

b. *y* direction

c. *z* direction

d. rocking about *x* direction

e. rocking about *y* direction

Figure 5.46. Acceleration spectra in SFP-isolated configuration, motion #5 per Table 4.4 (3D KCE), 5% damping

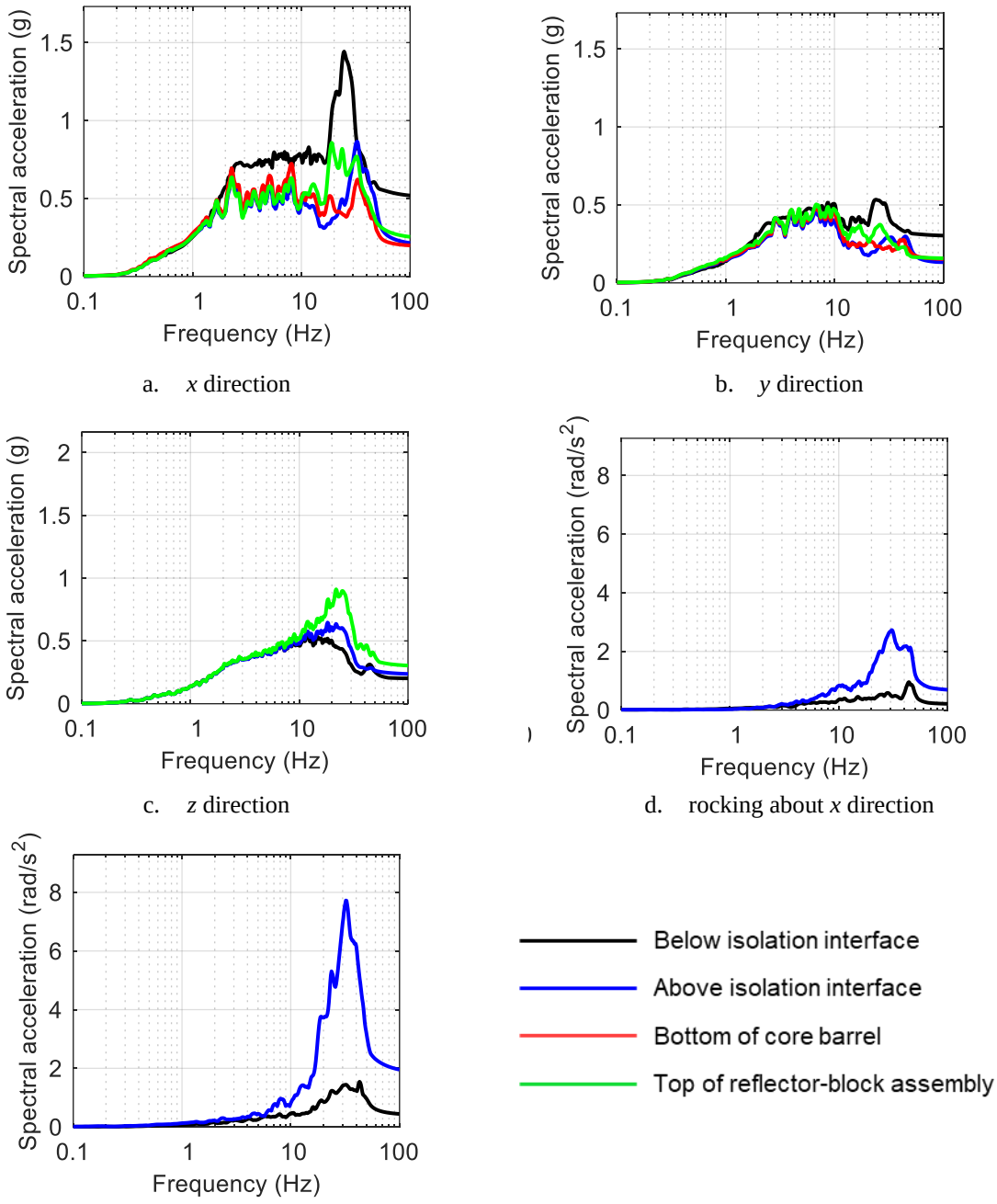

a. *x* direction

b. *y* direction

c. *z* direction

d. rocking about *x* direction

e. rocking about *y* direction

Figure 5.47. Acceleration spectra in SFP-isolated configuration, motion #6 per Table 4.4 (3D BBM), 5% damping

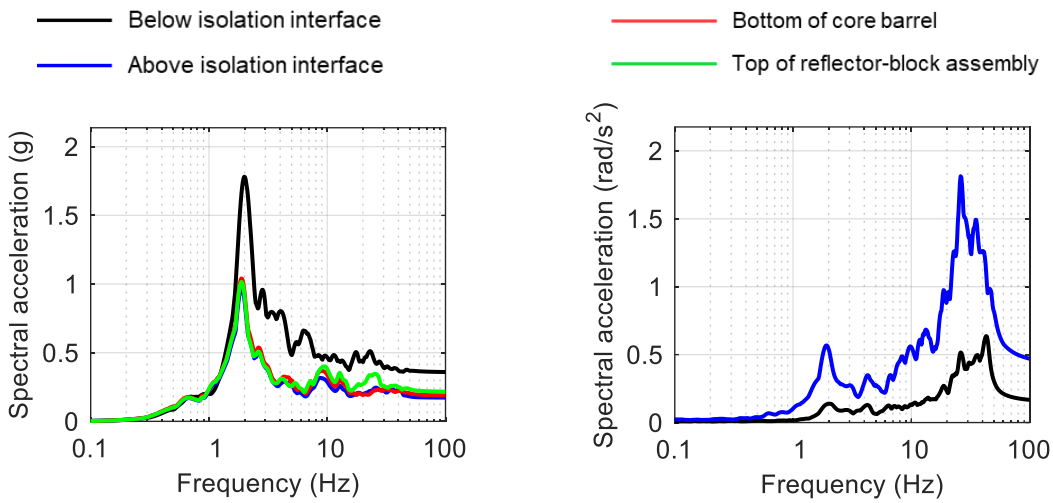

a. *x* direction b. rocking about *y* direction

Figure 5.48. Acceleration spectra in TFP-isolated configuration, motion #1 per Table 4.5 (1D CCE), 5% damping

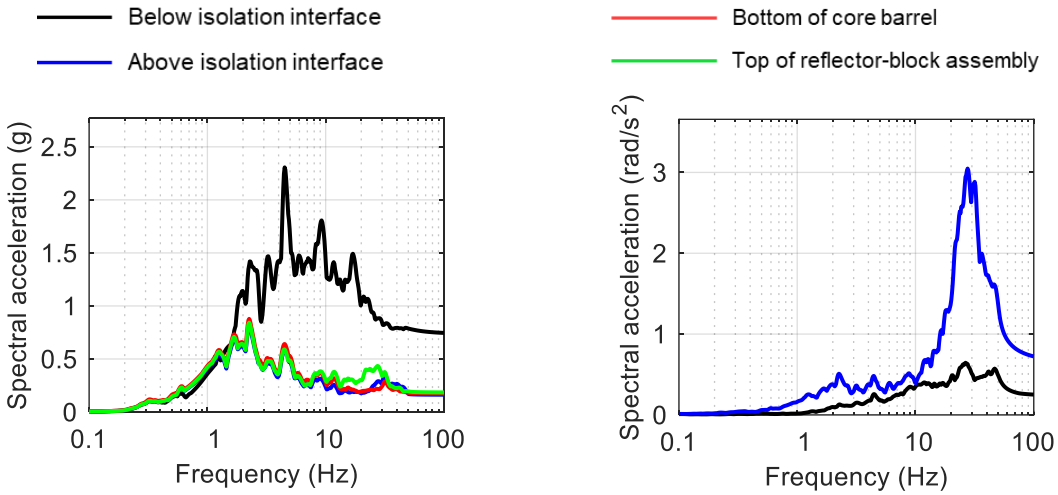

a. *x* direction b. rocking about *y* direction

Figure 5.49. Acceleration spectra in TFP-isolated configuration, motion #2 per Table 4.5 (1D KCE), 5% damping

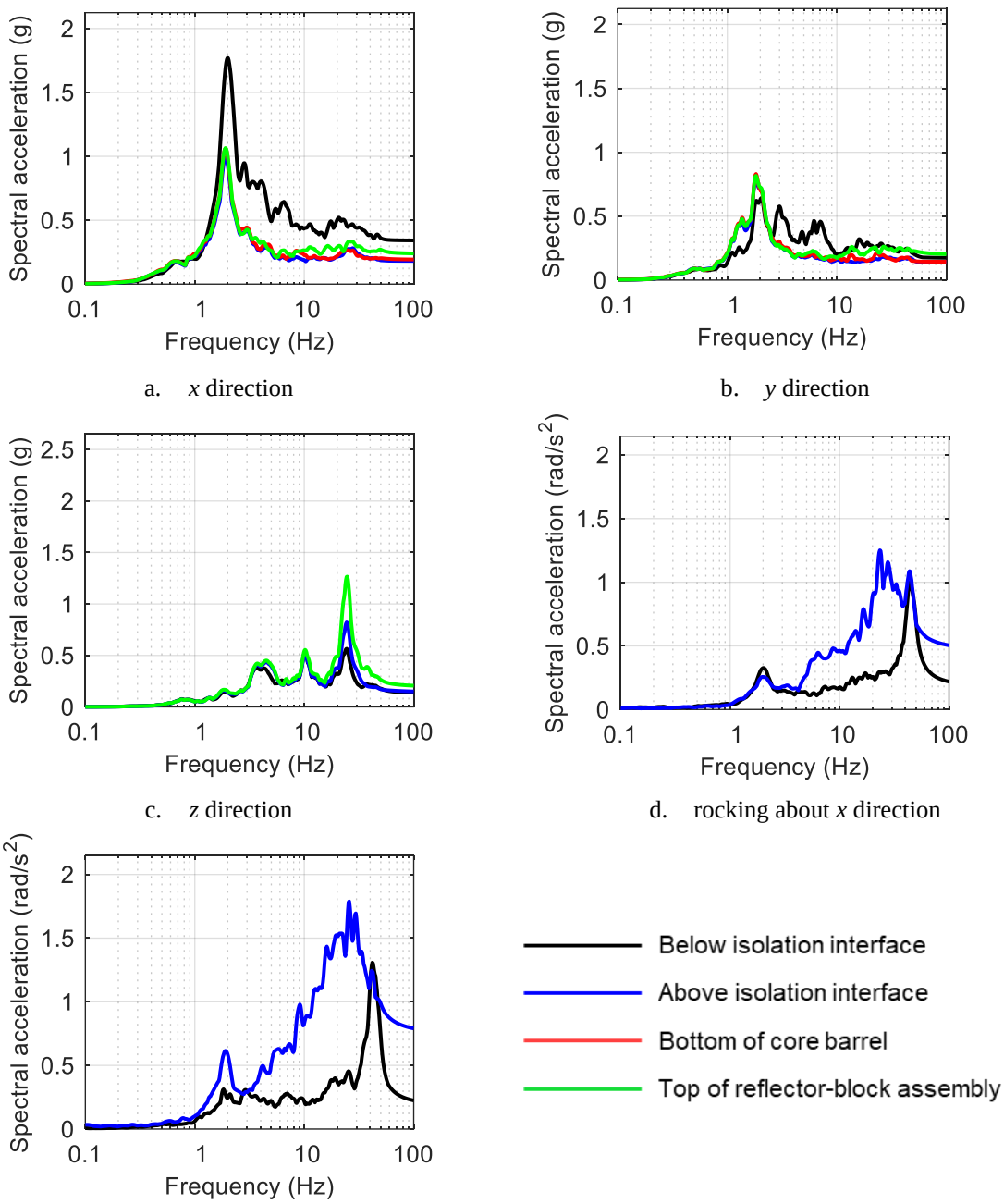

a. *x* direction

b. *y* direction

c. *z* direction

d. rocking about *x* direction

e. rocking about *y* direction

Figure 5.50. Acceleration spectra in TFP-isolated configuration, motion #3 per Table 4.5 (3D CCE), 5% damping

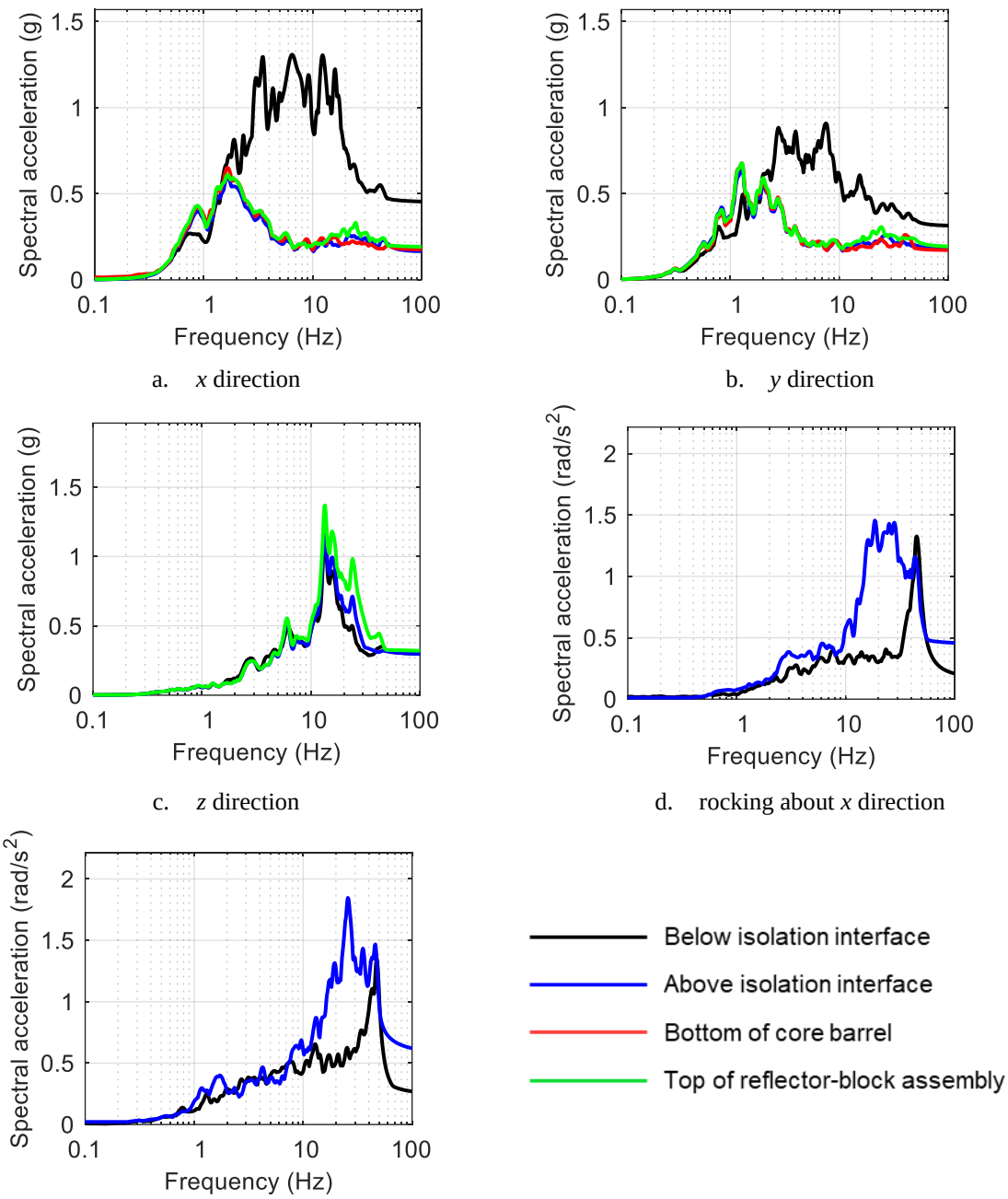

a. *x* direction

b. *y* direction

c. *z* direction

d. rocking about *x* direction

e. rocking about *y* direction

Figure 5.51. Acceleration spectra in TFP-isolated configuration, motion #4 per Table 4.5 (3D ECE), 5% damping

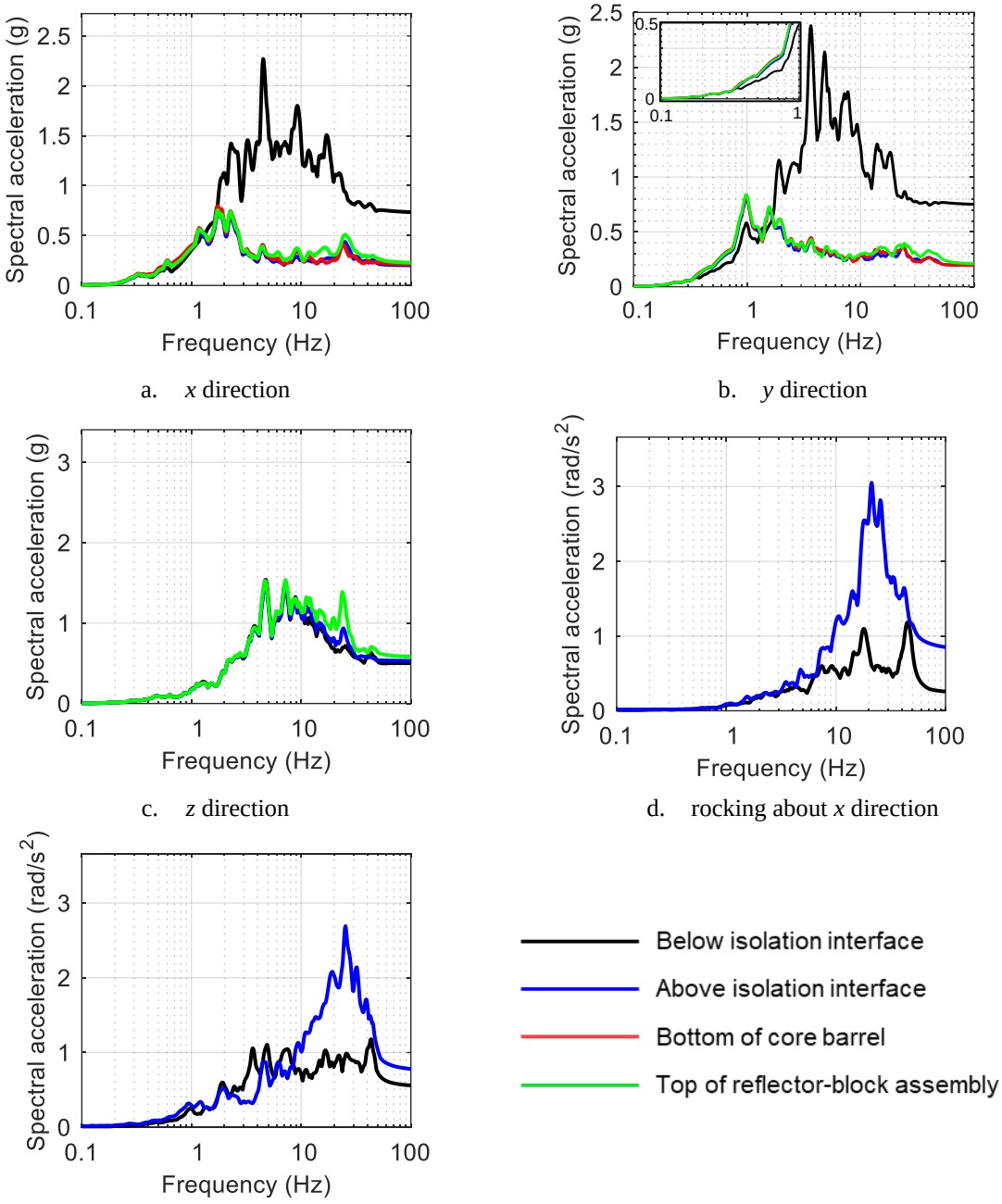

a. *x* direction

b. *y* direction

c. *z* direction

d. rocking about *x* direction

e. rocking about *y* direction

Figure 5.52. Acceleration spectra in TFP-isolated configuration, motion #5 per Table 4.5 (3D KCE), 5% damping

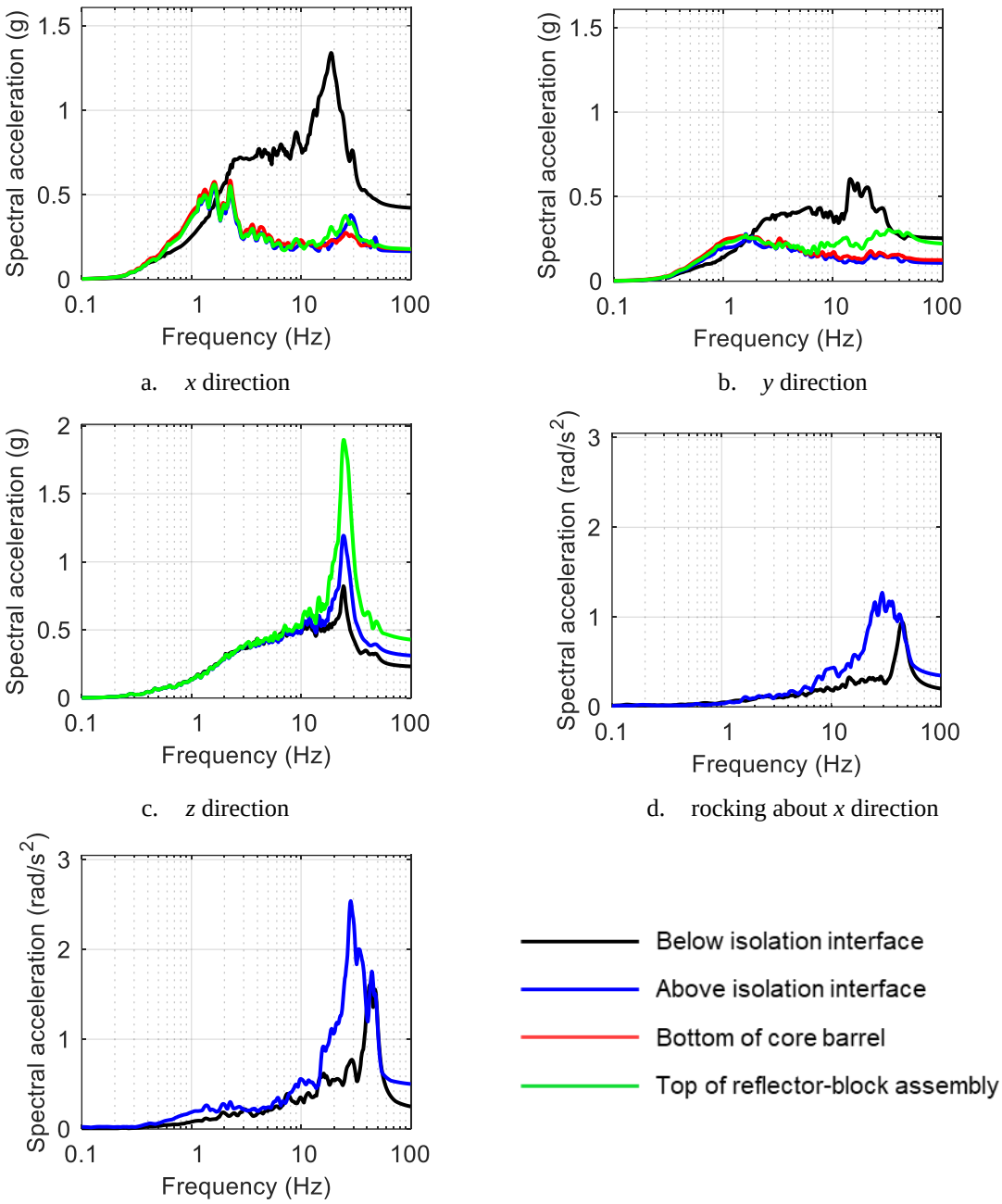

a. *x* direction

b. *y* direction

c. *z* direction

d. rocking about *x* direction

e. rocking about *y* direction

Figure 5.53. Acceleration spectra in TFP-isolated configuration, motion #6 per Table 4.5 (3D BBM), 5% damping

Figure 5.54 and Figure 5.55 present the horizontal displacement orbits of the bearings in tests of 2-SFP and 2-TFP, respectively. The horizontal displacements d_x and d_y along the *x* and *y* directions, respectively, were calculated using recordings from eight string potentiometers, per Figure 4.2, as follows:

$$d_x = ((SPNE1X + SPSE1X) - (SPNE0X + SPSE0X))/2 \quad (5\text{-}15)$$

$$d_y = ((SPNE1Y + SPNW1Y) - (SPNE0Y + SPNW0Y))/2 \quad (5\text{-}16)$$

The dashed blue open circle in each of these figures identifies the peak horizontal displacement.

Table 5.4 and Table 5.5 presents the peak accelerations at the locations identified in Table 5.3 and the peak isolator displacements for tests in the two base-isolated configurations. The peak horizontal accelerations above the isolation interface (on the base of the vessel) were between 1.4 and 3.8 (1.2 and 4.6) times smaller than those below the isolation interface in the SFP-isolated (TFP-isolated) tests. The reduction in peak horizontal accelerations for the high amplitude KCE input (1D or 3D) was greater than for other inputs. Expectedly, there was an increase, albeit very small, in spectral acceleration around the sliding frequencies of the isolators: see the insets to Figure 5.46b and Figure 5.52b for two examples. The peak displacements in TFP-isolated configuration were greater than in SFP-isolated configuration for similar inputs because of differences in sliding periods in the two isolation systems and the adaptive behavior of the TFP bearings, that is, sliding on multiple concave surfaces.

Spectral accelerations in the vertical direction above the isolation interface were amplified at high frequencies (25+ Hz). Rocking accelerations above the isolation interface were also amplified at high frequencies because of the vertical flexibility of the SFP and TFP bearings, as discussed in section 3.3[8]. The maximum amplification in peak vertical accelerations across all isolated-configuration tests was by a factor of 1.3 with respect to the vertical acceleration below the isolation interface.

[8]Modal analysis of the SFP- and TFP-isolated configurations, presented in section 6.4, indicated that the frequencies of the vertical and rocking modes are nearly 38 Hz and 30 Hz, respectively, in both configurations, which explains the amplification of accelerations noted here.

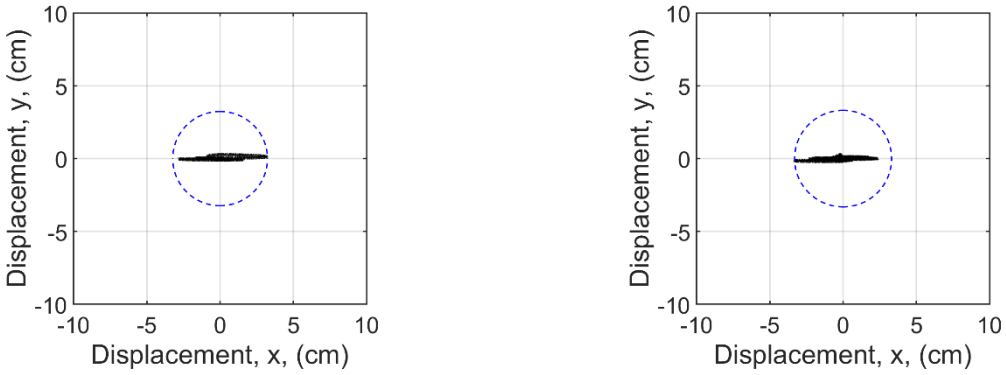

a. motion #1 (1D CCE)

b. motion #2 (1D KCE)

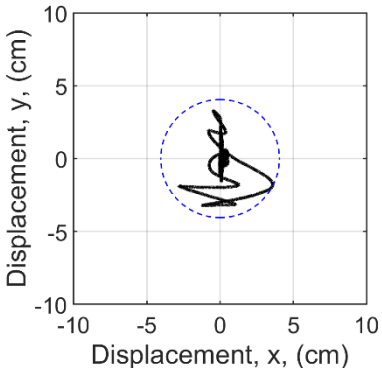

c. motion #3 (3D CCE)

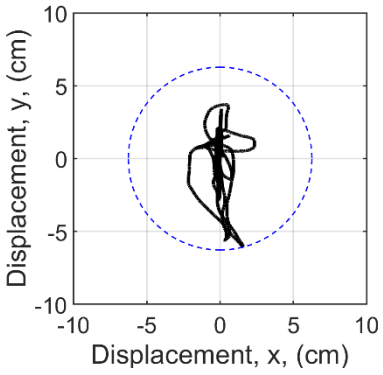

d. motion #4 (3D ECE)

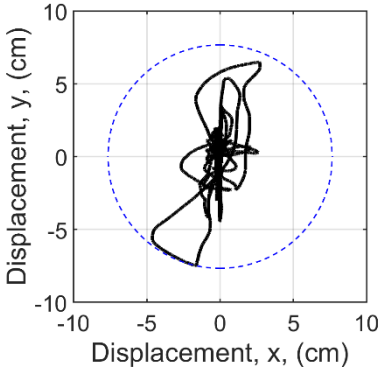

e. motion #5 (3D KCE)

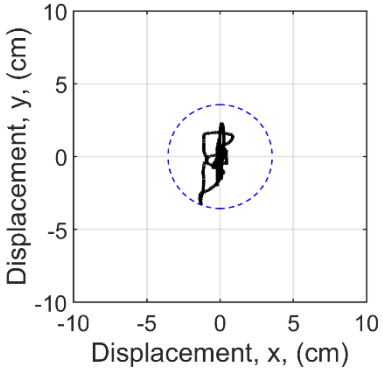

f. motion #6 (3D BBM)

Figure 5.54. Displacement orbits in SFP-isolated tests per Table 4.4, dashed blue open circles identify peak displacement, black curve traces movement of the slider

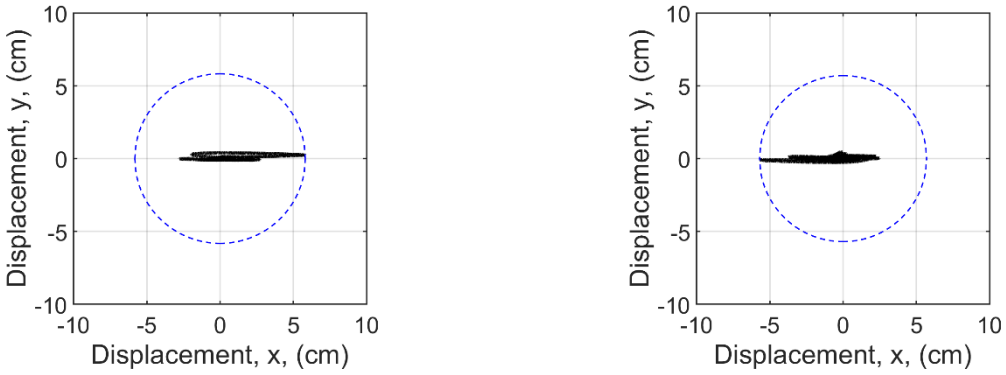

a. motion #1 (1D CCE)

b. motion #2 (1D KCE)

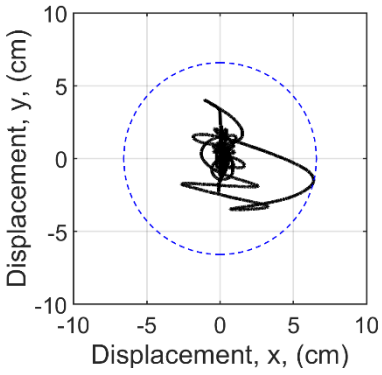

c. motion #3 (3D CCE)

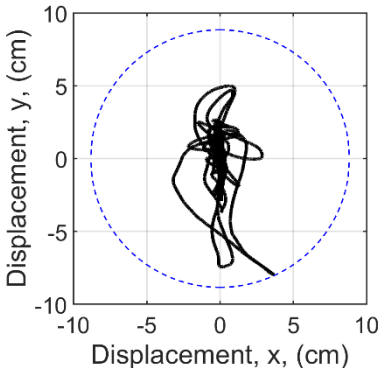

d. motion #4 (3D ECE)

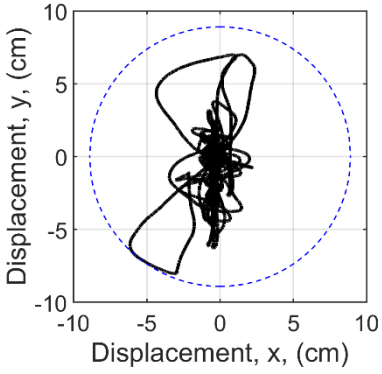

e. motion #5 (3D KCE)

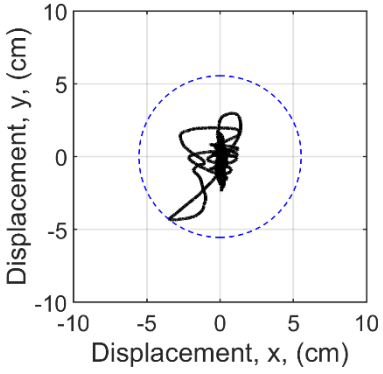

f. motion #6 (3D BBM)

Figure 5.55. Displacement orbits in TFP-isolated tests per Table 4.5, dashed blue open circles identify peak displacement, black curve traces movement of the slider

Table 5.4. Peak values of key responses in tests of the SFP-isolated configuration

Motion	Peak accelerations (g)											Peak isolator disp. (cm)
	Below isolation interface			Above isolation interface			Bottom of core barrel		Top of RB assembly			
	x	*y*	*z*	*x*	*y*	*z*	*x*	*y*	*x*	*y*	*z*	
#1 (1D CCE)	0.38	-	-	0.18	-	-	0.19	-	0.20	-	-	3.2
#2 (1D KCE)	0.71	-	-	0.19	-	-	0.18	-	0.23	-	-	3.3
#3 (3D CCE)	0.37	0.19	0.16	0.19	0.13	0.14	0.20	0.14	0.20	0.16	0.20	4.1
#4 (3D ECE)	0.43	0.34	0.30	0.17	0.17	0.32	0.18	0.17	0.27	0.30	0.35	6.3
#5 (3D KCE)	0.70	0.73	0.45	0.27	0.23	0.46	0.22	0.24	0.25	0.28	0.50	7.7
#6 (3D BBM)	0.52	0.30	0.20	0.21	0.13	0.24	0.20	0.15	0.25	0.16	0.30	3.6

Table 5.5. Peak values of key responses in tests of the TFP-isolated configuration

Motion	Peak accelerations (g)											Peak isolator disp. (cm)
	Below isolation interface			Above isolation interface			Bottom of core barrel		Top of RB assembly			
	x	*y*	*z*	*x*	*y*	*z*	*x*	*y*	*x*	*y*	*z*	
#1 (1D CCE)	0.36	-	-	0.17	-	-	0.19	-	0.22	-	-	5.8
#2 (1D KCE)	0.75	-	-	0.16	-	-	0.17	-	0.18	-	-	5.7
#3 (3D CCE)	0.34	0.17	0.14	0.18	0.14	0.15	0.19	0.14	0.24	0.20	0.21	6.6
#4 (3D ECE)	0.45	0.32	0.30	0.17	0.19	0.30	0.18	0.17	0.19	0.19	0.32	8.8
#5 (3D KCE)	0.73	0.75	0.50	0.20	0.19	0.53	0.21	0.20	0.23	0.21	0.58	8.9
#6 (3D BBM)	0.42	0.25	0.23	0.17	0.11	0.31	0.18	0.13	0.18	0.22	0.43	5.5

5.4 Summary

Results from earthquake-simulator experiments were discussed in this section and conclusions were drawn regarding the behavior of different components of the model. The outer vessel and the core barrel responded as a near-rigid unit with no relative displacements between them. Analysis of a lumped-mass model, wherein the mass of the test specimen was lumped at its center of mass, provided accurate estimates of base reactions.

The reflector-block assembly responded as one unit with negligible relative displacements between blocks. The high frequency responses of the core barrel and the reflector-block assembly were not particularly well-characterized.

The sloshing response of the fluid in the annulus between the reflector-block assembly and the core barrel was heavily damped and could be approximately recovered using an analytical solution for the sloshing response of a regular cylindrical tank and a large value of damping ratio.

The behavior of the pebble bed was studied by repeatedly running a strong 3D input and observing the change in height of the underside of the pebble bed. The packing fraction of the pebble bed changed by 3% after 150+ seconds of strong shaking.

Two isolation systems, utilizing SFP and TFP bearings were used to base-isolate the vessel. Peak horizontal accelerations at the base of the outer vessel reduced by a factor between 1.4 and 3.8 (1.2 and 4.6) with respect to inputs to the isolation system in the SFP-isolated (TFP-isolated) tests. Vertical and rocking accelerations were amplified by the isolation systems at high frequencies (25+ Hz) due their flexibility in the vertical direction.

SECTION 6
MODELLING AND ANALYSIS OF MOLTEN SALT REACTORS

6.1 Introduction

This section presents recommendations for analysis and modelling of different components of a base-isolated Fluoride-salt-cooled High temperature Reactor (FHR), based on results of tests described in the previous sections of this report. Section 6.2 presents recommendations for modelling fluid behavior to compute sloshing wave height and hydrodynamic pressure. Section 0 presents a practical approach to estimate forces in connections between blocks in a reflector assembly. Section 6.4 investigates modelling and analysis of the two base-isolation systems used in the physical tests. Recommendations are provided in Section 6.5.

6.2 Fluid behavior

6.2.1 Sloshing responses in small-width annuli

Sloshing of fluid in the annulus between the core barrel and the reflector-block assembly (see Figure 3.1) was discussed in section 5.2.5, wherein it was demonstrated that the use of a *regular tank approximation* with a fluid height equal to the distance between the underside of the reflector-block assembly and the base of the vessel, and a large value of damping for the sloshing mode (30% of critical, calibrated using the experimental data) resulted in reasonably accurate estimates of sloshing wave height.

Numerical estimation of sloshing responses in the thin annulus between the core barrel and reflector-block assembly is challenging for two reasons: 1) a computationally-expensive (fine) finite element mesh is required in the annulus to obtain meaningful results for wave height, and 2) the computation of the damping ratio in the sloshing mode, associated with boundary effects in the thin annulus and constricted flow between gaps in reflector blocks, is fluid- and geometry-specific.

To address the challenge of computational expense, two annular tank geometries were modelled using the Arbitrary Lagrangian Eulerian (ALE) solver of LS-DYNA (LSTC 2017): 1) model A with a large annulus, with a ratio (k) of outer tank radius to inner tank radius of 0.5, and 2) model B with a small (thin) annulus, with $k = 0.98$. The first model was chosen as a benchmark case. The width of the annulus in the second model was set equal to that between the reflector-block assembly and the core barrel in the test specimen. The radius of the outer tank in model A and model B was equal to that of the core barrel in the test specimen. Figure 6.1 shows the two finite element models and the used coordinate systems.

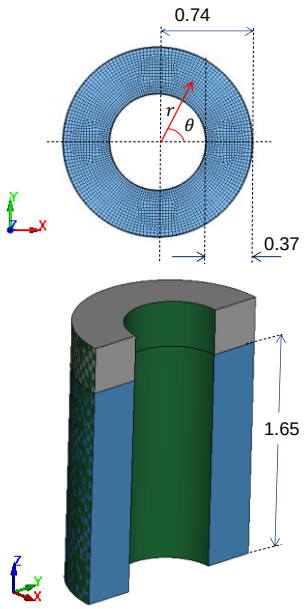

a. model A, k = 0.5, plan view of fluid-domain mesh and cutaway view

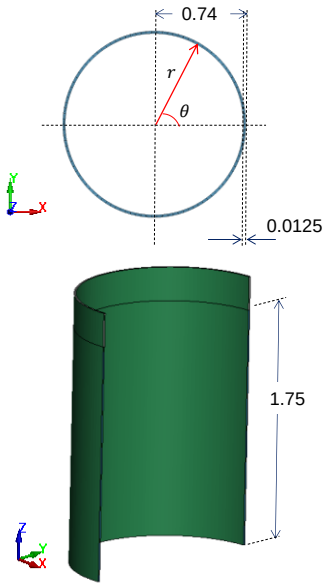

b. model B, k = 0.98, plan view of fluid-domain mesh and cutaway view

Figure 6.1. Annular tanks analyzed in LS-DYNA, dimensions in m

The outer tank, inner tank, and the base of each annular tank, shown in green in Figure 6.1, were modeled using Lagrangian, four-node, shell elements, and as a rigid material such that their mass was nearly zero. (Acceleration cannot be applied to an element(s) with zero mass in LS-DYNA.) The fluid (water) domain and the space above the free surface (to accommodate sloshing), shown in blue and gray, respectively, in Figure 6.1, were modeled using Eulerian, eight-node solid elements. These Eulerian elements do not deform but rather serve as a grid through which fluid can flow. The material properties of the fluid domain were assigned using the *MAT (material) and *EOS (equation of state) cards in LS-DYNA. Water was assigned a density of 1000 kg/m^3, a dynamic viscosity of 0 Ns/m^2, and a bulk modulus of 2.2 GPa, to simulate inviscid and incompressible properties per Yu and Whittaker (2022). The space above the water was assigned *void properties* using the *INITIAL_VOID card. The fluid-domain elements near the walls of the inner and the outer tanks in model A were smaller than elsewhere (see plan view in Figure 6.1a). The annular space in model B was meshed using four elements in plan (see Figure 6.1b). Solid elements in the fluid domain (including the *void space*) shared nodes with the structural shell elements. The vertical movement of the free surface (sloshing) under seismic inputs was tracked by defining massless nodes, referred to as *tracers*, on the free surface of water using the *DATABASE_TRACER card. A detailed discussion on *tracers* is presented in Yu and Whittaker (2021).

Both models were analyzed for a horizontal input of four cycles of a sinusoid with a frequency of 1 Hz and an amplitude of 0.1g. The acceleration history was input using the keyword BOUNDARY_PRESCRIBED_MOTION_RIGID. An acceleration of 9.81 m/s^2 was applied in the negative *z* direction in the models to simulate gravity. This acceleration was applied as a ramp from 0 to 9.81 m/s^2 in the initial 0.2 s of analysis, followed by a constant gravitational acceleration of 9.81 m/s^2 thereafter. Horizontal acceleration inputs to the models were applied after the initial 1 s of analysis. This ensured proper initialization and stabilization of hydrostatic pressure in the models before the application of the horizontal acceleration input.

The hydrodynamic pressure on the outer tank wall and the wave height (surface displacement) responses extracted from the numerical analysis of models A and B were compared with predictions using the analytical solution for hydrodynamic responses in annular tanks by Tang *et al.* (2010). For model A, the pressure histories near the base and the wave height histories at a point 10 mm from the outer tank wall were in close agreement: see Figure 6.2a and Figure 6.2b, respectively. (Errors in maximum values are indicated on plots as ϵ.) The numerically predicted wave height history 4 mm from the outer tank wall, shown in Figure 6.2c, does not agree with the analytical prediction. The differences between the analytical and numerical predictions for wave height close to the wall of the tank are a result of boundary effects: the vertical fluid velocity at the tank wall is zero because the fluid and shell elements at the boundary share common nodes, and waves do not form correctly; see Yu and Whittaker (2022) for details.

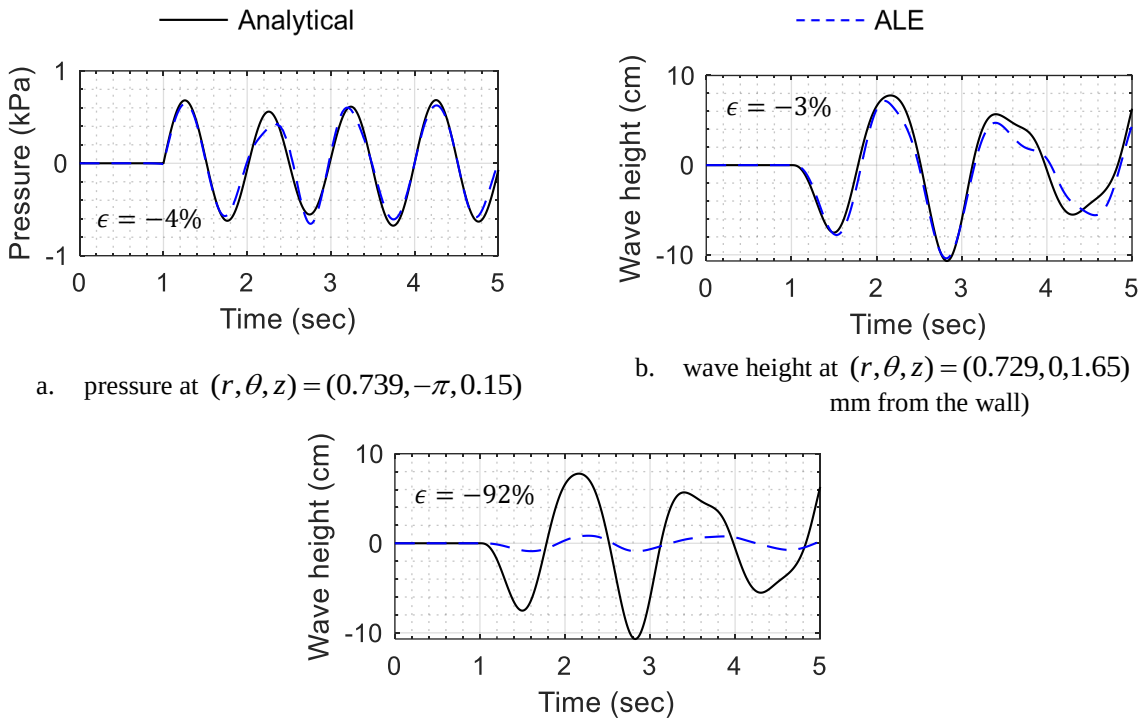

a. pressure at $(r, \theta, z) = (0.739, -\pi, 0.15)$

b. wave height at $(r, \theta, z) = (0.729, 0, 1.65)$ (10 mm from the wall)

c. wave height at $(r, \theta, z) = (0.735, 0, 1.65)$ (4 mm from the wall)

Figure 6.2. Model A, ALE results and analytical predictions, sinusoidal input, coordinates in m, errors (ϵ) in maximum values indicated

Results of analysis of model B are presented in Figure 6.3 and 6.4. Pressure histories at three heights along the wall (Figure 6.3) and wave height histories at two distances from the wall (Figure 6.4) are plotted. The plots presented in Figure 6.3 show that the numerical (ALE) results for hydrodynamic pressure are in reasonable agreement with the analytical predictions. Reasonably accurate estimates of wave height are obtained at a point 6 mm from the outer wall (see Figure 6.4a). However, similar to model A, the numerical predictions of wave height closer to the wall are inaccurate (see Figure 6.4b). To investigate whether analysis of a finer mesh would improve the numerical predictions of wave height near the edges of the annulus, model B was re-analyzed with element sizes reduced by a factor of 2. (In the original model B, four fluid elements were used along the radial direction in the annulus. In the model with a refined mesh, eight elements were used.) Results from model B with the refined mesh are shown in Figure 6.5 and Figure 6.6: the numerically predicted hydrodynamic pressure histories do not improve with mesh refinement (see Figure 6.5), although the numerically predicted wave-height history close to the wall improves. The mesh refinement was computationally expensive and led to a thirteen-fold increase in simulation run time. This is of significance for numerical simulation of sloshing responses in the small annular space in the FHR (and

reactor vessels with similar internal construction). An important outcome (to be used in the next sub-section) from the numerical results of model B described above is that the hydrodynamic pressure time series along the tank wall in the small annulus are predicted accurately, even though the wave height time series may not be captured as accurately across the width of the annulus.

The ALE solver was used to identify computational challenges in the estimation of sloshing responses in thin annular spaces. (The computational cost associated with other solvers in different finite element packages will almost certainly be different.) However, if computational expense is considered in conjunction with the challenges of defining damping in the sloshing modes accounting for boundary effects and flow between gaps, it would appear to be more reasonable (and practical) to use the *regular tank approximation* of section 5.2.5 to estimate wave height.

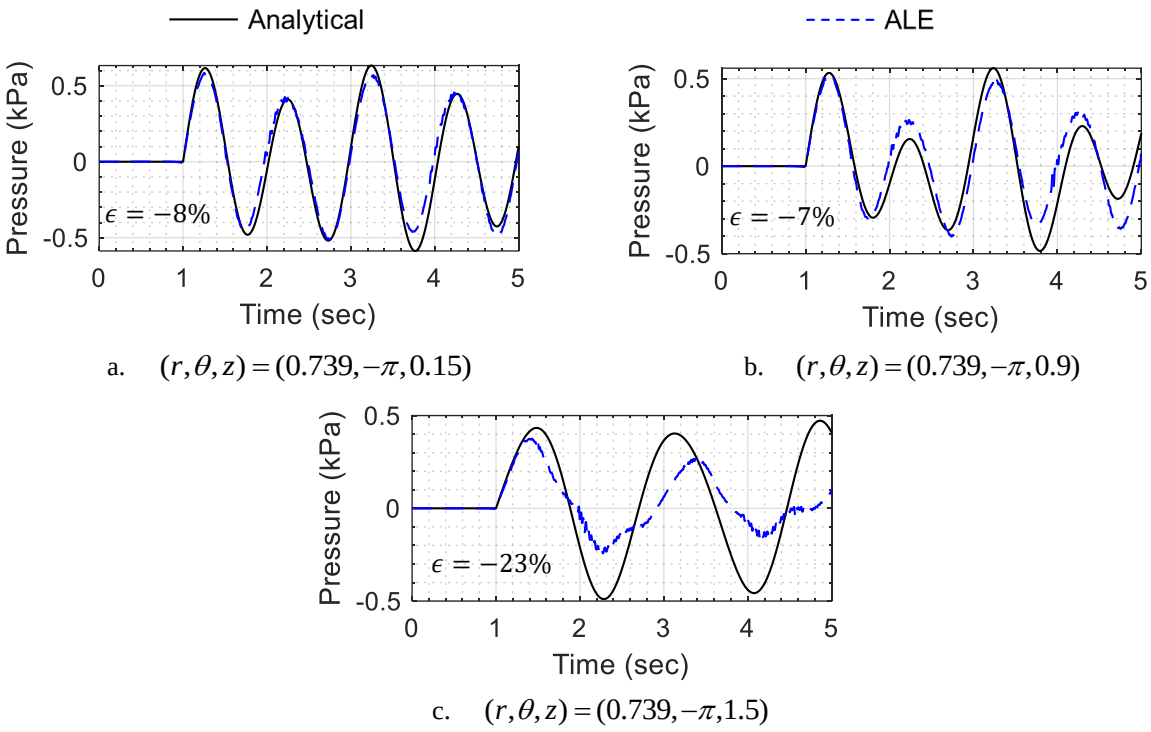

Figure 6.3. Model B, ALE results and analytical predictions for hydrodynamic pressure at three locations, sinusoidal input, coordinates in m, errors (ϵ) in maximum values indicated

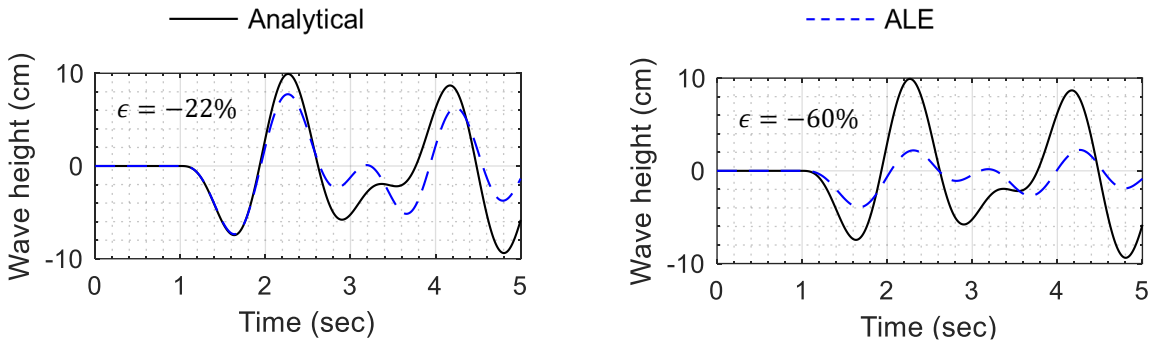

a. 6 mm from the wall b. 3 mm from the wall

Figure 6.4. Model B, ALE results and analytical predictions for wave height at two distances from the outer wall, sinusoidal input, errors (ϵ) in maximum values indicated

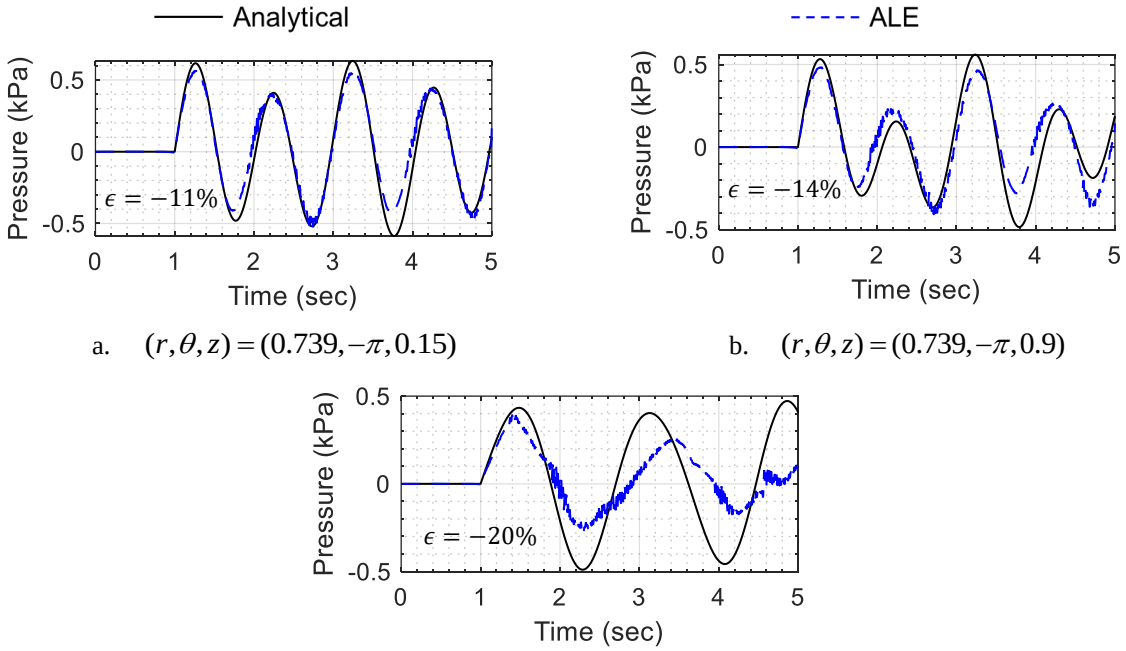

a. $(r,\theta,z) = (0.739, -\pi, 0.15)$ b. $(r,\theta,z) = (0.739, -\pi, 0.9)$

c. $(r,\theta,z) = (0.739, -\pi, 1.5)$

Figure 6.5. Model B with finer mesh, ALE results and analytical predictions for hydrodynamic pressure at three locations, sinusoidal input, coordinates in m, errors (ϵ) in maximum values indicated

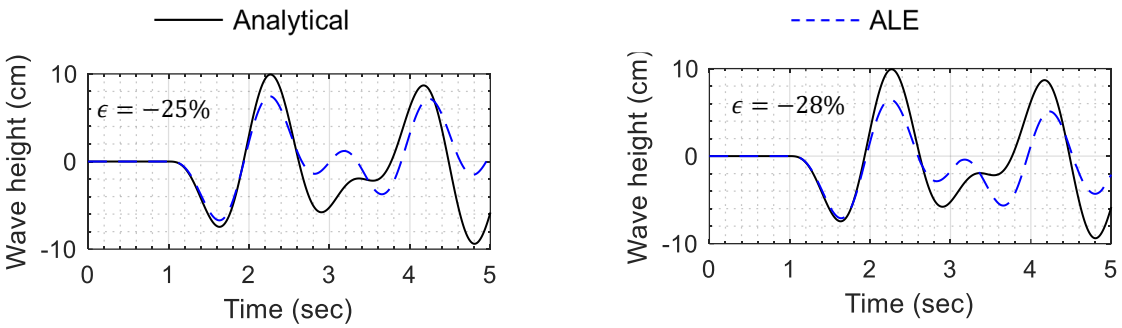

a. 6 mm from the wall b. 3 mm from the wall

Figure 6.6. Model B with finer mesh, ALE results and analytical predictions for wave height at two distances from the outer wall, sinusoidal input, errors (ϵ) in maximum values indicated

6.2.2 Estimation of hydrodynamic loads

Hydrodynamic pressure loadings are needed for the analysis of reactor components (e.g., vessel, core barrel). The hydrodynamic pressure loads would be calculated most precisely by analysis of finite element models that involve an explicit representation of the fluid, contact between reflector blocks, and gap elements between the core barrel and vessel. Such detailed models are computationally intractable currently. A practical solution is to de-couple the fluid and solid domains and use 1) a *fluid-only* model for estimating hydrodynamic pressure loads, and subsequently, 2) the calculated pressure histories for analysis of models of the structural and mechanical components. This approach is robust because the structural (solid domain) components of the model, including the vessel, core barrel, and reflector blocks, responded as a unit during earthquake shaking.

The efficacy of using a *fluid-only* model for estimation of hydrodynamic pressure histories was assessed using a *double-annulus* ALE model representative of the fluid-domain geometry in the test specimen. The *double-annulus* model, shown in Figure 6.7, considered the core barrel, the outer vessel, and the reflector-block assembly as rigid boundaries around (inside; in case of the core barrel) the fluid domain. These boundaries are shown in grey in Figure 6.7. The geometry of the lower surface of the reflector-block assembly was simplified for this modelling exercise and the fluid-domain inside the reflector-block assembly was not modelled. The fluid domain is shown in blue in Figure 6.7. The core barrel partially separated the fluid domain into two annuli. Sloshing was restrained in the outer annulus and allowed in the inner annulus. Accordingly, *void space* was modelled above the fluid domain in the inner annulus, as shown in light grey in Figure 6.7. Like model B described in section 6.2, four solid elements were used across the width of the inner annulus. The model definition was similar to that described earlier in this section, except

that fluid was assigned a dynamic viscosity of 10^{-6} Ns/m^2, representative of the water used in the experiments.

The *double-annulus* model was subjected to accelerations recorded at the base of the test specimen for the one-directional CCE and KCE motions per Table 4.3. The resulting numerical hydrodynamic pressure histories at three locations on the wall of the outer vessel (PW1, PW2, and PW3 in Figure 6.7) were compared with pressure gage data (gages with same names per Figure 4.2) at the same locations on the test specimen. Data from PW2 and PW3 characterize the behavior of the fluid in the outer annulus. The pressure gage PW1 was located below the lower end of the core barrel and was thus *common* to the outer and the inner annuli. In addition to comparing hydrodynamic pressure time series, the wave height recorded by the sensor TW (in the inner annulus; see Figure 4.7) was compared with numerically obtained wave height time series at the center of the annulus at a location corresponding to that of TW in the experiments. Figure 6.8 and Figure 6.9 present results for the two 1D motions.

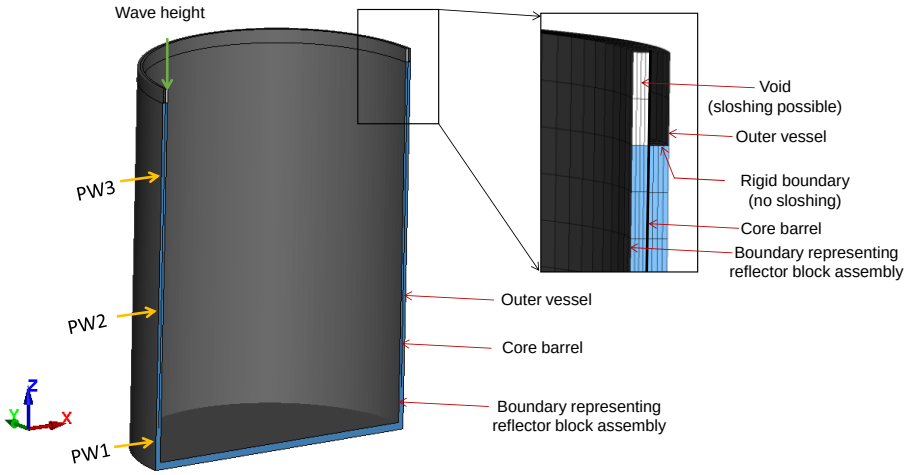

Figure 6.7. Cutaway view of the double-annulus model for estimating hydrodynamic pressure time series, LS-DYNA

Notably, the numerical and experimental pressure time series at the three locations are in good agreement (see Figure 6.8a, b, and c and Figure 6.9 a, b, and c). The predicted and measured wave height time series (see Figure 6.8d and Figure 6.9d) are substantially different in terms of both peak values and time variation, with possible reasons including:

1. The damping related to wave action in the numerical model, which results from the definition of fluid viscosity and a small value of the hourglass-control-related coefficient, does not address the

dissipation of energy due to flow between the gaps in the reflector blocks and in the narrow annulus.

2. The method for outputting wave height currently employed in the ALE solver of LS-DYNA is not robust: the tracers are not stationary in plan but rather move with the fluid (Yu and Whittaker 2021).

3. The breaking of waves in the annulus (see Figure 6.10) can neither be measured because there is no smooth free surface nor predicted with this ALE solver.

Like the observations made in the previous section, inaccuracies in the numerically predicted wave height histories do not translate into similar discrepancies in pressure responses on the boundary of the annulus. The pressure histories close to the base of the annulus are predicted more accurately than those near the top. Accordingly, and with little conservatism, an analyst could choose to use the pressure histories obtained at the base and mid-height of the double annulus model and extrapolate the latter to the top of the annulus.

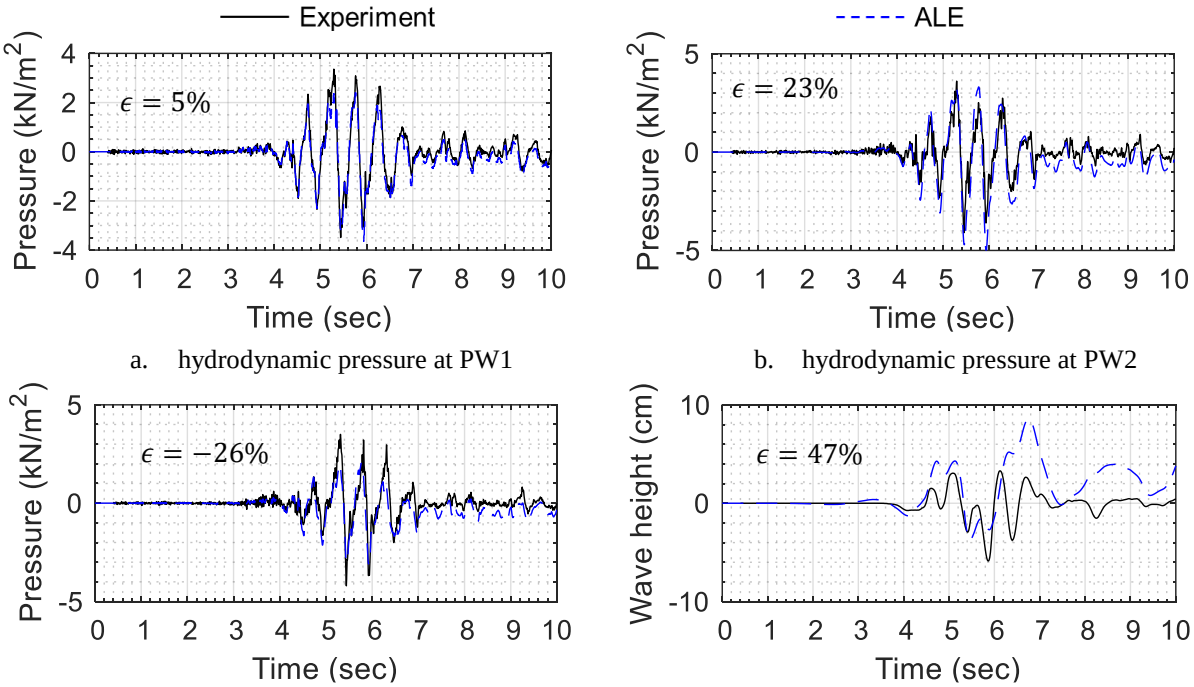

a. hydrodynamic pressure at PW1

b. hydrodynamic pressure at PW2

c. hydrodynamic pressure at PW3

d. wave height at TW

Figure 6.8. Numerical and experimental results, double-annulus model, 1D CCE motion per Table 4.3.

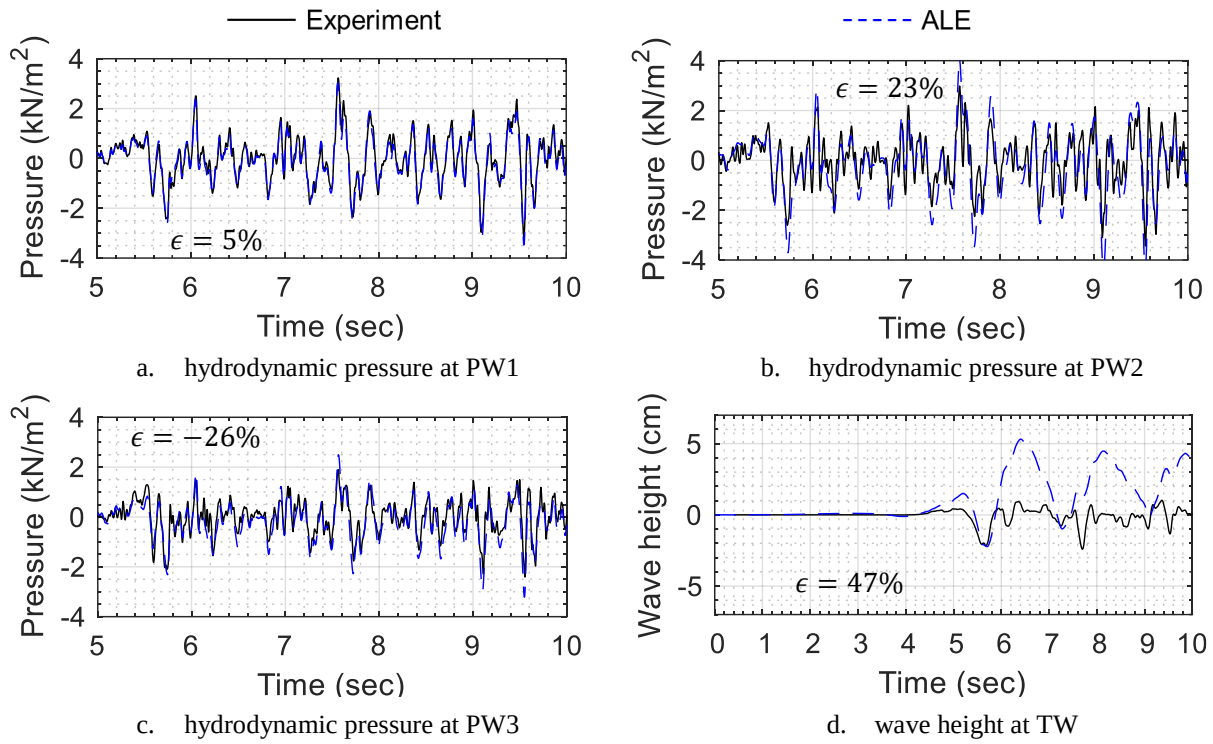

a. hydrodynamic pressure at PW1

b. hydrodynamic pressure at PW2

c. hydrodynamic pressure at PW3

d. wave height at TW

Figure 6.9. Numerical and experimental results, double-annulus model, 1D KCE motion per Table 4.3.

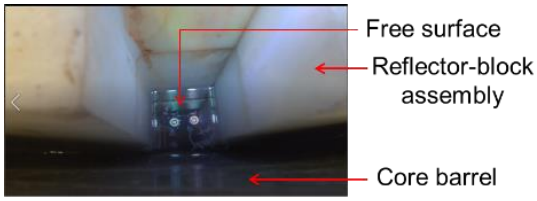

a. initial condition

b. images during shaking

Figure 6.10. Wave breaking in the annulus, 3D CCE motion

6.3 Estimating forces in the reflector-block assembly

6.3.1 Introduction

Section 6.3 provides a pathway to compute earthquake-induced forces in the pins and keys that join blocks in a reflector assembly, based in part on observations from the experiments introduced previously, and numerical analysis. Horizontal shaking is addressed in Section 6.3.2. Vertical shaking is addressed in Section 6.3.3.

6.3.2 Forces in pins and shear keys due to horizontal earthquake shaking

Blocks in the reflector assembly introduced in section 3.2 are joined by cylindrical pins and cuboidal shear keys made of polypropylene: pins and shear keys hereafter. Figure 6.11 presents the locations of the pins and shear keys in a layer of reflector blocks in the test specimen. Figure 6.12 presents the dimensions of the shear keys and pins. The shear keys were installed in the orientation of Figure 6.12a. The shear keys connect adjacent blocks in a layer and adjacent layers of blocks, and reduce fluid flow (or core bypass flow in the prototype reactor) between adjacent columns of blocks. Each key resists shearing forces along two planes identified as planes A1 and B in Figure 6.12a. The pins were used primarily to align blocks in adjacent layers but resist shearing forces through their cross section (plane A2 per Figure 6.12b). The shear strengths of the keys and pins along planes A1, B, and A2 per Figure 6.12 are 35 kN, 100 kN, and 3.4 kN, respectively. Here, shear strength is calculated as 0.577 times the assumed tensile strength of polypropylene (= 27 MPa): von Mises criterion.

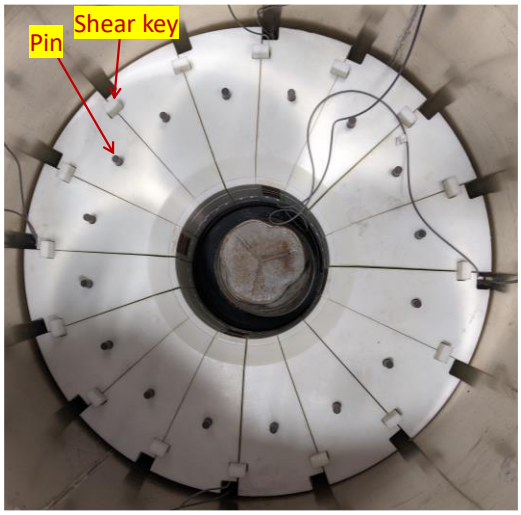

Figure 6.11. Shear keys and pins installed in a layer of reflector blocks in the test specimen

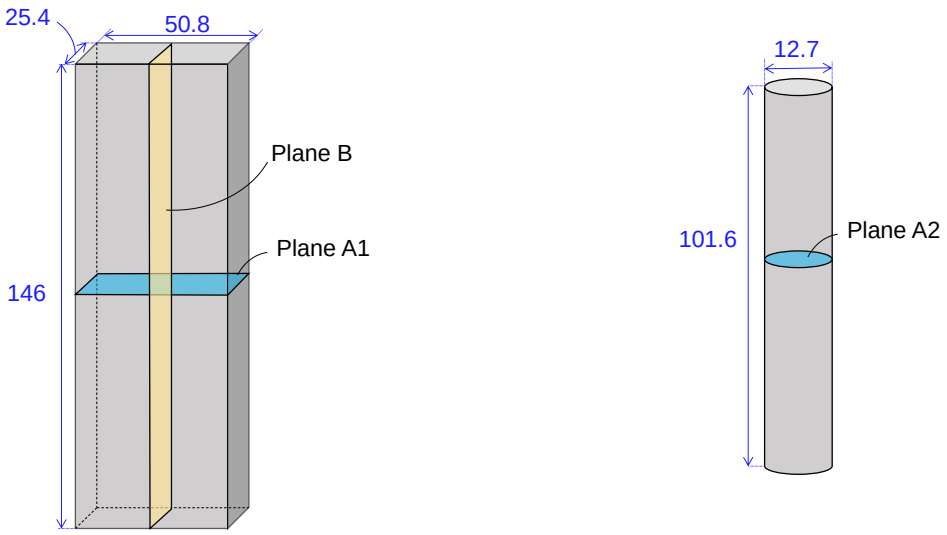

a. shear key b. pin

Figure 6.12. Dimensions (in mm) of a shear key and a pin and planes resisting shear forces

A simplified finite element model of the reflector-block assembly, presented in Figure 6.13, was constructed in SAP2000 (CSI 2017). The model comprised sixteen individual columns. Each column was modelled using five *master blocks* (referred as M-blocks hereafter), as shown in Figure 6.13, rather than the fourteen blocks in each column of the test specimen. Accordingly, the finite element model comprised five layers of master blocks (see Figure 6.13a). The five master blocks were chosen to mimic the shape of an individual column in the test specimen. Each M-block comprised a set of massless rigid beams (to track edges) and rigid area elements. The area elements were assigned *area masses* such that the mass of an M-block in the model equaled the mass of the group of test blocks it represented: for example, the mass of M-block 3 per Figure 6.13 was equal to the mass of blocks RB-5 through RB-10 per Figure 3.5. The total mass of the reflector assembly in the model was 1900 kg. The mass of the pebbles and water inside the reflector-block assembly (1000 kg) was distributed as an area mass on the inner area elements of M-blocks 1 through 4 in each column[9]. Similarly, the mass of the plug was equally distributed to the inner area elements of M-block 5 in each of the sixteen columns. Connections between adjacent M-blocks in a layer or column were modelled using four beam elements.[10] The beams were modelled using a stiff elastic material to ensure that

[9] The fluid-pebble mixture inside the core of the reflector block assembly is confined such that the hydrodynamic effects are purely impulsive. Modeling the fluid-pebble mixture as a distributed mass on the inside face of the reflector-block assembly is most reasonable.

[10]The frictional contact between blocks is ignored here, resulting in conservative (high) estimates of forces in the shear pins and keys.

the modal frequencies of the assembly were very high (> 300 Hz). The pins at the top (one per block, sixteen in one ring) and bottom (two per block, sixteen in each of two rings) of each column of blocks were fixed against rotation and translation, as shown in Figure 6.10b. (The locations of the pins in the double ring (bottom) and the single ring (top) of the test specimen are identified in Figure 3.3 and Figure 3.7, respectively.) Horizontal (H) section cuts were made between the five layers of the M-blocks: H1 through H4 in Figure 6.14. Vertical, radial (R) section cuts were made between adjacent M-blocks in layer 3: R1 through R16 in Figure 6.14. Forces were output at these section cuts. Additional horizontal section cuts, S1 through S16 were defined at the level of section cut H3 (see Figure 6.14) to output horizontal forces at the sixteen interfaces between M-blocks 3 and 4.

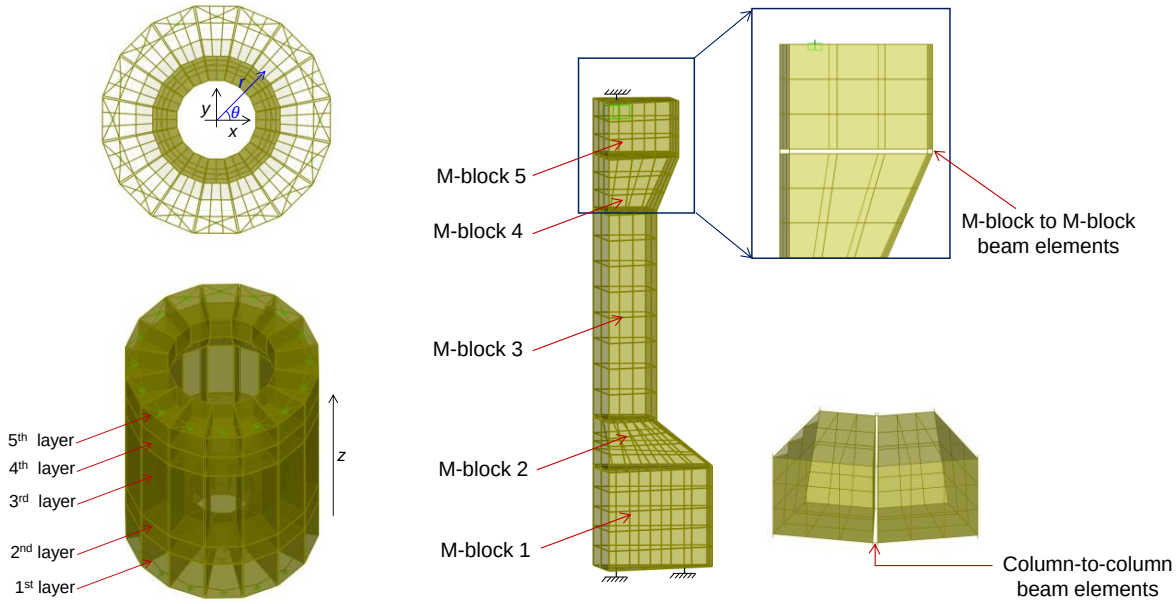

a. SAP model and coordinate systems

b. one column of five blocks and connecting beam elements

Figure 6.13. Model of the reflector-block assembly in SAP2000

To quantify seismic demands in the pins and shear keys, which were not measured in the physical experiments, a simplified loading environment involving a constant acceleration of 1g was input to the model along the *x* direction. Forces were output using the section cuts identified above. Figure 6.15 presents the orientations of the forces output on different section cuts for the one directional input; the orientations are defined per the coordinate systems introduced in Figure 6.13a. The in-plane forces recorded on section cuts H1 through H4 only had components along the excitation direction (as expected) whereas forces recorded on other section cuts had components in both in-plane directions, as indicated in Figure 6.15.

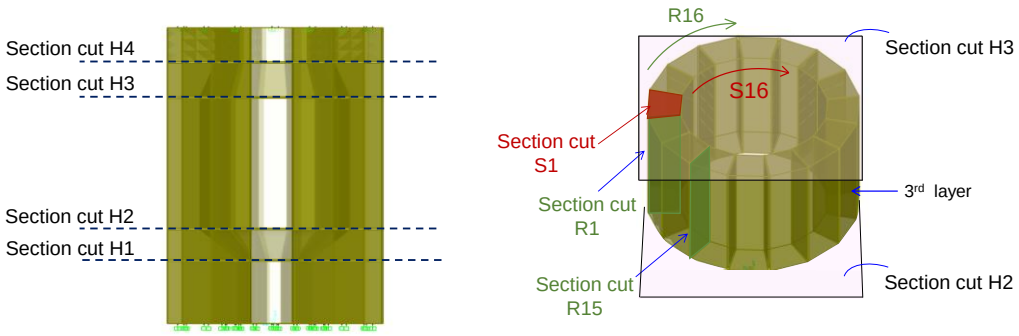

Figure 6.14. Section cuts defined in the model

Figure 6.16a presents the variation of total horizontal *shear* force along the height of the assembly, output using section cuts H1 through H4. The net inertial force associated with the 1 g horizontal acceleration of the model was 29 kN. The difference between the reactions at the top (13 kN) and bottom (16 kN) is due to the higher degree of restraint at the bottom (two pins per column) than at the top (one pin per column). (The reactions at the top and bottom were verified to be equal for a model with two pins per column at the top and bottom of the reflector-block assembly.) In the test specimen, the horizontal shear force at an H section cut is resisted by sixteen shear keys and sixteen pins along planes A1 and A2, respectively, per Figure 6.12 (assuming no friction). The distribution of the shear force in the keys and pins of the sixteen columns is addressed later in this section. The horizontal shear force in a single column is resisted by one shear key and one pin (planes A1 and A2 per Figure 6.12).

The magnitudes of the resultant in-plane forces on section cuts R1 through R16 (in layer 3) are presented in Figure 6.16b: the forces are maximized at the section cuts that are aligned with the excitation direction (*x*; 0, 180 degrees in Figure 6.16b) and minimized at the cuts nearly perpendicular to the excitation direction (90, 270 degrees in Figure 6.16b). Note that a single M-block in layer 3 of the finite element model represents six reflector blocks (RB-5 through RB-10 per Figure 3.4) of the test specimen. Accordingly, the force on an R section cut in the model is distributed to six shear keys, each resisting force along plane B per Figure 6.12b. The maximum resultant force at an R section cut per Figure 6.16b for the constant acceleration input of 1g is 0.5 kN which is three orders of magnitude smaller than the shear strength of the six keys, resisting force along plane B (= 6 × 100 kN).

Figure 6.16c presents the magnitudes of the resultant in-plane forces on section cuts S1 through S16, located at section cut H3. The vector sum of forces on the sixteen section cuts (S1 through S16) is equal to the *x*-direction force on section cut H3 (= 6.7 kN; see Figure 6.16a): an expected outcome. The resultant of the *y*-direction forces (F_y per Figure 6.15c) on section cuts S1 through S16 is zero: another expected outcome.

Note that the force on an individual section cut (e.g., S3) has components in both in-plane directions (F_x and F_Y per Figure 6.15c). The curve presented in Figure 6.16c indicates that the shear force at a horizontal section in the reflector assembly (e.g., H3) is not distributed equally to the sixteen columns. Rather, columns aligned with the excitation direction (0, 180 degrees in Figure 6.16c) resist a smaller shear force than those orthogonal to the excitation direction (90, 270 degrees in Figure 6.16c).[11] As noted previously, the force on an S section cut is resisted by a shear key and a pin in the test specimen, along planes A1 and A2, respectively, per Figure 6.12. Thus, the capacity of an S section cut in shear is 38 kN (shear key along plane A1 = 35 kN and pin along plane A2 = 3.4 kN). Per Figure 6.16c, the maximum shear force on an S section cut is 0.52 kN for the constant acceleration input of 1g, which is approximately two orders of magnitude smaller than the capacity of 38 kN.

The discussion presented above indicates that that for the 1g horizontal input, the calculated force demands along R and S section cuts are orders of magnitude smaller than the shear capacity of the keys and the pins used in the test specimen.

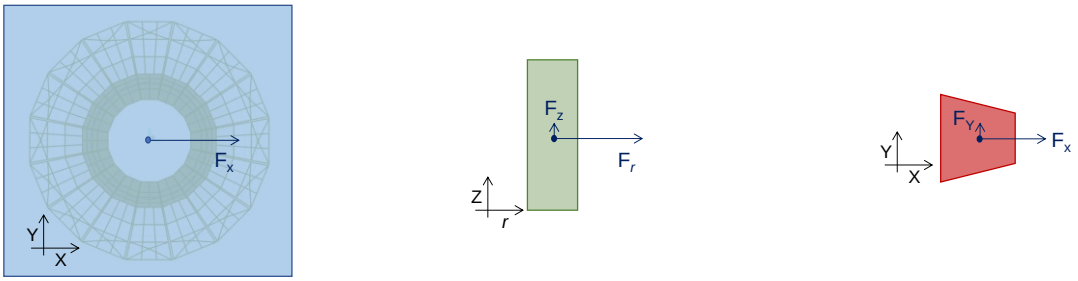

a. section cut H1 (through H4) b. section cut R1 (through R16) c. section cut S1 (through S16)

Figure 6.15. Orientation of in-plane forces output using section cuts (see Figure 6.14), one directional input, forces are denoted by the letter F and a subscript indicating direction, *r* is radial

[11]A useful analogy is here is the distribution of shear stresses along the cross-sectional depth in a prismatic circular beam: the stress is maximized near the neutral axis (mid-depth), and minimized at the top and bottom.

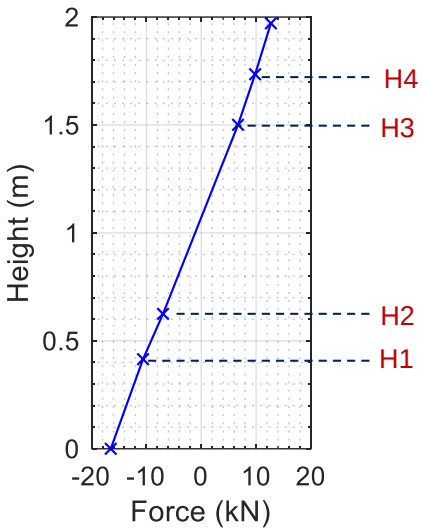

a. total shear forces at horizontal section cuts and reactions at ends

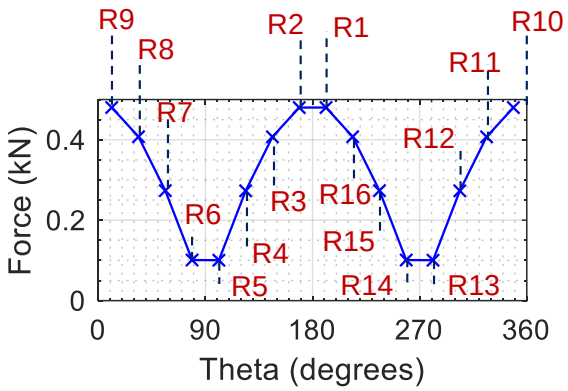

b. resultant forces at R section cuts between adjacent M-blocks (see Figure 6.14 and Figure 6.15b)

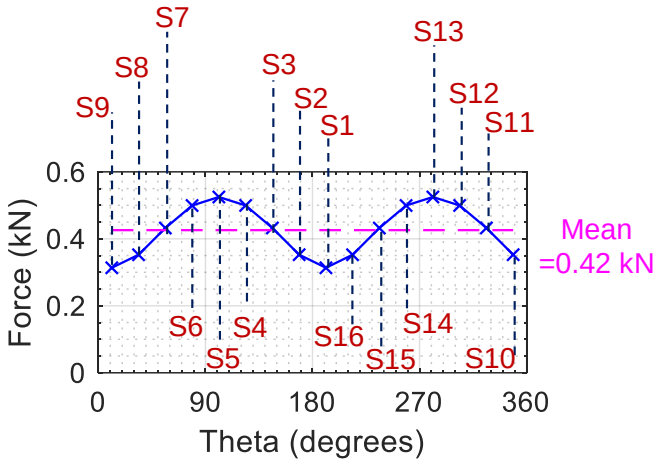

c. resultant forces at S section cuts between M-blocks 3 and 4 in the sixteen columns (see Figure 6.14 and Figure 6.15c)

Figure 6.16. Section cut forces for 1g horizontal input

The model of Figure 6.13 was analyzed for the horizontal accelerations recorded below and above the isolation interface for the 1D KCE input in tests with the Single concave Friction Pendulum bearings (motion 2 per Table 4.4). The inputs are presented in Figure 6.17 and denoted as motions E1 and E2; the motions enable a comparison of demands on the reflector-block assembly in the conventional (E1) and isolated (E2) configurations. The maximum values of the accelerations are noted in the panels of Figure 6.17. The force time series recorded at section cuts H1 through H4 for motion E1 are presented in Figure 6.18. All time series in the figure attain a maximum (absolute) value at 14.25 seconds, which is the time of

maximum acceleration of motion E1. (A similar outcome was obtained for motion E2.) Figure 6.19 presents the maximum forces at section cuts H1 through H4 and the reactions for motions E1 and E2. The maximum values of forces in motion E2 are a small fraction of those for motion E1 and the ratio of maximum forces at a given level in the two motions is equal to the ratio of (absolute) peak accelerations per Figure 6.17 (= 0.18/0.69 = 0.26). These are expected outcomes, since the model is linear and practically *rigid.* The distribution of forces along the R and S section cuts for any earthquake input can be obtained by scaling the distributions presented in Figure 6.16 for the 1g horizontal input. Such scaling requires multiplying the forces presented in Figure 6.16 by the peak acceleration (in *g*) of the earthquake input to the vessel. (The method of analysis described here does not consider tolerances (gaps) between the shear keys and pins and the corresponding slots machined in the reflector blocks. Tolerances will affect the number of shear keys and pins engaged in resisting forces, but this cannot be predicted. Importantly, the tolerances used to machine the plastic parts for the reflector block in the model are equal or similar to those planned for the graphite in the prototype reactor.)

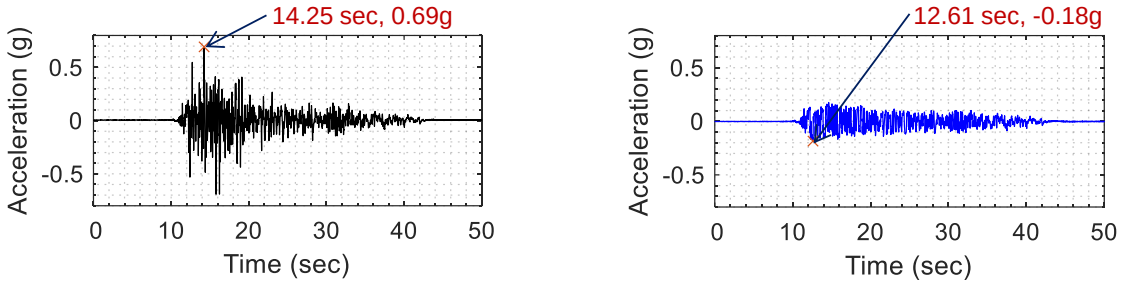

a. motion E1, below the isolation system

b. motion E2, above the isolation system

Figure 6.17. Acceleration time series recorded below and above the isolation interface, motion 2 per Table 4.4

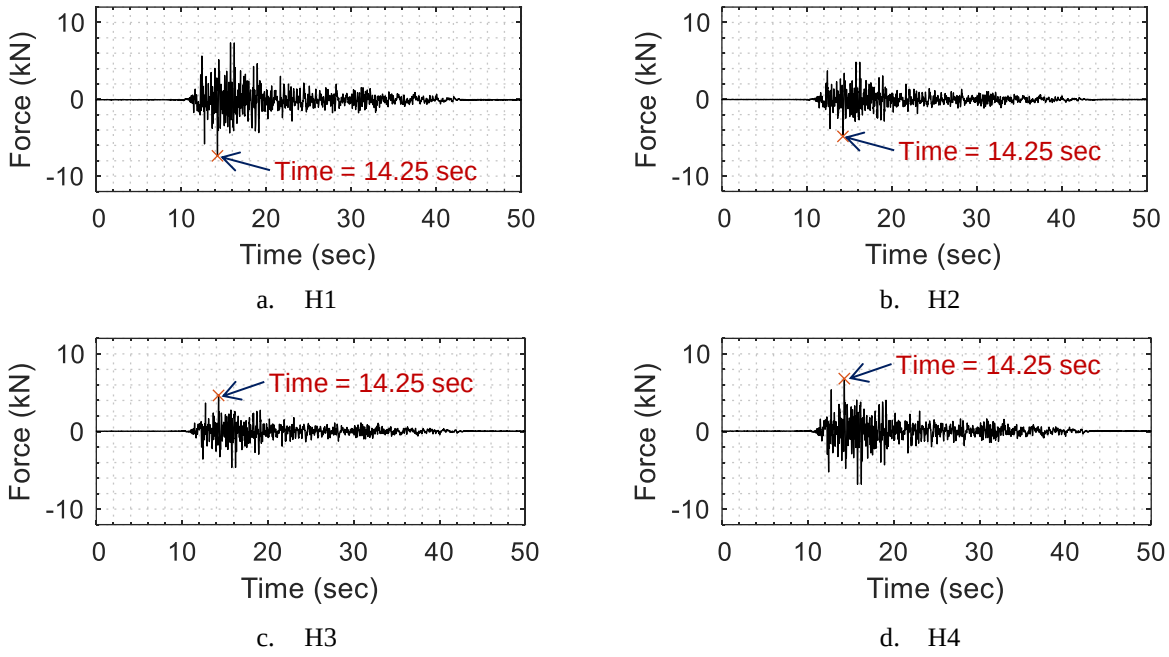

Figure 6.18. Force time series recorded on different section cuts, E1 acceleration input of Figure 6.17a

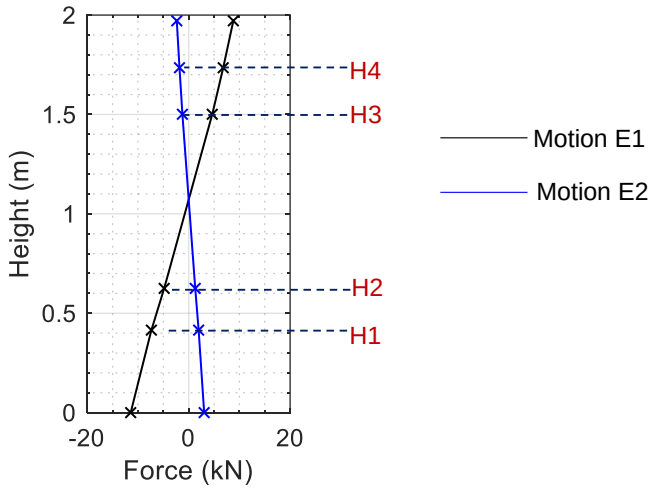

Figure 6.19. Maximum forces at horizontal section cuts and reactions for motions E1 and E2

The model described above does not consider the pressure loading on the outer surface of the reflector-block assembly. An approach to consider the pressure loading would be to extract the pressure histories on the surface representing the reflector-block assembly in the *double-annulus* model and apply those at corresponding points in the described reflector-block assembly model or, simply extract the pressure history at one location (say near PW1 per Figure 6.7), ignore the variation of pressure along the height of the

assembly, and use a cosθ-type variation of pressure loading along the circumference. (Figure 6.20 presents multipliers to be used on the pressure history at PW1 for defining loading on the sixteen columns of the reflector-block assembly). However, inclusion of pressure loading on the surface of the reflector-block assembly would lead to smaller design forces (at interfaces of layers/columns) than the case where the pressure loading is ignored. This is explained using the sketch presented in Figure 6.21a. Under a lateral acceleration (positive towards right in the figure), the total fluid pressure increases and decreases as indicated in the sketch. The direction of the net hydrodynamic load is such that it relieves the supports of the reflector-block assembly (and consequently, the pins and keys between blocks); see Figure 6.21b. Thus, analysis for lateral accelerations without pressure loading on the lateral surface of the reflector assembly will result in conservative (high) estimates of force.

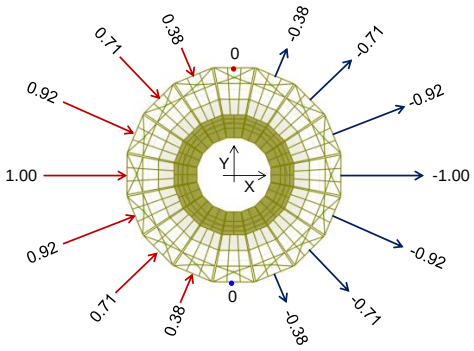

Figure 6.20. Multipliers on pressure history at PW1 that can be used to define pressure loading on the sixteen columns of the reflector-block assembly

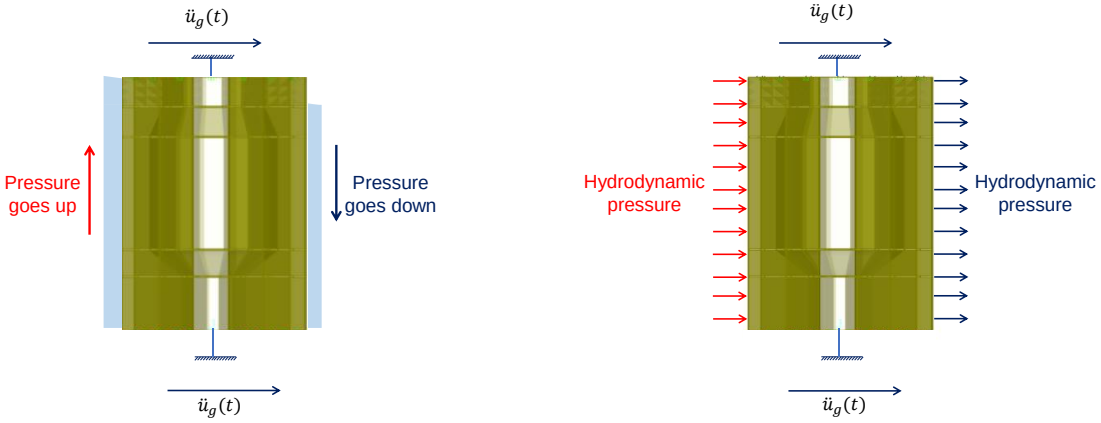

a. changes in fluid pressure around the reflector-block assembly under a lateral (constant) acceleration

b. direction of hydrodynamic pressure loading under a lateral (constant) acceleration

Figure 6.21. Pressure on the reflector-block assembly under a lateral acceleration

6.3.3 Tri-directional shaking of the reflector-block assembly

Figure 6.21 presents fluid pressure loading profiles on the lateral and bottom surfaces of the reflector-block assembly in the presence of horizontal and vertical seismic inputs: the reflector-block assembly, shown in grey, is subjected to a horizontal (a_x) and a vertical (a_z) acceleration shaking. The acceleration due to gravity (g) acts in the negative z direction per the coordinate system shown in the figure.

The acceleration due to gravity (g) results in the hydrostatic pressure profiles $P_l(g)$ and $P_b(g)$ on the lateral surface and the base of the assembly, respectively, as drawn in the figure. (Subscripts l and b denote lateral and base, respectively.) Pressure loading profiles due to the vertical acceleration input (a_z) are similar to those due to g and are denoted $P_l(a_z)$ and $P_b(a_z)$ in Figure 6.22. The pressure loading profiles due to the horizontal acceleration input (a_x), denoted $P_l(a_x)$ and $P_b(a_x)$, can be estimated using the double annulus model described in section 6.2.2, and each has a cosθ-type variation around the circumference of the assembly. All pressure loadings on the vertical cylindrical surface can be ignored: $P_l(g)$ and $P_l(a_z)$ because they sum up to zero net resultant force on the assembly, and $P_l(a_x)$ for the reason described in the previous section.

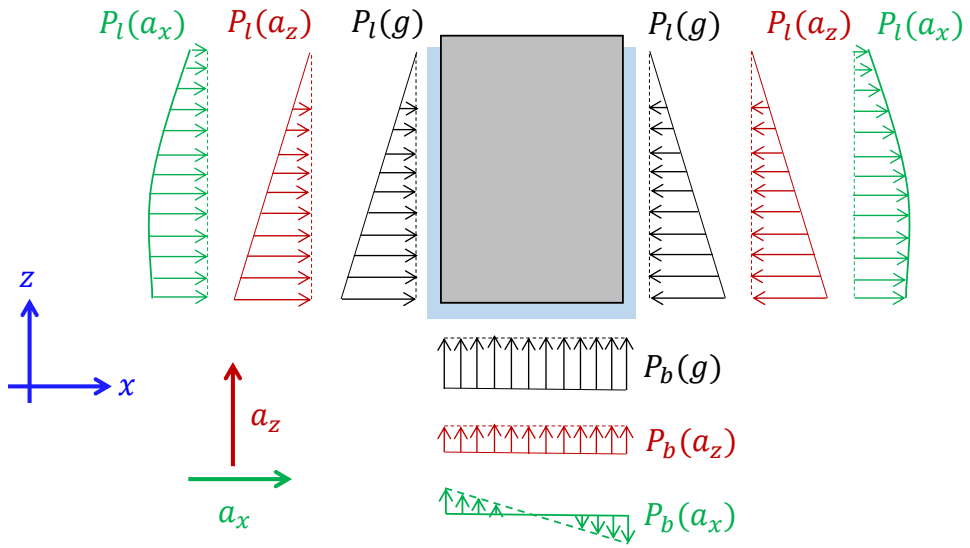

Figure 6.22. Fluid pressure loading profiles on the reflector-block assembly in the presence of vertical and lateral acceleration inputs

The SAP2000 finite element model described in the previous section was modified for analysis involving three-dimensional seismic inputs. The axial restraints at support points at the top and bottom of each column

were replaced by multi-linear springs to accommodate vertical movement of the reflector-block assembly under fluid loading. Figure 6.23 presents the axial force-deformation curve for one of the springs: effectively rigid in compression for a displacement greater than 25.4 mm and near-zero stiffness for smaller displacements in compression and all displacements in tension.

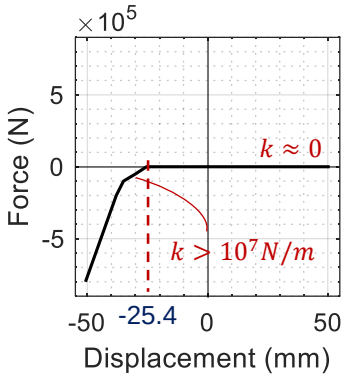

Figure 6.23. Force-deformation curve defined for multi-linear springs, *k* denotes stiffness

Figure 6.24 presents the state of the reflector-block assembly in the finite element model under no loading, gravity loading, and gravity and hydrostatic loading. Under gravity loading only, the springs at the base are compressed and carry the weight of the assembly (= 29 kN), and the springs at the top are in tension and provide negligible resistance ($k \approx 0$ in tension). An upward pressure is applied at the base of the assembly to simulate hydrostatic pressure ($P_b(g)$ per Figure 6.22, upward force = 30.7 kN)[12] producing compression in the springs at the top and tension in the springs at the bottom. Under the net loading, the springs in compression at the top resist the difference (=1.7 kN) between the weight of the assembly (=29 kN) and the (buoyant) force due to hydrostatic pressure (= 30.7 kN), and the springs in tension at the base of the vessel provide negligible resistance.

[12]The upwards (buoyant) force can be calculated as ρgAH, where ρ is the density of water (=1000 kg/m^3), A (= 1.66 m^2) is the area of a circle with a radius equal to the outer diameter of the reflector-block assembly, and H (= 1.89 m) is the height of water above the base of the assembly.

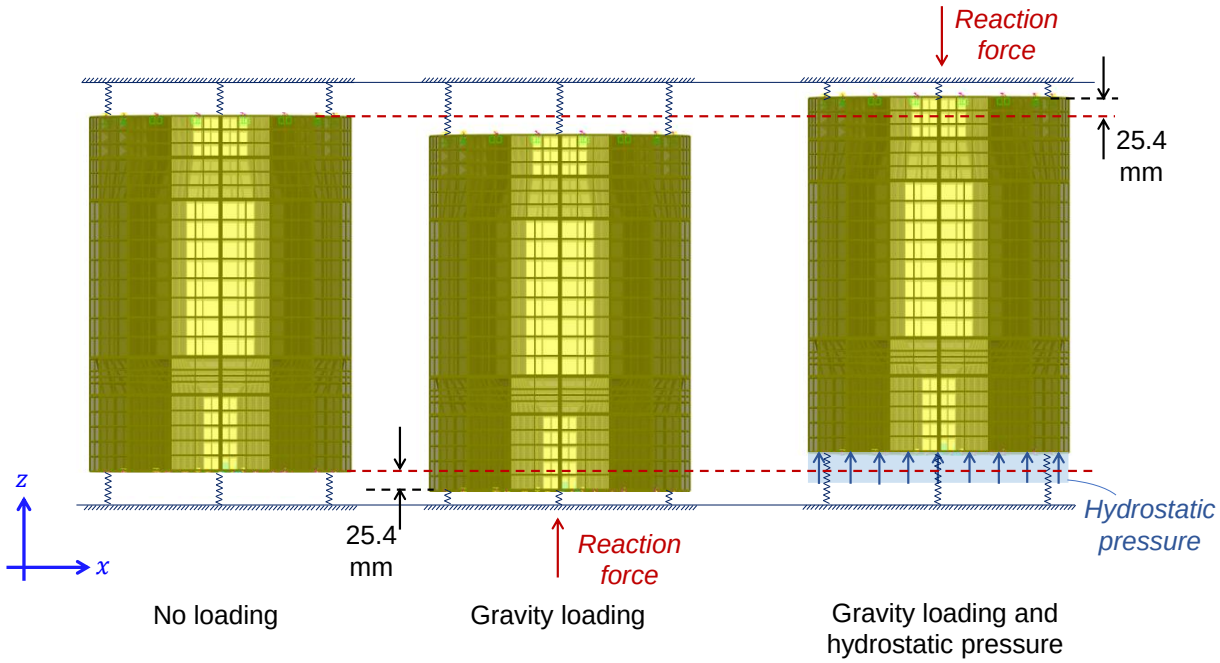

Figure 6.24. Reflector assembly in the finite element model, only three representative springs shown at top and bottom, displacements not to scale

The state of the finite element model for net loading under gravity and hydrostatic pressure (i.e., the reflector-block assembly floating inside the vessel but bearing against the head) can be used as the initial condition for dynamic analysis involving three-directional inputs. Herein, the finite element model is used to study the behavior of the assembly in two steps. A discussion of the behavior under a pure vertical input is presented first followed by a discussion of response under a horizontal input (introduced in the previous section).

A vertical input acceleration $a_z > -g$ was imposed on the reflector-block assembly and a pressure loading history corresponding to the vertical input, $P_b(a_z)$ per Figure 6.22, was defined on the base of the assembly: see Figure 6.25. Figure 6.26a presents the assumed vertical loading history: a sinusoid with an amplitude of 0.5g and a frequency of 1 Hz. Figure 6.25b presents the corresponding axial force history at the top of the vessel. Expectedly, the vertical reaction history at the head of the vessel is sinusoidal and can be calculated as $(W/g - \rho AH)(g + a_z(t))$, where W is the weight of the reflector-block assembly, t is time, and ρ, H, and A are defined in footnote 12. (If the sinusoid has an amplitude of 1g, the reaction varies between 0 kN and -3.4 kN.)

This analysis approach for vertical input applies for $a_z > -g$ because the reflector-block assembly bears against the head of the vessel (i.e., springs at the top in the finite element model) only if the vertical acceleration is greater than $-g$. For $a_z < -g$, the reflector-block assembly rests on the base of the vessel (in theory)[13] and the pressure loadings on the base of the assembly per Figure 6.22 do not apply.

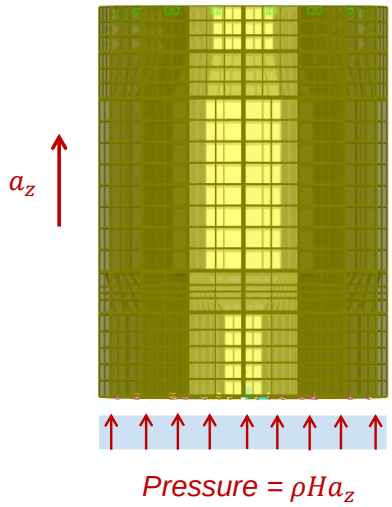

Figure 6.25. Pressure on the base of the reflector-block assembly due to vertical input; ρ is fluid (water) density and H is fluid height above the base of the assembly (= 1.9 m)

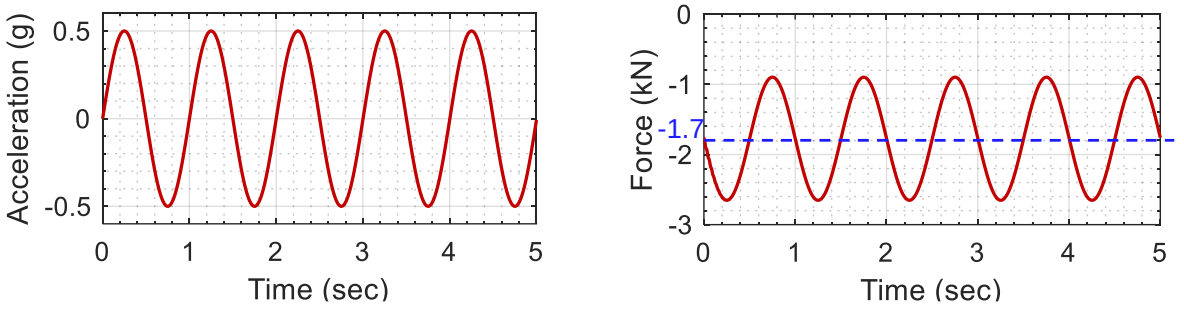

a. input b. vertical reaction at the top of the assembly

Figure 6.26. Vertical acceleration input to the reflector-block assembly after initialization of gravity and hydrostatic loading

[13]If the amplitude of the vertical acceleration input is smaller than -*g* only momentarily, the fluid between the base of the vessel and the underside of the assembly may not be able to *quickly* migrate out to allow the assembly to rest on the base of the vessel. However, such high magnitude vertical accelerations could lead to problems in the fluid flow paths inside the reactor. Hypothetically, if vertical accelerations smaller than -*g* are sustained for a *significant* duration, the fluid between the base of reflector-block assembly and the base of the vessel will migrate out, allowing the assembly to rest on the base of the vessel. In such a situation, there will be a gap between the top of the reflector-block assembly and the head of the vessel and it will be filled with fluid.

Analysis of the model described above for a lateral acceleration can be performed per section 6.3.2, but adjusted to accommodate the pressure loading $P_b(a_x)$ (per Figure 6.22) on the base of the assembly, which is addressed here. A sinusoidal pressure time series, as shown in Figure 6.27a, was assigned at the base of the reflector-block assembly. The radial variation of the pressure amplitude is linear per Figure 6.27b and a cosθ-type variation was assumed around the circumference of the assembly. Expectedly, this pressure loading resulted in a moment at the top support (see Figure 6.27c) but no horizontal shearing forces within the assembly.

The load associated with $P_b(a_x)$ per Figure 6.27b is *transferred* to the top support in the finite element model as vertical compressive or tensile forces in individual columns of blocks. In the prototype system, compressive loads would be transferred through block-to-block and block-to-head contact and the tensile loads would serve only to reduce the compressive load due to hydrostatic pressure and pressure due to the vertical component of ground motion, if present. If the net resultant force on a column due to pressure loading profiles $P_b(g)$, $P_b(a_z)$, and $P_b(a_x)$ is tensile, the above model is not suitable for estimating shearing loads between adjacent columns. A column with a net tensile load in the vertical direction would move downwards (see footnote 13) in a prototype system and disengage (i.e., lose contact) from the head, which is similar to the case of $a_z < -g$ presented above.

In summary, the internal forces in a reflector-block assembly can be analyzed using the modelling approach described here provided the input accelerations do not lead to its disengagement from the head. Cases in which a column (or an entire assembly) disengages from the head could be analyzed using finite element models considering contact and gap elements between blocks. However, such analysis is unnecessary if the amplitudes of the horizontal and vertical accelerations are small: resulting from siting the reactor building in a region of low seismic hazard or by implementing seismic isolation. As discussed in Section 5, the implementation of 2D horizontal isolation systems in the tests described in this report resulted in significant reductions in peak horizontal accelerations, particularly for high-intensity seismic inputs (by a factor of about 4 for the KCE inputs). Vertical and 3D isolation systems, not discussed in this report, have been tested and implemented (see Lee and Constantinou (2017)), and are effective in protecting equipment from large vertical accelerations.

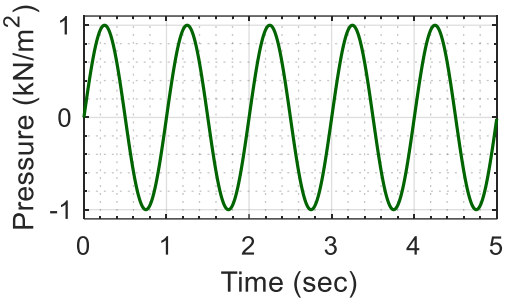

a. pressure time series defined at the base

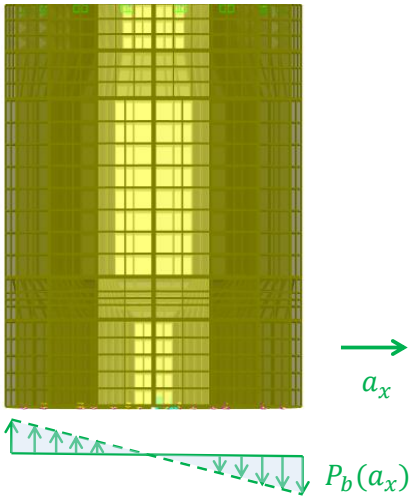

b. radial variation of pressure at base

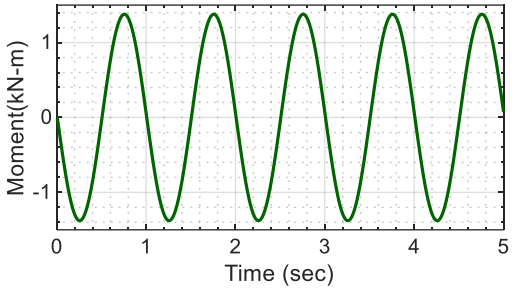

c. resulting moment at top support

Figure 6.27. Pressure loading on the base of the reflector assembly, lateral input

6.4 Isolation-system modelling

The modelling of friction pendulum bearings in the finite element package SAP2000 (CSI 2017) is addressed in this sub-section with the goal of evaluating isolation-system responses (e.g., accelerations above the isolation plane) that could be used as inputs for estimation of component responses in the *superstructure* (i.e., components above the isolation interface). It was demonstrated in Section 5 that the components of the test specimen including the vessel, core barrel, and the reflector-block assembly responded as a unit. Accordingly, these components were considered rigid for the analysis described in this section.

Figure 6.28 presents an isometric view of the model in SAP2000. The base plate, outer vessel, flange, and the top plate were modelled using rigid shell elements with thickness per measured dimensions and a mass density of carbon steel. The mass of the internal components (reflector assembly, core barrel, water, and pebbles = 3200 kg) was distributed (i.e., lumped) as an *area mass* on the wall of the vessel. Four isolators (SFP or TFP) were installed under the base plate at the centers of the green-colored squares in Figure 6.28.

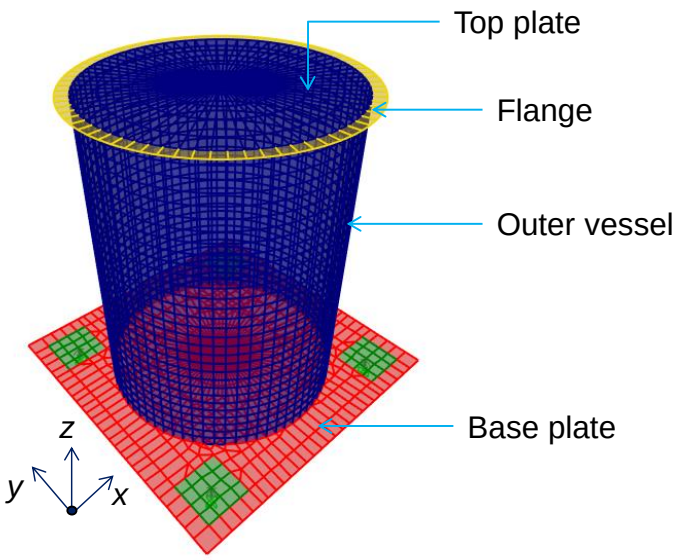

Figure 6.28. Isometric view of numerical model in SAP2000, and coordinate system

6.4.1 SFP-isolated model

The *friction isolator* link element in SAP2000 was used to model the Single concave Friction Pendulum isolators. Table 6.1 presents the key inputs used to define the force-deformation properties of the link element in the axial and the two horizontal directions.

Table 6.1. Key inputs for definition of *friction isolator* link element in SAP2000, SFP-isolated model

Input field (per SAP2000)		Description
Axial (U1) direction	Effective stiffness for linear or non-linear analysis cases	Axial compressive stiffness of the isolator. Value = 1.07×10^5 kN/m per Table 3.1.
	Effective damping for linear analysis case or damping coefficient for nonlinear analysis cases	Zero. Damping in the axial direction was defined as modal damping for the vertical mode under load case definition.
Horizontal (U2 or U3) direction	Effective stiffness for linear analysis cases	Post-elastic stiffness of the isolator for a given weight (K_{pe} per Figure 3.19). Value = 39.8 kN/m, consistent with a weight per bearing of 18.9 kN and a sliding-surface radius of 0.473 m (see Figure 3.18).
	Effective damping for linear analysis cases	Zero. (The response-history analyses were non-linear analysis cases and so this input is immaterial.)
	Stiffness for nonlinear analysis cases	Value = 7868 kN/m: the stiffness of the elastic region of the force-deformation loop, obtained as $\mu_{max}W / Y$, where μ_{max} is the maximum (fast) coefficient of friction (see below), W is the weight on the isolator, and Y is the yield displacement of the isolator = 0.3 mm, back-calculated using an experimental-force deformation loop.
	Friction coefficient, fast	Value = 12.5%: slightly greater than the 10.2% per Table 3.1, determined from the from characterization tests. The chosen value of 12.5% better represented the force-displacement behavior observed in earthquake-simulator tests, as presented in Figure 6.29.
	Friction coefficient, slow	Value = 3.3%, consistent with value chosen for the coefficient of fast friction and the ratio of fast and slow coefficients of friction per Table 3.1.
	Rate parameter	Value = 44 s/m per Table 3.1.
	Net pendulum radius	Value = 0.473 m per Figure 3.18.

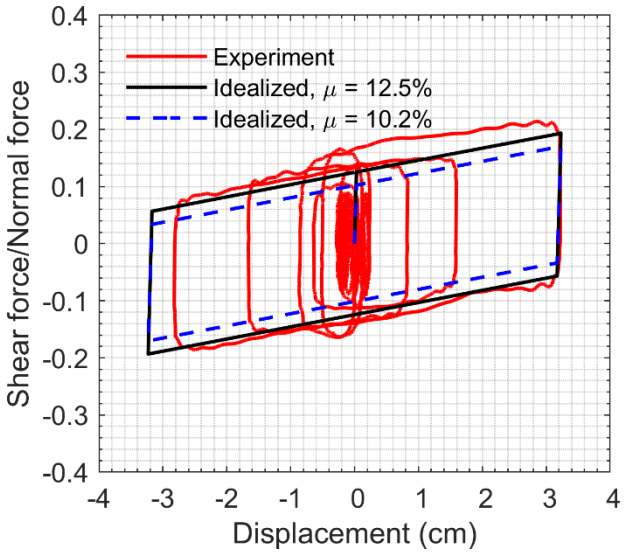

Figure 6.29. Comparison of experimental and idealized normalized force-displacement loops, motion #1 per Table 4.4

A modal analysis of the finite element model comprising the superstructure introduced in Figure 6.28 and four isolators defined per Table 6.1 was performed. Modal frequencies and mode-shape descriptions are presented in Table 6.2. As expected, the translational and rocking modes of the structure were symmetric in the two horizontal directions.

Non-linear response history analysis was performed using inputs corresponding to the six motions introduced in Table 4.4: translational and rocking accelerations recorded at the tops of the load cells (below the bearings) were used as inputs to the model. The end of the gravity load case served as the starting point for the dynamic analysis. The gravity load case involved *slow* application of acceleration due to gravity as a ramp from 0 to 9.81 m/s^2 in 7 seconds with a large value of modal damping (95% of critical) used to avoid vertical oscillations. In the response-history analyses, 5% damping was specified for modes 4 through 6 (rocking and vertical modes). Figure 6.30 through Figure 6.35 present isolation-system responses (acceleration spectra, isolator displacements, and force-displacement loops) for the six motions in Table 4.4. Table 6.3 and Table 6.4 present the absolute maximum experimental and numerical values of key isolation-system responses for the 1D and 3D inputs of Table 4.4, respectively. The agreement between experimental results and numerical predictions for isolation-system responses is excellent. The absolute differences between peak experimental and numerical responses are less than 7%, 4%, 11%, and 24% on average for isolator displacements, reaction forces, horizontal accelerations, and vertical accelerations, respectively. The shapes of the rocking acceleration response spectra are captured reasonably well using

the numerical model. However, hard-to-characterize differences in damping in the rocking modes (and in the vertical mode[14]) do exist between the experimental specimen and the numerical model.

Table 6.2. Summary of modal analysis in SAP2000, SFP-isolated model

Mode number	Description	Frequency
1	Translation along *x* axis	0.72 Hz
2	Translation along *y* axis	0.72 Hz
3	Torsion (rotation about *z* axis)	0.98 Hz
4	Rocking about *x* axis	29.8 Hz
5	Rocking about *y* axis	29.8 Hz
6	Translation along *z* axis	37.7 Hz

[14]At the time of this writing, the element for the friction pendulum bearing in SAP2000 does not track the change in height of the isolator as a function of its horizontal relative displacement.

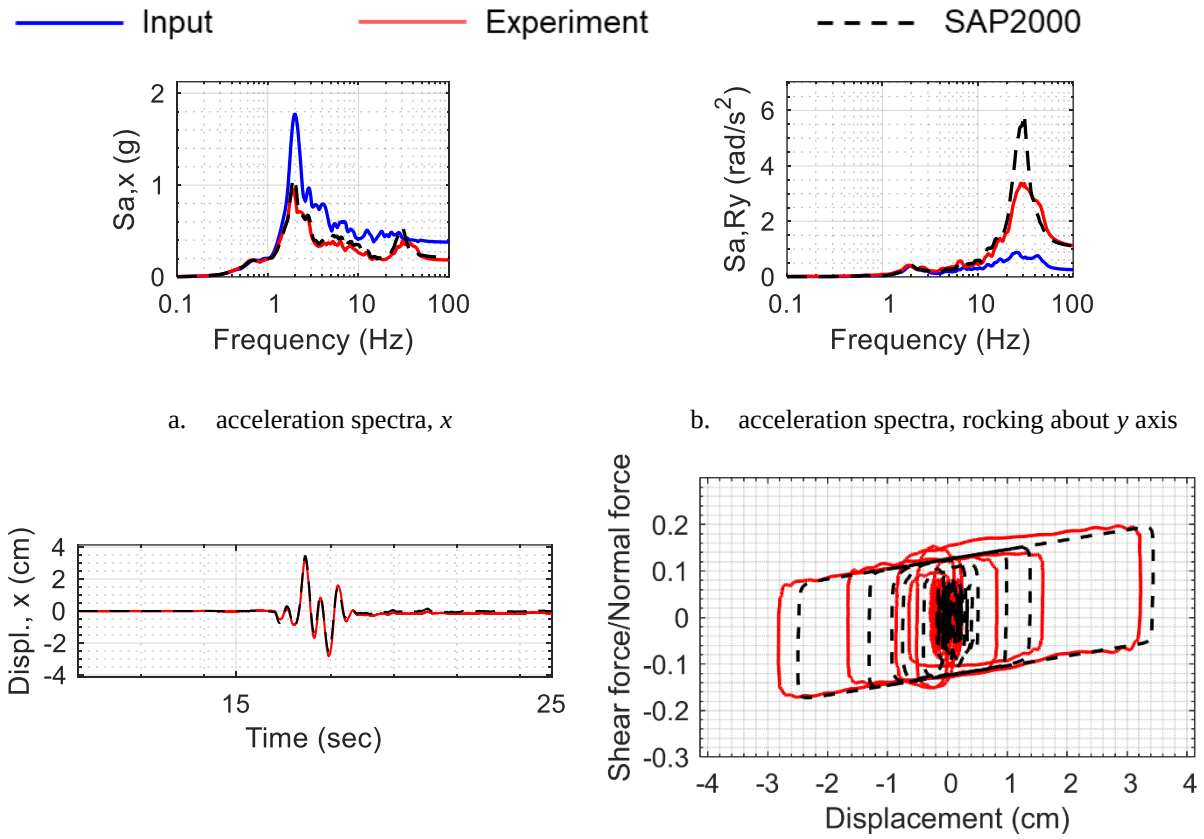

a. acceleration spectra, *x*

b. acceleration spectra, rocking about *y* axis

c. isolation-system displacement, *x*

d. normalized force-displacement loop, *x*

Figure 6.30. Numerical and experimental results, isolation-system responses, motion #1 in Table 4.4, acceleration spectra for 5% damping

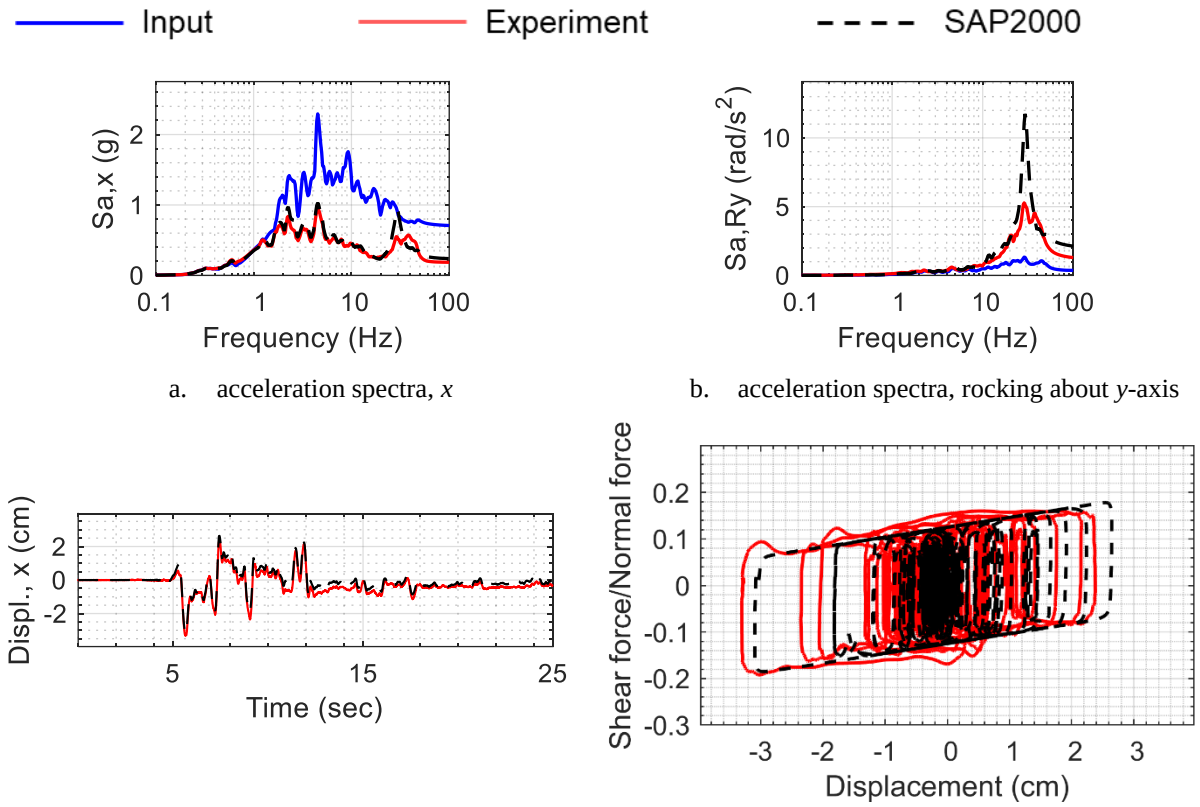

a. acceleration spectra, *x*

b. acceleration spectra, rocking about *y*-axis

c. isolation-system displacement, *x*

d. normalized force-displacement loop, *x*

Figure 6.31. Numerical and experimental results, isolation-system responses, motion #2 in Table 4.4, acceleration spectra for 5% damping

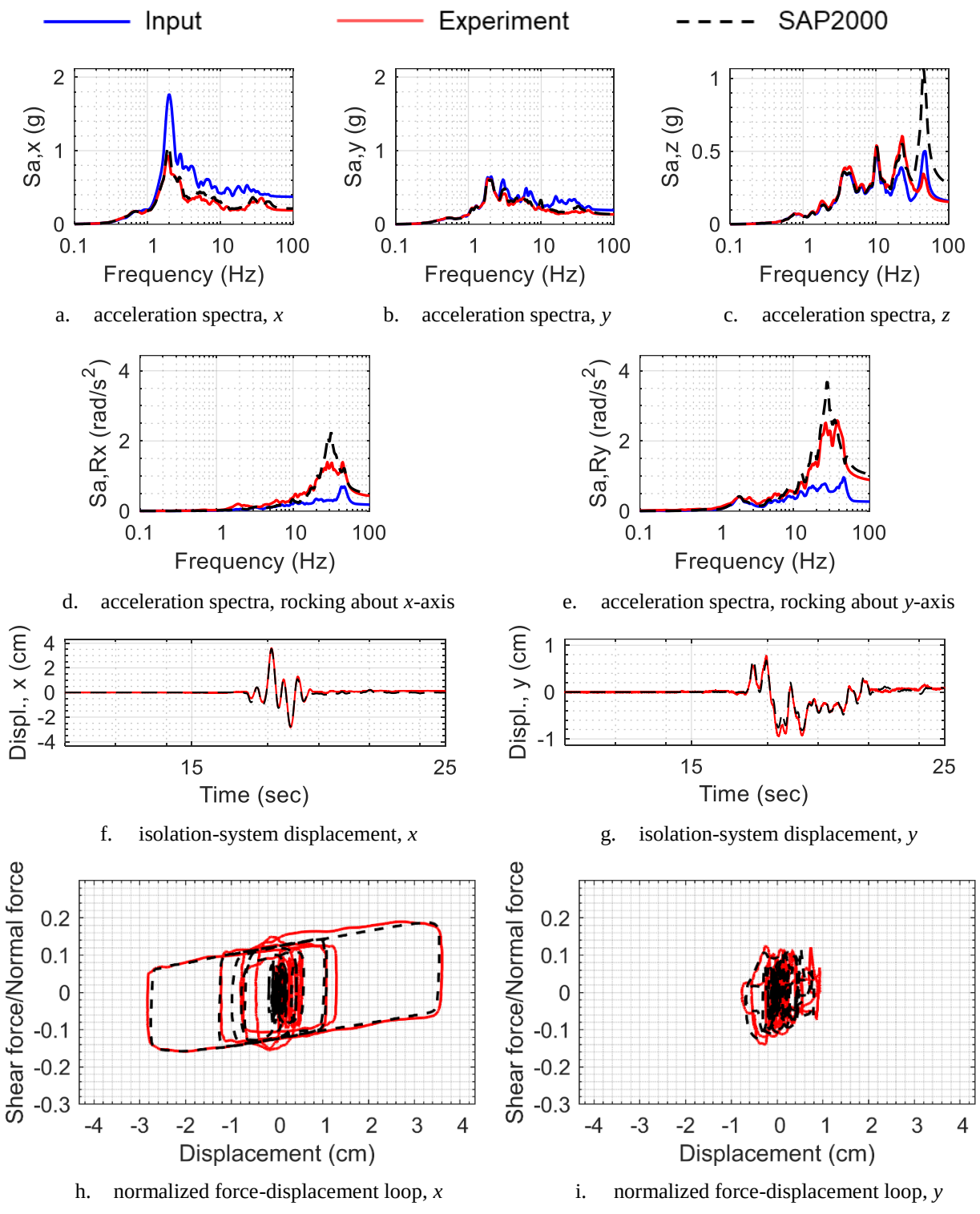

a. acceleration spectra, *x*

b. acceleration spectra, *y*

c. acceleration spectra, *z*

d. acceleration spectra, rocking about *x*-axis

e. acceleration spectra, rocking about *y*-axis

f. isolation-system displacement, *x*

g. isolation-system displacement, *y*

h. normalized force-displacement loop, *x*

i. normalized force-displacement loop, *y*

Figure 6.32. Numerical and experimental results, isolation-system responses, motion #3 in Table 4.4, acceleration spectra for 5% damping

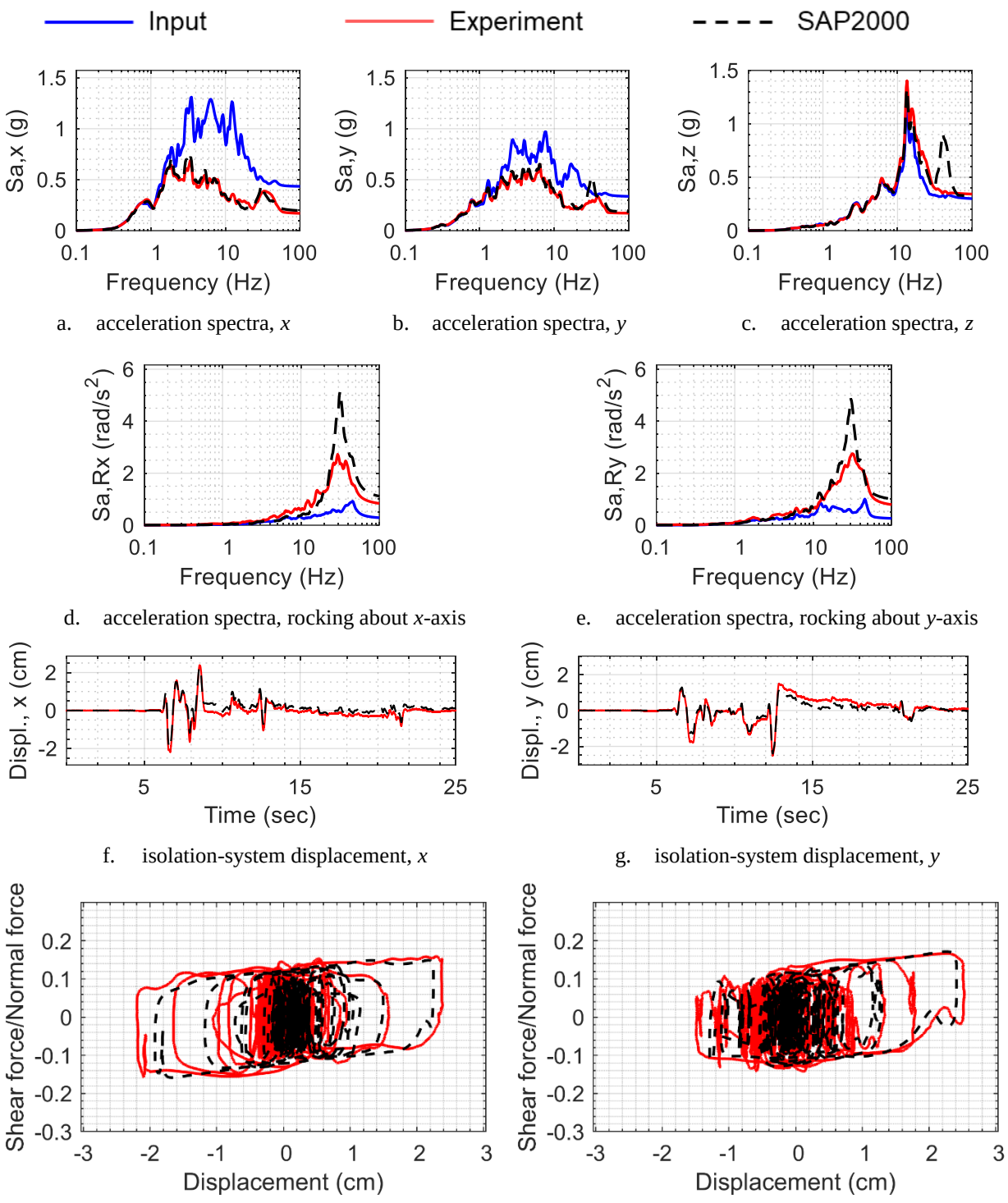

a. acceleration spectra, *x*

b. acceleration spectra, *y*

c. acceleration spectra, *z*

d. acceleration spectra, rocking about *x*-axis

e. acceleration spectra, rocking about *y*-axis

f. isolation-system displacement, *x*

g. isolation-system displacement, *y*

h. normalized force-displacement loop, *x*

i. normalized force-displacement loop, *y*

Figure 6.33. Numerical and experimental results, isolation-system responses, motion #4 in Table 4.4, acceleration spectra for 5% damping

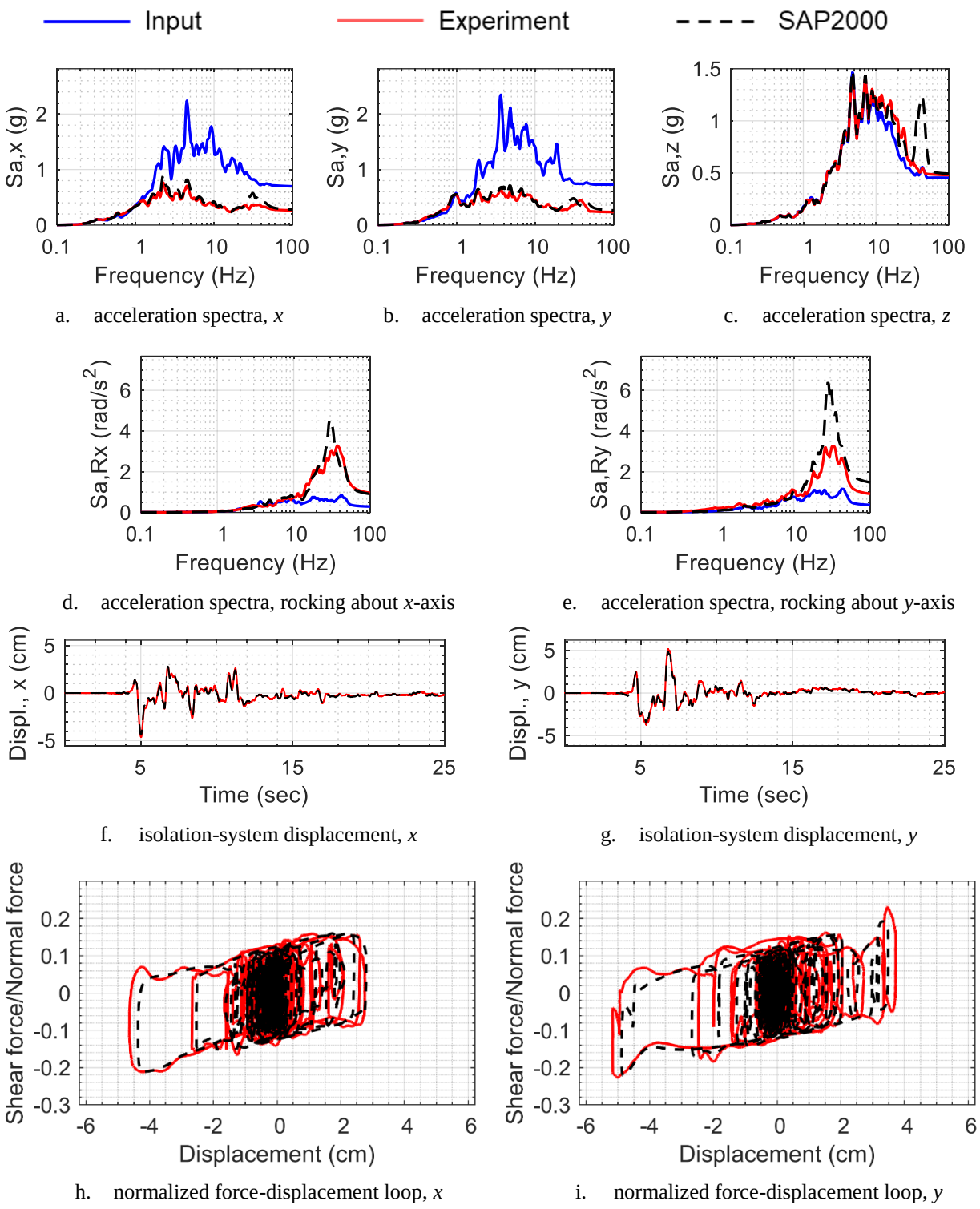

a. acceleration spectra, *x*

b. acceleration spectra, *y*

c. acceleration spectra, *z*

d. acceleration spectra, rocking about *x*-axis

e. acceleration spectra, rocking about *y*-axis

f. isolation-system displacement, *x*

g. isolation-system displacement, *y*

h. normalized force-displacement loop, *x*

i. normalized force-displacement loop, *y*

Figure 6.34. Numerical and experimental results, isolation-system responses, motion #5 in Table 4.4, acceleration spectra for 5% damping

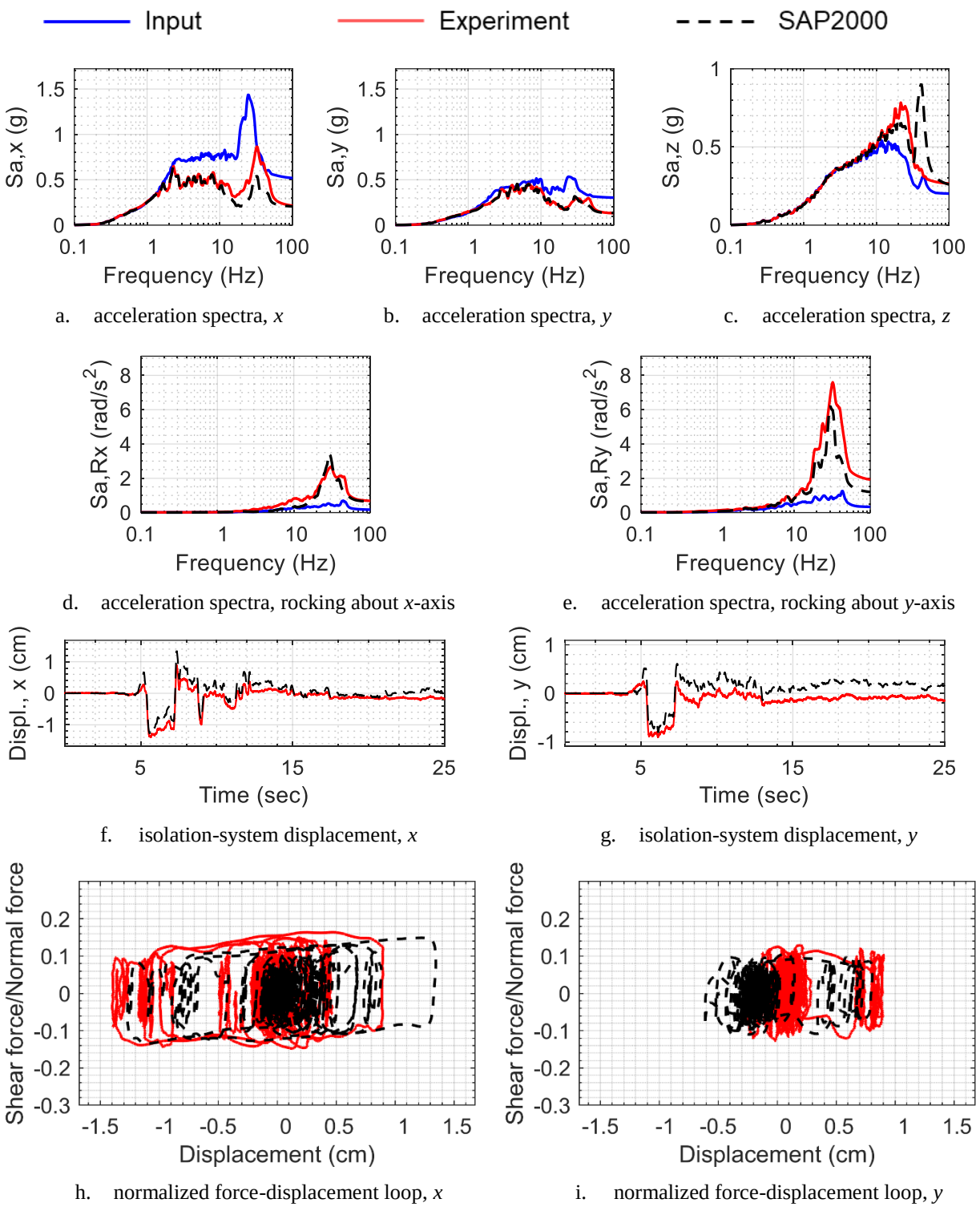

a. acceleration spectra, *x*

b. acceleration spectra, *y*

c. acceleration spectra, *z*

d. acceleration spectra, rocking about *x*-axis

e. acceleration spectra, rocking about *y*-axis

f. isolation-system displacement, *x*

g. isolation-system displacement, *y*

h. normalized force-displacement loop, *x*

i. normalized force-displacement loop, *y*

Figure 6.35. Numerical and experimental results, isolation-system responses, motion #6 in Table 4.4, acceleration spectra for 5% damping

Table 6.3. Maximum absolute isolation-system responses and percentage differences, 1D inputs, motion numbers per Table 4.4

Response	CCE 1D (Motion #1)			KCE 1D (Motion #2)		
	Model	Exp.	Diff., %	Model	Exp.	Diff., %
Isolator displacement, *x*, cm	3.4	3.2	7	3.1	3.3	-6
Shear force, *x*, kN	14.6	14.3	3	13.8	14.8	-6
Normal force, kN	78.9	77.0	2	80	77.6	3
Acceleration, *x*, g	0.21	0.18	16	0.23	0.18	28

Table 6.4. Maximum absolute isolation-system responses and percentage differences, 3D inputs, motion numbers per Table 4.4

Response	CCE 3D (Motion #3)			ECE 3D (Motion #4)			KCE 3D (Motion #5)			BBM 3D (Motion #6)		
	Model	Exp.	Diff., %	Model	Exp.	Diff., %	Model	Exp.	Diff., %	Model	Exp.	Diff., %
Isolator displacement, *x*, cm	3.5	3.6	-2	2.2	2.3	-6	4.3	4.6	-6	1.3	1.3	-4
Isolator displacement, *y*, cm	0.8	0.9	-14	2.4	2.5	-4	4.8	5.1	-6	0.8	0.9	-11
Shear force, *x*, kN	15.4	15.0	3	12.8	13.2	-3	19.3	19.8	-3	11.8	12.0	-2
Shear force, *y*, kN	9.8	10.7	-8	14.0	13.3	5	17.8	17.6	1	9.9	10.1	-3
Normal force, kN	92.8	86.9	7	92.1	92.4	0	103.4	105.4	-2	92.2	94.1	-2
Acceleration, *x*, g	0.21	0.18	12	0.19	0.17	16	0.28	0.26	6	0.20	0.21	-4
Acceleration, *y*, g	0.13	0.13	1	0.18	0.17	8	0.26	0.23	13	0.13	0.13	1
Acceleration, *z*, g	0.27	0.15	82	0.32	0.34	-6	0.49	0.47	3	0.26	0.26	-2

6.4.2 TFP-isolated model

The *triple pendulum isolator* link element in SAP2000 was used to model the TFP isolators. Table 6.5 presents the key inputs used to define the force-deformation properties of the link element in the axial and the two horizontal directions. Table 6.6 summarizes the results of the modal analysis.

Table 6.5. Key inputs for definition of *triple pendulum isolator* link element in SAP2000

Input field (per SAP2000)			Description
Axial (U1) direction	Effective stiffness for linear or non-linear analysis cases		Axial compressive stiffness of the isolators. Value = 1.05×10^5 kN/m per Table 3.2.
	Effective damping for linear analysis case or damping coefficient for nonlinear analysis cases		Zero. Damping in the axial direction was defined as modal damping for the vertical mode under load case definition.
Horizontal (U2 or U3) direction	Effective stiffness for linear analysis cases		Evaluated as $W / 2R_{eff}$, where W is the weight on the isolator and R_{eff} is the effective radius of the top (or bottom) sliding surface. Value = 21142 N/m. The effective radius R_{eff} is calculated as the difference between the radius of the sliding surface and one-half of the distance between the bottom and top sliding surfaces (height of bearing) and is equal to 0.441 m here.
	Effective damping for linear analysis cases		Zero (similar to Table 6.1).
	Stiffness for nonlinear analysis cases	Outer top and outer bottom	Stiffness before sliding. A reasonably large value, enough to distinguish sliding from not sliding, works well for this input field. Values of 9000 kN/m and 3000 kN/m were used for the outer and inner surfaces, respectively, consistent with the weight on the isolator, the fast friction coefficient of the surfaces (inner or outer) and an assumed yield displacement of 0.3 mm.
		Inner top and inner bottom	
	Friction coefficient, fast	Outer top and outer bottom	Value = 14.3% per Table 3.2.
		Inner top and inner bottom	Value = 5.1% per Table 3.2.
	Friction coefficient, slow	Outer top and outer bottom	Value = 6.2% per Table 3.2.
		Inner top and inner bottom	Value = 2.2% per Table 3.2.

Table 6.5. Key inputs for definition of *triple pendulum isolator* link element in SAP2000 (cont.)

Input field (per SAP2000)			Description
Horizontal (U2 or U3) direction	Rate parameter		Value = 42 s/m per Table 3.2.
	Radius of sliding surface	Outer top and outer bottom	Value = 0.473 m per Figure 3.22.
		Inner top and inner bottom	Value = 0.076 m per Figure 3.22.
	Stop distance	Outer top and outer bottom	Related to the displacement capacity for sliding on the outer surfaces (see Figure 75 in CSI (2017)). Since only a fraction of the displacement capacity of the bearings was used in the tests, a large value (0.5 m) was used here.
		Inner top and inner bottom	Value = 1.27 cm per Figure 3.22 and Figure 75 in CSI (2017)

Table 6.6. Summary of modal analysis in SAP2000, TFP-isolated model

Mode number	Description	Frequency
1	Translation along *x* axis	0.52 Hz
2	Translation along *y* axis	0.52 Hz
3	Torsion (rotation about *z* axis)	0.70 Hz
4	Rocking about *x* axis	29.6 Hz
5	Rocking about *y* axis	29.6 Hz
6	Translation along *z* axis	37.5 Hz

Non-linear response history analysis of the TFP-isolated model was performed using inputs corresponding to the six motions introduced in Table 4.5, as described previously for the SFP-isolated model. Figure 6.36 through Figure 6.41 present results of the analyses for the six motions. Table 6.7 and Table 6.8 present experimental and numerical values of key isolation-system responses for the 1D and 3D inputs of Table 4.5, respectively. The conclusion from these data is identical to that presented in the previous sub-section (SFP-isolated model): the agreement between experimental results and numerical predictions for isolation-system responses is excellent. The absolute magnitudes of differences between peak experimental and numerical responses are less than 8%, 6%, 17%, and 11% on average for isolator displacements, reaction forces, horizontal accelerations, and vertical accelerations, respectively.

The accuracy of the numerical results obtained from the SFP-isolated and the TFP-isolated models indicate that utilizing a *rigid superstructure with lumped internal mass* is sufficient for obtaining accurate isolation-system responses.

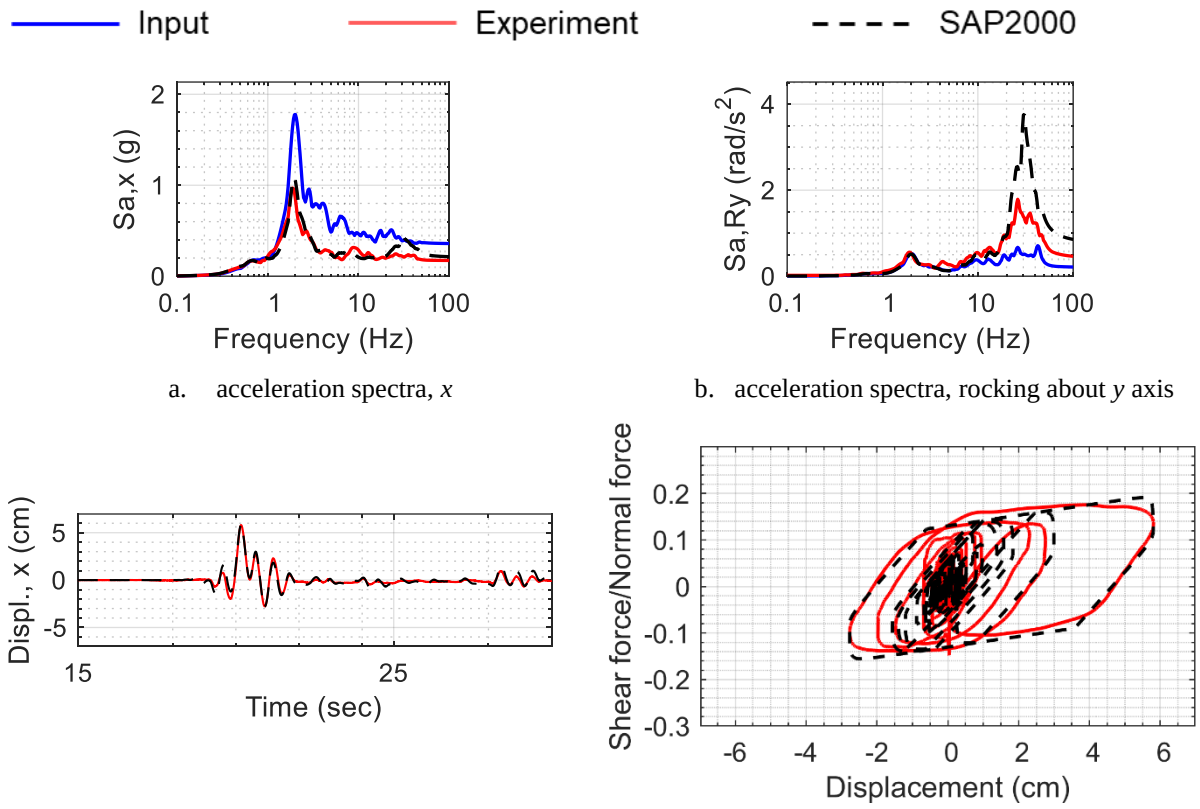

a. acceleration spectra, *x*

b. acceleration spectra, rocking about *y* axis

c. isolation-system displacement, *x*

d. normalized force-displacement loop, *x*

Figure 6.36. Numerical and experimental results, isolation-system responses, motion #1 in Table 4.5, acceleration spectra for 5% damping

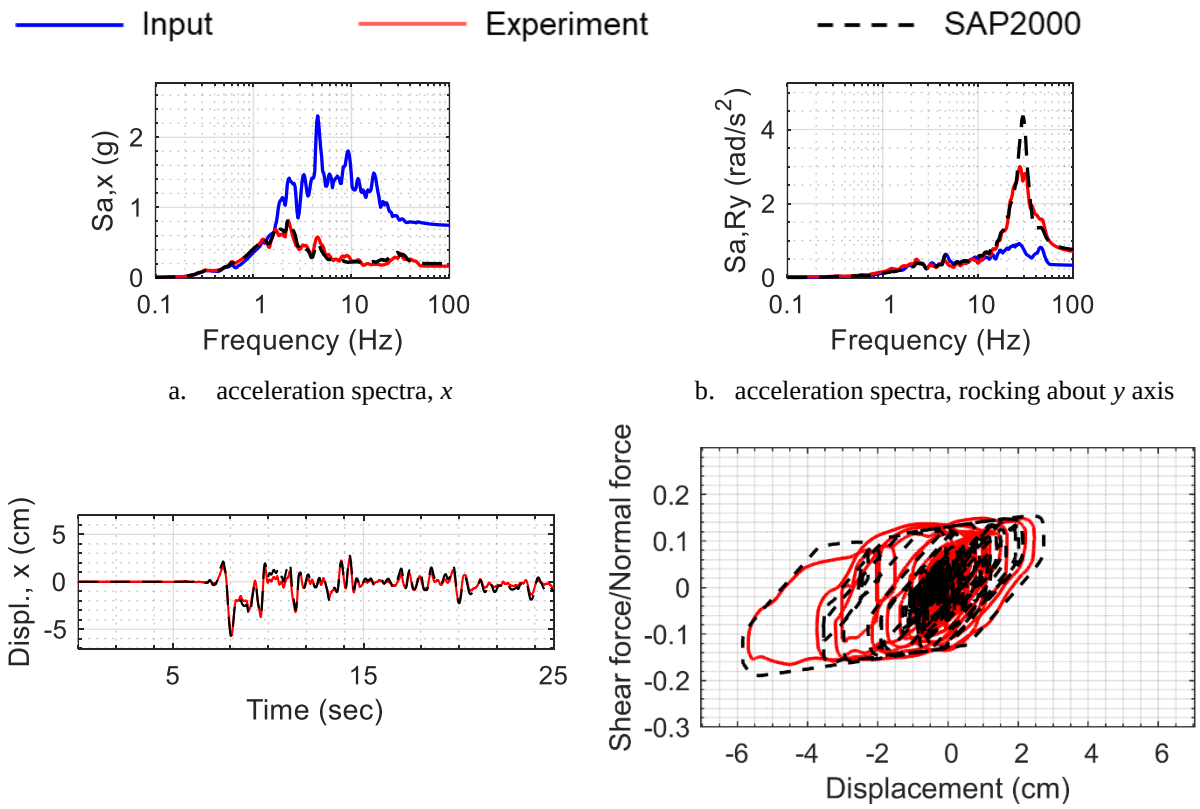

a. acceleration spectra, *x*

b. acceleration spectra, rocking about *y* axis

c. isolation-system displacement, *x*

d. normalized force-displacement loop, *x*

Figure 6.37. Numerical and experimental results, isolation-system responses, motion #2 in Table 4.5, acceleration spectra for 5% damping

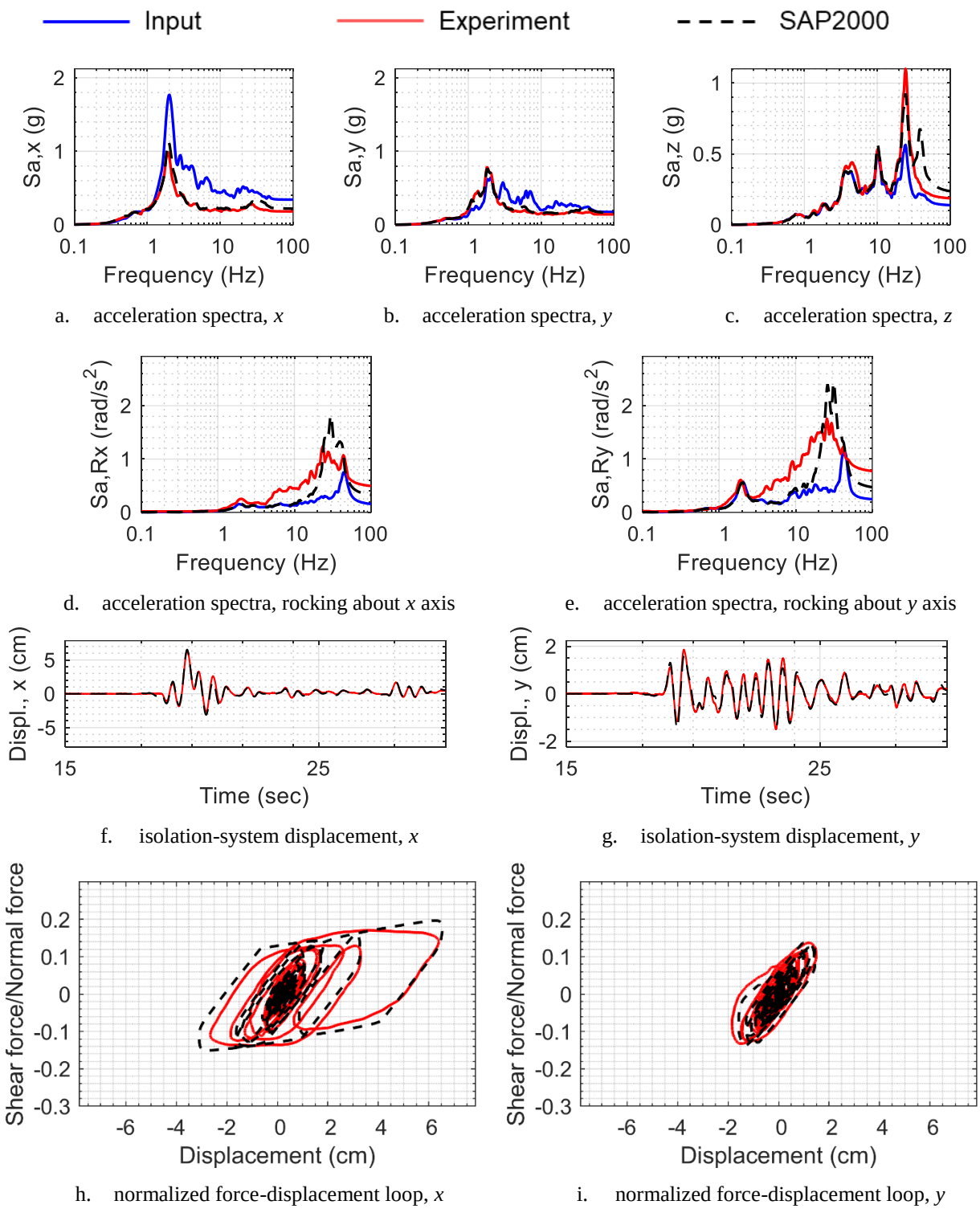

a. acceleration spectra, *x*

b. acceleration spectra, *y*

c. acceleration spectra, *z*

d. acceleration spectra, rocking about *x* axis

e. acceleration spectra, rocking about *y* axis

f. isolation-system displacement, *x*

g. isolation-system displacement, *y*

h. normalized force-displacement loop, *x*

i. normalized force-displacement loop, *y*

Figure 6.38. Numerical and experimental results, isolation-system responses, motion #3 in Table 4.5, acceleration spectra for 5% damping

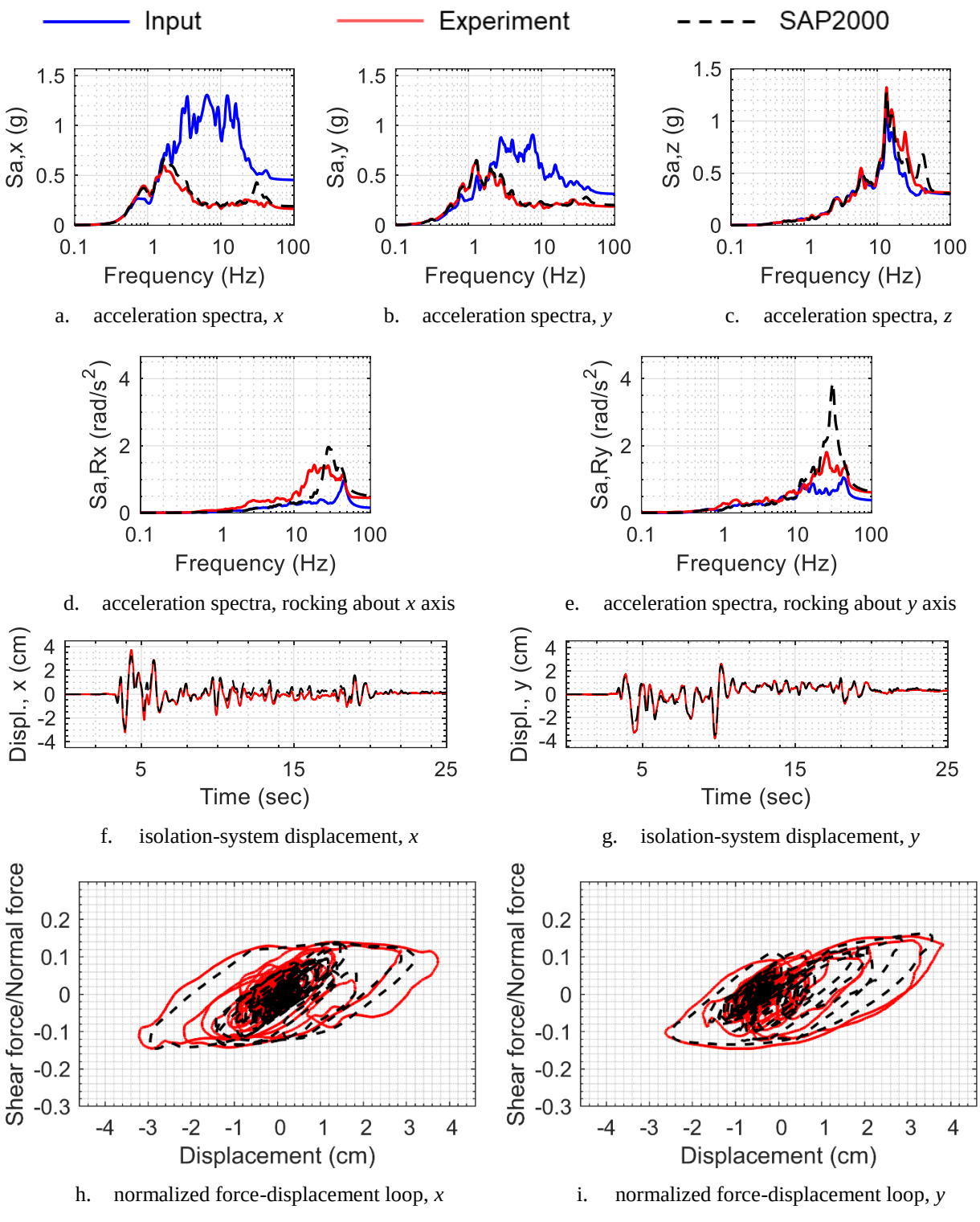

a. acceleration spectra, *x*

b. acceleration spectra, *y*

c. acceleration spectra, *z*

d. acceleration spectra, rocking about *x* axis

e. acceleration spectra, rocking about *y* axis

f. isolation-system displacement, *x*

g. isolation-system displacement, *y*

h. normalized force-displacement loop, *x*

i. normalized force-displacement loop, *y*

Figure 6.39. Numerical and experimental results, isolation-system responses, motion #4 in Table 4.5, acceleration spectra for 5% damping

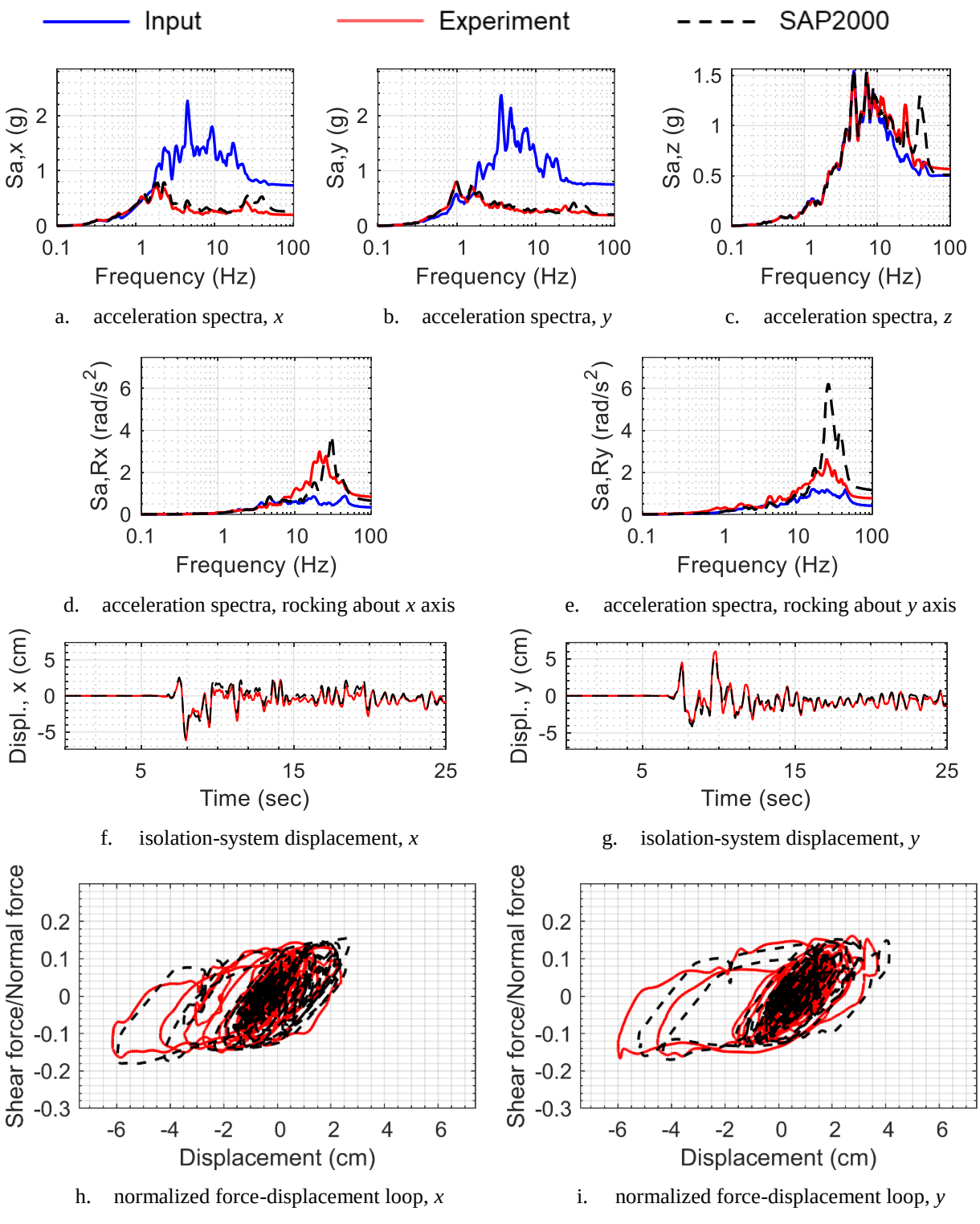

a. acceleration spectra, *x*

b. acceleration spectra, *y*

c. acceleration spectra, *z*

d. acceleration spectra, rocking about *x* axis

e. acceleration spectra, rocking about *y* axis

f. isolation-system displacement, *x*

g. isolation-system displacement, *y*

h. normalized force-displacement loop, *x*

i. normalized force-displacement loop, *y*

Figure 6.40. Numerical and experimental results, isolation-system responses, motion #5 in Table 4.5, acceleration spectra for 5% damping

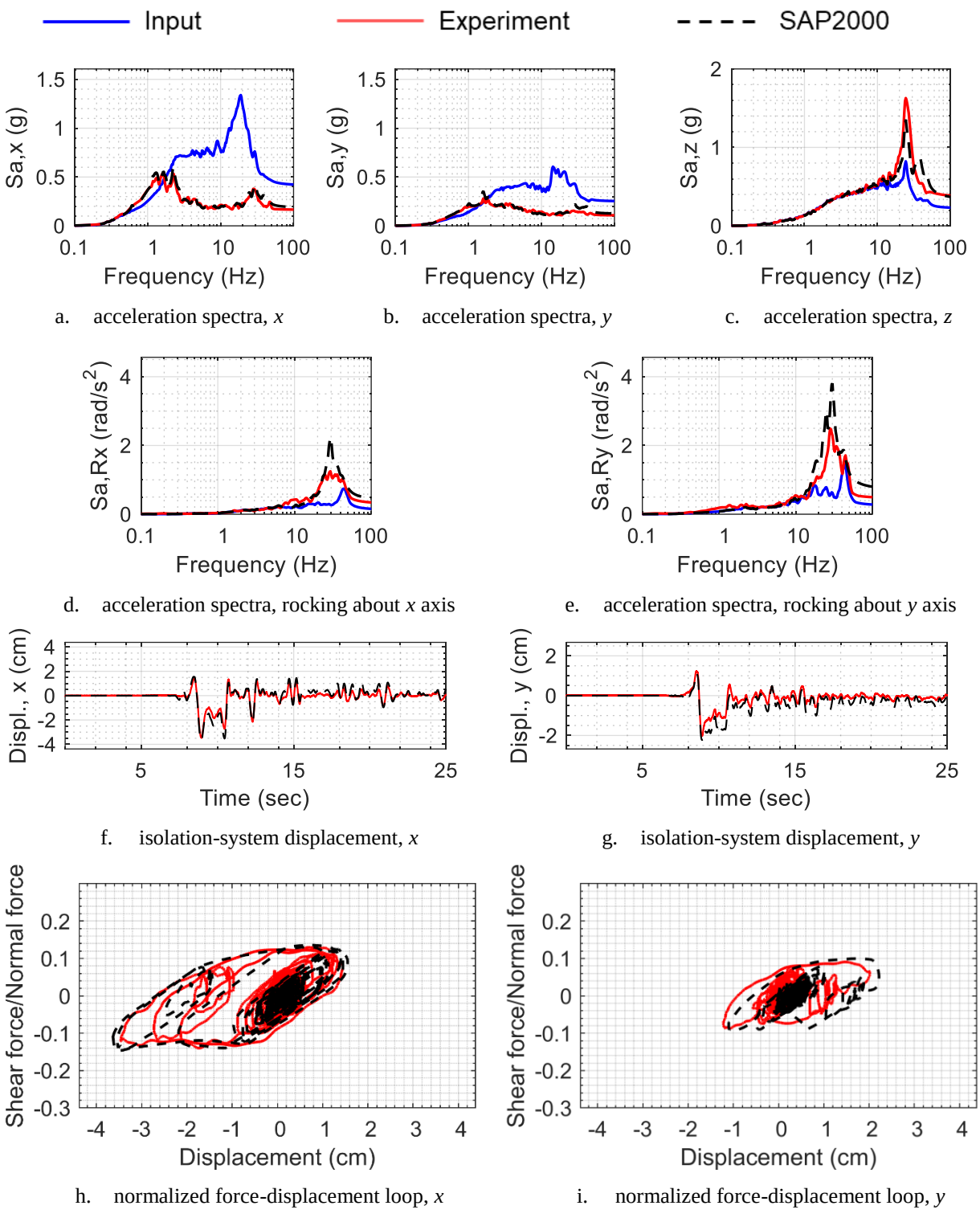

a. acceleration spectra, *x*

b. acceleration spectra, *y*

c. acceleration spectra, *z*

d. acceleration spectra, rocking about *x* axis

e. acceleration spectra, rocking about *y* axis

f. isolation-system displacement, *x*

g. isolation-system displacement, *y*

h. normalized force-displacement loop, *x*

i. normalized force-displacement loop, *y*

Figure 6.41. Numerical and experimental results, isolation-system responses, motion #6 in Table 4.5, acceleration spectra for 5% damping

Table 6.7. Maximum absolute isolation system responses and percentage differences, 1D inputs, motion numbers per Table 4.5

Response	CCE 1D (Motion #1)			KCE 1D (Motion #2)		
	Model	Exp.	Diff., %	Model	Exp.	Diff., %
Isolator displacement, *x*, cm	5.8	5.8	0	5.8	5.6	3
Shear force, *x*, kN	14.3	13	10	14	12.8	10
Normal force, kN	77.8	80.1	-3	79.4	83.4	-5
Acceleration, *x*, g	0.21	0.17	24	0.19	0.16	22

Table 6.8. Maximum absolute isolation system responses and percentage differences, 3D inputs, motion numbers per Table 4.5

Response	CCE 3D (Motion #3)			ECE 3D (Motion #4)			KCE 3D (Motion #5)			BBM 3D (Motion #6)		
	Model	Exp.	Diff., %	Model	Exp.	Diff., %	Model	Exp.	Diff., %	Model	Exp.	Diff., %
Isolator displacement, *x*, cm	6.5	6.3	2	3.2	3.7	-14	5.9	6.1	-3	3.6	3.4	5
Isolator displacement, *y*, cm	1.5	1.8	-14	3.5	3.8	-7	5.2	5.9	-13	2.2	2	10
Shear force, *x*, kN	15.5	13.6	14	12.3	12.5	-2	16.6	14.7	13	12.1	11.6	5
Shear force, *y*, kN	10.7	10.4	3	13.4	12.9	3	15.5	14.6	6	8.6	7.9	9
Normal force, kN	89.5	89.4	0	90.5	93.5	-3	106.4	104.9	1	99.4	101.5	-2
Acceleration, *x*, g	0.22	0.18	21	0.19	0.16	14	0.25	0.2	28	0.19	0.16	16
Acceleration, *y*, g	0.16	0.14	14	0.2	0.18	8	0.2	0.19	6	0.12	0.1	17
Acceleration, *z*, g	0.23	0.18	27	0.3	0.31	-3	0.5	0.56	-10	0.36	0.38	-4

6.5 Closing remarks

Recommendations for analysis and modelling of different components of a base-isolated Fluoride-salt-cooled High temperature Reactor (FHR) were presented previously in this section and are summarized below:

1. *Fluid behavior*: Numerical simulation of sloshing wave height responses is challenging using the ALE method. The double annulus, fluid-only model can be used to estimate hydrodynamic pressure histories for analysis of structural and mechanical components inside a reactor vessel.
2. *Internal forces in a reflector-block assembly*: The preliminary design of connectors in a reflector-block assembly can be use the approach presented in this report. Final design should address construction tolerances between the connectors and the blocks. Under extreme vertical and horizontal seismic inputs, dynamic fluid loadings on the reflector-block assembly may lead it to disengage from the head of the vessel, disrupting load paths and affecting fluid-flow paths inside the reactor vessel. Horizontal and vertical seismic isolation can substantially mitigate the effects of extreme earthquake shaking of a reactor vessel and its internals, permitting simpler design solutions and allowing the design approaches described in this chapter to be used.
3. *Base-isolation systems*: Accurate estimates of isolation-system responses can be made by analysis of a rigid vessel, with the mass of the internal components and fluid distributed over the area of its wall.

SECTION 7
SUMMARY AND OUTCOMES

7.1 Introduction

The Kairos Power Fluoride salt-cooled High temperature Reactor (KP-FHR) is a well-advanced Gen IV design (WNA 2022). This molten salt reactor uses circulating solid pebbles, filled with TRISO particles, as a fuel and graphite blocks as a moderator. The focus of this report is the behavior of components of the reactor under moderate to severe earthquake shaking. The reactor components studied here included an outer vessel, a concentric core barrel, positively-buoyant reflector blocks that act as a moderator, positively-buoyant spherical fuel pebbles, and a molten-salt coolant.

To support the seismic design of the reactor, this report: 1) describes the design of a seismically-isolated, scale model of the reactor for earthquake-simulator testing, 2) presents observations of component behaviors based on testing, and 3) presents recommendations for the seismic modelling and analysis of reactor components.

Section 1.3 identified the three broad objectives of this report. Objective 1, the design of a scale model of an FHR, is addressed in Section 2 and Section 3. The generation of experimental data for responses of model-scale reactor components to multi-directional earthquake inputs, objective 2, is addressed in Section 4. Objective 3, the analysis of experimental data for assessment of component behaviors and formulation of recommendations for analysis and modelling is addressed in Section 5 and Section 6.

The following section summarizes the work presented in Section 1 through Section 6 of this report.

7.2 Summary and Outcomes

Section 1 introduced the FHR and presented an overview of the available literature on the seismic behavior of some of its components. Some of the FHR components are similar to those used in other deigns (e.g., graphite reflector blocks in some high temperature gas-cooled reactor (HTGR) designs). However, none of the past studies involved experiments at the scale and level of complexity described in this report.

Section 2 presented a detailed scaling analysis for different test components of the model FHR for earthquake-simulator testing. Model components were scaled per different governing scaling laws with the aim of simulating important behaviors (e.g., buoyancy in the reflector blocks, fluid-structure interaction in the core barrel) as best as possible at the model scale. A length scale of 0.39 was used to design all the model components, except for the core barrel, for which a different length scale of 0.16 was used to scale the wall thickness.

Section 3 described the geometries of the model components. The sequence in which the components were assembled and the challenges encountered during model assembly were discussed. The geometric details and force-deformation characteristics of the two types of friction pendulum isolators used to seismically (base) isolate the vessel were also presented in this section.

Section 4 presented details of the instrumentation used to record responses of different test components during earthquake-simulator tests. The instrumentation recorded the dynamic response of the fluid (hydrodynamic pressure and sloshing displacements), base reactions, isolation system displacements, dynamic responses of the vessel, core barrel, and reflector blocks, and pebble bed compaction under shaking. Traditional earthquake engineering instruments, load cells, accelerometers, and pressure gages, were used in tandem with borescopes and bespoke float-and-Temposonic gages to measure wave height. The seismic inputs and the test plan were also described in Section 4. The earthquake-simulator tests of the test specimen were grouped into three series, each focused on specific objectives. Test series 1 and 3 were focused on the behaviors of the reflector-block assembly and the pebble bed, respectively. Series 2 involved earthquake-simulator tests of the entire assembly in fixed-base and base-isolated configurations.

Section 5 presented results from the earthquake-simulator experiments and discussed the behavior of different test components. A comparison of acceleration responses recorded on the outer vessel, core barrel, and the reflector-block assembly revealed that these components responded as a near-rigid unit. Accordingly, accurate estimates of base reactions were computed using a lumped-mass model, wherein the mass of the test specimen was lumped at its center of mass. The sloshing response of the fluid between the core barrel and the reflector-block assembly was heavily damped and the wave height time series was recovered approximately using an analytical solution for sloshing responses in a regular cylindrical tank. Data generated from tests run to study consolidation of the pebble bed under earthquake shaking were presented. The pebble bed packing fraction changed by no more than 3% after 150+ seconds of strong shaking and the percentage change depended on the initial packing fraction. The use of base isolation systems utilizing model-scale SFP and TFP bearings led to reductions in peak horizontal accelerations at the base of the outer vessel by factors between 1.2 and 4.6. The axial stiffness of the model-scale bearings used in the two isolations systems was *small* at the axial load developed in the tests and resulted in amplification in accelerations at high frequencies (25+ Hz) in the vertical and rocking directions.

Section 6 presented recommendations for analysis and modelling of different components of a base-isolated FHR. The challenges associated with accurate numerical estimation of sloshing responses in small annuli were discussed. A fluid-only, *double annulus* model was demonstrated to be effective for obtaining hydrodynamic pressure histories that could be used for analysis of structural and mechanical components

of the reactor. A practical approach to estimate forces for preliminary design of connectors within a reflector-block assembly was presented and the behavior of the assembly under extreme vertical and horizontal seismic inputs was noted to have a potential for disrupting load paths and affecting fluid-flow paths inside the reactor vessel. Horizontal base isolation systems mitigated the effects of extreme earthquake shaking. The responses of the horizontal isolation systems used in the experiments were recovered with good accuracy using a finite element model of a rigid outer vessel and considering the internal components (including fluid and pebbles) as a distributed mass on the wall of the vessel.

7.3 Closing remarks

The earthquake-simulator experiments on a seismically-isolated FHR, described in this report, were first-of-a-kind, considering the scale and the level of complexity involved. There were practical limitations in terms of available materials for model-scale components and available space (and access) for instruments. Possible future experiments include:

1. Experiments to further characterize the sloshing response of the coolant in the inner annulus of the FHR. In particular, the effect of fluid viscosity and size of gaps between columns of the reflector-block assembly on damping in the sloshing mode are worthy of study. Such experiments could use a number of fluids and utilize a model with simpler internal construction than that described in this report. As an example, fewer columns and fewer rows than used here could be used to construct the reflector-block assembly and the gaps between them accurately controlled.
2. Adding fluid-flow through the core of the assembly during earthquake simulations to study the effect, if any, on responses of the reactor's components.

The experimental results described in this report provided insights into the dynamic behavior of reactor components and enabled formulation of analysis and modelling recommendations. The use of horizontal (2D) base-isolation systems led to substantial reductions in peak horizontal accelerations at the base of the vessel. Base-isolation systems (2D and 3D) could significantly reduce demands on reactor component, thereby enabling simpler design approaches (see section 6.3.3 for an example) and supporting the deployment of standardized designs at sites with varying seismic hazards.

All data generated in the experiments will be made available on DesignSafe (Rathje *et al.* 2017).

SECTION 8

REFERENCES

Arias, A. (1970). "A measure of earthquake intensity." In *Seismic design for nuclear power plants*, edited by Hansen, R., 438-483. Massachusetts Institute of Technology, Cambridge, MA.

Auwerda, G. J. (2014). "Core physics of pebble bed high temperature nuclear reactors." Dissertation, presented to Delft Univeristy of Technology, Delft, Netherlands in partial fulfilment of the requirements for the degree of Doctor of Philosophy.

Bardet, P. M., and Peterson, P. F. (2008). "Options for scaled experiments for high temperature liquid salt and helium fluid mechanics and convective heat transfer." *Nuclear Technology*, 163(3), 344-357.

Buckingham, E. (1914). "On physically similar systems; illustrations of the use of dimensional equations." *Physical Review*, 4(4), 345.

Cai, M., Zhu, L., Huang, C., and Wang, X. (2018). "A preliminary study on seismic behavior of the graphite reflector in molten salt reactor." *Nuclear Engineering and Design*, 330, 282-288.

Chen, X., Dai, Y., Yan, R., Mei, M., Zhang, J., and Zou, Y. (2017). "Earthquake simulator experiments for the structure of the pebble bed in TMSR-SF." *Proceedings, 2017 International Congress on Advances in Nuclear Power Plants (ICAPP'17)*, Fukui-Kyoto, Japan.

Chen, X., Zhang, J., Dai, Y., Mei, M., Ji, R., Yan, R., Zou, Y., and Cai, X. (2018). "Experimental investigation of the bed structure in liquid salt cooled pebble bed reactor." *Nuclear Engineering and Design*, 331, 24-31.

Constantinou, M. C., Whittaker, A. S., Kalpakidis, Y., Fenz, D. M., and Warn, G. P. (2007). "Performance of seismic isolation hardware under service and seismic loading." *Report MCEER-07-0012*, The State University of New York at Buffalo, Buffalo, NY.

CSI (2017). "CSI analysis reference manual." Computer and Structures, Inc., Berkeley, CA, USA.

DeLangre, E. (2020). "Fundamentals of fluid-solid interactions (module 4, week 1)." <https://www.coursera.org/learn/fluid-solid-interaction>. (5 February, 2020).

DOE (2019). "TRISO particles: the most robust nuclear fuel on earth." United States Department of Energy, Washington, D.C.

Dove, R., Dunwoody, W., and Rhorer, R. (1981). "Scale-model study of the seismic response of a nuclear reactor core." *NUREG/CR-2108*, Los Alamos Scientific Laboratory, NM.

Dullien, F. A. (1992). *Porous media: fluid transport and pore structure, 2nd Edition*, Academic Press Inc., San Diego, CA.

Fenz, D. M., and Constantinou, M. C. (2008). "Mechanical behavior of multi-spherical sliding bearings." *Report MCEER-08-0007*, The State University of New York at Buffalo, Buffalo, NY.

Ichikawa, T., Yonemoto, S., Murakoso, H., Nakamura, T., Morita, H., Murota, M., Tanaka, T., and Kimura, M. (2003). "Seismic analysis & verification test on a neutron reflector for APWR reactor internals." *Proceedings, 17th International Conference on Structural Mechanics in Reactor Technology (SMiRT-17)*, Prague, Czech Republic.

Ikushima, T. (1982a). "Aseismic study of high temperature gas-cooled reactor core with block-type fuel: 2nd report: an analytical method of two-dimensional vibration of interacting columns." *Mechanical Engineering Journal (Bulletin of JSME)*, 25(208), 1610-1617.

Ikushima, T. (1982b). "SONATINA-2V: a computer program for seismic analysis of the two-dimensional vertical slice HTGR core." *JAERI 1279*, Japan Atomic Energy Research Institute, Tokai, Japan.

Ikushima, T. (1990). "SONATINA-2H: a computer program for seismic analysis of the two-dimensional horizontal slice HTGR core." *JAER1-M 90-003*, Japan Atomic Energy Research Institute, Tokai, Japan.

Ikushima, T., and Honma, T. (1989). "Seismic response of high temperature gas-cooled reactor core with block-typed fuel - analytical method of seismic response for two-dimensional horizontal slice core model." *Journal of Nuclear Science and Technology*, 26(10), 913-930.

Ikushima, T., Honma, T., and Ishizuka, H. (1982). "Seismic research on block-type HTGR core." *Nuclear Engineering and Design*, 71(2), 195-215.

Ikushima, T., and Nakazawa, T. (1979). "A seismic analysis method for a block column gas-cooled reactor core." *Nuclear Engineering and Design*, 55(3), 331-342.

Iyoku, T., Futakawa, M., and Ishihara, M. (1994). "Evaluation of aseismic integrity in HTTR core-bottom structure. I. Aseismic test for core-bottom structure." *Nuclear Engineering and Design*, 148(1), 71-81.

Iyoku, T., Inagaki, Y., Shiozawa, S., Futakawa, M., and Miki, T. (1992a). "Seismic response of the high-temperature engineering test reactor core bottom structure." *Nuclear Technology*, 99(2), 169-176.

Iyoku, T., Inagaki, Y., Shiozawa, S., and Nishiguchi, I. (1992b). "Seismic study of high-temperature engineering test reactor core graphite structures." *Nuclear Technology*, 99(2), 158-168.

Iyoku, T., Smita, J., Ishihara, M., and Ueta, S. (2004). "R&D on core seismic design." *Nuclear Engineering and Design*, 233(1-3), 225-234.

Jin, L., Wang, H., Sun, L., Wang, H., and Ma, S. (2014). "Experimental and numerical researches on collision of graphite bricks." *Nuclear Engineering and Design*, 275, 179-189.

Lal, K. M., Parsi, S. S., Kosbab, B. D., Ingersoll, E. D., Charkas, H., and Whittaker, A. S. (2022). "Towards standardized nuclear reactors: seismic isolation and the cost impact of the earthquake load case." *Nuclear Engineering and Design*, 386, 111487.

Laufer, M. R. (2013). "Granular dynamics in pebble bed reactor cores." Dissertation, presented to University of California, Berkeley, CA, in partial fulfillment of the requirements for the degree of Doctor of Philosophy.

Lee, D., and Constantinou, M. C. (2017). "Development and validation of a combined horizontal-vertical seismic isolation system for high-voltage-power transformers." *Report MCEER-17-0007*, The State University of New York at Buffalo, Buffalo, NY.

Livermore Software Technology Corporation (LSTC) (2017). "LS-DYNA user's manual – Version R 11.0." Livermore Software Technology Corporation, Livermore, CA, USA.

Malhotra, P. K., Wenk, T., and Wieland, M. (2000). "Simple procedure for seismic analysis of liquid-storage tanks." *Structural Engineering International*, 10(3), 197-201.

Material Properties (2022). "Mechanical properties of polypropylene." <https://material-properties.org/polypropylene-density-strength-melting-point-thermal-conductivity/>. (8 August, 2022).

McVitty, W. J., and Constantinou, M. C. (2015). "Property modification factors for seismic isolators: design guidance for buildings." *Report MCEER 15-0005*, The State University of New York at Buffalo, Buffalo, NY.

Mir, F. U. H., Lal, K. M., Kosbab, B. D., Tilow, K., Song, B., Nguyen, N., Clavelli, M., Pérès, M., and Whittaker, A. S. (2022a). "Earthquake simulator experiments of a seismically isolated generation IV reactor model." *Proceedings, 12th United States National Conference on Earthquake Engineering,* Salt Lake City, UT.

Mir, F. U. H., Yu, C.-C., Whittaker, A. S., and Constantinou, M. C. (2022b). "Physical and numerical simulations of fluid-structure interaction in advanced nuclear reactors " *Report MCEER-22-0002*, The State University of New York at Buffalo, Buffalo, NY.

Mir, F. U. H., Yu, C. C., and Whittaker, A. S. (2021). "Experimental and numerical studies of seismic fluid-structure interaction in a base-supported cylindrical vessel." *Earthquake Engineering & Structural Dynamics*, 50(5), 1395-1413.

NRC (2021). "Preliminary safety analysis report for the Kairos Power fluoride salt- cooled, high temperature non-power reactor (Hermes) - revision 0." *ML21272A375*, September 29, 2021, United States Nuclear Regulatory Commission, Washington, D.C.

Olsen, B., Neylan, A., and Gorholt, W. (1976). "Seismic test on a one-fifth scale HTGR core model." *Nuclear Engineering and Design*, 36(3), 355-365.

Parsi, S. S., Lal, K. M., Kosbab, B. D., Ingersoll, E. D., Shirvan, K., and Whittaker, A. S. (2022). "Seismic isolation: a pathway to standardized advanced nuclear reactors." *Nuclear Engineering and Design*, 387, 111445.

Rathje, E. M., Dawson, C., Padgett, J. E., Pinelli, J.-P., Stanzione, D., Adair, A., Arduino, P., Brandenberg, S. J., Cockerill, T., and Dey, C. (2017). "DesignSafe: new cyberinfrastructure for natural hazards engineering." *Natural Hazards Review*, 18(3), 06017001.

Rickard, N. (1977). "CRUNCH 1D: a computer program for seismic analysis of the HTGR core." *GA-A14120*, General Atomic Company, San Diego, CA.

Sarlis, A. A., Constantinou, M. C., and Reinhorn, A. M. (2013). "Shake table testing of triple friction pendulum isolators under extreme conditions." *Report MCEER-13-0011*, The State University of New York at Buffalo, Buffalo, NY.

Satvat, N., Sarikurt, F., Johnson, K., Kolaja, I., Fratoni, M., Haugh, B., and Blandford, E. (2021). "Neutronics, thermal-hydraulics, and multi-physics benchmark models for a generic pebble-bed fluoride-salt-cooled high temperature reactor (FHR)." *Nuclear Engineering and Design*, 384, 111461.

Sun, L., Shi, L., Wang, H., Wang, H., Hu, Y., and Zhang, Z. (2012). "Seismic test and analyses on double-layer model of HTR-PM graphite structure." *Proceedings, 20th International Conference on Nuclear Engineering collocated with the ASME 2012 Power Conference (ICONE20-POWER2012),* Anaheim, CA.

Tang, Y., Grandy, C., and Seidensticker, R. (2010). "Seismic response of annular cylindrical tanks." *Nuclear Engineering and Design*, 240(10), 2614-2625.

Theymann, W., Kemter, F., and Schmidt, G. (1989). "Seismic behaviour of the core structure in a medium-sized HTR." *Proceedings, 10th International Conference on Structural Mechanics in Reactor Technology (SMiRT-10),* Anahiem, CA.

Veletsos, A. S. (1984). "Seismic response and design of liquid storage tanks." *Guidelines for the seismic design of oil and gas pipeline systems*, Committee on Gas and Liquid Fuel Lifelines, American Society of Civil Engineers (ASCE), Reston, VA, 255-370.

Warn, G. P., and Whittaker, A. S. (2006). "A study of the coupled horizontal-vertical behavior of elastomeric and lead-rubber seismic isolation bearings." *Report MCEER-06-0011*, The State University of New York at Buffalo, Buffalo, NY.

World Nuclear Association (WNA) (2022). "Small nuclear power reactors." <https://www.world-nuclear.org/information-library/nuclear-fuel-cycle/nuclear-power-reactors/small-nuclear-power-reactors.aspx>. (July 15, 2022).

Yu, C.-C., and Whittaker, A. S. (2021). "Analytical and numerical studies of fluid-structure interaction in liquid-filled vessels - revision 1." *Report MCEER-20-0003*, The State University of New York at Buffalo, Buffalo, NY.

Yu, C.-C., and Whittaker, A. S. (2022). "A process to verify numerical models for seismic fluid-structure interaction in advanced reactor vessels." *Nuclear Engineering and Design*, 387, 111580.

APPENDIX A
CHARACTERIZATION TESTS OF SINGLE AND TRIPLE FRICTION PENDULUM BEARINGS

A.1 Introduction

This appendix describes characterization tests for the four Single concave Friction Pendulum (SFP) and the four Triple Friction Pendulum (TFP) bearings used to seismically isolate the specimen in the earthquake-simulator tests described in this report. The SFP bearings are denoted SFP1, SFP2, SFP3, and SFP4, and the TFP bearings are denoted TFP1, TFP2, TFP3, and TFP4.

This appendix comprises eight sections including this introduction. Sections A.2 and A.3 present descriptions of the SFP and TFP bearings, respectively. The test set-up used to characterize the behavior of the bearings in the horizontal direction is described in section A.4. The tests performed to characterize behavior of the bearings in the horizontal direction and results are presented in sections A.5 and A.6. Section A.7 describes the tests performed to determine the axial stiffness of the bearings. Section A.8 summarizes the test results.

A.2 Description of SFP bearings

An SFP bearing consists of a sliding surface (concave plate), a housing plate, and a slider that is coated with a PTFE-type composite as shown in Figure A.1. Figure A.2 shows the fabrication drawings provided by the manufacturer (Earthquake Protection Systems).

Figure A.1. Components of an SFP bearing

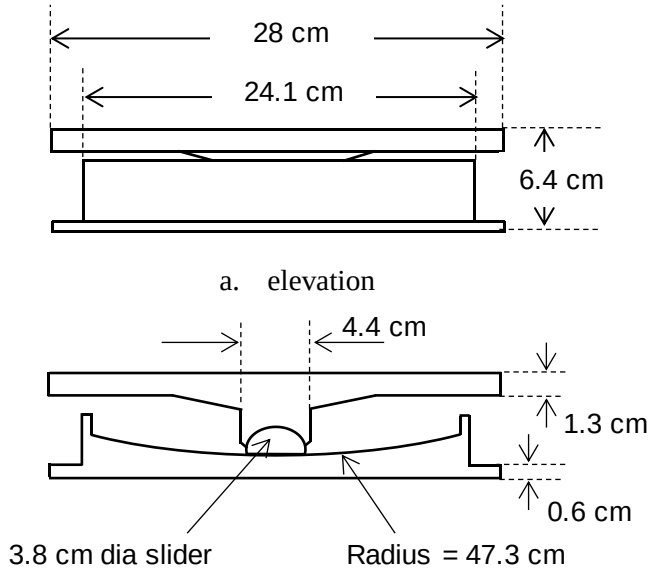

Figure A.2. Fabrication drawings of SFP bearings, provided by Earthquake Protection Systems

The idealized force-displacement behavior of an SFP bearing, shown in Figure A.3, is characterized by the radius of curvature of the sliding surface (R) and the coefficient of friction at the sliding surface (μ). The characteristic strength (Q) and the post elastic stiffness (K_{pe}) are related to these parameters and the imposed instantaneous axial load (W) on the bearing as indicated in Figure A.3. The radius of curvature (R) is a known geometric property of the SFP bearing. The primary goal of the characterization tests is to determine the coefficient of friction (μ).

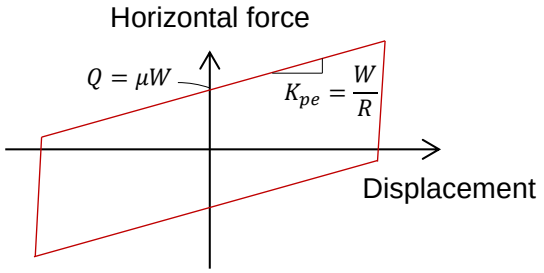

Figure A.3. Idealized force-displacement behavior of an SFP bearing, horizontal direction

The coefficient of friction is a function of the axial load on the bearing, the sliding velocity, and the temperature of the sliding surface (Constantinou *et al.* 2007) The dependence on axial load and sliding velocity is illustrated in Figure A.4. An increase in the axial load leads to a reduction in the coefficient of friction. The coefficient of friction at near zero sliding velocity is defined as the breakaway coefficient of friction (μ_B). As the sliding velocity increases, the coefficient of friction drops to a minimum ($\mu_{\min}$) before attaining a maximum value ($\mu_{\max}$) at high velocities. In general, for a fixed value of axial load, the relation of the coefficient of friction and the sliding velocity (V) can be described by (Constantinou *et al.* 2007):

$$\mu = \mu_{\max} - (\mu_{\max} - \mu_{\min})e^{-aV} \tag{A-1}$$

where a is a rate parameter. The coefficient of friction reduces with an increase in the temperature of the sliding surface. (The temperature dependence of the coefficient of friction is not characterized here.)

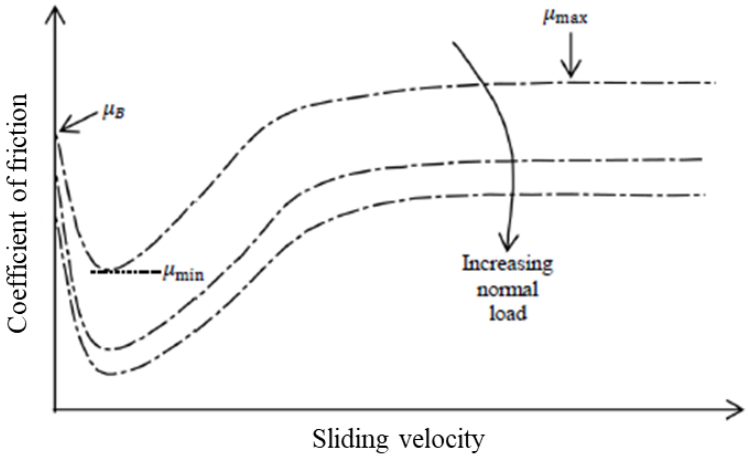

Figure A.4. Variation of the coefficient of friction with sliding velocity and axial load, adapted from Constantinou *et al.* (2007)

A.3 Description of TFP bearings

A Triple Friction Pendulum bearing comprises two concave plates and a nested slider assembly. The two concave plates are separated by the slider assembly that is enclosed in a rubber seal; see Figure A.5. The surfaces of the slider assembly in contact with the top and bottom concave plates and the surfaces of the slider in contact with the concave plates of the slider assembly are coated with a PTFE-type material. Figure A.6 presents the construction of a TFP bearing. Sliding is permitted on all four concave surfaces, denoted 1 through 4 in Figure A.6b.

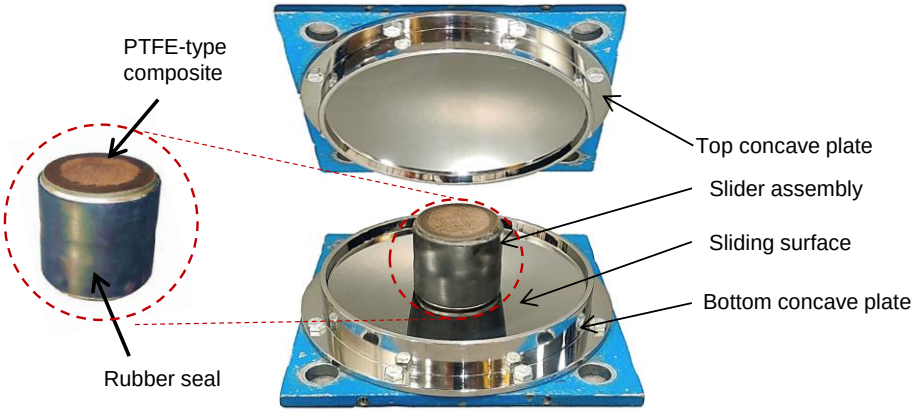

Figure A.5. Components of a TFP isolator

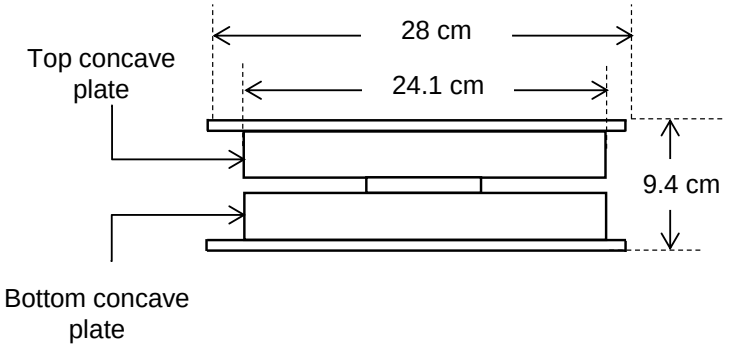

a. elevation

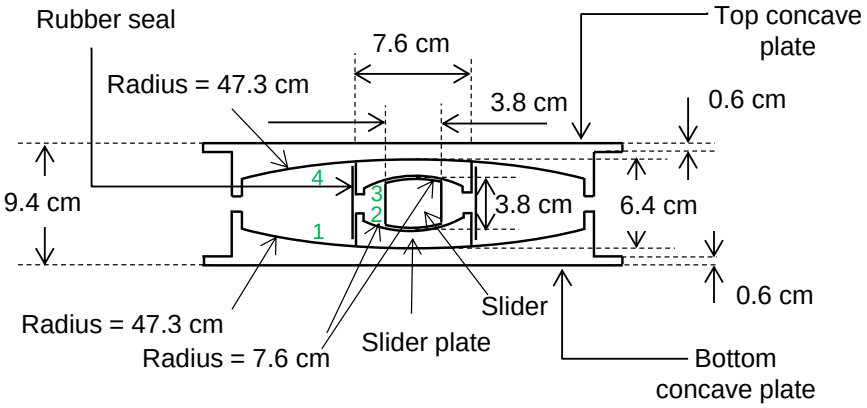

b. cross-section, sliding surfaces 1 through 4 indicated in green

Figure A.6. Fabrication drawings of TFP isolators (provided by Earthquake Protection Systems)

Figure A.7 presents the horizontal force-displacement behavior of a TFP bearing. The force-displacement relationship in a TFP depends on the bearing displacement and the engaged sliding surfaces. Sliding regimes I through V are identified in Figure A.7. Fenz and Constantinou (2008) present a detailed

discussion of the force-displacement relationships of a TFP bearing in different *sliding* regimes. The relationships are characterized by the radii of curvature of the sliding surfaces and the coefficients of friction at the four sliding surfaces but detailed information is not reproduced here. The radii of curvature of the surfaces are known geometric quantities (see Figure A.6b). The coefficients of friction of the four surfaces and their velocity dependence (see equation A.1) were determined from the characterization tests.

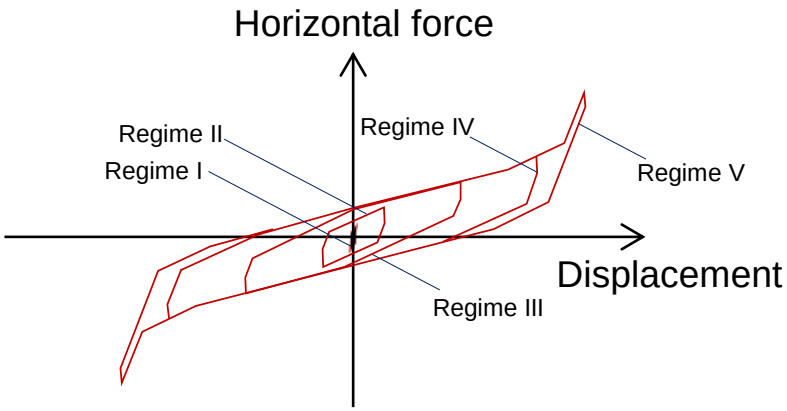

Figure A.7. Idealized force-displacement behavior of a TFP bearing, horizontal direction

A.4 Test set-up for characterization of horizontal force-displacement behavior

The single bearing testing machine (SBTM) at the University at Buffalo was used to test the bearings. The machine comprises a loading beam, a horizontal actuator, two vertical actuators, a load cell, and supporting frame structures, as shown in Figure A.8 and Figure A.9. The horizontal and vertical actuators transmit horizontal and axial forces or displacements, respectively, to the bearing via the loading beam. For the tests described herein, the vertical actuators were run under force control to accommodate changes in the bearing height while maintaining a predefined axial load on the bearings. The axial load recorded by the load cell beneath the bearing was used to control the vertical actuators. The horizontal actuator was run in displacement control to impose a predefined displacement history.

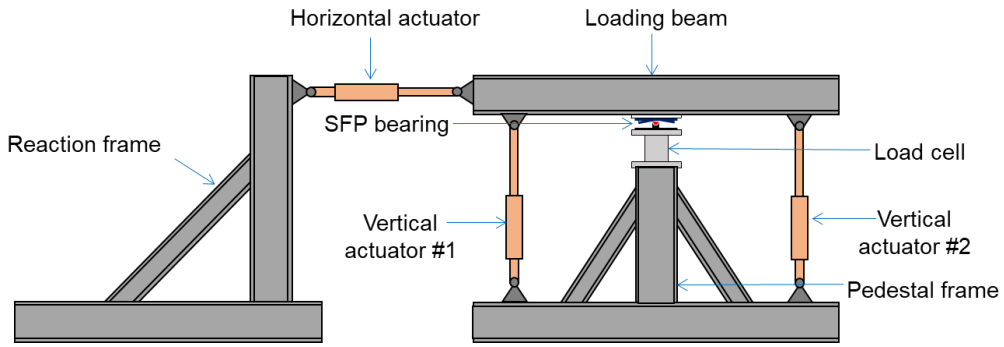

Figure A.8. Schematic of the SBTM at the University at Buffalo, SFP bearings

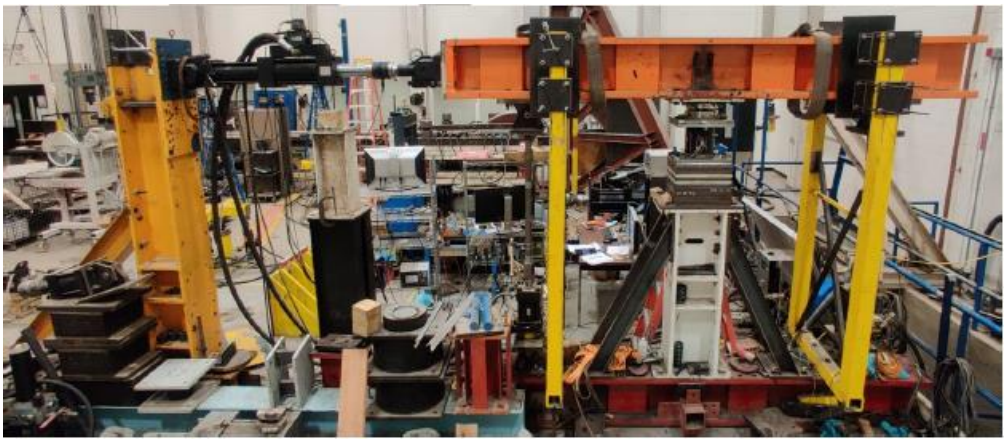

Figure A.9. SBTM at the University at Buffalo

Ten channels were used to record data in the tests. Each of the three actuators has an inline uniaxial load cell and an internal or an external displacement transducer to measure axial force and displacement, respectively. The shear force and axial force imposed on the bearing were recorded using the load cell. The acceleration of the loading beam and the command horizontal displacement (used as command for the horizontal actuator) were also recorded.

A.5 Test program and results for horizontal force-displacement behavior of SFP bearings

The goal of the characterization tests was to determine the coefficient of friction (μ_{max} and μ_{min}) and its velocity dependence for each SFP bearing. A constant value of axial load (20 kN or 4.5 kips) was used throughout the bearing characterization test program. This value is approximately equal to the axial load per bearing in the earthquake-simulator tests described in this report.

Table A.1 describes the displacement histories used for testing the bearings. Tests S1 and S4 utilized low velocity triangular displacement histories (see Figure A.10) with different maximum displacements. These tests provide hysteresis loops with clearly defined transition points. Tests S2, S3, S5, and S6 utilized a

displacement history first proposed by Constantinou *et al.* (2007) The profile of the displacement history is presented in Figure A.11. The displacement history (termed *cosine* in this section) begins with an idle time in which data is acquired to establish the breakaway friction force. A build-up time of 60 to 180 seconds follows, in which the displacement amplitude, u_o, is reached at a very low sliding velocity (less than 0.13 cm/sec). During this part of the imposed motion, $\mu_{\min}$ can be measured under truly quasi-static conditions. An idle time of 10 s is then imposed to allow the temperature at the sliding interface to stabilize. The idle time is followed by 3.25 cycles of harmonic displacement, as shown in Figure A.11, which enables calculation of the maximum coefficient of friction ($\mu_{\max}$). The maximum coefficient of friction ($\mu_{\max}$) is attained in the first cycle of displacement, after which the coefficient of friction reduces due to heating. The reduced value of friction in the third cycle can be used to characterize heating effects in the bearings. Tests S2 and S5 have nearly equal peak velocities (4.8 cm/s and 5.3 cm/s) and tests S3 and S6 have the same peak velocity (31.9 cm/sec).

Figure A.12 presents the normalized force-displacement loop for test S2 of SFP2 and the different friction values computed per Constantinou *et al.* (2007) to illustrate the procedure used to determine the coefficients of friction. The minimum coefficient of friction ($\mu_{\min}$) occurs immediately after the initiation of sliding (when the sliding velocity is close to zero) as identified in Figure A.12. The maximum value of the coefficient of friction ($\mu_{\max} = \mu_{1st\_cycle}$) occurs in the first cycle of loading, at the time instant when the highest velocity is first attained. In the subsequent cycles, the coefficient of friction reduces due to heating of the sliding surface, characterized herein as the value of friction in the third cycle (μ_{3rd_cycle}).

Table A.1. Test program for the bearings, axial load = 20 kN (nominal axial pressure = 17.6 MPa)

Test	Signal	Frequency (Hz)	Build-up time (sec)	Max. displacement (cm)	Max. velocity (cm/s)
S1	Triangular	-	-	2.54	0.13
S2	Cosine	0.3	60	2.54	4.8
S3	Cosine	2.0	60	2.54	31.9
S4	Triangular	-	-	8.4	0.13
S5	Cosine	0.1	180	8.4	5.3
S6	Cosine	0.6	180	8.4	31.9

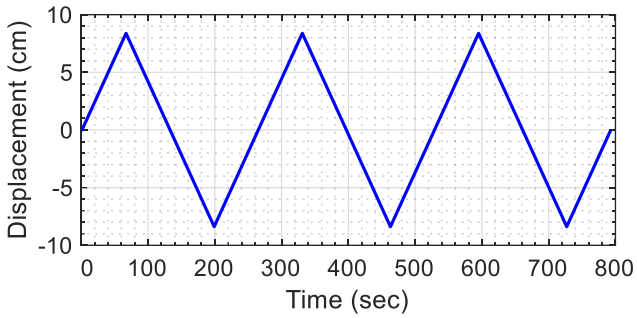

Figure A.10. Triangular displacement history, test S4

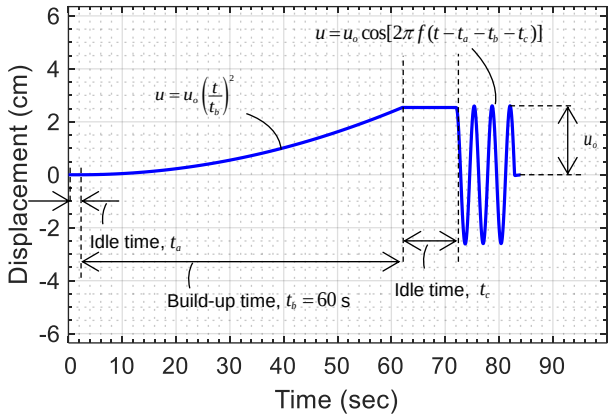

Figure A.11. Displacement history for test S2, u is displacement and f is frequency

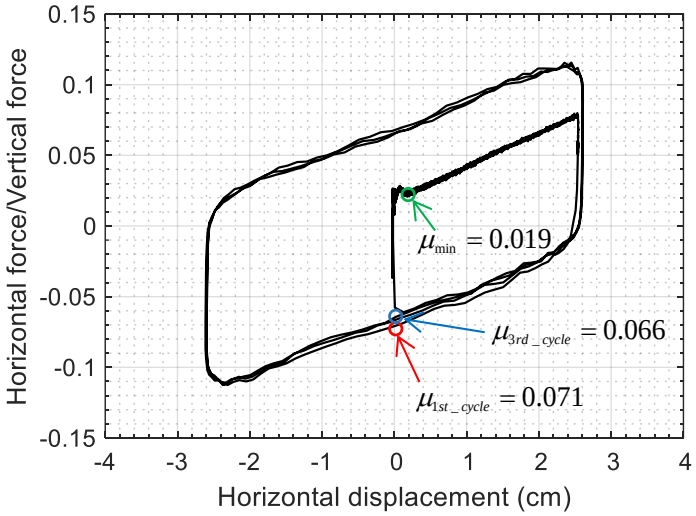

Figure A.12. Determining friction properties for SFP2 bearing, test S2

The velocity dependence of the friction coefficient is entirely characterized by $\mu_{\max}$, $\mu_{\min}$, and the rate parameter a in equation (A-1) The coefficients of friction, $\mu_{\max}$ and $\mu_{\min}$, are determined from tests S2, S3, S5, and S6 using the procedure described above. To evaluate the parameter a for a bearing, a dataset comprising four pairs of velocity and friction is used. A curve per equation (A-1) is fit to the dataset to obtain a. The four pairs are:

1) velocity is zero, friction coefficient is equal to the average of $\mu_{\min}$ from tests S2, S3, S5, and S6
2) velocity is 0.13 cm/s (tests S1and S4), friction coefficient is equal to the average of μ determined from tests S1 and S4
3) velocity is 5 cm/s (average of velocities in tests S2 and S5), friction coefficient is equal to the average of μ_{Ist_cycle} from tests S2 and S5
4) velocity is 31.9 cm/s (tests S3 and S6), friction coefficient is equal to the average of μ_{Ist_cycle} from tests S3 and S6

Table A.2 presents the minimum (slow), first cycle, and third cycle values of the coefficient of friction, determined from the test data, for the four SFP bearings. The coefficients of friction increase with sliding velocity and reduce with heating of the sliding surface, which is consistent with the behavior of a PTFE-type composite and polished stainless-steel interface (see Constantinou *et al.* (2007)). The variability in the estimated parameters for the four bearings here is typical for friction pendulum bearings at both model and prototype scales (e.g., see Sarlis *et al.* (2013) and McVitty and Constantinou (2015)).

Normalized force-displacement loops for all tests of the four bearings are presented in Figure A.13 through Figure A.16. The force-displacement behavior of the bearings for the high displacement, high velocity test S6 is erratic at high displacements because the axial load used in the tests is low (= 20 kN), which makes the control of the vertical actuators at high horizontal velocities and displacements challenging: the axial load reduces to near zero at multiple instants during the test. Similar outcomes are observed for the high horizontal velocity Test S3. Test S6 was repeated for SFP4 at a higher axial load of 62.3 kN (nominal axial pressure = 55 MPa). The resulting force-displacement loop is shown in Figure A.17. From the figure, it is evident the behavior of the bearing is stable at the higher axial load.

Table A.2. Coefficients of friction (%) determined from tests, SFP bearings, axial load = 20 kN (nominal axial pressure = 17.6 MPa)

	Test	S1	S2	S3	S4	S5	S6
	Displacement (cm)	2.54	2.54	2.54	8.4	8.4	8.4
	Velocity (cm/sec)	0.13	4.8	31.9	0.13	5.3	31.9
SF1	Slow	-	3.7	3.4	-	3.1	4.5
	1st cycle	4.9	10.5	12	5.2	10.5	13
	3rd cycle	-	9.8	10.5	-	10.5	10
SF2	Slow	-	1.9	2.5	-	2.5	2.3
	1st cycle	2.7	7.1	7.1	3.9	7.2	7.9
	3rd cycle	-	6.6	6	-	7.2	6.9
SF3	Slow	-	2.4	2.7	-	2.8	2.6
	1st cycle	3.3	8.2	9.2	4.7	8.9	11.8
	3rd cycle	-	8.2	7.8	-	8.9	8.7
SF4	Slow	-	1.8	2.5	-	2.8	2.5
	1st cycle	2.3	7.9	8.7	4.1	8.8	11.5
	3rd cycle	-	7.9	7.5	-	8.8	8.2

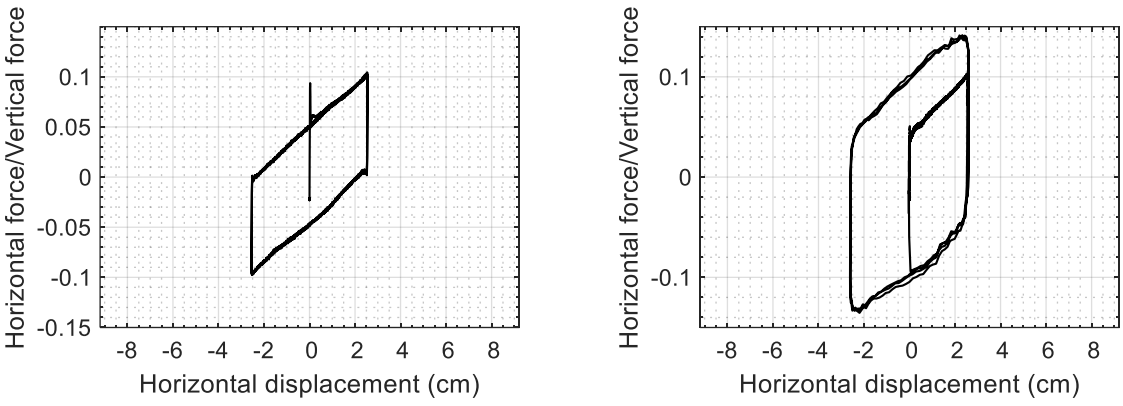

a. test S1

b. test S2

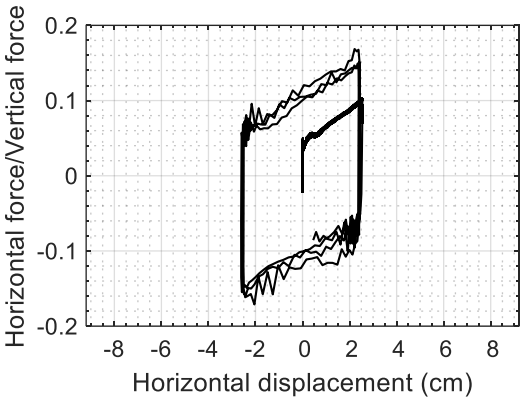

c. test S3

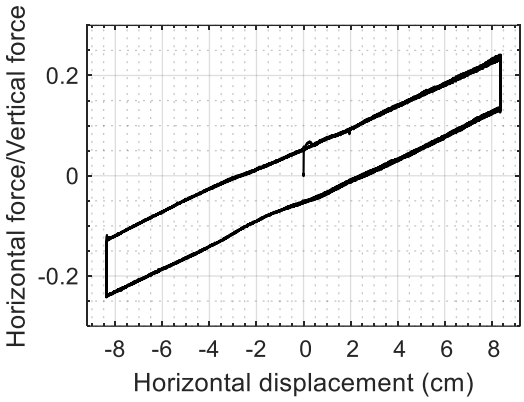

d. test S4

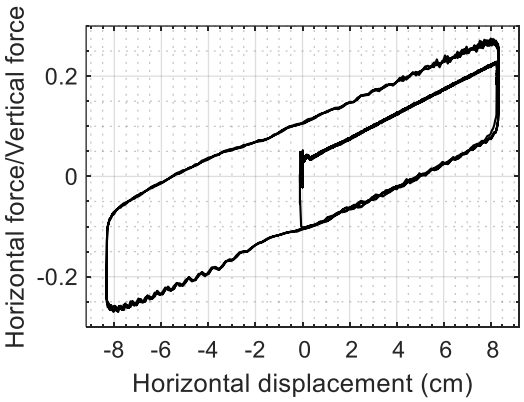

e. test S5

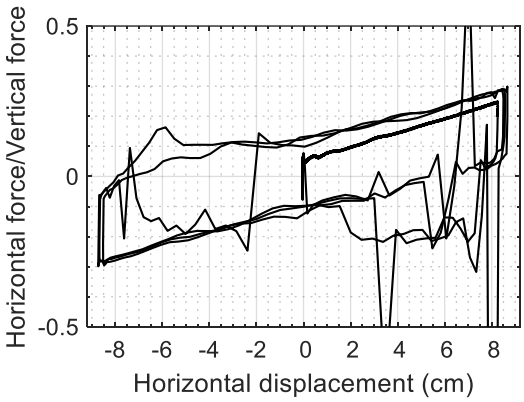

f. test S6

Figure A.13. Normalized force-displacement loops for SFP1, axial load = 20 kN, nominal axial pressure = 17.6 MPa

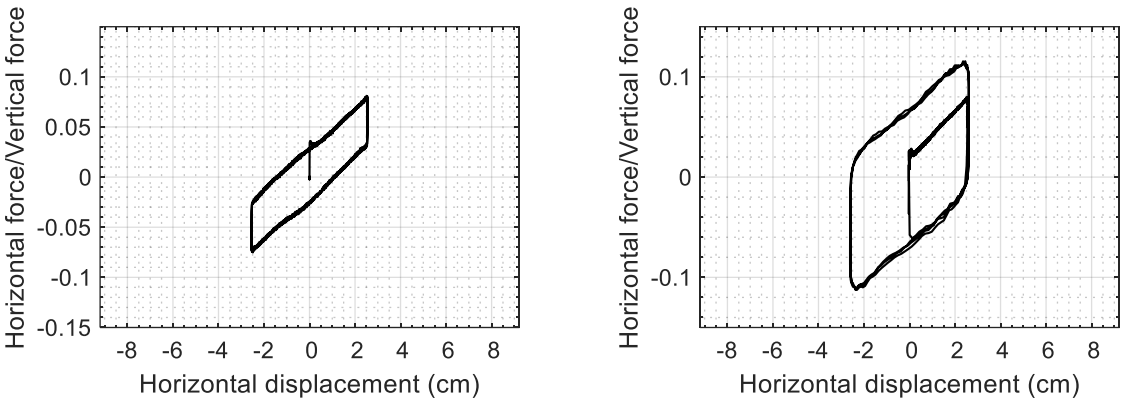

a. test S1

b. test S2

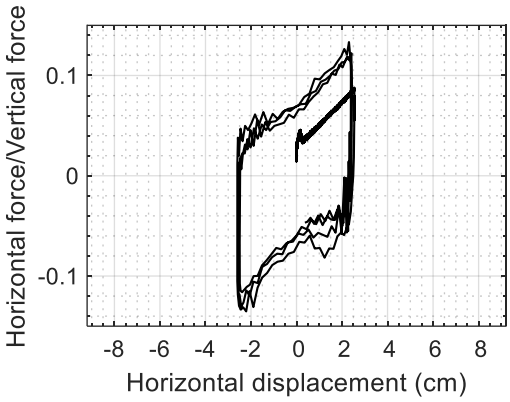

c. test S3

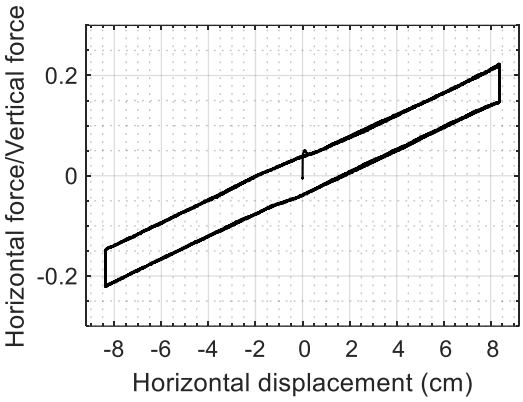

d. test S4

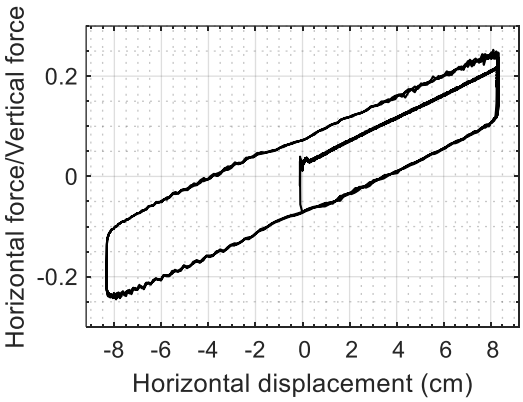

e. test S5

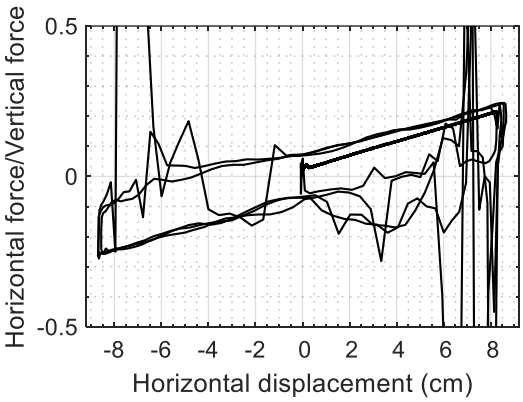

f. test S6

Figure A.14. Normalized force-displacement loops for SFP2, axial load = 20 kN, nominal axial pressure = 17.6 MPa

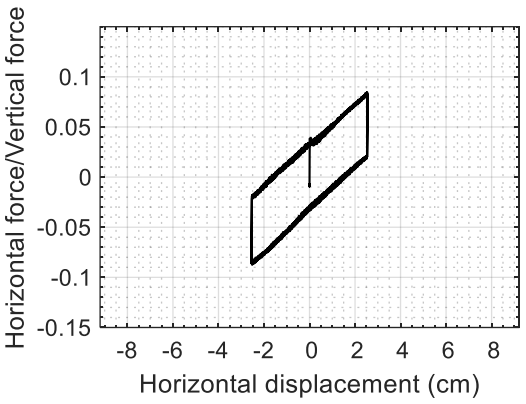

a. test S1

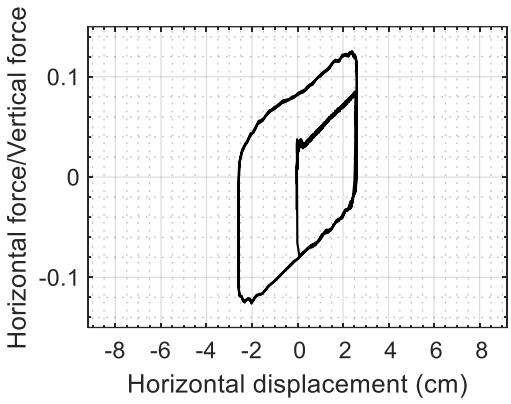

b. test S2

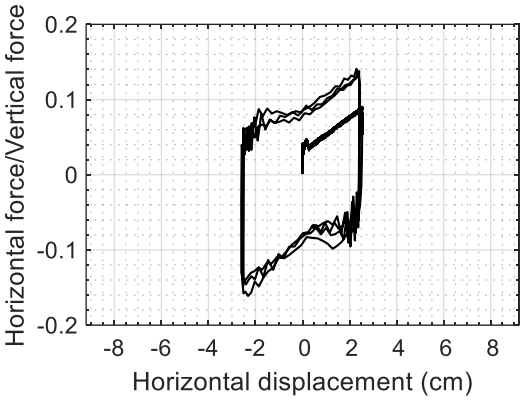

c. test S3

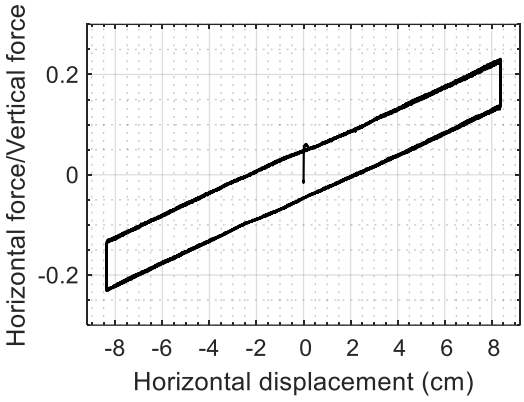

d. test S4

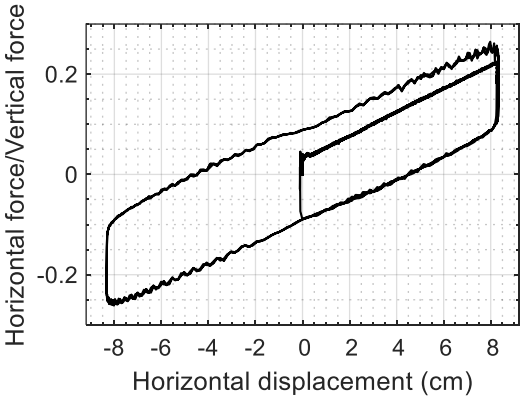

e. test S5

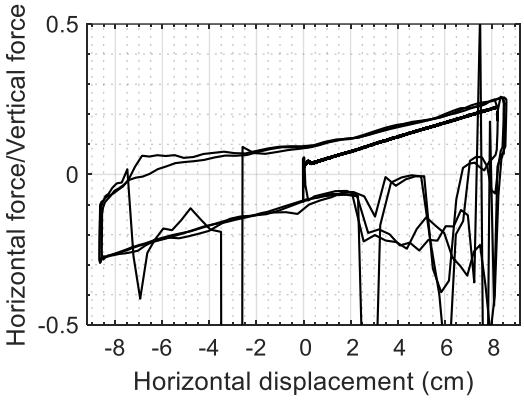

f. test S6

Figure A.15. Normalized force-displacement loops for SFP3, axial load = 20 kN, nominal axial pressure = 17.6 MPa

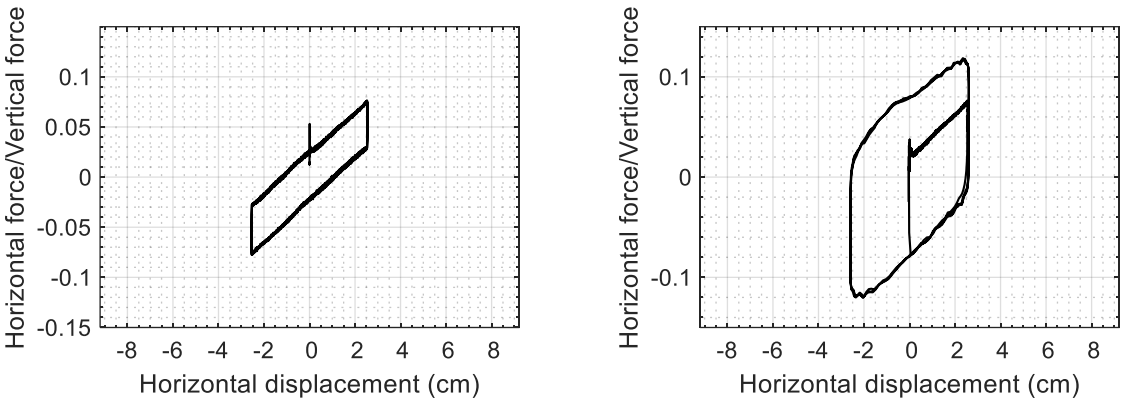

a. test S1

b. test S2

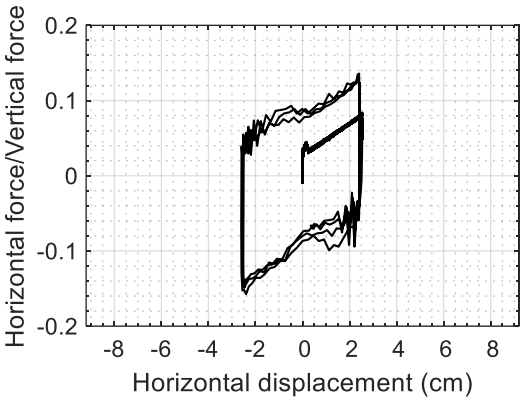

c. test S3

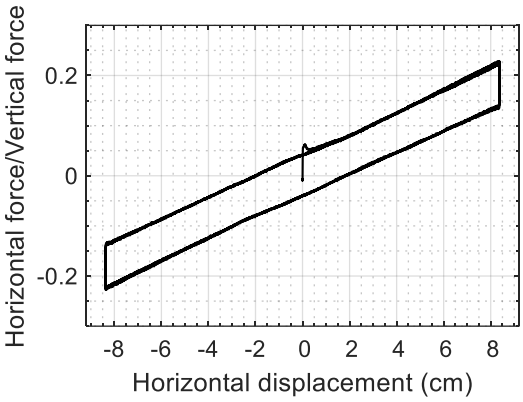

d. test S4

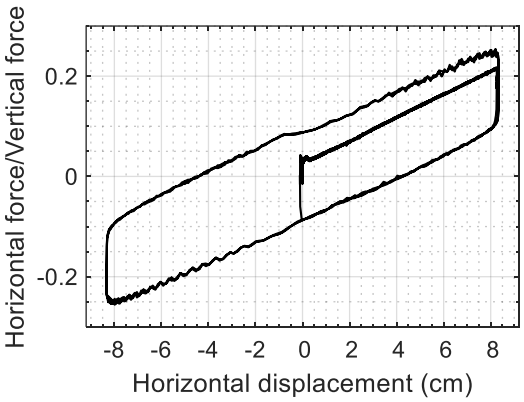

e. test S5

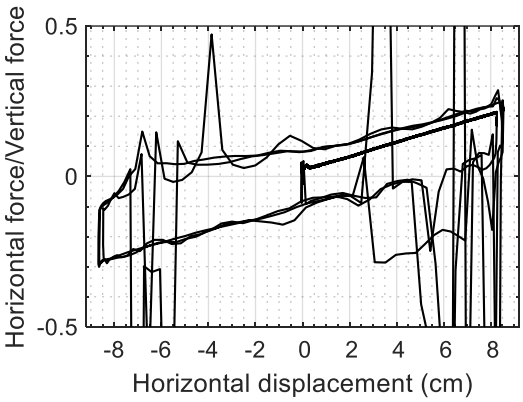

f. test S6

Figure A.16. Normalized force-displacement loops for SFP4, axial load = 20 kN, nominal axial pressure = 17.6 MPa

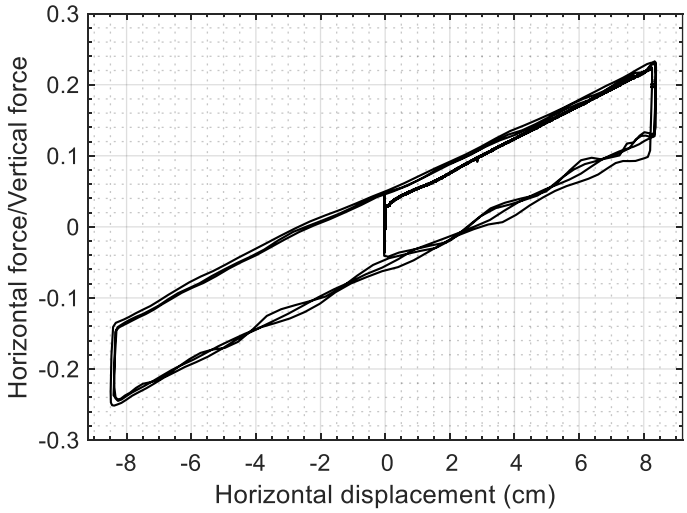

Figure A.17. Normalized force-displacement loop for SFP4, test S6, axial load = 62.3 kN, nominal axial pressure = 55 MPa

Table A.3 presents friction coefficients for the four bearings at four velocities (evaluated as described above). Figure A.18 presents best-fit curves per equation (A-1) plotted to determine the rate parameter. An average rate parameter of 0.44 s/cm was obtained for the four SFP bearings.

Table A.3. Average coefficients of friction (%) at different velocities, axial load = 20 kN (nominal axial pressure = 17.6 MPa)

	Velocity (cm/sec)			
	0	0.13	5.0	31.9
SFP1	3.7	5.1	10.5	12.5
SFP2	2.3	3.3	7.2	7.5
SFP3	2.6	4.0	8.6	10.5
SFP4	2.4	3.2	8.4	10.1

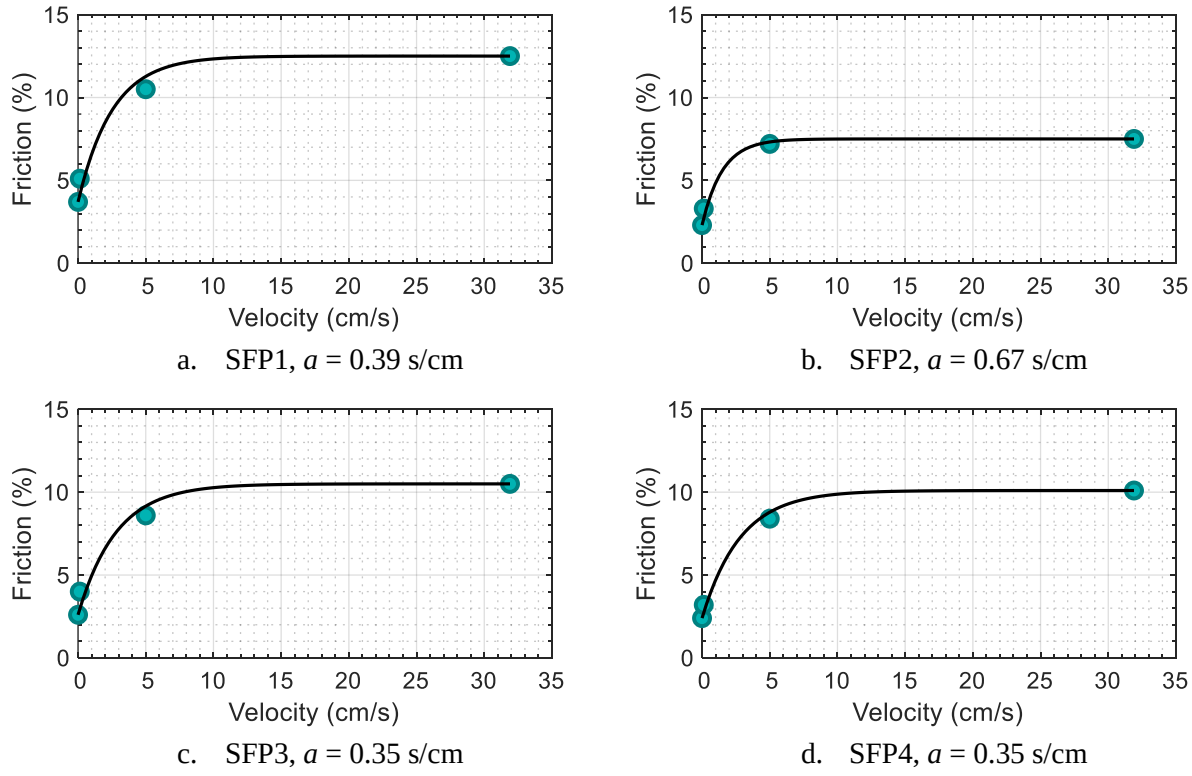

a. SFP1, a = 0.39 s/cm

b. SFP2, a = 0.67 s/cm

c. SFP3, a = 0.35 s/cm

d. SFP4, a = 0.35 s/cm

Figure A.18. Rate parameter a for the four bearings, average a = 0.44 s/cm

A.6 Test program and results for horizontal force-displacement behavior of TFP bearings

Table A.4 describes the displacement histories used for testing the TFP bearings. An axial load of 20 kN was used, like the SFP bearing tests. Test T1 utilized a triangular displacement history similar in profile to that shown in Figure A.10 and was a low velocity test (velocity = 0.13 cm/sec). Tests T2 and T3 utilized cosine displacements and involved intermediate (4.8 cm/sec) and high (31.9 cm/sec) velocities, respectively. The displacements in all three tests were large (> 8 cm). Such large displacement tests provide the data necessary to characterize the force-displacement behavior of a TFP bearing.

Table A.4. Test program for the bearings, axial load = 20 kN (nominal axial pressure, inner surfaces = 17.6 MPa, outer surfaces = 4.4 MPa)

Test	Signal	Frequency (Hz)	Build-up time (sec)	Max. displacement (cm)	Max. velocity (cm/sec)
T1	Triangular	-	-	8.4	0.13
T2	Cosine	0.06	180	12.7	4.8
T3	Cosine	0.4	180	12.7	31.9

Figure A.19 through Figure A.22 present the normalized force-displacement loops for the four bearings. The erratic force-displacement behavior of the bearings in the case of the high-velocity test (T3), visible in panel c of Figure A.19 through Figure A.22 is related to challenges with actuator control at high velocities and displacements, as explained in the previous section.

The coefficients of friction (μ_1 through μ_4) of the four sliding surfaces were determined per Section 3 of Lal *et al*. (2022) and are presented in Table A.5. The coefficients of friction were such that $\mu_1 = \mu_4 > \mu_2 = \mu_3$, which is typical for prototype TFP bearings.

The coefficient of friction of the outer surfaces determined from the low velocity tests T1 was assumed to be the minimum value of the coefficient. The maximum coefficient of friction of the outer surfaces was determined using data from the high velocity test T3. Data from test T2 was used to determine the rate parameter, as explained below. The minimum coefficient of friction for the two inner surfaces in a test was estimated as one-half of the reduction in the normalized horizontal force at the maximum displacement (where the velocity reverses sign) per Fenz and Constantinou (2008). The average of the minimum values of μ_2 (= μ_3) obtained from tests T1, T2, and T3 was considered as the minimum value of μ_2 (= μ_3) for a bearing. Achieving high sliding velocities on the inner surfaces (2 and 3) in tests is difficult. Thus, only the minimum value of μ_2 (= μ_3) (inner surface friction) was determined in tests. The maximum value of μ_2 (= μ_3) for a bearing was assumed to be equal to the product of the estimated minimum value and the ratio of the maximum and minimum values of μ_1 (= μ_4).

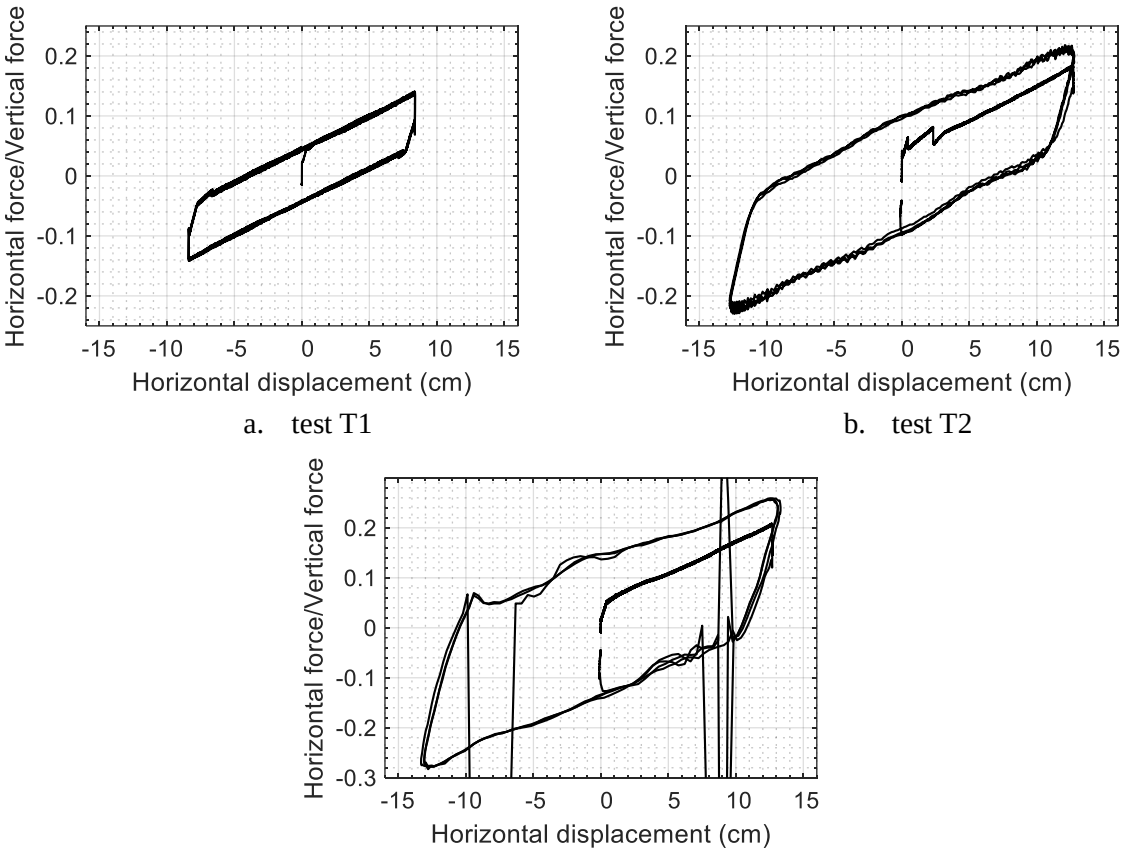

a. test T1

b. test T2

c. test T3

Figure A.19. Normalized force-displacement loops for TFP1, axial load = 20 kN (nominal axial pressure, inner surfaces = 17.6 MPa, outer surfaces = 4.4 MPa)

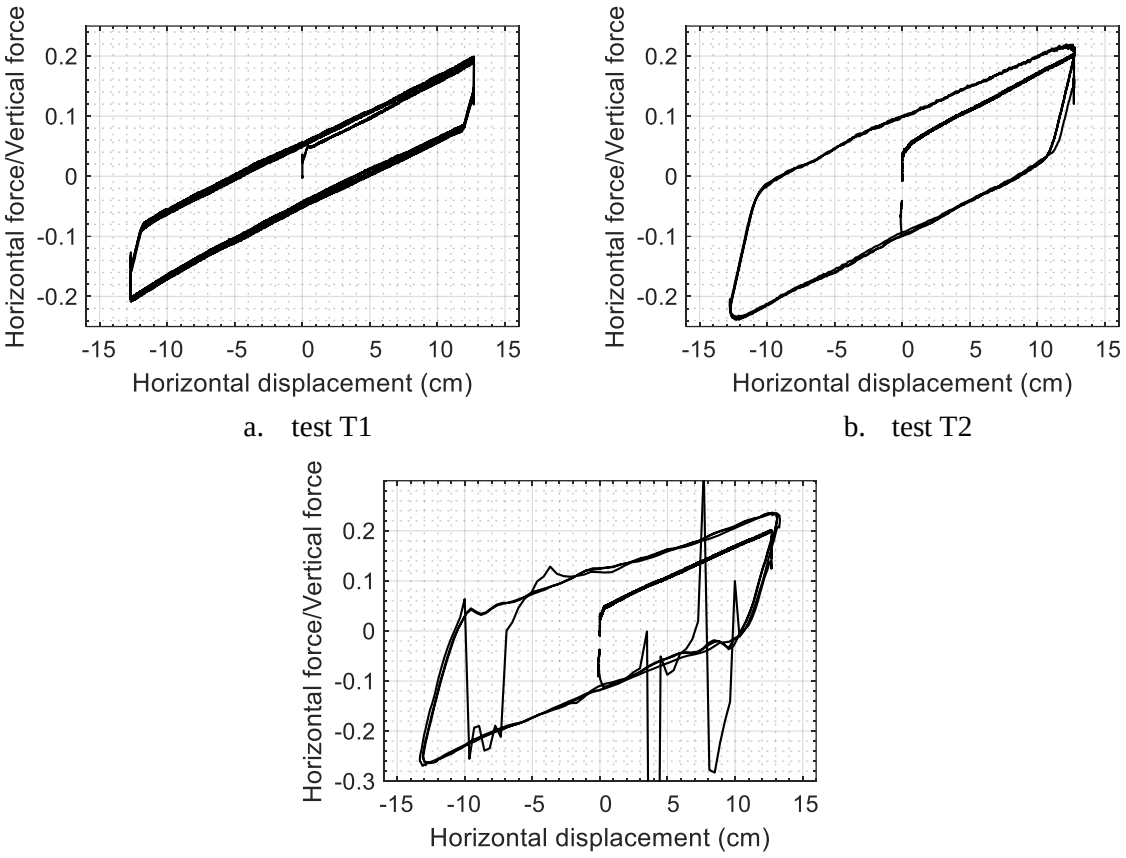

a. test T1

b. test T2

c. test T3

Figure A.20. Normalized force-displacement loops for TFP2, axial load = 20 kN, (nominal axial pressure, inner surfaces = 17.6 MPa, outer surfaces = 4.4 MPa)

.

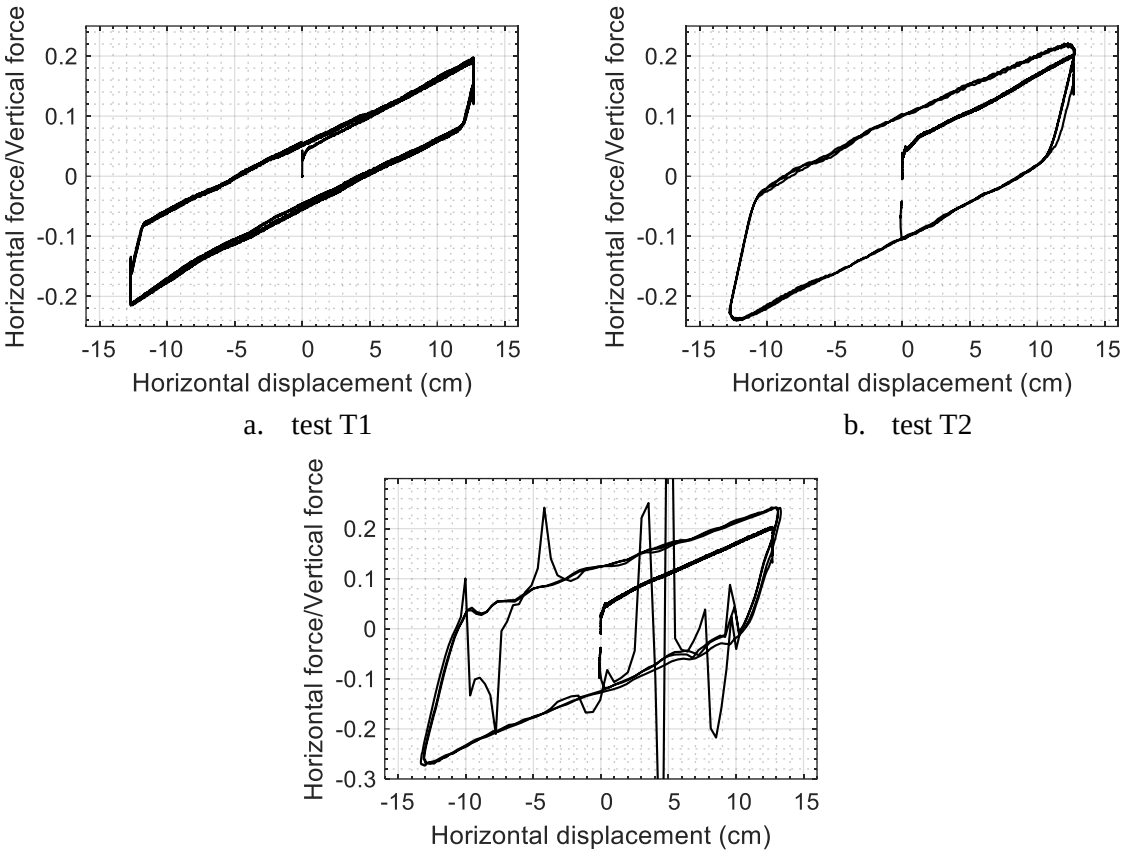

a. test T1

b. test T2

c. test T3

Figure A.21. Normalized force-displacement loops for TFP3, axial load = 20 kN, (nominal axial pressure, inner surfaces = 17.6 MPa, outer surfaces = 4.4 MPa)

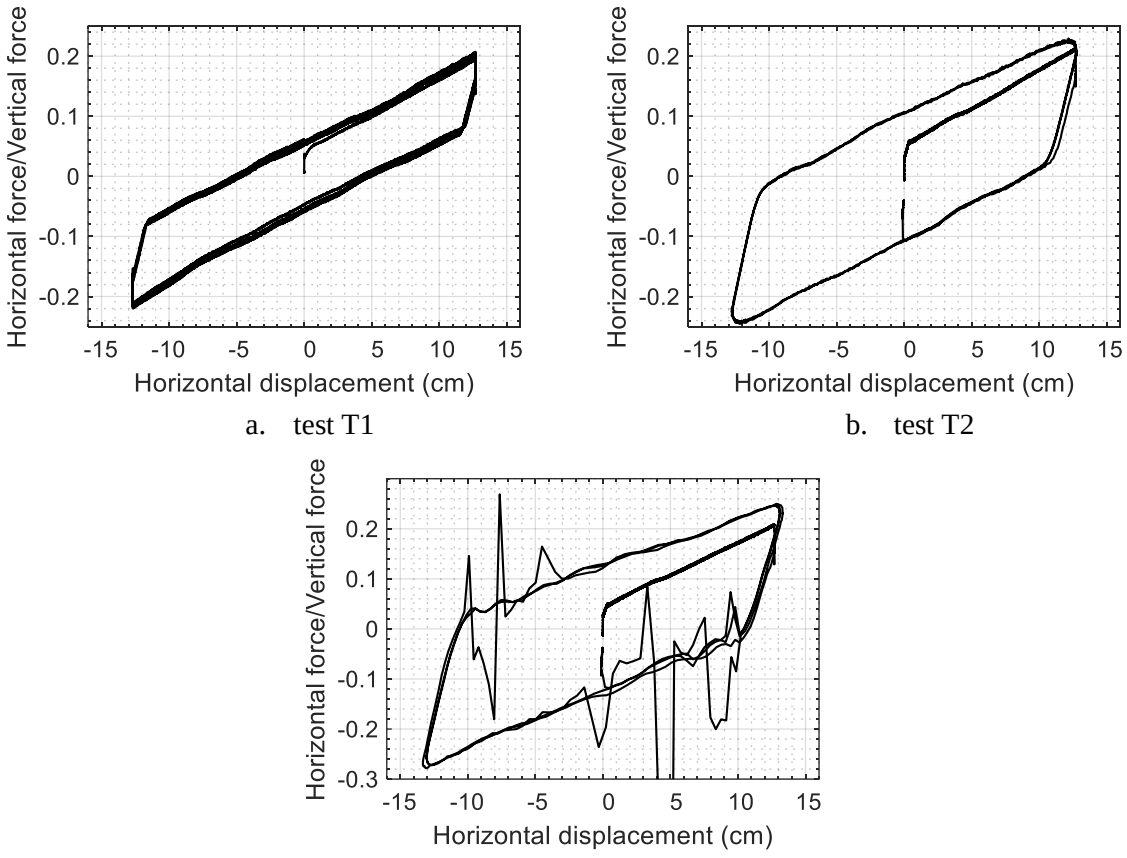

a. test T1

b. test T2

c. test T3

Figure A.22. Normalized force-displacement loops for TFP4, axial load = 20 kN, (nominal axial pressure, inner surfaces = 17.6 MPa, outer surfaces = 4.4 MPa)

.

Table A.5. Coefficients of friction (%) determined from tests, TFP bearings, axial load = 20 kN (nominal axial pressure, inner surfaces = 17.6 MPa, outer surfaces = 4.4 MPa)

	Test	T1	T2	T3	Minimum	Maximum
TFP1	$\mu_1 = \mu_4$	7.0	11.0	15.5	7.0	15.5
	$\mu_2 = \mu_3$	2.2	2.0	2.2	2.1	4.7
TFP2	$\mu_1 = \mu_4$	6.0	11.0	13.6	6.0	13.6
	$\mu_2 = \mu_3$	2.4	2.0	2.2	2.2	5.0
TFP3	$\mu_1 = \mu_4$	5.2	11.5	13.8	5.2	13.8
	$\mu_2 = \mu_3$	2.2	2.1	2.0	2.1	5.6
TFP4	$\mu_1 = \mu_4$	6.6	12.0	14.3	6.6	14.3
	$\mu_2 = \mu_3$	2.2	2.4	2.3	2.3	5.0

The velocity dependence of friction on the outer surfaces was determined using a procedure similar to that described in the previous section for SFP bearings. A data set comprising three pairs of test velocity and estimated friction was used and a curve per equation (A-1) was fit to the data to obtain a. The three pairs are:

1) velocity is 0.064 cm/s (= half the velocity in test T1; the maximum sliding velocity for each surface is one-half of the values presented in Table A.4 because the sliding motion is divided equally between the two surfaces), friction coefficient is equal to that determined from test T1

2) velocity is 2.4 cm/s (= half the velocity in test T2), friction coefficient is equal to that determined from test T2

3) velocity is 15.9 cm/s (= half the velocity in test T3), friction coefficient is equal to that determined from test T3

Table A.6 presents the velocity-friction pairs used to estimate the rate parameter for friction on the outer surfaces of the four bearings. Figure A.23 presents best-fit curves per equation (A-1) plotted to determine the rate parameter. An average rate parameter of 0.42 s/cm was obtained. (The rate parameter for the inner surfaces was assumed identical to that for the outer surfaces. The assumptions regarding maximum friction and rate parameter for the inner surfaces are not important because the behavior of a TFP bearing is primarily governed by sliding on the outer surfaces; see McVitty and Constantinou (2015) for details.)

Table A.6. Average coefficients of friction (%) at different velocities, TFP bearings, axial load = 20 kN (nominal axial pressure, inner surfaces = 17.6 MPa, outer surfaces = 4.4 MPa)

	Velocity (cm/sec)		
	0.064	2.4	15.9
TFP1	7.0	11.0	15.5
TFP2	6.0	11.0	13.6
TFP3	5.2	11.5	13.8
TFP4	6.6	12.0	14.3

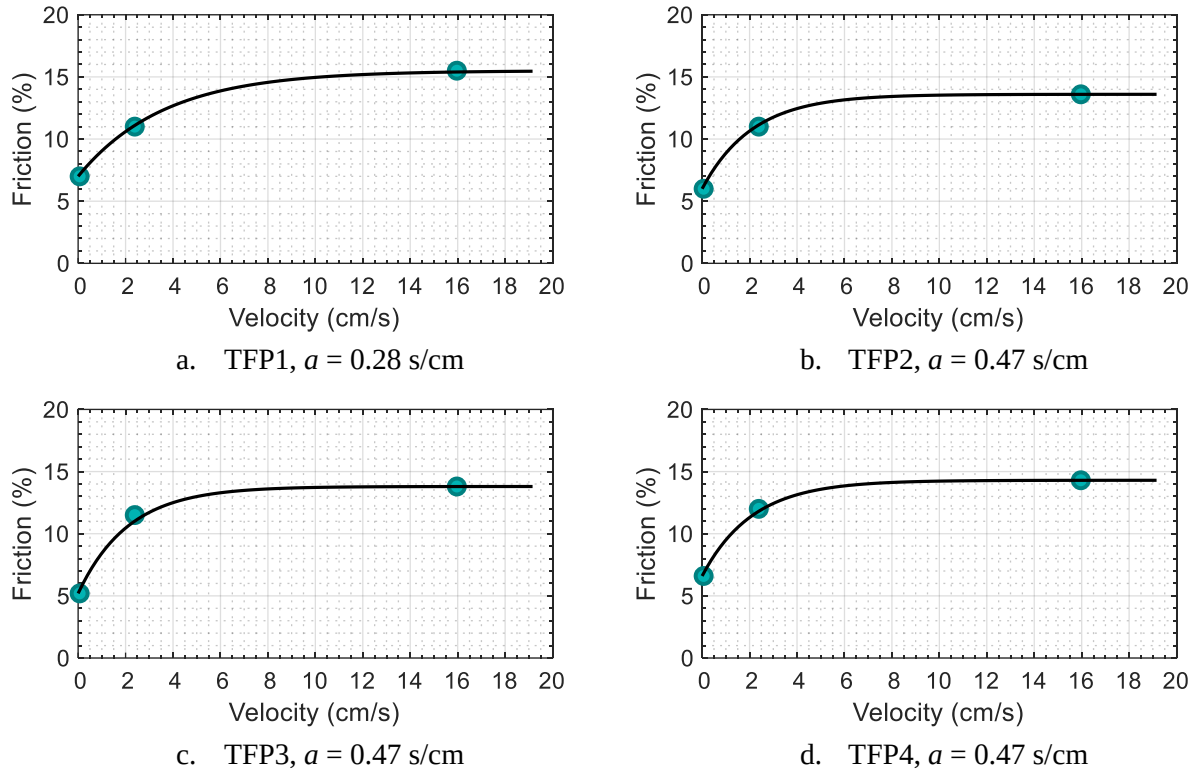

a. TFP1, a = 0.28 s/cm

b. TFP2, a = 0.47 s/cm

c. TFP3, a = 0.47 s/cm

d. TFP4, a = 0.47 s/cm

Figure A.23. Rate parameter a for the four bearings, average a = 0.42 s/cm

A.7 Characterization of behavior in the vertical direction

The representative force displacement behavior of an SFP or a TFP bearing under axial compressive (vertical) load is shown in Figure A.24. The axial stiffness is low at low axial loads. The behavior at a particular axial load is characterized by the slope of the load-displacement curve at that load. The goal of

the characterization tests described here was to estimate the axial stiffness of the eight bearings at an axial load of 20 kN.

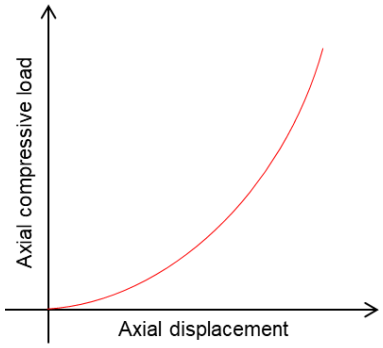

Figure A.24. Representative behavior of an SFP or a TFP isolator in compression

The vertical stiffness characterization tests were carried out using the MTS tension-compression machine, manufactured by MTS Systems Corporation. Figure A.25 shows the setup used for testing. Linear potentiometers at the four corners of a bearing were used to record the relative movement of the top and the bottom plates. The tension-compression machine has an inbuilt load and displacement sensor. Six channels of data were recorded. The average of the displacements recorded by the four linear potentiometers and the actuator's displacement transducer was used as the measure of the axial displacement in the bearing.

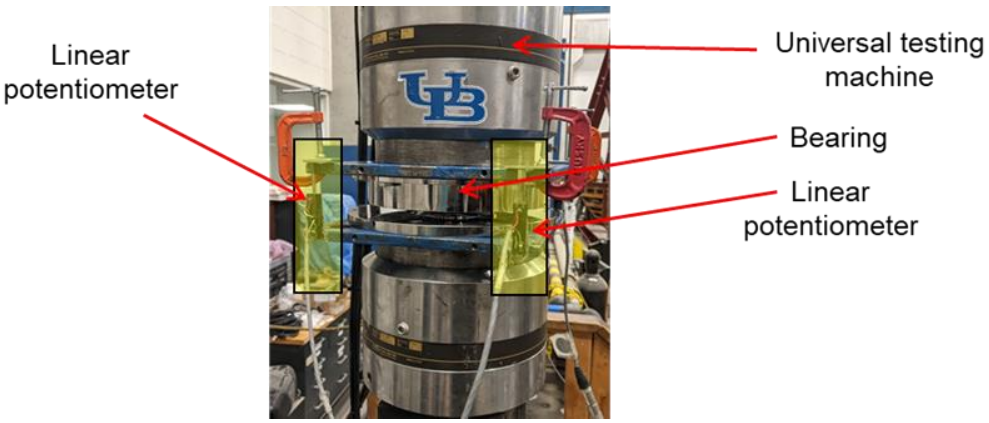

Figure A.25. Test setup used for vertical characterization tests

The loading history of Figure A.26 was used for testing. A pre-load of 5 kN was applied before the start of data acquisition, followed by a ramp up to a load of 20 kN (4.5 kips) in 10 s and 2.75 cycles of ±8.9 kN (2 kips) at 0.1 Hz.

Figure A.27 and Figure A.28 present axial load–axial displacement plots for the four SFP and the four TFP bearings, respectively. The estimated stiffness for each bearing is indicated on each plot. The average stiffness of the SFP bearings and the TFP bearings is 1.07×10^5 kN/m and 1.05×10^5 kN/m, respectively, at an axial load of 20 kN.

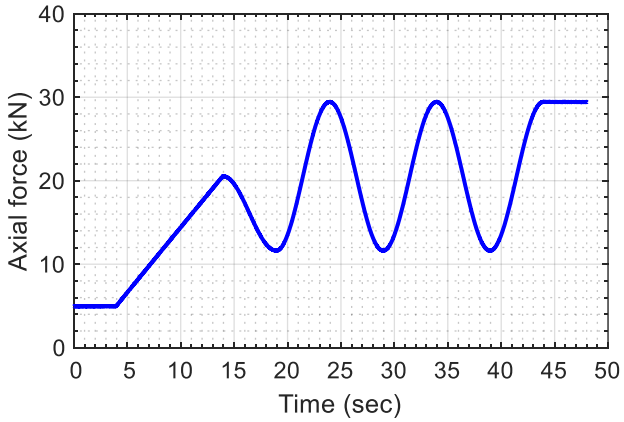

Figure A.26. Loading history used for characterizing vertical stiffness

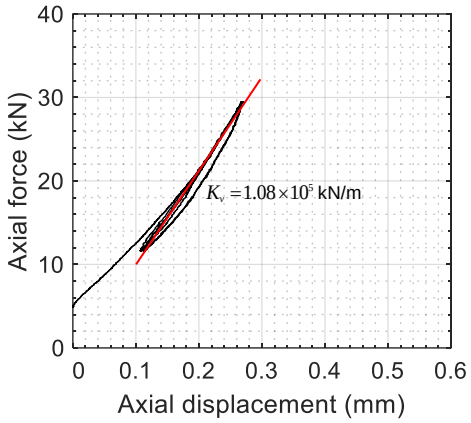

a. SFP1

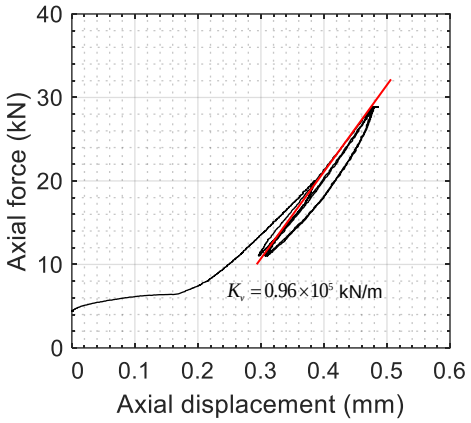

b. SFP2

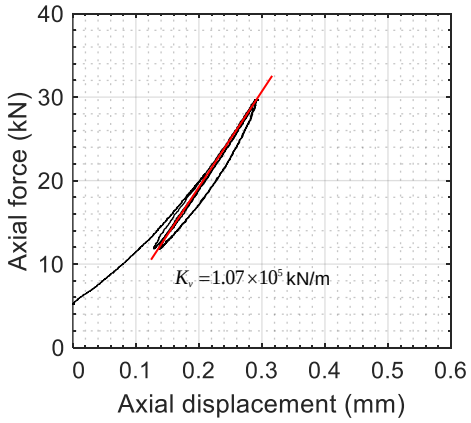

c. SFP3

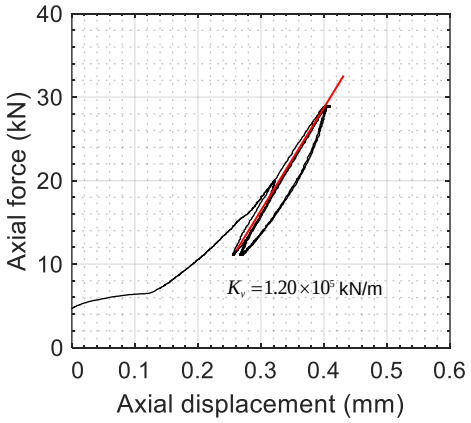

d. SFP4

Figure A.27. Axial load vs displacement plots for SFP bearings, K_v is axial stiffness

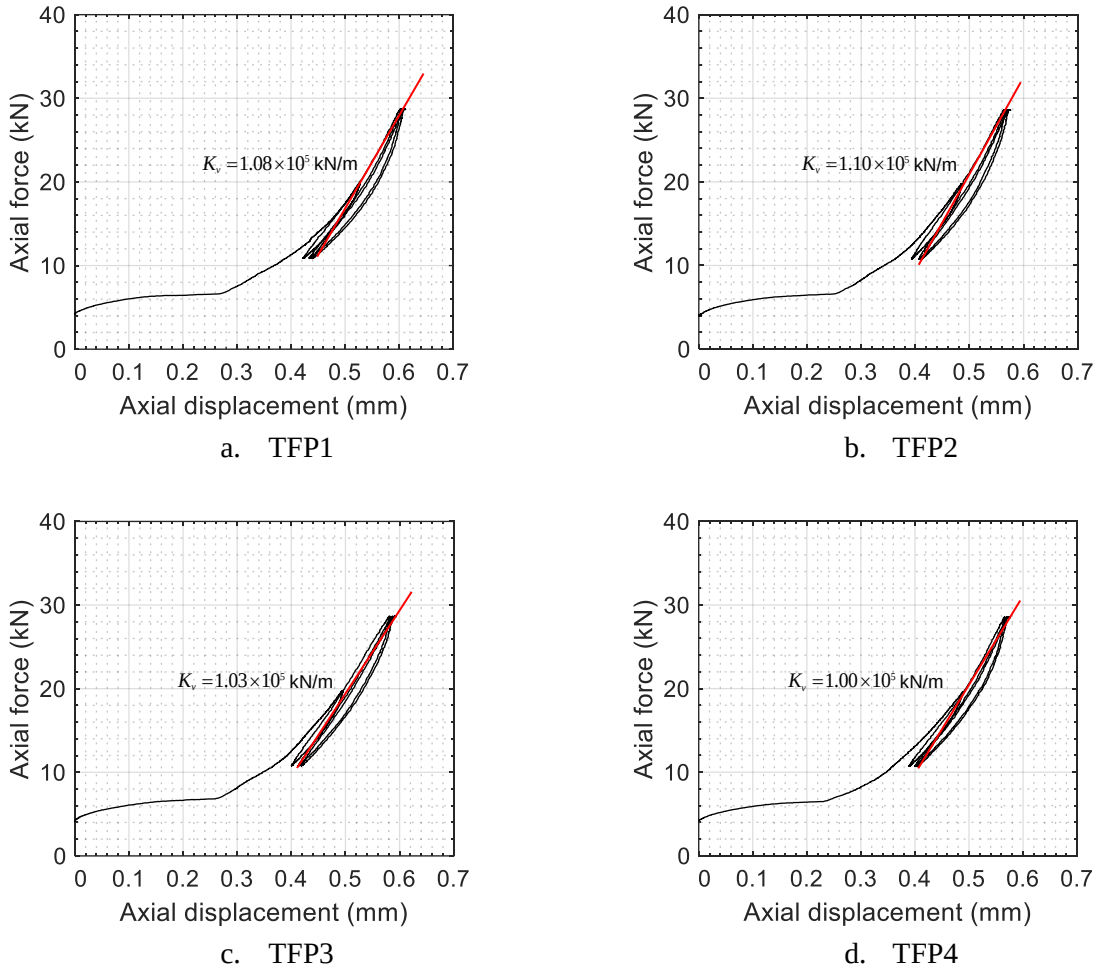

a. TFP1 b. TFP2

c. TFP3 d. TFP4

Figure A.28. Axial load vs displacement plots for TFP bearings, K_v is axial stiffness

The average stiffness of the SFP (TFP) bearings is approximately 3% of the axial stiffness of a cylindrical steel column with diameter equal to the slider diameter (= 3.8 cm) and height equal to that of the bearing (nested slider assembly) (=6.4 cm). The size of the sliders and the housing plate cavity (inner concave plates) in the SFP (TFP) bearings used here is small compared to bearings used in practice. Machining small-sized sliders, housing plate cavities, and inner concave plates to the tight tolerances required for achieving high axial stiffness at low axial loads is challenging. (Based on experiments, a reasonable axial stiffness for prototype sliders is 10% of column stiffness.)

A.8 Conclusions

The behavior of four SFP and four TFP bearings under horizontal and vertical loads was characterized. An axial load of 20 kN (4.5 kips) was considered for the characterization tests. Behavior under horizontal loads was characterized by estimating slow and fast coefficients of friction at the different surfaces. The velocity dependence of the coefficient of friction for each bearing was characterized by a rate parameter. The behavior under vertical load was established by estimating the vertical stiffness of each bearing at an axial load of 20 kN. Table A.7 and Table A.8 summarizes results for the SFP and TFP bearings, respectively.

Table A.7. Summary of characterization tests for SFP bearings, axial load = 20 kN

Bearing	Friction coefficient, slow (%)	Friction coefficient, fast (%)	Rate parameter (s/cm)	Axial stiffness ($\times 10^5$ kN/m)
SFP1	3.7	12.5	0.39	1.08
SFP2	2.3	7.5	0.67	0.96
SFP3	2.6	10.5	0.35	1.07
SFP4	2.4	10.1	0.35	1.20
Average	2.8	10.2	0.44	1.07

Table A.8. Summary of characterization tests for TFP bearings, axial load = 20 kN

Bearing	Friction coefficients				Rate parameter (s/cm)	Axial stiffness ($\times 10^5$ kN/m)
	$\mu_2 = \mu_3$ (%)		$\mu_1 = \mu_4$ (%)			
	Minimum (slow)	Maximum (fast)	Minimum (slow)	Maximum (fast)		
TFP1	2.1	4.7	7.0	15.5	0.28	1.08
TFP2	2.2	5.0	6.0	13.6	0.47	1.10
TFP3	2.1	5.6	5.2	13.8	0.47	1.03
TFP4	2.3	5.0	6.6	14.3	0.47	1.00
Average	2.2	5.1	6.2	14.3	0.42	1.05

A.9 References

Constantinou, M. C., Whittaker, A. S., Kalpakidis, Y., Fenz, D. M., and Warn, G. P. (2007). "Performance of seismic isolation hardware under service and seismic loading." *Report MCEER-07-0012*, The State University of New York at Buffalo, Buffalo, NY.

Fenz, D. M., and Constantinou, M. C. (2008). "Mechanical behavior of multi-spherical sliding bearings." *Report MCEER-08-0007*, The State University of New York at Buffalo, Buffalo, NY.

Lal, K. M. (in progress). "Standardization of advanced reactors: role of seismic isolation." Dissertation, presented to University at Buffalo, Buffalo, NY, in partial fulfilment of the requirements for the degree of Doctor of Philosophy.

McVitty, W. J., and Constantinou, M. C. (2015). "Property modification factors for seismic isolators: design guidance for buildings." *Report MCEER 15-0005*, The State University of New York at Buffalo, Buffalo, NY.

Sarlis, A. A., Constantinou, M. C., and Reinhorn, A. M. (2013). "Shake table testing of triple friction pendulum isolators under extreme conditions." *Report MCEER-13-0011*, The State University of New York at Buffalo, Buffalo, NY.

MCEER Technical Reports

MCEER publishes technical reports on a variety of subjects written by authors funded through MCEER. These reports can be downloaded from the MCEER website at http://www.buffalo.edu/mceer. They can also be requested through NTIS, P.O. Box 1425, Springfield, Virginia 22151. NTIS accession numbers are shown in parenthesis, if available.

NCEER-87-0001 "First-Year Program in Research, Education and Technology Transfer," 3/5/87, (PB88-134275, A04, MF-A01).

NCEER-87-0002 "Experimental Evaluation of Instantaneous Optimal Algorithms for Structural Control," by R.C. Lin, T.T. Soong and A.M. Reinhorn, 4/20/87, (PB88-134341, A04, MF-A01).

NCEER-87-0003 "Experimentation Using the Earthquake Simulation Facilities at University at Buffalo," by A.M. Reinhorn and R.L. Ketter, not available.

NCEER-87-0004 "The System Characteristics and Performance of a Shaking Table," by J.S. Hwang, K.C. Chang and G.C. Lee, 6/1/87, (PB88-134259, A03, MF-A01). This report is available only through NTIS (see address given above).

NCEER-87-0005 "A Finite Element Formulation for Nonlinear Viscoplastic Material Using a Q Model," by O. Gyebi and G. Dasgupta, 11/2/87, (PB88-213764, A08, MF-A01).

NCEER-87-0006 "Symbolic Manipulation Program (SMP) - Algebraic Codes for Two and Three Dimensional Finite Element Formulations," by X. Lee and G. Dasgupta, 11/9/87, (PB88-218522, A05, MF-A01).

NCEER-87-0007 "Instantaneous Optimal Control Laws for Tall Buildings Under Seismic Excitations," by J.N. Yang, A. Akbarpour and P. Ghaemmaghami, 6/10/87, (PB88-134333, A06, MF-A01). This report is only available through NTIS (see address given above).

NCEER-87-0008 "IDARC: Inelastic Damage Analysis of Reinforced Concrete Frame - Shear-Wall Structures," by Y.J. Park, A.M. Reinhorn and S.K. Kunnath, 7/20/87, (PB88-134325, A09, MF-A01). This report is only available through NTIS (see address given above).

NCEER-87-0009 "Liquefaction Potential for New York State: A Preliminary Report on Sites in Manhattan and Buffalo," by M. Budhu, V. Vijayakumar, R.F. Giese and L. Baumgras, 8/31/87, (PB88-163704, A03, MF-A01). This report is available only through NTIS (see address given above).

NCEER-87-0010 "Vertical and Torsional Vibration of Foundations in Inhomogeneous Media," by A.S. Veletsos and K.W. Dotson, 6/1/87, (PB88-134291, A03, MF-A01). This report is only available through NTIS (see address given above).

NCEER-87-0011 "Seismic Probabilistic Risk Assessment and Seismic Margins Studies for Nuclear Power Plants," by Howard H.M. Hwang, 6/15/87, (PB88-134267, A03, MF-A01). This report is only available through NTIS (see address given above).

NCEER-87-0012 "Parametric Studies of Frequency Response of Secondary Systems Under Ground-Acceleration Excitations," by Y. Yong and Y.K. Lin, 6/10/87, (PB88-134309, A03, MF-A01). This report is only available through NTIS (see address given above).

NCEER-87-0013 "Frequency Response of Secondary Systems Under Seismic Excitation," by J.A. HoLung, J. Cai and Y.K. Lin, 7/31/87, (PB88-134317, A05, MF-A01). This report is only available through NTIS (see address given above).

NCEER-87-0014 "Modelling Earthquake Ground Motions in Seismically Active Regions Using Parametric Time Series Methods," by G.W. Ellis and A.S. Cakmak, 8/25/87, (PB88-134283, A08, MF-A01). This report is only available through NTIS (see address given above).

NCEER-87-0015 "Detection and Assessment of Seismic Structural Damage," by E. DiPasquale and A.S. Cakmak, 8/25/87, (PB88-163712, A05, MF-A01). This report is only available through NTIS (see address given above).

NCEER-87-0016 "Pipeline Experiment at Parkfield, California," by J. Isenberg and E. Richardson, 9/15/87, (PB88-163720, A03, MF-A01). This report is available only through NTIS (see address given above).

NCEER-87-0017 "Digital Simulation of Seismic Ground Motion," by M. Shinozuka, G. Deodatis and T. Harada, 8/31/87, (PB88-155197, A04, MF-A01). This report is available only through NTIS (see address given above).

NCEER-87-0018 "Practical Considerations for Structural Control: System Uncertainty, System Time Delay and Truncation of Small Control Forces," J.N. Yang and A. Akbarpour, 8/10/87, (PB88-163738, A08, MF-A01). This report is only available through NTIS (see address given above).

NCEER-87-0019 "Modal Analysis of Nonclassically Damped Structural Systems Using Canonical Transformation," by J.N. Yang, S. Sarkani and F.X. Long, 9/27/87, (PB88-187851, A04, MF-A01).

NCEER-87-0020 "A Nonstationary Solution in Random Vibration Theory," by J.R. Red-Horse and P.D. Spanos, 11/3/87, (PB88-163746, A03, MF-A01).

NCEER-87-0021 "Horizontal Impedances for Radially Inhomogeneous Viscoelastic Soil Layers," by A.S. Veletsos and K.W. Dotson, 10/15/87, (PB88-150859, A04, MF-A01).

NCEER-87-0022 "Seismic Damage Assessment of Reinforced Concrete Members," by Y.S. Chung, C. Meyer and M. Shinozuka, 10/9/87, (PB88-150867, A05, MF-A01). This report is available only through NTIS (see address given above).

NCEER-87-0023 "Active Structural Control in Civil Engineering," by T.T. Soong, 11/11/87, (PB88-187778, A03, MF-A01).

NCEER-87-0024 "Vertical and Torsional Impedances for Radially Inhomogeneous Viscoelastic Soil Layers," by K.W. Dotson and A.S. Veletsos, 12/87, (PB88-187786, A03, MF-A01).

NCEER-87-0025 "Proceedings from the Symposium on Seismic Hazards, Ground Motions, Soil-Liquefaction and Engineering Practice in Eastern North America," October 20-22, 1987, edited by K.H. Jacob, 12/87, (PB88-188115, A23, MF-A01). This report is available only through NTIS (see address given above).

NCEER-87-0026 "Report on the Whittier-Narrows, California, Earthquake of October 1, 1987," by J. Pantelic and A. Reinhorn, 11/87, (PB88-187752, A03, MF-A01). This report is available only through NTIS (see address given above).

NCEER-87-0027 "Design of a Modular Program for Transient Nonlinear Analysis of Large 3-D Building Structures," by S. Srivastav and J.F. Abel, 12/30/87, (PB88-187950, A05, MF-A01). This report is only available through NTIS (see address given above).

NCEER-87-0028 "Second-Year Program in Research, Education and Technology Transfer," 3/8/88, (PB88-219480, A04, MF-A01).

NCEER-88-0001 "Workshop on Seismic Computer Analysis and Design of Buildings With Interactive Graphics," by W. McGuire, J.F. Abel and C.H. Conley, 1/18/88, (PB88-187760, A03, MF-A01). This report is only available through NTIS (see address given above).

NCEER-88-0002 "Optimal Control of Nonlinear Flexible Structures," by J.N. Yang, F.X. Long and D. Wong, 1/22/88, (PB88-213772, A06, MF-A01).

NCEER-88-0003 "Substructuring Techniques in the Time Domain for Primary-Secondary Structural Systems," by G.D. Manolis and G. Juhn, 2/10/88, (PB88-213780, A04, MF-A01).

NCEER-88-0004 "Iterative Seismic Analysis of Primary-Secondary Systems," by A. Singhal, L.D. Lutes and P.D. Spanos, 2/23/88, (PB88-213798, A04, MF-A01).

NCEER-88-0005 "Stochastic Finite Element Expansion for Random Media," by P.D. Spanos and R. Ghanem, 3/14/88, (PB88-213806, A03, MF-A01).

NCEER-88-0006 "Combining Structural Optimization and Structural Control," by F.Y. Cheng and C.P. Pantelides, 1/10/88, (PB88-213814, A05, MF-A01).

NCEER-88-0007 "Seismic Performance Assessment of Code-Designed Structures," by H.H-M. Hwang, J-W. Jaw and H-J. Shau, 3/20/88, (PB88-219423, A04, MF-A01). This report is only available through NTIS (see address given above).

NCEER-88-0008 "Reliability Analysis of Code-Designed Structures Under Natural Hazards," by H.H-M. Hwang, H. Ushiba and M. Shinozuka, 2/29/88, (PB88-229471, A07, MF-A01). This report is only available through NTIS (see address given above).

NCEER-88-0009 "Seismic Fragility Analysis of Shear Wall Structures," by J-W Jaw and H.H-M. Hwang, 4/30/88, (PB89-102867, A04, MF-A01).

NCEER-88-0010 "Base Isolation of a Multi-Story Building Under a Harmonic Ground Motion - A Comparison of Performances of Various Systems," by F-G Fan, G. Ahmadi and I.G. Tadjbakhsh, 5/18/88, (PB89-122238, A06, MF-A01). This report is only available through NTIS (see address given above).

NCEER-88-0011 "Seismic Floor Response Spectra for a Combined System by Green's Functions," by F.M. Lavelle, L.A. Bergman and P.D. Spanos, 5/1/88, (PB89-102875, A03, MF-A01).

NCEER-88-0012 "A New Solution Technique for Randomly Excited Hysteretic Structures," by G.Q. Cai and Y.K. Lin, 5/16/88, (PB89-102883, A03, MF-A01).

NCEER-88-0013 "A Study of Radiation Damping and Soil-Structure Interaction Effects in the Centrifuge," by K. Weissman, supervised by J.H. Prevost, 5/24/88, (PB89-144703, A06, MF-A01).

NCEER-88-0014 "Parameter Identification and Implementation of a Kinematic Plasticity Model for Frictional Soils," by J.H. Prevost and D.V. Griffiths, not available.

NCEER-88-0015 "Two- and Three- Dimensional Dynamic Finite Element Analyses of the Long Valley Dam," by D.V. Griffiths and J.H. Prevost, 6/17/88, (PB89-144711, A04, MF-A01).

NCEER-88-0016 "Damage Assessment of Reinforced Concrete Structures in Eastern United States," by A.M. Reinhorn, M.J. Seidel, S.K. Kunnath and Y.J. Park, 6/15/88, (PB89-122220, A04, MF-A01). This report is only available through NTIS (see address given above).

NCEER-88-0017 "Dynamic Compliance of Vertically Loaded Strip Foundations in Multilayered Viscoelastic Soils," by S. Ahmad and A.S.M. Israil, 6/17/88, (PB89-102891, A04, MF-A01).

NCEER-88-0018 "An Experimental Study of Seismic Structural Response With Added Viscoelastic Dampers," by R.C. Lin, Z. Liang, T.T. Soong and R.H. Zhang, 6/30/88, (PB89-122212, A05, MF-A01). This report is available only through NTIS (see address given above).

NCEER-88-0019 "Experimental Investigation of Primary - Secondary System Interaction," by G.D. Manolis, G. Juhn and A.M. Reinhorn, 5/27/88, (PB89-122204, A04, MF-A01).

NCEER-88-0020 "A Response Spectrum Approach For Analysis of Nonclassically Damped Structures," by J.N. Yang, S. Sarkani and F.X. Long, 4/22/88, (PB89-102909, A04, MF-A01).

NCEER-88-0021 "Seismic Interaction of Structures and Soils: Stochastic Approach," by A.S. Veletsos and A.M. Prasad, 7/21/88, (PB89-122196, A04, MF-A01). This report is only available through NTIS (see address given above).

NCEER-88-0022 "Identification of the Serviceability Limit State and Detection of Seismic Structural Damage," by E. DiPasquale and A.S. Cakmak, 6/15/88, (PB89-122188, A05, MF-A01). This report is available only through NTIS (see address given above).

NCEER-88-0023 "Multi-Hazard Risk Analysis: Case of a Simple Offshore Structure," by B.K. Bhartia and E.H. Vanmarcke, 7/21/88, (PB89-145213, A05, MF-A01).

NCEER-88-0024 "Automated Seismic Design of Reinforced Concrete Buildings," by Y.S. Chung, C. Meyer and M. Shinozuka, 7/5/88, (PB89-122170, A06, MF-A01). This report is available only through NTIS (see address given above).

NCEER-88-0025 "Experimental Study of Active Control of MDOF Structures Under Seismic Excitations," by L.L. Chung, R.C. Lin, T.T. Soong and A.M. Reinhorn, 7/10/88, (PB89-122600, A04, MF-A01).

NCEER-88-0026 "Earthquake Simulation Tests of a Low-Rise Metal Structure," by J.S. Hwang, K.C. Chang, G.C. Lee and R.L. Ketter, 8/1/88, (PB89-102917, A04, MF-A01).

NCEER-88-0027 "Systems Study of Urban Response and Reconstruction Due to Catastrophic Earthquakes," by F. Kozin and H.K. Zhou, 9/22/88, (PB90-162348, A04, MF-A01).

NCEER-88-0028 "Seismic Fragility Analysis of Plane Frame Structures," by H.H-M. Hwang and Y.K. Low, 7/31/88, (PB89-131445, A06, MF-A01).

NCEER-88-0029 "Response Analysis of Stochastic Structures," by A. Kardara, C. Bucher and M. Shinozuka, 9/22/88, (PB89-174429, A04, MF-A01).

NCEER-88-0030 "Nonnormal Accelerations Due to Yielding in a Primary Structure," by D.C.K. Chen and L.D. Lutes, 9/19/88, (PB89-131437, A04, MF-A01).

NCEER-88-0031 "Design Approaches for Soil-Structure Interaction," by A.S. Veletsos, A.M. Prasad and Y. Tang, 12/30/88, (PB89-174437, A03, MF-A01). This report is available only through NTIS (see address given above).

NCEER-88-0032 "A Re-evaluation of Design Spectra for Seismic Damage Control," by C.J. Turkstra and A.G. Tallin, 11/7/88, (PB89-145221, A05, MF-A01).

NCEER-88-0033 "The Behavior and Design of Noncontact Lap Splices Subjected to Repeated Inelastic Tensile Loading," by V.E. Sagan, P. Gergely and R.N. White, 12/8/88, (PB89-163737, A08, MF-A01).

NCEER-88-0034 "Seismic Response of Pile Foundations," by S.M. Mamoon, P.K. Banerjee and S. Ahmad, 11/1/88, (PB89-145239, A04, MF-A01).

NCEER-88-0035 "Modeling of R/C Building Structures With Flexible Floor Diaphragms (IDARC2)," by A.M. Reinhorn, S.K. Kunnath and N. Panahshahi, 9/7/88, (PB89-207153, A07, MF-A01).

NCEER-88-0036 "Solution of the Dam-Reservoir Interaction Problem Using a Combination of FEM, BEM with Particular Integrals, Modal Analysis, and Substructuring," by C-S. Tsai, G.C. Lee and R.L. Ketter, 12/31/88, (PB89-207146, A04, MF-A01).

NCEER-88-0037 "Optimal Placement of Actuators for Structural Control," by F.Y. Cheng and C.P. Pantelides, 8/15/88, (PB89-162846, A05, MF-A01).

NCEER-88-0038 "Teflon Bearings in Aseismic Base Isolation: Experimental Studies and Mathematical Modeling," by A. Mokha, M.C. Constantinou and A.M. Reinhorn, 12/5/88, (PB89-218457, A10, MF-A01). This report is available only through NTIS (see address given above).

NCEER-88-0039 "Seismic Behavior of Flat Slab High-Rise Buildings in the New York City Area," by P. Weidlinger and M. Ettouney, 10/15/88, (PB90-145681, A04, MF-A01).

NCEER-88-0040 "Evaluation of the Earthquake Resistance of Existing Buildings in New York City," by P. Weidlinger and M. Ettouney, 10/15/88, not available.

NCEER-88-0041 "Small-Scale Modeling Techniques for Reinforced Concrete Structures Subjected to Seismic Loads," by W. Kim, A. El-Attar and R.N. White, 11/22/88, (PB89-189625, A05, MF-A01).

NCEER-88-0042 "Modeling Strong Ground Motion from Multiple Event Earthquakes," by G.W. Ellis and A.S. Cakmak, 10/15/88, (PB89-174445, A03, MF-A01).

NCEER-88-0043 "Nonstationary Models of Seismic Ground Acceleration," by M. Grigoriu, S.E. Ruiz and E. Rosenblueth, 7/15/88, (PB89-189617, A04, MF-A01).

NCEER-88-0044 "SARCF User's Guide: Seismic Analysis of Reinforced Concrete Frames," by Y.S. Chung, C. Meyer and M. Shinozuka, 11/9/88, (PB89-174452, A08, MF-A01).

NCEER-88-0045 "First Expert Panel Meeting on Disaster Research and Planning," edited by J. Pantelic and J. Stoyle, 9/15/88, (PB89-174460, A05, MF-A01).

NCEER-88-0046 "Preliminary Studies of the Effect of Degrading Infill Walls on the Nonlinear Seismic Response of Steel Frames," by C.Z. Chrysostomou, P. Gergely and J.F. Abel, 12/19/88, (PB89-208383, A05, MF-A01).

NCEER-88-0047 "Reinforced Concrete Frame Component Testing Facility - Design, Construction, Instrumentation and Operation," by S.P. Pessiki, C. Conley, T. Bond, P. Gergely and R.N. White, 12/16/88, (PB89-174478, A04, MF-A01).

NCEER-89-0001 "Effects of Protective Cushion and Soil Compliancy on the Response of Equipment Within a Seismically Excited Building," by J.A. HoLung, 2/16/89, (PB89-207179, A04, MF-A01).

NCEER-89-0002 "Statistical Evaluation of Response Modification Factors for Reinforced Concrete Structures," by H.H-M. Hwang and J-W. Jaw, 2/17/89, (PB89-207187, A05, MF-A01).

NCEER-89-0003 "Hysteretic Columns Under Random Excitation," by G-Q. Cai and Y.K. Lin, 1/9/89, (PB89-196513, A03, MF-A01).

NCEER-89-0004 "Experimental Study of `Elephant Foot Bulge' Instability of Thin-Walled Metal Tanks," by Z-H. Jia and R.L. Ketter, 2/22/89, (PB89-207195, A03, MF-A01).

NCEER-89-0005 "Experiment on Performance of Buried Pipelines Across San Andreas Fault," by J. Isenberg, E. Richardson and T.D. O'Rourke, 3/10/89, (PB89-218440, A04, MF-A01). This report is available only through NTIS (see address given above).

NCEER-89-0006 "A Knowledge-Based Approach to Structural Design of Earthquake-Resistant Buildings," by M. Subramani, P. Gergely, C.H. Conley, J.F. Abel and A.H. Zaghw, 1/15/89, (PB89-218465, A06, MF-A01).

NCEER-89-0007 "Liquefaction Hazards and Their Effects on Buried Pipelines," by T.D. O'Rourke and P.A. Lane, 2/1/89, (PB89-218481, A09, MF-A01).

NCEER-89-0008 "Fundamentals of System Identification in Structural Dynamics," by H. Imai, C-B. Yun, O. Maruyama and M. Shinozuka, 1/26/89, (PB89-207211, A04, MF-A01).

NCEER-89-0009 "Effects of the 1985 Michoacan Earthquake on Water Systems and Other Buried Lifelines in Mexico," by A.G. Ayala and M.J. O'Rourke, 3/8/89, (PB89-207229, A06, MF-A01).

NCEER-89-R010 "NCEER Bibliography of Earthquake Education Materials," by K.E.K. Ross, Second Revision, 9/1/89, (PB90-125352, A05, MF-A01). This report is replaced by NCEER-92-0018.

NCEER-89-0011 "Inelastic Three-Dimensional Response Analysis of Reinforced Concrete Building Structures (IDARC-3D), Part I - Modeling," by S.K. Kunnath and A.M. Reinhorn, 4/17/89, (PB90-114612, A07, MF-A01). This report is available only through NTIS (see address given above).

NCEER-89-0012 "Recommended Modifications to ATC-14," by C.D. Poland and J.O. Malley, 4/12/89, (PB90-108648, A15, MF-A01).

NCEER-89-0013 "Repair and Strengthening of Beam-to-Column Connections Subjected to Earthquake Loading," by M. Corazao and A.J. Durrani, 2/28/89, (PB90-109885, A06, MF-A01).

NCEER-89-0014 "Program EXKAL2 for Identification of Structural Dynamic Systems," by O. Maruyama, C-B. Yun, M. Hoshiya and M. Shinozuka, 5/19/89, (PB90-109877, A09, MF-A01).

NCEER-89-0015 "Response of Frames With Bolted Semi-Rigid Connections, Part I - Experimental Study and Analytical Predictions," by P.J. DiCorso, A.M. Reinhorn, J.R. Dickerson, J.B. Radziminski and W.L. Harper, 6/1/89, not available.

NCEER-89-0016 "ARMA Monte Carlo Simulation in Probabilistic Structural Analysis," by P.D. Spanos and M.P. Mignolet, 7/10/89, (PB90-109893, A03, MF-A01).

NCEER-89-P017 "Preliminary Proceedings from the Conference on Disaster Preparedness - The Place of Earthquake Education in Our Schools," Edited by K.E.K. Ross, 6/23/89, (PB90-108606, A03, MF-A01).

NCEER-89-0017 "Proceedings from the Conference on Disaster Preparedness - The Place of Earthquake Education in Our Schools," Edited by K.E.K. Ross, 12/31/89, (PB90-207895, A012, MF-A02). This report is available only through NTIS (see address given above).

NCEER-89-0018 "Multidimensional Models of Hysteretic Material Behavior for Vibration Analysis of Shape Memory Energy Absorbing Devices, by E.J. Graesser and F.A. Cozzarelli, 6/7/89, (PB90-164146, A04, MF-A01).

NCEER-89-0019 "Nonlinear Dynamic Analysis of Three-Dimensional Base Isolated Structures (3D-BASIS)," by S. Nagarajaiah, A.M. Reinhorn and M.C. Constantinou, 8/3/89, (PB90-161936, A06, MF-A01). This report has been replaced by NCEER-93-0011.

NCEER-89-0020 "Structural Control Considering Time-Rate of Control Forces and Control Rate Constraints," by F.Y. Cheng and C.P. Pantelides, 8/3/89, (PB90-120445, A04, MF-A01).

NCEER-89-0021 "Subsurface Conditions of Memphis and Shelby County," by K.W. Ng, T-S. Chang and H-H.M. Hwang, 7/26/89, (PB90-120437, A03, MF-A01).

NCEER-89-0022 "Seismic Wave Propagation Effects on Straight Jointed Buried Pipelines," by K. Elhmadi and M.J. O'Rourke, 8/24/89, (PB90-162322, A10, MF-A02).

NCEER-89-0023 "Workshop on Serviceability Analysis of Water Delivery Systems," edited by M. Grigoriu, 3/6/89, (PB90-127424, A03, MF-A01).

NCEER-89-0024 "Shaking Table Study of a 1/5 Scale Steel Frame Composed of Tapered Members," by K.C. Chang, J.S. Hwang and G.C. Lee, 9/18/89, (PB90-160169, A04, MF-A01).

NCEER-89-0025 "DYNA1D: A Computer Program for Nonlinear Seismic Site Response Analysis - Technical Documentation," by Jean H. Prevost, 9/14/89, (PB90-161944, A07, MF-A01). This report is available only through NTIS (see address given above).

NCEER-89-0026 "1:4 Scale Model Studies of Active Tendon Systems and Active Mass Dampers for Aseismic Protection," by A.M. Reinhorn, T.T. Soong, R.C. Lin, Y.P. Yang, Y. Fukao, H. Abe and M. Nakai, 9/15/89, (PB90-173246, A10, MF-A02). This report is available only through NTIS (see address given above).

NCEER-89-0027 "Scattering of Waves by Inclusions in a Nonhomogeneous Elastic Half Space Solved by Boundary Element Methods," by P.K. Hadley, A. Askar and A.S. Cakmak, 6/15/89, (PB90-145699, A07, MF-A01).

NCEER-89-0028 "Statistical Evaluation of Deflection Amplification Factors for Reinforced Concrete Structures," by H.H.M. Hwang, J-W. Jaw and A.L. Ch'ng, 8/31/89, (PB90-164633, A05, MF-A01).

NCEER-89-0029 "Bedrock Accelerations in Memphis Area Due to Large New Madrid Earthquakes," by H.H.M. Hwang, C.H.S. Chen and G. Yu, 11/7/89, (PB90-162330, A04, MF-A01).

NCEER-89-0030 "Seismic Behavior and Response Sensitivity of Secondary Structural Systems," by Y.Q. Chen and T.T. Soong, 10/23/89, (PB90-164658, A08, MF-A01).

NCEER-89-0031 "Random Vibration and Reliability Analysis of Primary-Secondary Structural Systems," by Y. Ibrahim, M. Grigoriu and T.T. Soong, 11/10/89, (PB90-161951, A04, MF-A01).

NCEER-89-0032 "Proceedings from the Second U.S. - Japan Workshop on Liquefaction, Large Ground Deformation and Their Effects on Lifelines, September 26-29, 1989," Edited by T.D. O'Rourke and M. Hamada, 12/1/89, (PB90-209388, A22, MF-A03).

NCEER-89-0033 "Deterministic Model for Seismic Damage Evaluation of Reinforced Concrete Structures," by J.M. Bracci, A.M. Reinhorn, J.B. Mander and S.K. Kunnath, 9/27/89, (PB91-108803, A06, MF-A01).

NCEER-89-0034 "On the Relation Between Local and Global Damage Indices," by E. DiPasquale and A.S. Cakmak, 8/15/89, (PB90-173865, A05, MF-A01).

NCEER-89-0035 "Cyclic Undrained Behavior of Nonplastic and Low Plasticity Silts," by A.J. Walker and H.E. Stewart, 7/26/89, (PB90-183518, A10, MF-A01).

NCEER-89-0036 "Liquefaction Potential of Surficial Deposits in the City of Buffalo, New York," by M. Budhu, R. Giese and L. Baumgrass, 1/17/89, (PB90-208455, A04, MF-A01).

NCEER-89-0037 "A Deterministic Assessment of Effects of Ground Motion Incoherence," by A.S. Veletsos and Y. Tang, 7/15/89, (PB90-164294, A03, MF-A01).

NCEER-89-0038 "Workshop on Ground Motion Parameters for Seismic Hazard Mapping," July 17-18, 1989, edited by R.V. Whitman, 12/1/89, (PB90-173923, A04, MF-A01).

NCEER-89-0039 "Seismic Effects on Elevated Transit Lines of the New York City Transit Authority," by C.J. Costantino, C.A. Miller and E. Heymsfield, 12/26/89, (PB90-207887, A06, MF-A01).

NCEER-89-0040 "Centrifugal Modeling of Dynamic Soil-Structure Interaction," by K. Weissman, Supervised by J.H. Prevost, 5/10/89, (PB90-207879, A07, MF-A01).

NCEER-89-0041 "Linearized Identification of Buildings With Cores for Seismic Vulnerability Assessment," by I-K. Ho and A.E. Aktan, 11/1/89, (PB90-251943, A07, MF-A01).

NCEER-90-0001 "Geotechnical and Lifeline Aspects of the October 17, 1989 Loma Prieta Earthquake in San Francisco," by T.D. O'Rourke, H.E. Stewart, F.T. Blackburn and T.S. Dickerman, 1/90, (PB90-208596, A05, MF-A01).

NCEER-90-0002 "Nonnormal Secondary Response Due to Yielding in a Primary Structure," by D.C.K. Chen and L.D. Lutes, 2/28/90, (PB90-251976, A07, MF-A01).

NCEER-90-0003 "Earthquake Education Materials for Grades K-12," by K.E.K. Ross, 4/16/90, (PB91-251984, A05, MF-A05). This report has been replaced by NCEER-92-0018.

NCEER-90-0004 "Catalog of Strong Motion Stations in Eastern North America," by R.W. Busby, 4/3/90, (PB90-251984, A05, MF-A01).

NCEER-90-0005 "NCEER Strong-Motion Data Base: A User Manual for the GeoBase Release (Version 1.0 for the Sun3)," by P. Friberg and K. Jacob, 3/31/90 (PB90-258062, A04, MF-A01).

NCEER-90-0006 "Seismic Hazard Along a Crude Oil Pipeline in the Event of an 1811-1812 Type New Madrid Earthquake," by H.H.M. Hwang and C-H.S. Chen, 4/16/90, (PB90-258054, A04, MF-A01).

NCEER-90-0007 "Site-Specific Response Spectra for Memphis Sheahan Pumping Station," by H.H.M. Hwang and C.S. Lee, 5/15/90, (PB91-108811, A05, MF-A01).

NCEER-90-0008 "Pilot Study on Seismic Vulnerability of Crude Oil Transmission Systems," by T. Ariman, R. Dobry, M. Grigoriu, F. Kozin, M. O'Rourke, T. O'Rourke and M. Shinozuka, 5/25/90, (PB91-108837, A06, MF-A01).

NCEER-90-0009 "A Program to Generate Site Dependent Time Histories: EQGEN," by G.W. Ellis, M. Srinivasan and A.S. Cakmak, 1/30/90, (PB91-108829, A04, MF-A01).

NCEER-90-0010 "Active Isolation for Seismic Protection of Operating Rooms," by M.E. Talbott, Supervised by M. Shinozuka, 6/8/9, (PB91-110205, A05, MF-A01).

NCEER-90-0011 "Program LINEARID for Identification of Linear Structural Dynamic Systems," by C-B. Yun and M. Shinozuka, 6/25/90, (PB91-110312, A08, MF-A01).

NCEER-90-0012 "Two-Dimensional Two-Phase Elasto-Plastic Seismic Response of Earth Dams," by A.N. Yiagos, Supervised by J.H. Prevost, 6/20/90, (PB91-110197, A13, MF-A02).

NCEER-90-0013 "Secondary Systems in Base-Isolated Structures: Experimental Investigation, Stochastic Response and Stochastic Sensitivity," by G.D. Manolis, G. Juhn, M.C. Constantinou and A.M. Reinhorn, 7/1/90, (PB91-110320, A08, MF-A01).

NCEER-90-0014 "Seismic Behavior of Lightly-Reinforced Concrete Column and Beam-Column Joint Details," by S.P. Pessiki, C.H. Conley, P. Gergely and R.N. White, 8/22/90, (PB91-108795, A11, MF-A02).

NCEER-90-0015 "Two Hybrid Control Systems for Building Structures Under Strong Earthquakes," by J.N. Yang and A. Danielians, 6/29/90, (PB91-125393, A04, MF-A01).

NCEER-90-0016 "Instantaneous Optimal Control with Acceleration and Velocity Feedback," by J.N. Yang and Z. Li, 6/29/90, (PB91-125401, A03, MF-A01).

NCEER-90-0017 "Reconnaissance Report on the Northern Iran Earthquake of June 21, 1990," by M. Mehrain, 10/4/90, (PB91-125377, A03, MF-A01).

NCEER-90-0018 "Evaluation of Liquefaction Potential in Memphis and Shelby County," by T.S. Chang, P.S. Tang, C.S. Lee and H. Hwang, 8/10/90, (PB91-125427, A09, MF-A01).

NCEER-90-0019 "Experimental and Analytical Study of a Combined Sliding Disc Bearing and Helical Steel Spring Isolation System," by M.C. Constantinou, A.S. Mokha and A.M. Reinhorn, 10/4/90, (PB91-125385, A06, MF-A01). This report is available only through NTIS (see address given above).

NCEER-90-0020 "Experimental Study and Analytical Prediction of Earthquake Response of a Sliding Isolation System with a Spherical Surface," by A.S. Mokha, M.C. Constantinou and A.M. Reinhorn, 10/11/90, (PB91-125419, A05, MF-A01).

NCEER-90-0021 "Dynamic Interaction Factors for Floating Pile Groups," by G. Gazetas, K. Fan, A. Kaynia and E. Kausel, 9/10/90, (PB91-170381, A05, MF-A01).

NCEER-90-0022 "Evaluation of Seismic Damage Indices for Reinforced Concrete Structures," by S. Rodriguez-Gomez and A.S. Cakmak, 9/30/90, PB91-171322, A06, MF-A01).

NCEER-90-0023 "Study of Site Response at a Selected Memphis Site," by H. Desai, S. Ahmad, E.S. Gazetas and M.R. Oh, 10/11/90, (PB91-196857, A03, MF-A01).

NCEER-90-0024 "A User's Guide to Strongmo: Version 1.0 of NCEER's Strong-Motion Data Access Tool for PCs and Terminals," by P.A. Friberg and C.A.T. Susch, 11/15/90, (PB91-171272, A03, MF-A01).

NCEER-90-0025 "A Three-Dimensional Analytical Study of Spatial Variability of Seismic Ground Motions," by L-L. Hong and A.H.-S. Ang, 10/30/90, (PB91-170399, A09, MF-A01).

NCEER-90-0026 "MUMOID User's Guide - A Program for the Identification of Modal Parameters," by S. Rodriguez-Gomez and E. DiPasquale, 9/30/90, (PB91-171298, A04, MF-A01).

NCEER-90-0027 "SARCF-II User's Guide - Seismic Analysis of Reinforced Concrete Frames," by S. Rodriguez-Gomez, Y.S. Chung and C. Meyer, 9/30/90, (PB91-171280, A05, MF-A01).

NCEER-90-0028 "Viscous Dampers: Testing, Modeling and Application in Vibration and Seismic Isolation," by N. Makris and M.C. Constantinou, 12/20/90 (PB91-190561, A06, MF-A01).

NCEER-90-0029 "Soil Effects on Earthquake Ground Motions in the Memphis Area," by H. Hwang, C.S. Lee, K.W. Ng and T.S. Chang, 8/2/90, (PB91-190751, A05, MF-A01).

NCEER-91-0001 "Proceedings from the Third Japan-U.S. Workshop on Earthquake Resistant Design of Lifeline Facilities and Countermeasures for Soil Liquefaction, December 17-19, 1990," edited by T.D. O'Rourke and M. Hamada, 2/1/91, (PB91-179259, A99, MF-A04).

NCEER-91-0002 "Physical Space Solutions of Non-Proportionally Damped Systems," by M. Tong, Z. Liang and G.C. Lee, 1/15/91, (PB91-179242, A04, MF-A01).

NCEER-91-0003 "Seismic Response of Single Piles and Pile Groups," by K. Fan and G. Gazetas, 1/10/91, (PB92-174994, A04, MF-A01).

NCEER-91-0004 "Damping of Structures: Part 1 - Theory of Complex Damping," by Z. Liang and G. Lee, 10/10/91, (PB92-197235, A12, MF-A03).

NCEER-91-0005 "3D-BASIS - Nonlinear Dynamic Analysis of Three Dimensional Base Isolated Structures: Part II," by S. Nagarajaiah, A.M. Reinhorn and M.C. Constantinou, 2/28/91, (PB91-190553, A07, MF-A01). This report has been replaced by NCEER-93-0011.

NCEER-91-0006 "A Multidimensional Hysteretic Model for Plasticity Deforming Metals in Energy Absorbing Devices," by E.J. Graesser and F.A. Cozzarelli, 4/9/91, (PB92-108364, A04, MF-A01).

NCEER-91-0007 "A Framework for Customizable Knowledge-Based Expert Systems with an Application to a KBES for Evaluating the Seismic Resistance of Existing Buildings," by E.G. Ibarra-Anaya and S.J. Fenves, 4/9/91, (PB91-210930, A08, MF-A01).

NCEER-91-0008 "Nonlinear Analysis of Steel Frames with Semi-Rigid Connections Using the Capacity Spectrum Method," by G.G. Deierlein, S-H. Hsieh, Y-J. Shen and J.F. Abel, 7/2/91, (PB92-113828, A05, MF-A01).

NCEER-91-0009 "Earthquake Education Materials for Grades K-12," by K.E.K. Ross, 4/30/91, (PB91-212142, A06, MF-A01). This report has been replaced by NCEER-92-0018.

NCEER-91-0010 "Phase Wave Velocities and Displacement Phase Differences in a Harmonically Oscillating Pile," by N. Makris and G. Gazetas, 7/8/91, (PB92-108356, A04, MF-A01).

NCEER-91-0011 "Dynamic Characteristics of a Full-Size Five-Story Steel Structure and a 2/5 Scale Model," by K.C. Chang, G.C. Yao, G.C. Lee, D.S. Hao and Y.C. Yeh," 7/2/91, (PB93-116648, A06, MF-A02).

NCEER-91-0012 "Seismic Response of a 2/5 Scale Steel Structure with Added Viscoelastic Dampers," by K.C. Chang, T.T. Soong, S-T. Oh and M.L. Lai, 5/17/91, (PB92-110816, A05, MF-A01).

NCEER-91-0013 "Earthquake Response of Retaining Walls; Full-Scale Testing and Computational Modeling," by S. Alampalli and A-W.M. Elgamal, 6/20/91, not available.

NCEER-91-0014 "3D-BASIS-M: Nonlinear Dynamic Analysis of Multiple Building Base Isolated Structures," by P.C. Tsopelas, S. Nagarajaiah, M.C. Constantinou and A.M. Reinhorn, 5/28/91, (PB92-113885, A09, MF-A02).

NCEER-91-0015 "Evaluation of SEAOC Design Requirements for Sliding Isolated Structures," by D. Theodossiou and M.C. Constantinou, 6/10/91, (PB92-114602, A11, MF-A03).

NCEER-91-0016 "Closed-Loop Modal Testing of a 27-Story Reinforced Concrete Flat Plate-Core Building," by H.R. Somaprasad, T. Toksoy, H. Yoshiyuki and A.E. Aktan, 7/15/91, (PB92-129980, A07, MF-A02).

NCEER-91-0017 "Shake Table Test of a 1/6 Scale Two-Story Lightly Reinforced Concrete Building," by A.G. El-Attar, R.N. White and P. Gergely, 2/28/91, (PB92-222447, A06, MF-A02).

NCEER-91-0018 "Shake Table Test of a 1/8 Scale Three-Story Lightly Reinforced Concrete Building," by A.G. El-Attar, R.N. White and P. Gergely, 2/28/91, (PB93-116630, A08, MF-A02).

NCEER-91-0019 "Transfer Functions for Rigid Rectangular Foundations," by A.S. Veletsos, A.M. Prasad and W.H. Wu, 7/31/91, not available.

NCEER-91-0020 "Hybrid Control of Seismic-Excited Nonlinear and Inelastic Structural Systems," by J.N. Yang, Z. Li and A. Danielians, 8/1/91, (PB92-143171, A06, MF-A02).

NCEER-91-0021 "The NCEER-91 Earthquake Catalog: Improved Intensity-Based Magnitudes and Recurrence Relations for U.S. Earthquakes East of New Madrid," by L. Seeber and J.G. Armbruster, 8/28/91, (PB92-176742, A06, MF-A02).

NCEER-91-0022 "Proceedings from the Implementation of Earthquake Planning and Education in Schools: The Need for Change - The Roles of the Changemakers," by K.E.K. Ross and F. Winslow, 7/23/91, (PB92-129998, A12, MF-A03).

NCEER-91-0023 "A Study of Reliability-Based Criteria for Seismic Design of Reinforced Concrete Frame Buildings," by H.H.M. Hwang and H-M. Hsu, 8/10/91, (PB92-140235, A09, MF-A02).

NCEER-91-0024 "Experimental Verification of a Number of Structural System Identification Algorithms," by R.G. Ghanem, H. Gavin and M. Shinozuka, 9/18/91, (PB92-176577, A18, MF-A04).

NCEER-91-0025 "Probabilistic Evaluation of Liquefaction Potential," by H.H.M. Hwang and C.S. Lee," 11/25/91, (PB92-143429, A05, MF-A01).

NCEER-91-0026 "Instantaneous Optimal Control for Linear, Nonlinear and Hysteretic Structures - Stable Controllers," by J.N. Yang and Z. Li, 11/15/91, (PB92-163807, A04, MF-A01).

NCEER-91-0027 "Experimental and Theoretical Study of a Sliding Isolation System for Bridges," by M.C. Constantinou, A. Kartoum, A.M. Reinhorn and P. Bradford, 11/15/91, (PB92-176973, A10, MF-A03).

NCEER-92-0001 "Case Studies of Liquefaction and Lifeline Performance During Past Earthquakes, Volume 1: Japanese Case Studies," Edited by M. Hamada and T. O'Rourke, 2/17/92, (PB92-197243, A18, MF-A04).

NCEER-92-0002 "Case Studies of Liquefaction and Lifeline Performance During Past Earthquakes, Volume 2: United States Case Studies," Edited by T. O'Rourke and M. Hamada, 2/17/92, (PB92-197250, A20, MF-A04).

NCEER-92-0003 "Issues in Earthquake Education," Edited by K. Ross, 2/3/92, (PB92-222389, A07, MF-A02).

NCEER-92-0004 "Proceedings from the First U.S. - Japan Workshop on Earthquake Protective Systems for Bridges," Edited by I.G. Buckle, 2/4/92, (PB94-142239, A99, MF-A06).

NCEER-92-0005 "Seismic Ground Motion from a Haskell-Type Source in a Multiple-Layered Half-Space," A.P. Theoharis, G. Deodatis and M. Shinozuka, 1/2/92, not available.

NCEER-92-0006 "Proceedings from the Site Effects Workshop," Edited by R. Whitman, 2/29/92, (PB92-197201, A04, MF-A01).

NCEER-92-0007 "Engineering Evaluation of Permanent Ground Deformations Due to Seismically-Induced Liquefaction," by M.H. Baziar, R. Dobry and A-W.M. Elgamal, 3/24/92, (PB92-222421, A13, MF-A03).

NCEER-92-0008 "A Procedure for the Seismic Evaluation of Buildings in the Central and Eastern United States," by C.D. Poland and J.O. Malley, 4/2/92, (PB92-222439, A20, MF-A04).

NCEER-92-0009 "Experimental and Analytical Study of a Hybrid Isolation System Using Friction Controllable Sliding Bearings," by M.Q. Feng, S. Fujii and M. Shinozuka, 5/15/92, (PB93-150282, A06, MF-A02).

NCEER-92-0010 "Seismic Resistance of Slab-Column Connections in Existing Non-Ductile Flat-Plate Buildings," by A.J. Durrani and Y. Du, 5/18/92, (PB93-116812, A06, MF-A02).

NCEER-92-0011 "The Hysteretic and Dynamic Behavior of Brick Masonry Walls Upgraded by Ferrocement Coatings Under Cyclic Loading and Strong Simulated Ground Motion," by H. Lee and S.P. Prawel, 5/11/92, not available.

NCEER-92-0012 "Study of Wire Rope Systems for Seismic Protection of Equipment in Buildings," by G.F. Demetriades, M.C. Constantinou and A.M. Reinhorn, 5/20/92, (PB93-116655, A08, MF-A02).

NCEER-92-0013 "Shape Memory Structural Dampers: Material Properties, Design and Seismic Testing," by P.R. Witting and F.A. Cozzarelli, 5/26/92, (PB93-116663, A05, MF-A01).

NCEER-92-0014 "Longitudinal Permanent Ground Deformation Effects on Buried Continuous Pipelines," by M.J. O'Rourke, and C. Nordberg, 6/15/92, (PB93-116671, A08, MF-A02).

NCEER-92-0015 "A Simulation Method for Stationary Gaussian Random Functions Based on the Sampling Theorem," by M. Grigoriu and S. Balopoulou, 6/11/92, (PB93-127496, A05, MF-A01).

NCEER-92-0016 "Gravity-Load-Designed Reinforced Concrete Buildings: Seismic Evaluation of Existing Construction and Detailing Strategies for Improved Seismic Resistance," by G.W. Hoffmann, S.K. Kunnath, A.M. Reinhorn and J.B. Mander, 7/15/92, (PB94-142007, A08, MF-A02).

NCEER-92-0017 "Observations on Water System and Pipeline Performance in the Limón Area of Costa Rica Due to the April 22, 1991 Earthquake," by M. O'Rourke and D. Ballantyne, 6/30/92, (PB93-126811, A06, MF-A02).

NCEER-92-0018 "Fourth Edition of Earthquake Education Materials for Grades K-12," Edited by K.E.K. Ross, 8/10/92, (PB93-114023, A07, MF-A02).

NCEER-92-0019 "Proceedings from the Fourth Japan-U.S. Workshop on Earthquake Resistant Design of Lifeline Facilities and Countermeasures for Soil Liquefaction," Edited by M. Hamada and T.D. O'Rourke, 8/12/92, (PB93-163939, A99, MF-E11).

NCEER-92-0020 "Active Bracing System: A Full Scale Implementation of Active Control," by A.M. Reinhorn, T.T. Soong, R.C. Lin, M.A. Riley, Y.P. Wang, S. Aizawa and M. Higashino, 8/14/92, (PB93-127512, A06, MF-A02).

NCEER-92-0021 "Empirical Analysis of Horizontal Ground Displacement Generated by Liquefaction-Induced Lateral Spreads," by S.F. Bartlett and T.L. Youd, 8/17/92, (PB93-188241, A06, MF-A02).

NCEER-92-0022 "IDARC Version 3.0: Inelastic Damage Analysis of Reinforced Concrete Structures," by S.K. Kunnath, A.M. Reinhorn and R.F. Lobo, 8/31/92, (PB93-227502, A07, MF-A02).

NCEER-92-0023 "A Semi-Empirical Analysis of Strong-Motion Peaks in Terms of Seismic Source, Propagation Path and Local Site Conditions, by M. Kamiyama, M.J. O'Rourke and R. Flores-Berrones, 9/9/92, (PB93-150266, A08, MF-A02).

NCEER-92-0024 "Seismic Behavior of Reinforced Concrete Frame Structures with Nonductile Details, Part I: Summary of Experimental Findings of Full Scale Beam-Column Joint Tests," by A. Beres, R.N. White and P. Gergely, 9/30/92, (PB93-227783, A05, MF-A01).

NCEER-92-0025 "Experimental Results of Repaired and Retrofitted Beam-Column Joint Tests in Lightly Reinforced Concrete Frame Buildings," by A. Beres, S. El-Borgi, R.N. White and P. Gergely, 10/29/92, (PB93-227791, A05, MF-A01).

NCEER-92-0026 "A Generalization of Optimal Control Theory: Linear and Nonlinear Structures," by J.N. Yang, Z. Li and S. Vongchavalitkul, 11/2/92, (PB93-188621, A05, MF-A01).

NCEER-92-0027 "Seismic Resistance of Reinforced Concrete Frame Structures Designed Only for Gravity Loads: Part I - Design and Properties of a One-Third Scale Model Structure," by J.M. Bracci, A.M. Reinhorn and J.B. Mander, 12/1/92, (PB94-104502, A08, MF-A02).

NCEER-92-0028 "Seismic Resistance of Reinforced Concrete Frame Structures Designed Only for Gravity Loads: Part II - Experimental Performance of Subassemblages," by L.E. Aycardi, J.B. Mander and A.M. Reinhorn, 12/1/92, (PB94-104510, A08, MF-A02).

NCEER-92-0029 "Seismic Resistance of Reinforced Concrete Frame Structures Designed Only for Gravity Loads: Part III - Experimental Performance and Analytical Study of a Structural Model," by J.M. Bracci, A.M. Reinhorn and J.B. Mander, 12/1/92, (PB93-227528, A09, MF-A01).

NCEER-92-0030 "Evaluation of Seismic Retrofit of Reinforced Concrete Frame Structures: Part I - Experimental Performance of Retrofitted Subassemblages," by D. Choudhuri, J.B. Mander and A.M. Reinhorn, 12/8/92, (PB93-198307, A07, MF-A02).

NCEER-92-0031 "Evaluation of Seismic Retrofit of Reinforced Concrete Frame Structures: Part II - Experimental Performance and Analytical Study of a Retrofitted Structural Model," by J.M. Bracci, A.M. Reinhorn and J.B. Mander, 12/8/92, (PB93-198315, A09, MF-A03).

NCEER-92-0032 "Experimental and Analytical Investigation of Seismic Response of Structures with Supplemental Fluid Viscous Dampers," by M.C. Constantinou and M.D. Symans, 12/21/92, (PB93-191435, A10, MF-A03). This report is available only through NTIS (see address given above).

NCEER-92-0033 "Reconnaissance Report on the Cairo, Egypt Earthquake of October 12, 1992," by M. Khater, 12/23/92, (PB93-188621, A03, MF-A01).

NCEER-92-0034 "Low-Level Dynamic Characteristics of Four Tall Flat-Plate Buildings in New York City," by H. Gavin, S. Yuan, J. Grossman, E. Pekelis and K. Jacob, 12/28/92, (PB93-188217, A07, MF-A02).

NCEER-93-0001 "An Experimental Study on the Seismic Performance of Brick-Infilled Steel Frames With and Without Retrofit," by J.B. Mander, B. Nair, K. Wojtkowski and J. Ma, 1/29/93, (PB93-227510, A07, MF-A02).

NCEER-93-0002 "Social Accounting for Disaster Preparedness and Recovery Planning," by S. Cole, E. Pantoja and V. Razak, 2/22/93, (PB94-142114, A12, MF-A03).

NCEER-93-0003 "Assessment of 1991 NEHRP Provisions for Nonstructural Components and Recommended Revisions," by T.T. Soong, G. Chen, Z. Wu, R-H. Zhang and M. Grigoriu, 3/1/93, (PB93-188639, A06, MF-A02).

NCEER-93-0004 "Evaluation of Static and Response Spectrum Analysis Procedures of SEAOC/UBC for Seismic Isolated Structures," by C.W. Winters and M.C. Constantinou, 3/23/93, (PB93-198299, A10, MF-A03).

NCEER-93-0005 "Earthquakes in the Northeast - Are We Ignoring the Hazard? A Workshop on Earthquake Science and Safety for Educators," edited by K.E.K. Ross, 4/2/93, (PB94-103066, A09, MF-A02).

NCEER-93-0006 "Inelastic Response of Reinforced Concrete Structures with Viscoelastic Braces," by R.F. Lobo, J.M. Bracci, K.L. Shen, A.M. Reinhorn and T.T. Soong, 4/5/93, (PB93-227486, A05, MF-A02).

NCEER-93-0007 "Seismic Testing of Installation Methods for Computers and Data Processing Equipment," by K. Kosar, T.T. Soong, K.L. Shen, J.A. HoLung and Y.K. Lin, 4/12/93, (PB93-198299, A07, MF-A02).

NCEER-93-0008 "Retrofit of Reinforced Concrete Frames Using Added Dampers," by A. Reinhorn, M. Constantinou and C. Li, not available.

NCEER-93-0009 "Seismic Behavior and Design Guidelines for Steel Frame Structures with Added Viscoelastic Dampers," by K.C. Chang, M.L. Lai, T.T. Soong, D.S. Hao and Y.C. Yeh, 5/1/93, (PB94-141959, A07, MF-A02).

NCEER-93-0010 "Seismic Performance of Shear-Critical Reinforced Concrete Bridge Piers," by J.B. Mander, S.M. Waheed, M.T.A. Chaudhary and S.S. Chen, 5/12/93, (PB93-227494, A08, MF-A02).

NCEER-93-0011 "3D-BASIS-TABS: Computer Program for Nonlinear Dynamic Analysis of Three Dimensional Base Isolated Structures," by S. Nagarajaiah, C. Li, A.M. Reinhorn and M.C. Constantinou, 8/2/93, (PB94-141819, A09, MF-A02).

NCEER-93-0012 "Effects of Hydrocarbon Spills from an Oil Pipeline Break on Ground Water," by O.J. Helweg and H.H.M. Hwang, 8/3/93, (PB94-141942, A06, MF-A02).

NCEER-93-0013 "Simplified Procedures for Seismic Design of Nonstructural Components and Assessment of Current Code Provisions," by M.P. Singh, L.E. Suarez, E.E. Matheu and G.O. Maldonado, 8/4/93, (PB94-141827, A09, MF-A02).

NCEER-93-0014 "An Energy Approach to Seismic Analysis and Design of Secondary Systems," by G. Chen and T.T. Soong, 8/6/93, (PB94-142767, A11, MF-A03).

NCEER-93-0015 "Proceedings from School Sites: Becoming Prepared for Earthquakes - Commemorating the Third Anniversary of the Loma Prieta Earthquake," Edited by F.E. Winslow and K.E.K. Ross, 8/16/93, (PB94-154275, A16, MF-A02).

NCEER-93-0016 "Reconnaissance Report of Damage to Historic Monuments in Cairo, Egypt Following the October 12, 1992 Dahshur Earthquake," by D. Sykora, D. Look, G. Croci, E. Karaesmen and E. Karaesmen, 8/19/93, (PB94-142221, A08, MF-A02).

NCEER-93-0017 "The Island of Guam Earthquake of August 8, 1993," by S.W. Swan and S.K. Harris, 9/30/93, (PB94-141843, A04, MF-A01).

NCEER-93-0018 "Engineering Aspects of the October 12, 1992 Egyptian Earthquake," by A.W. Elgamal, M. Amer, K. Adalier and A. Abul-Fadl, 10/7/93, (PB94-141983, A05, MF-A01).

NCEER-93-0019 "Development of an Earthquake Motion Simulator and its Application in Dynamic Centrifuge Testing," by I. Krstelj, Supervised by J.H. Prevost, 10/23/93, (PB94-181773, A-10, MF-A03).

NCEER-93-0020 "NCEER-Taisei Corporation Research Program on Sliding Seismic Isolation Systems for Bridges: Experimental and Analytical Study of a Friction Pendulum System (FPS)," by M.C. Constantinou, P. Tsopelas, Y-S. Kim and S. Okamoto, 11/1/93, (PB94-142775, A08, MF-A02).

NCEER-93-0021 "Finite Element Modeling of Elastomeric Seismic Isolation Bearings," by L.J. Billings, Supervised by R. Shepherd, 11/8/93, not available.

NCEER-93-0022 "Seismic Vulnerability of Equipment in Critical Facilities: Life-Safety and Operational Consequences," by K. Porter, G.S. Johnson, M.M. Zadeh, C. Scawthorn and S. Eder, 11/24/93, (PB94-181765, A16, MF-A03).

NCEER-93-0023 "Hokkaido Nansei-oki, Japan Earthquake of July 12, 1993, by P.I. Yanev and C.R. Scawthorn, 12/23/93, (PB94-181500, A07, MF-A01).

NCEER-94-0001 "An Evaluation of Seismic Serviceability of Water Supply Networks with Application to the San Francisco Auxiliary Water Supply System," by I. Markov, Supervised by M. Grigoriu and T. O'Rourke, 1/21/94, (PB94-204013, A07, MF-A02).

NCEER-94-0002 "NCEER-Taisei Corporation Research Program on Sliding Seismic Isolation Systems for Bridges: Experimental and Analytical Study of Systems Consisting of Sliding Bearings, Rubber Restoring Force Devices and Fluid Dampers," Volumes I and II, by P. Tsopelas, S. Okamoto, M.C. Constantinou, D. Ozaki and S. Fujii, 2/4/94, (PB94-181740, A09, MF-A02 and PB94-181757, A12, MF-A03).

NCEER-94-0003 "A Markov Model for Local and Global Damage Indices in Seismic Analysis," by S. Rahman and M. Grigoriu, 2/18/94, (PB94-206000, A12, MF-A03).

NCEER-94-0004 "Proceedings from the NCEER Workshop on Seismic Response of Masonry Infills," edited by D.P. Abrams, 3/1/94, (PB94-180783, A07, MF-A02).

NCEER-94-0005 "The Northridge, California Earthquake of January 17, 1994: General Reconnaissance Report," edited by J.D. Goltz, 3/11/94, (PB94-193943, A10, MF-A03).

NCEER-94-0006 "Seismic Energy Based Fatigue Damage Analysis of Bridge Columns: Part I - Evaluation of Seismic Capacity," by G.A. Chang and J.B. Mander, 3/14/94, (PB94-219185, A11, MF-A03).

NCEER-94-0007 "Seismic Isolation of Multi-Story Frame Structures Using Spherical Sliding Isolation Systems," by T.M. Al-Hussaini, V.A. Zayas and M.C. Constantinou, 3/17/94, (PB94-193745, A09, MF-A02).

NCEER-94-0008 "The Northridge, California Earthquake of January 17, 1994: Performance of Highway Bridges," edited by I.G. Buckle, 3/24/94, (PB94-193851, A06, MF-A02).

NCEER-94-0009 "Proceedings of the Third U.S.-Japan Workshop on Earthquake Protective Systems for Bridges," edited by I.G. Buckle and I. Friedland, 3/31/94, (PB94-195815, A99, MF-A06).

NCEER-94-0010 "3D-BASIS-ME: Computer Program for Nonlinear Dynamic Analysis of Seismically Isolated Single and Multiple Structures and Liquid Storage Tanks," by P.C. Tsopelas, M.C. Constantinou and A.M. Reinhorn, 4/12/94, (PB94-204922, A09, MF-A02).

NCEER-94-0011 "The Northridge, California Earthquake of January 17, 1994: Performance of Gas Transmission Pipelines," by T.D. O'Rourke and M.C. Palmer, 5/16/94, (PB94-204989, A05, MF-A01).

NCEER-94-0012 "Feasibility Study of Replacement Procedures and Earthquake Performance Related to Gas Transmission Pipelines," by T.D. O'Rourke and M.C. Palmer, 5/25/94, (PB94-206638, A09, MF-A02).

NCEER-94-0013 "Seismic Energy Based Fatigue Damage Analysis of Bridge Columns: Part II - Evaluation of Seismic Demand," by G.A. Chang and J.B. Mander, 6/1/94, (PB95-18106, A08, MF-A02).

NCEER-94-0014 "NCEER-Taisei Corporation Research Program on Sliding Seismic Isolation Systems for Bridges: Experimental and Analytical Study of a System Consisting of Sliding Bearings and Fluid Restoring Force/Damping Devices," by P. Tsopelas and M.C. Constantinou, 6/13/94, (PB94-219144, A10, MF-A03).

NCEER-94-0015 "Generation of Hazard-Consistent Fragility Curves for Seismic Loss Estimation Studies," by H. Hwang and J-R. Huo, 6/14/94, (PB95-181996, A09, MF-A02).

NCEER-94-0016 "Seismic Study of Building Frames with Added Energy-Absorbing Devices," by W.S. Pong, C.S. Tsai and G.C. Lee, 6/20/94, (PB94-219136, A10, A03).

NCEER-94-0017 "Sliding Mode Control for Seismic-Excited Linear and Nonlinear Civil Engineering Structures," by J. Yang, J. Wu, A. Agrawal and Z. Li, 6/21/94, (PB95-138483, A06, MF-A02).

NCEER-94-0018 "3D-BASIS-TABS Version 2.0: Computer Program for Nonlinear Dynamic Analysis of Three Dimensional Base Isolated Structures," by A.M. Reinhorn, S. Nagarajaiah, M.C. Constantinou, P. Tsopelas and R. Li, 6/22/94, (PB95-182176, A08, MF-A02).

NCEER-94-0019 "Proceedings of the International Workshop on Civil Infrastructure Systems: Application of Intelligent Systems and Advanced Materials on Bridge Systems," Edited by G.C. Lee and K.C. Chang, 7/18/94, (PB95-252474, A20, MF-A04).

NCEER-94-0020 "Study of Seismic Isolation Systems for Computer Floors," by V. Lambrou and M.C. Constantinou, 7/19/94, (PB95-138533, A10, MF-A03).

NCEER-94-0021 "Proceedings of the U.S.-Italian Workshop on Guidelines for Seismic Evaluation and Rehabilitation of Unreinforced Masonry Buildings," Edited by D.P. Abrams and G.M. Calvi, 7/20/94, (PB95-138749, A13, MF-A03).

NCEER-94-0022 "NCEER-Taisei Corporation Research Program on Sliding Seismic Isolation Systems for Bridges: Experimental and Analytical Study of a System Consisting of Lubricated PTFE Sliding Bearings and Mild Steel Dampers," by P. Tsopelas and M.C. Constantinou, 7/22/94, (PB95-182184, A08, MF-A02).

NCEER-94-0023 “Development of Reliability-Based Design Criteria for Buildings Under Seismic Load,” by Y.K. Wen, H. Hwang and M. Shinozuka, 8/1/94, (PB95-211934, A08, MF-A02).

NCEER-94-0024 “Experimental Verification of Acceleration Feedback Control Strategies for an Active Tendon System,” by S.J. Dyke, B.F. Spencer, Jr., P. Quast, M.K. Sain, D.C. Kaspari, Jr. and T.T. Soong, 8/29/94, (PB95-212320, A05, MF-A01).

NCEER-94-0025 “Seismic Retrofitting Manual for Highway Bridges,” Edited by I.G. Buckle and I.F. Friedland, published by the Federal Highway Administration (PB95-212676, A15, MF-A03).

NCEER-94-0026 “Proceedings from the Fifth U.S.-Japan Workshop on Earthquake Resistant Design of Lifeline Facilities and Countermeasures Against Soil Liquefaction,” Edited by T.D. O’Rourke and M. Hamada, 11/7/94, (PB95-220802, A99, MF-E08).

NCEER-95-0001 “Experimental and Analytical Investigation of Seismic Retrofit of Structures with Supplemental Damping: Part 1 - Fluid Viscous Damping Devices,” by A.M. Reinhorn, C. Li and M.C. Constantinou, 1/3/95, (PB95-266599, A09, MF-A02).

NCEER-95-0002 “Experimental and Analytical Study of Low-Cycle Fatigue Behavior of Semi-Rigid Top-And-Seat Angle Connections,” by G. Pekcan, J.B. Mander and S.S. Chen, 1/5/95, (PB95-220042, A07, MF-A02).

NCEER-95-0003 “NCEER-ATC Joint Study on Fragility of Buildings,” by T. Anagnos, C. Rojahn and A.S. Kiremidjian, 1/20/95, (PB95-220026, A06, MF-A02).

NCEER-95-0004 “Nonlinear Control Algorithms for Peak Response Reduction,” by Z. Wu, T.T. Soong, V. Gattulli and R.C. Lin, 2/16/95, (PB95-220349, A05, MF-A01).

NCEER-95-0005 “Pipeline Replacement Feasibility Study: A Methodology for Minimizing Seismic and Corrosion Risks to Underground Natural Gas Pipelines,” by R.T. Eguchi, H.A. Seligson and D.G. Honegger, 3/2/95, (PB95-252326, A06, MF-A02).

NCEER-95-0006 “Evaluation of Seismic Performance of an 11-Story Frame Building During the 1994 Northridge Earthquake,” by F. Naeim, R. DiSulio, K. Benuska, A. Reinhorn and C. Li, not available.

NCEER-95-0007 “Prioritization of Bridges for Seismic Retrofitting,” by N. Basöz and A.S. Kiremidjian, 4/24/95, (PB95-252300, A08, MF-A02).

NCEER-95-0008 “Method for Developing Motion Damage Relationships for Reinforced Concrete Frames,” by A. Singhal and A.S. Kiremidjian, 5/11/95, (PB95-266607, A06, MF-A02).

NCEER-95-0009 “Experimental and Analytical Investigation of Seismic Retrofit of Structures with Supplemental Damping: Part II - Friction Devices,” by C. Li and A.M. Reinhorn, 7/6/95, (PB96-128087, A11, MF-A03).

NCEER-95-0010 “Experimental Performance and Analytical Study of a Non-Ductile Reinforced Concrete Frame Structure Retrofitted with Elastomeric Spring Dampers,” by G. Pekcan, J.B. Mander and S.S. Chen, 7/14/95, (PB96-137161, A08, MF-A02).

NCEER-95-0011 “Development and Experimental Study of Semi-Active Fluid Damping Devices for Seismic Protection of Structures,” by M.D. Symans and M.C. Constantinou, 8/3/95, (PB96-136940, A23, MF-A04).

NCEER-95-0012 “Real-Time Structural Parameter Modification (RSPM): Development of Innervated Structures,” by Z. Liang, M. Tong and G.C. Lee, 4/11/95, (PB96-137153, A06, MF-A01).

NCEER-95-0013 “Experimental and Analytical Investigation of Seismic Retrofit of Structures with Supplemental Damping: Part III - Viscous Damping Walls,” by A.M. Reinhorn and C. Li, 10/1/95, (PB96-176409, A11, MF-A03).

NCEER-95-0014 “Seismic Fragility Analysis of Equipment and Structures in a Memphis Electric Substation,” by J-R. Huo and H.H.M. Hwang, 8/10/95, (PB96-128087, A09, MF-A02).

NCEER-95-0015 “The Hanshin-Awaji Earthquake of January 17, 1995: Performance of Lifelines,” Edited by M. Shinozuka, 11/3/95, (PB96-176383, A15, MF-A03).

NCEER-95-0016 “Highway Culvert Performance During Earthquakes,” by T.L. Youd and C.J. Beckman, available as NCEER-96-0015.

NCEER-95-0017 “The Hanshin-Awaji Earthquake of January 17, 1995: Performance of Highway Bridges,” Edited by I.G. Buckle, 12/1/95, not available.

NCEER-95-0018 “Modeling of Masonry Infill Panels for Structural Analysis,” by A.M. Reinhorn, A. Madan, R.E. Valles, Y. Reichmann and J.B. Mander, 12/8/95, (PB97-110886, MF-A01, A06).

NCEER-95-0019 “Optimal Polynomial Control for Linear and Nonlinear Structures,” by A.K. Agrawal and J.N. Yang, 12/11/95, (PB96-168737, A07, MF-A02).

NCEER-95-0020 "Retrofit of Non-Ductile Reinforced Concrete Frames Using Friction Dampers," by R.S. Rao, P. Gergely and R.N. White, 12/22/95, (PB97-133508, A10, MF-A02).

NCEER-95-0021 "Parametric Results for Seismic Response of Pile-Supported Bridge Bents," by G. Mylonakis, A. Nikolaou and G. Gazetas, 12/22/95, (PB97-100242, A12, MF-A03).

NCEER-95-0022 "Kinematic Bending Moments in Seismically Stressed Piles," by A. Nikolaou, G. Mylonakis and G. Gazetas, 12/23/95, (PB97-113914, MF-A03, A13).

NCEER-96-0001 "Dynamic Response of Unreinforced Masonry Buildings with Flexible Diaphragms," by A.C. Costley and D.P. Abrams," 10/10/96, (PB97-133573, MF-A03, A15).

NCEER-96-0002 "State of the Art Review: Foundations and Retaining Structures," by I. Po Lam, not available.

NCEER-96-0003 "Ductility of Rectangular Reinforced Concrete Bridge Columns with Moderate Confinement," by N. Wehbe, M. Saiidi, D. Sanders and B. Douglas, 11/7/96, (PB97-133557, A06, MF-A02).

NCEER-96-0004 "Proceedings of the Long-Span Bridge Seismic Research Workshop," edited by I.G. Buckle and I.M. Friedland, not available.

NCEER-96-0005 "Establish Representative Pier Types for Comprehensive Study: Eastern United States," by J. Kulicki and Z. Prucz, 5/28/96, (PB98-119217, A07, MF-A02).

NCEER-96-0006 "Establish Representative Pier Types for Comprehensive Study: Western United States," by R. Imbsen, R.A. Schamber and T.A. Osterkamp, 5/28/96, (PB98-118607, A07, MF-A02).

NCEER-96-0007 "Nonlinear Control Techniques for Dynamical Systems with Uncertain Parameters," by R.G. Ghanem and M.I. Bujakov, 5/27/96, (PB97-100259, A17, MF-A03).

NCEER-96-0008 "Seismic Evaluation of a 30-Year Old Non-Ductile Highway Bridge Pier and Its Retrofit," by J.B. Mander, B. Mahmoodzadegan, S. Bhadra and S.S. Chen, 5/31/96, (PB97-110902, MF-A03, A10).

NCEER-96-0009 "Seismic Performance of a Model Reinforced Concrete Bridge Pier Before and After Retrofit," by J.B. Mander, J.H. Kim and C.A. Ligozio, 5/31/96, (PB97-110910, MF-A02, A10).

NCEER-96-0010 "IDARC2D Version 4.0: A Computer Program for the Inelastic Damage Analysis of Buildings," by R.E. Valles, A.M. Reinhorn, S.K. Kunnath, C. Li and A. Madan, 6/3/96, (PB97-100234, A17, MF-A03).

NCEER-96-0011 "Estimation of the Economic Impact of Multiple Lifeline Disruption: Memphis Light, Gas and Water Division Case Study," by S.E. Chang, H.A. Seligson and R.T. Eguchi, 8/16/96, (PB97-133490, A11, MF-A03).

NCEER-96-0012 "Proceedings from the Sixth Japan-U.S. Workshop on Earthquake Resistant Design of Lifeline Facilities and Countermeasures Against Soil Liquefaction, Edited by M. Hamada and T. O'Rourke, 9/11/96, (PB97-133581, A99, MF-A06).

NCEER-96-0013 "Chemical Hazards, Mitigation and Preparedness in Areas of High Seismic Risk: A Methodology for Estimating the Risk of Post-Earthquake Hazardous Materials Release," by H.A. Seligson, R.T. Eguchi, K.J. Tierney and K. Richmond, 11/7/96, (PB97-133565, MF-A02, A08).

NCEER-96-0014 "Response of Steel Bridge Bearings to Reversed Cyclic Loading," by J.B. Mander, D-K. Kim, S.S. Chen and G.J. Premus, 11/13/96, (PB97-140735, A12, MF-A03).

NCEER-96-0015 "Highway Culvert Performance During Past Earthquakes," by T.L. Youd and C.J. Beckman, 11/25/96, (PB97-133532, A06, MF-A01).

NCEER-97-0001 "Evaluation, Prevention and Mitigation of Pounding Effects in Building Structures," by R.E. Valles and A.M. Reinhorn, 2/20/97, (PB97-159552, A14, MF-A03).

NCEER-97-0002 "Seismic Design Criteria for Bridges and Other Highway Structures," by C. Rojahn, R. Mayes, D.G. Anderson, J. Clark, J.H. Hom, R.V. Nutt and M.J. O'Rourke, 4/30/97, (PB97-194658, A06, MF-A03).

NCEER-97-0003 “Proceedings of the U.S.-Italian Workshop on Seismic Evaluation and Retrofit,” Edited by D.P. Abrams and G.M. Calvi, 3/19/97, (PB97-194666, A13, MF-A03).

NCEER-97-0004 "Investigation of Seismic Response of Buildings with Linear and Nonlinear Fluid Viscous Dampers," by A.A. Seleemah and M.C. Constantinou, 5/21/97, (PB98-109002, A15, MF-A03).

NCEER-97-0005 "Proceedings of the Workshop on Earthquake Engineering Frontiers in Transportation Facilities," edited by G.C. Lee and I.M. Friedland, 8/29/97, (PB98-128911, A25, MR-A04).

NCEER-97-0006 "Cumulative Seismic Damage of Reinforced Concrete Bridge Piers," by S.K. Kunnath, A. El-Bahy, A. Taylor and W. Stone, 9/2/97, (PB98-108814, A11, MF-A03).

NCEER-97-0007 "Structural Details to Accommodate Seismic Movements of Highway Bridges and Retaining Walls," by R.A. Imbsen, R.A. Schamber, E. Thorkildsen, A. Kartoum, B.T. Martin, T.N. Rosser and J.M. Kulicki, 9/3/97, (PB98-108996, A09, MF-A02).

NCEER-97-0008 "A Method for Earthquake Motion-Damage Relationships with Application to Reinforced Concrete Frames," by A. Singhal and A.S. Kiremidjian, 9/10/97, (PB98-108988, A13, MF-A03).

NCEER-97-0009 "Seismic Analysis and Design of Bridge Abutments Considering Sliding and Rotation," by K. Fishman and R. Richards, Jr., 9/15/97, (PB98-108897, A06, MF-A02).

NCEER-97-0010 "Proceedings of the FHWA/NCEER Workshop on the National Representation of Seismic Ground Motion for New and Existing Highway Facilities," edited by I.M. Friedland, M.S. Power and R.L. Mayes, 9/22/97, (PB98-128903, A21, MF-A04).

NCEER-97-0011 "Seismic Analysis for Design or Retrofit of Gravity Bridge Abutments," by K.L. Fishman, R. Richards, Jr. and R.C. Divito, 10/2/97, (PB98-128937, A08, MF-A02).

NCEER-97-0012 "Evaluation of Simplified Methods of Analysis for Yielding Structures," by P. Tsopelas, M.C. Constantinou, C.A. Kircher and A.S. Whittaker, 10/31/97, (PB98-128929, A10, MF-A03).

NCEER-97-0013 "Seismic Design of Bridge Columns Based on Control and Repairability of Damage," by C-T. Cheng and J.B. Mander, 12/8/97, (PB98-144249, A11, MF-A03).

NCEER-97-0014 "Seismic Resistance of Bridge Piers Based on Damage Avoidance Design," by J.B. Mander and C-T. Cheng, 12/10/97, (PB98-144223, A09, MF-A02).

NCEER-97-0015 “Seismic Response of Nominally Symmetric Systems with Strength Uncertainty,” by S. Balopoulou and M. Grigoriu, 12/23/97, (PB98-153422, A11, MF-A03).

NCEER-97-0016 “Evaluation of Seismic Retrofit Methods for Reinforced Concrete Bridge Columns,” by T.J. Wipf, F.W. Klaiber and F.M. Russo, 12/28/97, (PB98-144215, A12, MF-A03).

NCEER-97-0017 “Seismic Fragility of Existing Conventional Reinforced Concrete Highway Bridges,” by C.L. Mullen and A.S. Cakmak, 12/30/97, (PB98-153406, A08, MF-A02).

NCEER-97-0018 “Loss Asssessment of Memphis Buildings,” edited by D.P. Abrams and M. Shinozuka, 12/31/97, (PB98-144231, A13, MF-A03).

NCEER-97-0019 “Seismic Evaluation of Frames with Infill Walls Using Quasi-static Experiments,” by K.M. Mosalam, R.N. White and P. Gergely, 12/31/97, (PB98-153455, A07, MF-A02).

NCEER-97-0020 “Seismic Evaluation of Frames with Infill Walls Using Pseudo-dynamic Experiments,” by K.M. Mosalam, R.N. White and P. Gergely, 12/31/97, (PB98-153430, A07, MF-A02).

NCEER-97-0021 “Computational Strategies for Frames with Infill Walls: Discrete and Smeared Crack Analyses and Seismic Fragility,” by K.M. Mosalam, R.N. White and P. Gergely, 12/31/97, (PB98-153414, A10, MF-A02).

NCEER-97-0022 "Proceedings of the NCEER Workshop on Evaluation of Liquefaction Resistance of Soils," edited by T.L. Youd and I.M. Idriss, 12/31/97, (PB98-155617, A15, MF-A03).

MCEER-98-0001 "Extraction of Nonlinear Hysteretic Properties of Seismically Isolated Bridges from Quick-Release Field Tests," by Q. Chen, B.M. Douglas, E.M. Maragakis and I.G. Buckle, 5/26/98, (PB99-118838, A06, MF-A01).

MCEER-98-0002 "Methodologies for Evaluating the Importance of Highway Bridges," by A. Thomas, S. Eshenaur and J. Kulicki, 5/29/98, (PB99-118846, A10, MF-A02).

MCEER-98-0003 "Capacity Design of Bridge Piers and the Analysis of Overstrength," by J.B. Mander, A. Dutta and P. Goel, 6/1/98, (PB99-118853, A09, MF-A02).

MCEER-98-0004 "Evaluation of Bridge Damage Data from the Loma Prieta and Northridge, California Earthquakes," by N. Basoz and A. Kiremidjian, 6/2/98, (PB99-118861, A15, MF-A03).

MCEER-98-0005 "Screening Guide for Rapid Assessment of Liquefaction Hazard at Highway Bridge Sites," by T. L. Youd, 6/16/98, (PB99-118879, A06, not available on microfiche).

MCEER-98-0006 "Structural Steel and Steel/Concrete Interface Details for Bridges," by P. Ritchie, N. Kauhl and J. Kulicki, 7/13/98, (PB99-118945, A06, MF-A01).

MCEER-98-0007 "Capacity Design and Fatigue Analysis of Confined Concrete Columns," by A. Dutta and J.B. Mander, 7/14/98, (PB99-118960, A14, MF-A03).

MCEER-98-0008 "Proceedings of the Workshop on Performance Criteria for Telecommunication Services Under Earthquake Conditions," edited by A.J. Schiff, 7/15/98, (PB99-118952, A08, MF-A02).

MCEER-98-0009 "Fatigue Analysis of Unconfined Concrete Columns," by J.B. Mander, A. Dutta and J.H. Kim, 9/12/98, (PB99-123655, A10, MF-A02).

MCEER-98-0010 "Centrifuge Modeling of Cyclic Lateral Response of Pile-Cap Systems and Seat-Type Abutments in Dry Sands," by A.D. Gadre and R. Dobry, 10/2/98, (PB99-123606, A13, MF-A03).

MCEER-98-0011 "IDARC-BRIDGE: A Computational Platform for Seismic Damage Assessment of Bridge Structures," by A.M. Reinhorn, V. Simeonov, G. Mylonakis and Y. Reichman, 10/2/98, (PB99-162919, A15, MF-A03).

MCEER-98-0012 "Experimental Investigation of the Dynamic Response of Two Bridges Before and After Retrofitting with Elastomeric Bearings," by D.A. Wendichansky, S.S. Chen and J.B. Mander, 10/2/98, (PB99-162927, A15, MF-A03).

MCEER-98-0013 "Design Procedures for Hinge Restrainers and Hinge Sear Width for Multiple-Frame Bridges," by R. Des Roches and G.L. Fenves, 11/3/98, (PB99-140477, A13, MF-A03).

MCEER-98-0014 "Response Modification Factors for Seismically Isolated Bridges," by M.C. Constantinou and J.K. Quarshie, 11/3/98, (PB99-140485, A14, MF-A03).

MCEER-98-0015 "Proceedings of the U.S.-Italy Workshop on Seismic Protective Systems for Bridges," edited by I.M. Friedland and M.C. Constantinou, 11/3/98, (PB2000-101711, A22, MF-A04).

MCEER-98-0016 "Appropriate Seismic Reliability for Critical Equipment Systems: Recommendations Based on Regional Analysis of Financial and Life Loss," by K. Porter, C. Scawthorn, C. Taylor and N. Blais, 11/10/98, (PB99-157265, A08, MF-A02).

MCEER-98-0017 "Proceedings of the U.S. Japan Joint Seminar on Civil Infrastructure Systems Research," edited by M. Shinozuka and A. Rose, 11/12/98, (PB99-156713, A16, MF-A03).

MCEER-98-0018 "Modeling of Pile Footings and Drilled Shafts for Seismic Design," by I. PoLam, M. Kapuskar and D. Chaudhuri, 12/21/98, (PB99-157257, A09, MF-A02).

MCEER-99-0001 "Seismic Evaluation of a Masonry Infilled Reinforced Concrete Frame by Pseudodynamic Testing," by S.G. Buonopane and R.N. White, 2/16/99, (PB99-162851, A09, MF-A02).

MCEER-99-0002 "Response History Analysis of Structures with Seismic Isolation and Energy Dissipation Systems: Verification Examples for Program SAP2000," by J. Scheller and M.C. Constantinou, 2/22/99, (PB99-162869, A08, MF-A02).

MCEER-99-0003 "Experimental Study on the Seismic Design and Retrofit of Bridge Columns Including Axial Load Effects," by A. Dutta, T. Kokorina and J.B. Mander, 2/22/99, (PB99-162877, A09, MF-A02).

MCEER-99-0004 "Experimental Study of Bridge Elastomeric and Other Isolation and Energy Dissipation Systems with Emphasis on Uplift Prevention and High Velocity Near-source Seismic Excitation," by A. Kasalanati and M. C. Constantinou, 2/26/99, (PB99-162885, A12, MF-A03).

MCEER-99-0005 "Truss Modeling of Reinforced Concrete Shear-flexure Behavior," by J.H. Kim and J.B. Mander, 3/8/99, (PB99-163693, A12, MF-A03).

MCEER-99-0006 "Experimental Investigation and Computational Modeling of Seismic Response of a 1:4 Scale Model Steel Structure with a Load Balancing Supplemental Damping System," by G. Pekcan, J.B. Mander and S.S. Chen, 4/2/99, (PB99-162893, A11, MF-A03).

MCEER-99-0007 "Effect of Vertical Ground Motions on the Structural Response of Highway Bridges," by M.R. Button, C.J. Cronin and R.L. Mayes, 4/10/99, (PB2000-101411, A10, MF-A03).

MCEER-99-0008 "Seismic Reliability Assessment of Critical Facilities: A Handbook, Supporting Documentation, and Model Code Provisions," by G.S. Johnson, R.E. Sheppard, M.D. Quilici, S.J. Eder and C.R. Scawthorn, 4/12/99, (PB2000-101701, A18, MF-A04).

MCEER-99-0009 "Impact Assessment of Selected MCEER Highway Project Research on the Seismic Design of Highway Structures," by C. Rojahn, R. Mayes, D.G. Anderson, J.H. Clark, D'Appolonia Engineering, S. Gloyd and R.V. Nutt, 4/14/99, (PB99-162901, A10, MF-A02).

MCEER-99-0010 "Site Factors and Site Categories in Seismic Codes," by R. Dobry, R. Ramos and M.S. Power, 7/19/99, (PB2000-101705, A08, MF-A02).

MCEER-99-0011 "Restrainer Design Procedures for Multi-Span Simply-Supported Bridges," by M.J. Randall, M. Saiidi, E. Maragakis and T. Isakovic, 7/20/99, (PB2000-101702, A10, MF-A02).

MCEER-99-0012 "Property Modification Factors for Seismic Isolation Bearings," by M.C. Constantinou, P. Tsopelas, A. Kasalanati and E. Wolff, 7/20/99, (PB2000-103387, A11, MF-A03).

MCEER-99-0013 "Critical Seismic Issues for Existing Steel Bridges," by P. Ritchie, N. Kauhl and J. Kulicki, 7/20/99, (PB2000-101697, A09, MF-A02).

MCEER-99-0014 "Nonstructural Damage Database," by A. Kao, T.T. Soong and A. Vender, 7/24/99, (PB2000-101407, A06, MF-A01).

MCEER-99-0015 "Guide to Remedial Measures for Liquefaction Mitigation at Existing Highway Bridge Sites," by H.G. Cooke and J. K. Mitchell, 7/26/99, (PB2000-101703, A11, MF-A03).

MCEER-99-0016 "Proceedings of the MCEER Workshop on Ground Motion Methodologies for the Eastern United States," edited by N. Abrahamson and A. Becker, 8/11/99, (PB2000-103385, A07, MF-A02).

MCEER-99-0017 "Quindío, Colombia Earthquake of January 25, 1999: Reconnaissance Report," by A.P. Asfura and P.J. Flores, 10/4/99, (PB2000-106893, A06, MF-A01).

MCEER-99-0018 "Hysteretic Models for Cyclic Behavior of Deteriorating Inelastic Structures," by M.V. Sivaselvan and A.M. Reinhorn, 11/5/99, (PB2000-103386, A08, MF-A02).

MCEER-99-0019 "Proceedings of the 7th U.S.- Japan Workshop on Earthquake Resistant Design of Lifeline Facilities and Countermeasures Against Soil Liquefaction," edited by T.D. O'Rourke, J.P. Bardet and M. Hamada, 11/19/99, (PB2000-103354, A99, MF-A06).

MCEER-99-0020 "Development of Measurement Capability for Micro-Vibration Evaluations with Application to Chip Fabrication Facilities," by G.C. Lee, Z. Liang, J.W. Song, J.D. Shen and W.C. Liu, 12/1/99, (PB2000-105993, A08, MF-A02).

MCEER-99-0021 "Design and Retrofit Methodology for Building Structures with Supplemental Energy Dissipating Systems," by G. Pekcan, J.B. Mander and S.S. Chen, 12/31/99, (PB2000-105994, A11, MF-A03).

MCEER-00-0001 "The Marmara, Turkey Earthquake of August 17, 1999: Reconnaissance Report," edited by C. Scawthorn; with major contributions by M. Bruneau, R. Eguchi, T. Holzer, G. Johnson, J. Mander, J. Mitchell, W. Mitchell, A. Papageorgiou, C. Scaethorn, and G. Webb, 3/23/00, (PB2000-106200, A11, MF-A03).

MCEER-00-0002 "Proceedings of the MCEER Workshop for Seismic Hazard Mitigation of Health Care Facilities," edited by G.C. Lee, M. Ettouney, M. Grigoriu, J. Hauer and J. Nigg, 3/29/00, (PB2000-106892, A08, MF-A02).

MCEER-00-0003 "The Chi-Chi, Taiwan Earthquake of September 21, 1999: Reconnaissance Report," edited by G.C. Lee and C.H. Loh, with major contributions by G.C. Lee, M. Bruneau, I.G. Buckle, S.E. Chang, P.J. Flores, T.D. O'Rourke, M. Shinozuka, T.T. Soong, C-H. Loh, K-C. Chang, Z-J. Chen, J-S. Hwang, M-L. Lin, G-Y. Liu, K-C. Tsai, G.C. Yao and C-L. Yen, 4/30/00, (PB2001-100980, A10, MF-A02).

MCEER-00-0004 "Seismic Retrofit of End-Sway Frames of Steel Deck-Truss Bridges with a Supplemental Tendon System: Experimental and Analytical Investigation," by G. Pekcan, J.B. Mander and S.S. Chen, 7/1/00, (PB2001-100982, A10, MF-A02).

MCEER-00-0005 "Sliding Fragility of Unrestrained Equipment in Critical Facilities," by W.H. Chong and T.T. Soong, 7/5/00, (PB2001-100983, A08, MF-A02).

MCEER-00-0006 "Seismic Response of Reinforced Concrete Bridge Pier Walls in the Weak Direction," by N. Abo-Shadi, M. Saiidi and D. Sanders, 7/17/00, (PB2001-100981, A17, MF-A03).

MCEER-00-0007 "Low-Cycle Fatigue Behavior of Longitudinal Reinforcement in Reinforced Concrete Bridge Columns," by J. Brown and S.K. Kunnath, 7/23/00, (PB2001-104392, A08, MF-A02).

MCEER-00-0008 "Soil Structure Interaction of Bridges for Seismic Analysis," I. PoLam and H. Law, 9/25/00, (PB2001-105397, A08, MF-A02).

MCEER-00-0009 "Proceedings of the First MCEER Workshop on Mitigation of Earthquake Disaster by Advanced Technologies (MEDAT-1), edited by M. Shinozuka, D.J. Inman and T.D. O'Rourke, 11/10/00, (PB2001-105399, A14, MF-A03).

MCEER-00-0010 "Development and Evaluation of Simplified Procedures for Analysis and Design of Buildings with Passive Energy Dissipation Systems, Revision 01," by O.M. Ramirez, M.C. Constantinou, C.A. Kircher, A.S. Whittaker, M.W. Johnson, J.D. Gomez and C. Chrysostomou, 11/16/01, (PB2001-105523, A23, MF-A04).

MCEER-00-0011 "Dynamic Soil-Foundation-Structure Interaction Analyses of Large Caissons," by C-Y. Chang, C-M. Mok, Z-L. Wang, R. Settgast, F. Waggoner, M.A. Ketchum, H.M. Gonnermann and C-C. Chin, 12/30/00, (PB2001-104373, A07, MF-A02).

MCEER-00-0012 "Experimental Evaluation of Seismic Performance of Bridge Restrainers," by A.G. Vlassis, E.M. Maragakis and M. Saiid Saiidi, 12/30/00, (PB2001-104354, A09, MF-A02).

MCEER-00-0013 "Effect of Spatial Variation of Ground Motion on Highway Structures," by M. Shinozuka, V. Saxena and G. Deodatis, 12/31/00, (PB2001-108755, A13, MF-A03).

MCEER-00-0014 "A Risk-Based Methodology for Assessing the Seismic Performance of Highway Systems," by S.D. Werner, C.E. Taylor, J.E. Moore, II, J.S. Walton and S. Cho, 12/31/00, (PB2001-108756, A14, MF-A03).

MCEER-01-0001 "Experimental Investigation of P-Delta Effects to Collapse During Earthquakes," by D. Vian and M. Bruneau, 6/25/01, (PB2002-100534, A17, MF-A03).

MCEER-01-0002 "Proceedings of the Second MCEER Workshop on Mitigation of Earthquake Disaster by Advanced Technologies (MEDAT-2)," edited by M. Bruneau and D.J. Inman, 7/23/01, (PB2002-100434, A16, MF-A03).

MCEER-01-0003 "Sensitivity Analysis of Dynamic Systems Subjected to Seismic Loads," by C. Roth and M. Grigoriu, 9/18/01, (PB2003-100884, A12, MF-A03).

MCEER-01-0004 "Overcoming Obstacles to Implementing Earthquake Hazard Mitigation Policies: Stage 1 Report," by D.J. Alesch and W.J. Petak, 12/17/01, (PB2002-107949, A07, MF-A02).

MCEER-01-0005 "Updating Real-Time Earthquake Loss Estimates: Methods, Problems and Insights," by C.E. Taylor, S.E. Chang and R.T. Eguchi, 12/17/01, (PB2002-107948, A05, MF-A01).

MCEER-01-0006 "Experimental Investigation and Retrofit of Steel Pile Foundations and Pile Bents Under Cyclic Lateral Loadings," by A. Shama, J. Mander, B. Blabac and S. Chen, 12/31/01, (PB2002-107950, A13, MF-A03).

MCEER-02-0001 "Assessment of Performance of Bolu Viaduct in the 1999 Duzce Earthquake in Turkey" by P.C. Roussis, M.C. Constantinou, M. Erdik, E. Durukal and M. Dicleli, 5/8/02, (PB2003-100883, A08, MF-A02).

MCEER-02-0002 "Seismic Behavior of Rail Counterweight Systems of Elevators in Buildings," by M.P. Singh, Rildova and L.E. Suarez, 5/27/02. (PB2003-100882, A11, MF-A03).

MCEER-02-0003 "Development of Analysis and Design Procedures for Spread Footings," by G. Mylonakis, G. Gazetas, S. Nikolaou and A. Chauncey, 10/02/02, (PB2004-101636, A13, MF-A03, CD-A13).

MCEER-02-0004 "Bare-Earth Algorithms for Use with SAR and LIDAR Digital Elevation Models," by C.K. Huyck, R.T. Eguchi and B. Houshmand, 10/16/02, (PB2004-101637, A07, CD-A07).

MCEER-02-0005 "Review of Energy Dissipation of Compression Members in Concentrically Braced Frames," by K.Lee and M. Bruneau, 10/18/02, (PB2004-101638, A10, CD-A10).

MCEER-03-0001 "Experimental Investigation of Light-Gauge Steel Plate Shear Walls for the Seismic Retrofit of Buildings" by J. Berman and M. Bruneau, 5/2/03, (PB2004-101622, A10, MF-A03, CD-A10).

MCEER-03-0002 "Statistical Analysis of Fragility Curves," by M. Shinozuka, M.Q. Feng, H. Kim, T. Uzawa and T. Ueda, 6/16/03, (PB2004-101849, A09, CD-A09).

MCEER-03-0003 "Proceedings of the Eighth U.S.-Japan Workshop on Earthquake Resistant Design f Lifeline Facilities and Countermeasures Against Liquefaction," edited by M. Hamada, J.P. Bardet and T.D. O'Rourke, 6/30/03, (PB2004-104386, A99, CD-A99).

MCEER-03-0004 "Proceedings of the PRC-US Workshop on Seismic Analysis and Design of Special Bridges," edited by L.C. Fan and G.C. Lee, 7/15/03, (PB2004-104387, A14, CD-A14).

MCEER-03-0005 "Urban Disaster Recovery: A Framework and Simulation Model," by S.B. Miles and S.E. Chang, 7/25/03, (PB2004-104388, A07, CD-A07).

MCEER-03-0006 "Behavior of Underground Piping Joints Due to Static and Dynamic Loading," by R.D. Meis, M. Maragakis and R. Siddharthan, 11/17/03, (PB2005-102194, A13, MF-A03, CD-A00).

MCEER-04-0001 "Experimental Study of Seismic Isolation Systems with Emphasis on Secondary System Response and Verification of Accuracy of Dynamic Response History Analysis Methods," by E. Wolff and M. Constantinou, 1/16/04 (PB2005-102195, A99, MF-E08, CD-A00).

MCEER-04-0002 "Tension, Compression and Cyclic Testing of Engineered Cementitious Composite Materials," by K. Kesner and S.L. Billington, 3/1/04, (PB2005-102196, A08, CD-A08).

MCEER-04-0003 "Cyclic Testing of Braces Laterally Restrained by Steel Studs to Enhance Performance During Earthquakes," by O.C. Celik, J.W. Berman and M. Bruneau, 3/16/04, (PB2005-102197, A13, MF-A03, CD-A00).

MCEER-04-0004 "Methodologies for Post Earthquake Building Damage Detection Using SAR and Optical Remote Sensing: Application to the August 17, 1999 Marmara, Turkey Earthquake," by C.K. Huyck, B.J. Adams, S. Cho, R.T. Eguchi, B. Mansouri and B. Houshmand, 6/15/04, (PB2005-104888, A10, CD-A00).

MCEER-04-0005 "Nonlinear Structural Analysis Towards Collapse Simulation: A Dynamical Systems Approach," by M.V. Sivaselvan and A.M. Reinhorn, 6/16/04, (PB2005-104889, A11, MF-A03, CD-A00).

MCEER-04-0006 "Proceedings of the Second PRC-US Workshop on Seismic Analysis and Design of Special Bridges," edited by G.C. Lee and L.C. Fan, 6/25/04, (PB2005-104890, A16, CD-A00).

MCEER-04-0007 "Seismic Vulnerability Evaluation of Axially Loaded Steel Built-up Laced Members," by K. Lee and M. Bruneau, 6/30/04, (PB2005-104891, A16, CD-A00).

MCEER-04-0008 "Evaluation of Accuracy of Simplified Methods of Analysis and Design of Buildings with Damping Systems for Near-Fault and for Soft-Soil Seismic Motions," by E.A. Pavlou and M.C. Constantinou, 8/16/04, (PB2005-104892, A08, MF-A02, CD-A00).

MCEER-04-0009 "Assessment of Geotechnical Issues in Acute Care Facilities in California," by M. Lew, T.D. O'Rourke, R. Dobry and M. Koch, 9/15/04, (PB2005-104893, A08, CD-A00).

MCEER-04-0010 "Scissor-Jack-Damper Energy Dissipation System," by A.N. Sigaher-Boyle and M.C. Constantinou, 12/1/04 (PB2005-108221).

MCEER-04-0011 "Seismic Retrofit of Bridge Steel Truss Piers Using a Controlled Rocking Approach," by M. Pollino and M. Bruneau, 12/20/04 (PB2006-105795).

MCEER-05-0001 "Experimental and Analytical Studies of Structures Seismically Isolated with an Uplift-Restraint Isolation System," by P.C. Roussis and M.C. Constantinou, 1/10/05 (PB2005-108222).

MCEER-05-0002 "A Versatile Experimentation Model for Study of Structures Near Collapse Applied to Seismic Evaluation of Irregular Structures," by D. Kusumastuti, A.M. Reinhorn and A. Rutenberg, 3/31/05 (PB2006-101523).

MCEER-05-0003 "Proceedings of the Third PRC-US Workshop on Seismic Analysis and Design of Special Bridges," edited by L.C. Fan and G.C. Lee, 4/20/05, (PB2006-105796).

MCEER-05-0004 "Approaches for the Seismic Retrofit of Braced Steel Bridge Piers and Proof-of-Concept Testing of an Eccentrically Braced Frame with Tubular Link," by J.W. Berman and M. Bruneau, 4/21/05 (PB2006-101524).

MCEER-05-0005 "Simulation of Strong Ground Motions for Seismic Fragility Evaluation of Nonstructural Components in Hospitals," by A. Wanitkorkul and A. Filiatrault, 5/26/05 (PB2006-500027).

MCEER-05-0006 "Seismic Safety in California Hospitals: Assessing an Attempt to Accelerate the Replacement or Seismic Retrofit of Older Hospital Facilities," by D.J. Alesch, L.A. Arendt and W.J. Petak, 6/6/05 (PB2006-105794).

MCEER-05-0007 "Development of Seismic Strengthening and Retrofit Strategies for Critical Facilities Using Engineered Cementitious Composite Materials," by K. Kesner and S.L. Billington, 8/29/05 (PB2006-111701).

MCEER-05-0008 "Experimental and Analytical Studies of Base Isolation Systems for Seismic Protection of Power Transformers," by N. Murota, M.Q. Feng and G-Y. Liu, 9/30/05 (PB2006-111702).

MCEER-05-0009 "3D-BASIS-ME-MB: Computer Program for Nonlinear Dynamic Analysis of Seismically Isolated Structures," by P.C. Tsopelas, P.C. Roussis, M.C. Constantinou, R. Buchanan and A.M. Reinhorn, 10/3/05 (PB2006-111703).

MCEER-05-0010 "Steel Plate Shear Walls for Seismic Design and Retrofit of Building Structures," by D. Vian and M. Bruneau, 12/15/05 (PB2006-111704).

MCEER-05-0011 "The Performance-Based Design Paradigm," by M.J. Astrella and A. Whittaker, 12/15/05 (PB2006-111705).

MCEER-06-0001 "Seismic Fragility of Suspended Ceiling Systems," H. Badillo-Almaraz, A.S. Whittaker, A.M. Reinhorn and G.P. Cimellaro, 2/4/06 (PB2006-111706).

MCEER-06-0002 "Multi-Dimensional Fragility of Structures," by G.P. Cimellaro, A.M. Reinhorn and M. Bruneau, 3/1/06 (PB2007-106974, A09, MF-A02, CD A00).

MCEER-06-0003 "Built-Up Shear Links as Energy Dissipators for Seismic Protection of Bridges," by P. Dusicka, A.M. Itani and I.G. Buckle, 3/15/06 (PB2006-111708).

MCEER-06-0004 "Analytical Investigation of the Structural Fuse Concept," by R.E. Vargas and M. Bruneau, 3/16/06 (PB2006-111709).

MCEER-06-0005 "Experimental Investigation of the Structural Fuse Concept," by R.E. Vargas and M. Bruneau, 3/17/06 (PB2006-111710).

MCEER-06-0006 "Further Development of Tubular Eccentrically Braced Frame Links for the Seismic Retrofit of Braced Steel Truss Bridge Piers," by J.W. Berman and M. Bruneau, 3/27/06 (PB2007-105147).

MCEER-06-0007 "REDARS Validation Report," by S. Cho, C.K. Huyck, S. Ghosh and R.T. Eguchi, 8/8/06 (PB2007-106983).

MCEER-06-0008 "Review of Current NDE Technologies for Post-Earthquake Assessment of Retrofitted Bridge Columns," by J.W. Song, Z. Liang and G.C. Lee, 8/21/06 (PB2007-106984).

MCEER-06-0009 "Liquefaction Remediation in Silty Soils Using Dynamic Compaction and Stone Columns," by S. Thevanayagam, G.R. Martin, R. Nashed, T. Shenthan, T. Kanagalingam and N. Ecemis, 8/28/06 (PB2007-106985).

MCEER-06-0010 "Conceptual Design and Experimental Investigation of Polymer Matrix Composite Infill Panels for Seismic Retrofitting," by W. Jung, M. Chiewanichakorn and A.J. Aref, 9/21/06 (PB2007-106986).

MCEER-06-0011 "A Study of the Coupled Horizontal-Vertical Behavior of Elastomeric and Lead-Rubber Seismic Isolation Bearings," by G.P. Warn and A.S. Whittaker, 9/22/06 (PB2007-108679).

MCEER-06-0012 "Proceedings of the Fourth PRC-US Workshop on Seismic Analysis and Design of Special Bridges: Advancing Bridge Technologies in Research, Design, Construction and Preservation," Edited by L.C. Fan, G.C. Lee and L. Ziang, 10/12/06 (PB2007-109042).

MCEER-06-0013 "Cyclic Response and Low Cycle Fatigue Characteristics of Plate Steels," by P. Dusicka, A.M. Itani and I.G. Buckle, 11/1/06 06 (PB2007-106987).

MCEER-06-0014 "Proceedings of the Second US-Taiwan Bridge Engineering Workshop," edited by W.P. Yen, J. Shen, J-Y. Chen and M. Wang, 11/15/06 (PB2008-500041).

MCEER-06-0015 "User Manual and Technical Documentation for the REDARS^{TM} Import Wizard," by S. Cho, S. Ghosh, C.K. Huyck and S.D. Werner, 11/30/06 (PB2007-114766).

MCEER-06-0016 "Hazard Mitigation Strategy and Monitoring Technologies for Urban and Infrastructure Public Buildings: Proceedings of the China-US Workshops," edited by X.Y. Zhou, A.L. Zhang, G.C. Lee and M. Tong, 12/12/06 (PB2008-500018).

MCEER-07-0001 "Static and Kinetic Coefficients of Friction for Rigid Blocks," by C. Kafali, S. Fathali, M. Grigoriu and A.S. Whittaker, 3/20/07 (PB2007-114767).

MCEER-07-0002 "Hazard Mitigation Investment Decision Making: Organizational Response to Legislative Mandate," by L.A. Arendt, D.J. Alesch and W.J. Petak, 4/9/07 (PB2007-114768).

MCEER-07-0003 "Seismic Behavior of Bidirectional-Resistant Ductile End Diaphragms with Unbonded Braces in Straight or Skewed Steel Bridges," by O. Celik and M. Bruneau, 4/11/07 (PB2008-105141).

MCEER-07-0004 "Modeling Pile Behavior in Large Pile Groups Under Lateral Loading," by A.M. Dodds and G.R. Martin, 4/16/07(PB2008-105142).

MCEER-07-0005 "Experimental Investigation of Blast Performance of Seismically Resistant Concrete-Filled Steel Tube Bridge Piers," by S. Fujikura, M. Bruneau and D. Lopez-Garcia, 4/20/07 (PB2008-105143).

MCEER-07-0006 "Seismic Analysis of Conventional and Isolated Liquefied Natural Gas Tanks Using Mechanical Analogs," by I.P. Christovasilis and A.S. Whittaker, 5/1/07, not available.

MCEER-07-0007 "Experimental Seismic Performance Evaluation of Isolation/Restraint Systems for Mechanical Equipment – Part 1: Heavy Equipment Study," by S. Fathali and A. Filiatrault, 6/6/07 (PB2008-105144).

MCEER-07-0008 "Seismic Vulnerability of Timber Bridges and Timber Substructures," by A.A. Sharma, J.B. Mander, I.M. Friedland and D.R. Allicock, 6/7/07 (PB2008-105145).

MCEER-07-0009 "Experimental and Analytical Study of the XY-Friction Pendulum (XY-FP) Bearing for Bridge Applications," by C.C. Marin-Artieda, A.S. Whittaker and M.C. Constantinou, 6/7/07 (PB2008-105191).

MCEER-07-0010 "Proceedings of the PRC-US Earthquake Engineering Forum for Young Researchers," Edited by G.C. Lee and X.Z. Qi, 6/8/07 (PB2008-500058).

MCEER-07-0011 "Design Recommendations for Perforated Steel Plate Shear Walls," by R. Purba and M. Bruneau, 6/18/07, (PB2008-105192).

MCEER-07-0012 "Performance of Seismic Isolation Hardware Under Service and Seismic Loading," by M.C. Constantinou, A.S. Whittaker, Y. Kalpakidis, D.M. Fenz and G.P. Warn, 8/27/07, (PB2008-105193).

MCEER-07-0013 "Experimental Evaluation of the Seismic Performance of Hospital Piping Subassemblies," by E.R. Goodwin, E. Maragakis and A.M. Itani, 9/4/07, (PB2008-105194).

MCEER-07-0014 "A Simulation Model of Urban Disaster Recovery and Resilience: Implementation for the 1994 Northridge Earthquake," by S. Miles and S.E. Chang, 9/7/07, (PB2008-106426).

MCEER-07-0015 "Statistical and Mechanistic Fragility Analysis of Concrete Bridges," by M. Shinozuka, S. Banerjee and S-H. Kim, 9/10/07, (PB2008-106427).

MCEER-07-0016 "Three-Dimensional Modeling of Inelastic Buckling in Frame Structures," by M. Schachter and AM. Reinhorn, 9/13/07, (PB2008-108125).

MCEER-07-0017 "Modeling of Seismic Wave Scattering on Pile Groups and Caissons," by I. Po Lam, H. Law and C.T. Yang, 9/17/07 (PB2008-108150).

MCEER-07-0018 "Bridge Foundations: Modeling Large Pile Groups and Caissons for Seismic Design," by I. Po Lam, H. Law and G.R. Martin (Coordinating Author), 12/1/07 (PB2008-111190).

MCEER-07-0019 "Principles and Performance of Roller Seismic Isolation Bearings for Highway Bridges," by G.C. Lee, Y.C. Ou, Z. Liang, T.C. Niu and J. Song, 12/10/07 (PB2009-110466).

MCEER-07-0020 "Centrifuge Modeling of Permeability and Pinning Reinforcement Effects on Pile Response to Lateral Spreading," by L.L Gonzalez-Lagos, T. Abdoun and R. Dobry, 12/10/07 (PB2008-111191).

MCEER-07-0021 "Damage to the Highway System from the Pisco, Perú Earthquake of August 15, 2007," by J.S. O'Connor, L. Mesa and M. Nykamp, 12/10/07, (PB2008-108126).

MCEER-07-0022 "Experimental Seismic Performance Evaluation of Isolation/Restraint Systems for Mechanical Equipment – Part 2: Light Equipment Study," by S. Fathali and A. Filiatrault, 12/13/07 (PB2008-111192).

MCEER-07-0023 "Fragility Considerations in Highway Bridge Design," by M. Shinozuka, S. Banerjee and S.H. Kim, 12/14/07 (PB2008-111193).

MCEER-07-0024 "Performance Estimates for Seismically Isolated Bridges," by G.P. Warn and A.S. Whittaker, 12/30/07 (PB2008-112230).

MCEER-08-0001 "Seismic Performance of Steel Girder Bridge Superstructures with Conventional Cross Frames," by L.P. Carden, A.M. Itani and I.G. Buckle, 1/7/08, (PB2008-112231).

MCEER-08-0002 "Seismic Performance of Steel Girder Bridge Superstructures with Ductile End Cross Frames with Seismic Isolators," by L.P. Carden, A.M. Itani and I.G. Buckle, 1/7/08 (PB2008-112232).

MCEER-08-0003 "Analytical and Experimental Investigation of a Controlled Rocking Approach for Seismic Protection of Bridge Steel Truss Piers," by M. Pollino and M. Bruneau, 1/21/08 (PB2008-112233).

MCEER-08-0004 "Linking Lifeline Infrastructure Performance and Community Disaster Resilience: Models and Multi-Stakeholder Processes," by S.E. Chang, C. Pasion, K. Tatebe and R. Ahmad, 3/3/08 (PB2008-112234).

MCEER-08-0005 "Modal Analysis of Generally Damped Linear Structures Subjected to Seismic Excitations," by J. Song, Y-L. Chu, Z. Liang and G.C. Lee, 3/4/08 (PB2009-102311).

MCEER-08-0006 "System Performance Under Multi-Hazard Environments," by C. Kafali and M. Grigoriu, 3/4/08 (PB2008-112235).

MCEER-08-0007 "Mechanical Behavior of Multi-Spherical Sliding Bearings," by D.M. Fenz and M.C. Constantinou, 3/6/08 (PB2008-112236).

MCEER-08-0008 "Post-Earthquake Restoration of the Los Angeles Water Supply System," by T.H.P. Tabucchi and R.A. Davidson, 3/7/08 (PB2008-112237).

MCEER-08-0009 "Fragility Analysis of Water Supply Systems," by A. Jacobson and M. Grigoriu, 3/10/08 (PB2009-105545).

MCEER-08-0010 "Experimental Investigation of Full-Scale Two-Story Steel Plate Shear Walls with Reduced Beam Section Connections," by B. Qu, M. Bruneau, C-H. Lin and K-C. Tsai, 3/17/08 (PB2009-106368).

MCEER-08-0011 "Seismic Evaluation and Rehabilitation of Critical Components of Electrical Power Systems," S. Ersoy, B. Feizi, A. Ashrafi and M. Ala Saadeghvaziri, 3/17/08 (PB2009-105546).

MCEER-08-0012 "Seismic Behavior and Design of Boundary Frame Members of Steel Plate Shear Walls," by B. Qu and M. Bruneau, 4/26/08 . (PB2009-106744).

MCEER-08-0013 "Development and Appraisal of a Numerical Cyclic Loading Protocol for Quantifying Building System Performance," by A. Filiatrault, A. Wanitkorkul and M. Constantinou, 4/27/08 (PB2009-107906).

MCEER-08-0014 "Structural and Nonstructural Earthquake Design: The Challenge of Integrating Specialty Areas in Designing Complex, Critical Facilities," by W.J. Petak and D.J. Alesch, 4/30/08 (PB2009-107907).

MCEER-08-0015 "Seismic Performance Evaluation of Water Systems," by Y. Wang and T.D. O'Rourke, 5/5/08 (PB2009-107908).

MCEER-08-0016 "Seismic Response Modeling of Water Supply Systems," by P. Shi and T.D. O'Rourke, 5/5/08 (PB2009-107910).

MCEER-08-0017 "Numerical and Experimental Studies of Self-Centering Post-Tensioned Steel Frames," by D. Wang and A. Filiatrault, 5/12/08 (PB2009-110479).

MCEER-08-0018 "Development, Implementation and Verification of Dynamic Analysis Models for Multi-Spherical Sliding Bearings," by D.M. Fenz and M.C. Constantinou, 8/15/08 (PB2009-107911).

MCEER-08-0019 "Performance Assessment of Conventional and Base Isolated Nuclear Power Plants for Earthquake Blast Loadings," by Y.N. Huang, A.S. Whittaker and N. Luco, 10/28/08 (PB2009-107912).

MCEER-08-0020 "Remote Sensing for Resilient Multi-Hazard Disaster Response – Volume I: Introduction to Damage Assessment Methodologies," by B.J. Adams and R.T. Eguchi, 11/17/08 (PB2010-102695).

MCEER-08-0021 "Remote Sensing for Resilient Multi-Hazard Disaster Response – Volume II: Counting the Number of Collapsed Buildings Using an Object-Oriented Analysis: Case Study of the 2003 Bam Earthquake," by L. Gusella, C.K. Huyck and B.J. Adams, 11/17/08 (PB2010-100925).

MCEER-08-0022 "Remote Sensing for Resilient Multi-Hazard Disaster Response – Volume III: Multi-Sensor Image Fusion Techniques for Robust Neighborhood-Scale Urban Damage Assessment," by B.J. Adams and A. McMillan, 11/17/08 (PB2010-100926).

MCEER-08-0023 "Remote Sensing for Resilient Multi-Hazard Disaster Response – Volume IV: A Study of Multi-Temporal and Multi-Resolution SAR Imagery for Post-Katrina Flood Monitoring in New Orleans," by A. McMillan, J.G. Morley, B.J. Adams and S. Chesworth, 11/17/08 (PB2010-100927).

MCEER-08-0024 "Remote Sensing for Resilient Multi-Hazard Disaster Response – Volume V: Integration of Remote Sensing Imagery and VIEWS^{TM} Field Data for Post-Hurricane Charley Building Damage Assessment," by J.A. Womble, K. Mehta and B.J. Adams, 11/17/08 (PB2009-115532).

MCEER-08-0025 "Building Inventory Compilation for Disaster Management: Application of Remote Sensing and Statistical Modeling," by P. Sarabandi, A.S. Kiremidjian, R.T. Eguchi and B. J. Adams, 11/20/08 (PB2009-110484).

MCEER-08-0026 "New Experimental Capabilities and Loading Protocols for Seismic Qualification and Fragility Assessment of Nonstructural Systems," by R. Retamales, G. Mosqueda, A. Filiatrault and A. Reinhorn, 11/24/08 (PB2009-110485).

MCEER-08-0027 "Effects of Heating and Load History on the Behavior of Lead-Rubber Bearings," by I.V. Kalpakidis and M.C. Constantinou, 12/1/08 (PB2009-115533).

MCEER-08-0028 "Experimental and Analytical Investigation of Blast Performance of Seismically Resistant Bridge Piers," by S.Fujikura and M. Bruneau, 12/8/08 (PB2009-115534).

MCEER-08-0029 "Evolutionary Methodology for Aseismic Decision Support," by Y. Hu and G. Dargush, 12/15/08.

MCEER-08-0030 "Development of a Steel Plate Shear Wall Bridge Pier System Conceived from a Multi-Hazard Perspective," by D. Keller and M. Bruneau, 12/19/08 (PB2010-102696).

MCEER-09-0001 "Modal Analysis of Arbitrarily Damped Three-Dimensional Linear Structures Subjected to Seismic Excitations," by Y.L. Chu, J. Song and G.C. Lee, 1/31/09 (PB2010-100922).

MCEER-09-0002 "Air-Blast Effects on Structural Shapes," by G. Ballantyne, A.S. Whittaker, A.J. Aref and G.F. Dargush, 2/2/09 (PB2010-102697).

MCEER-09-0003 "Water Supply Performance During Earthquakes and Extreme Events," by A.L. Bonneau and T.D. O'Rourke, 2/16/09 (PB2010-100923).

MCEER-09-0004 "Generalized Linear (Mixed) Models of Post-Earthquake Ignitions," by R.A. Davidson, 7/20/09 (PB2010-102698).

MCEER-09-0005 "Seismic Testing of a Full-Scale Two-Story Light-Frame Wood Building: NEESWood Benchmark Test," by I.P. Christovasilis, A. Filiatrault and A. Wanitkorkul, 7/22/09 (PB2012-102401).

MCEER-09-0006 "IDARC2D Version 7.0: A Program for the Inelastic Damage Analysis of Structures," by A.M. Reinhorn, H. Roh, M. Sivaselvan, S.K. Kunnath, R.E. Valles, A. Madan, C. Li, R. Lobo and Y.J. Park, 7/28/09 (PB2010-103199).

MCEER-09-0007 "Enhancements to Hospital Resiliency: Improving Emergency Planning for and Response to Hurricanes," by D.B. Hess and L.A. Arendt, 7/30/09 (PB2010-100924).

MCEER-09-0008 "Assessment of Base-Isolated Nuclear Structures for Design and Beyond-Design Basis Earthquake Shaking," by Y.N. Huang, A.S. Whittaker, R.P. Kennedy and R.L. Mayes, 8/20/09 (PB2010-102699).

MCEER-09-0009 "Quantification of Disaster Resilience of Health Care Facilities," by G.P. Cimellaro, C. Fumo, A.M Reinhorn and M. Bruneau, 9/14/09 (PB2010-105384).

MCEER-09-0010 "Performance-Based Assessment and Design of Squat Reinforced Concrete Shear Walls," by C.K. Gulec and A.S. Whittaker, 9/15/09 (PB2010-102700).

MCEER-09-0011 "Proceedings of the Fourth US-Taiwan Bridge Engineering Workshop," edited by W.P. Yen, J.J. Shen, T.M. Lee and R.B. Zheng, 10/27/09 (PB2010-500009).

MCEER-09-0012 "Proceedings of the Special International Workshop on Seismic Connection Details for Segmental Bridge Construction," edited by W. Phillip Yen and George C. Lee, 12/21/09 (PB2012-102402).

MCEER-10-0001 "Direct Displacement Procedure for Performance-Based Seismic Design of Multistory Woodframe Structures," by W. Pang and D. Rosowsky, 4/26/10 (PB2012-102403).

MCEER-10-0002 "Simplified Direct Displacement Design of Six-Story NEESWood Capstone Building and Pre-Test Seismic Performance Assessment," by W. Pang, D. Rosowsky, J. van de Lindt and S. Pei, 5/28/10 (PB2012-102404).

MCEER-10-0003 "Integration of Seismic Protection Systems in Performance-Based Seismic Design of Woodframed Structures," by J.K. Shinde and M.D. Symans, 6/18/10 (PB2012-102405).

MCEER-10-0004 "Modeling and Seismic Evaluation of Nonstructural Components: Testing Frame for Experimental Evaluation of Suspended Ceiling Systems," by A.M. Reinhorn, K.P. Ryu and G. Maddaloni, 6/30/10 (PB2012-102406).

MCEER-10-0005 "Analytical Development and Experimental Validation of a Structural-Fuse Bridge Pier Concept," by S. El-Bahey and M. Bruneau, 10/1/10 (PB2012-102407).

MCEER-10-0006 "A Framework for Defining and Measuring Resilience at the Community Scale: The PEOPLES Resilience Framework," by C.S. Renschler, A.E. Frazier, L.A. Arendt, G.P. Cimellaro, A.M. Reinhorn and M. Bruneau, 10/8/10 (PB2012-102408).

MCEER-10-0007 "Impact of Horizontal Boundary Elements Design on Seismic Behavior of Steel Plate Shear Walls," by R. Purba and M. Bruneau, 11/14/10 (PB2012-102409).

MCEER-10-0008 "Seismic Testing of a Full-Scale Mid-Rise Building: The NEESWood Capstone Test," by S. Pei, J.W. van de Lindt, S.E. Pryor, H. Shimizu, H. Isoda and D.R. Rammer, 12/1/10 (PB2012-102410).

MCEER-10-0009 "Modeling the Effects of Detonations of High Explosives to Inform Blast-Resistant Design," by P. Sherkar, A.S. Whittaker and A.J. Aref, 12/1/10 (PB2012-102411).

MCEER-10-0010 "L'Aquila Earthquake of April 6, 2009 in Italy: Rebuilding a Resilient City to Withstand Multiple Hazards," by G.P. Cimellaro, I.P. Christovasilis, A.M. Reinhorn, A. De Stefano and T. Kirova, 12/29/10.

MCEER-11-0001 "Numerical and Experimental Investigation of the Seismic Response of Light-Frame Wood Structures," by I.P. Christovasilis and A. Filiatrault, 8/8/11 (PB2012-102412).

MCEER-11-0002 "Seismic Design and Analysis of a Precast Segmental Concrete Bridge Model," by M. Anagnostopoulou, A. Filiatrault and A. Aref, 9/15/11.

MCEER-11-0003 'Proceedings of the Workshop on Improving Earthquake Response of Substation Equipment," Edited by A.M. Reinhorn, 9/19/11 (PB2012-102413).

MCEER-11-0004 "LRFD-Based Analysis and Design Procedures for Bridge Bearings and Seismic Isolators," by M.C. Constantinou, I. Kalpakidis, A. Filiatrault and R.A. Ecker Lay, 9/26/11.

MCEER-11-0005 "Experimental Seismic Evaluation, Model Parameterization, and Effects of Cold-Formed Steel-Framed Gypsum Partition Walls on the Seismic Performance of an Essential Facility," by R. Davies, R. Retamales, G. Mosqueda and A. Filiatrault, 10/12/11.

MCEER-11-0006 "Modeling and Seismic Performance Evaluation of High Voltage Transformers and Bushings," by A.M. Reinhorn, K. Oikonomou, H. Roh, A. Schiff and L. Kempner, Jr., 10/3/11.

MCEER-11-0007 "Extreme Load Combinations: A Survey of State Bridge Engineers," by G.C. Lee, Z. Liang, J.J. Shen and J.S. O'Connor, 10/14/11.

MCEER-12-0001 "Simplified Analysis Procedures in Support of Performance Based Seismic Design," by Y.N. Huang and A.S. Whittaker.

MCEER-12-0002 "Seismic Protection of Electrical Transformer Bushing Systems by Stiffening Techniques," by M. Koliou, A. Filiatrault, A.M. Reinhorn and N. Oliveto, 6/1/12.

MCEER-12-0003 "Post-Earthquake Bridge Inspection Guidelines," by J.S. O'Connor and S. Alampalli, 6/8/12.

MCEER-12-0004 "Integrated Design Methodology for Isolated Floor Systems in Single-Degree-of-Freedom Structural Fuse Systems," by S. Cui, M. Bruneau and M.C. Constantinou, 6/13/12.

MCEER-12-0005 "Characterizing the Rotational Components of Earthquake Ground Motion," by D. Basu, A.S. Whittaker and M.C. Constantinou, 6/15/12.

MCEER-12-0006 "Bayesian Fragility for Nonstructural Systems," by C.H. Lee and M.D. Grigoriu, 9/12/12.

MCEER-12-0007 "A Numerical Model for Capturing the In-Plane Seismic Response of Interior Metal Stud Partition Walls," by R.L. Wood and T.C. Hutchinson, 9/12/12.

MCEER-12-0008 "Assessment of Floor Accelerations in Yielding Buildings," by J.D. Wieser, G. Pekcan, A.E. Zaghi, A.M. Itani and E. Maragakis, 10/5/12.

MCEER-13-0001 "Experimental Seismic Study of Pressurized Fire Sprinkler Piping Systems," by Y. Tian, A. Filiatrault and G. Mosqueda, 4/8/13.

MCEER-13-0002 "Enhancing Resource Coordination for Multi-Modal Evacuation Planning," by D.B. Hess, B.W. Conley and C.M. Farrell, 2/8/13.

MCEER-13-0003 "Seismic Response of Base Isolated Buildings Considering Pounding to Moat Walls," by A. Masroor and G. Mosqueda, 2/26/13.

MCEER-13-0004 "Seismic Response Control of Structures Using a Novel Adaptive Passive Negative Stiffness Device," by D.T.R. Pasala, A.A. Sarlis, S. Nagarajaiah, A.M. Reinhorn, M.C. Constantinou and D.P. Taylor, 6/10/13.

MCEER-13-0005 "Negative Stiffness Device for Seismic Protection of Structures," by A.A. Sarlis, D.T.R. Pasala, M.C. Constantinou, A.M. Reinhorn, S. Nagarajaiah and D.P. Taylor, 6/12/13.

MCEER-13-0006 "Emilia Earthquake of May 20, 2012 in Northern Italy: Rebuilding a Resilient Community to Withstand Multiple Hazards," by G.P. Cimellaro, M. Chiriatti, A.M. Reinhorn and L. Tirca, June 30, 2013.

MCEER-13-0007 "Precast Concrete Segmental Components and Systems for Accelerated Bridge Construction in Seismic Regions," by A.J. Aref, G.C. Lee, Y.C. Ou and P. Sideris, with contributions from K.C. Chang, S. Chen, A. Filiatrault and Y. Zhou, June 13, 2013.

MCEER-13-0008 "A Study of U.S. Bridge Failures (1980-2012)," by G.C. Lee, S.B. Mohan, C. Huang and B.N. Fard, June 15, 2013.

MCEER-13-0009 "Development of a Database Framework for Modeling Damaged Bridges," by G.C. Lee, J.C. Qi and C. Huang, June 16, 2013.

MCEER-13-0010 "Model of Triple Friction Pendulum Bearing for General Geometric and Frictional Parameters and for Uplift Conditions," by A.A. Sarlis and M.C. Constantinou, July 1, 2013.

MCEER-13-0011 "Shake Table Testing of Triple Friction Pendulum Isolators under Extreme Conditions," by A.A. Sarlis, M.C. Constantinou and A.M. Reinhorn, July 2, 2013.

MCEER-13-0012 "Theoretical Framework for the Development of MH-LRFD," by G.C. Lee (coordinating author), H.A Capers, Jr., C. Huang, J.M. Kulicki, Z. Liang, T. Murphy, J.J.D. Shen, M. Shinozuka and P.W.H. Yen, July 31, 2013.

MCEER-13-0013 "Seismic Protection of Highway Bridges with Negative Stiffness Devices," by N.K.A. Attary, M.D. Symans, S. Nagarajaiah, A.M. Reinhorn, M.C. Constantinou, A.A. Sarlis, D.T.R. Pasala, and D.P. Taylor, September 3, 2014.

MCEER-14-0001 "Simplified Seismic Collapse Capacity-Based Evaluation and Design of Frame Buildings with and without Supplemental Damping Systems," by M. Hamidia, A. Filiatrault, and A. Aref, May 19, 2014.

MCEER-14-0002 "Comprehensive Analytical Seismic Fragility of Fire Sprinkler Piping Systems," by Siavash Soroushian, Emmanuel "Manos" Maragakis, Arash E. Zaghi, Alicia Echevarria, Yuan Tian and Andre Filiatrault, August 26, 2014.

MCEER-14-0003 "Hybrid Simulation of the Seismic Response of a Steel Moment Frame Building Structure through Collapse," by M. Del Carpio Ramos, G. Mosqueda and D.G. Lignos, October 30, 2014.

MCEER-14-0004 "Blast and Seismic Resistant Concrete-Filled Double Skin Tubes and Modified Steel Jacketed Bridge Columns," by P.P. Fouche and M. Bruneau, June 30, 2015.

MCEER-14-0005 "Seismic Performance of Steel Plate Shear Walls Considering Various Design Approaches," by R. Purba and M. Bruneau, October 31, 2014.

MCEER-14-0006 "Air-Blast Effects on Civil Structures," by Jinwon Shin, Andrew S. Whittaker, Amjad J. Aref and David Cormie, October 30, 2014.

MCEER-14-0007 "Seismic Performance Evaluation of Precast Girders with Field-Cast Ultra High Performance Concrete (UHPC) Connections," by G.C. Lee, C. Huang, J. Song, and J. S. O'Connor, July 31, 2014.

MCEER-14-0008 "Post-Earthquake Fire Resistance of Ductile Concrete-Filled Double-Skin Tube Columns," by Reza Imani, Gilberto Mosqueda and Michel Bruneau, December 1, 2014.

MCEER-14-0009 "Cyclic Inelastic Behavior of Concrete Filled Sandwich Panel Walls Subjected to In-Plane Flexure," by Y. Alzeni and M. Bruneau, December 19, 2014.

MCEER-14-0010 "Analytical and Experimental Investigation of Self-Centering Steel Plate Shear Walls," by D.M. Dowden and M. Bruneau, December 19, 2014.

MCEER-15-0001 "Seismic Analysis of Multi-story Unreinforced Masonry Buildings with Flexible Diaphragms," by J. Aleman, G. Mosqueda and A.S. Whittaker, June 12, 2015.

MCEER-15-0002 "Site Response, Soil-Structure Interaction and Structure-Soil-Structure Interaction for Performance Assessment of Buildings and Nuclear Structures," by C. Bolisetti and A.S. Whittaker, June 15, 2015.

MCEER-15-0003 "Stress Wave Attenuation in Solids for Mitigating Impulsive Loadings," by R. Rafiee-Dehkharghani, A.J. Aref and G. Dargush, August 15, 2015.

MCEER-15-0004 "Computational, Analytical, and Experimental Modeling of Masonry Structures," by K.M. Dolatshahi and A.J. Aref, November 16, 2015.

MCEER-15-0005 "Property Modification Factors for Seismic Isolators: Design Guidance for Buildings," by W.J. McVitty and M.C. Constantinou, June 30, 2015.

MCEER-15-0006 "Seismic Isolation of Nuclear Power Plants using Sliding Bearings," by Manish Kumar, Andrew S. Whittaker and Michael C. Constantinou, December 27, 2015.

MCEER-15-0007 "Quintuple Friction Pendulum Isolator Behavior, Modeling and Validation," by Donghun Lee and Michael C. Constantinou, December 28, 2015.

MCEER-15-0008 "Seismic Isolation of Nuclear Power Plants using Elastomeric Bearings," by Manish Kumar, Andrew S. Whittaker and Michael C. Constantinou, December 29, 2015.

MCEER-16-0001 "Experimental, Numerical and Analytical Studies on the Seismic Response of Steel-Plate Concrete (SC) Composite Shear Walls," by Siamak Epackachi and Andrew S. Whittaker, June 15, 2016.

MCEER-16-0002 "Seismic Demand in Columns of Steel Frames," by Lisa Shrestha and Michel Bruneau, June 17, 2016.

MCEER-16-0003 "Development and Evaluation of Procedures for Analysis and Design of Buildings with Fluidic Self-Centering Systems" by Shoma Kitayama and Michael C. Constantinou, July 21, 2016.

MCEER-16-0004 "Real Time Control of Shake Tables for Nonlinear Hysteretic Systems," by Ki Pung Ryu and Andrei M. Reinhorn, October 22, 2016.

MCEER-16-0006 "Seismic Isolation of High Voltage Electrical Power Transformers," by Kostis Oikonomou, Michael C. Constantinou, Andrei M. Reinhorn and Leon Kemper, Jr., November 2, 2016.

MCEER-16-0007 "Open Space Damping System Theory and Experimental Validation," by Erkan Polat and Michael C. Constantinou, December 13, 2016.

MCEER-16-0008 "Seismic Response of Low Aspect Ratio Reinforced Concrete Walls for Buildings and Safety-Related Nuclear Applications," by Bismarck N. Luna and Andrew S. Whittaker.

MCEER-16-0009 "Buckling Restrained Braces Applications for Superstructure and Substructure Protection in Bridges," by Xiaone Wei and Michel Bruneau, December 28, 2016.

MCEER-16-0010 "Procedures and Results of Assessment of Seismic Performance of Seismically Isolated Electrical Transformers with Due Consideration for Vertical Isolation and Vertical Ground Motion Effects," by Shoma Kitayama, Michael C. Constantinou and Donghun Lee, December 31, 2016.

MCEER-17-0001 "Diagonal Tension Field Inclination Angle in Steel Plate Shear Walls," by Yushan Fu, Fangbo Wang and Michel Bruneau, February 10, 2017.

MCEER-17-0002 "Behavior of Steel Plate Shear Walls Subjected to Long Duration Earthquakes," by Ramla Qureshi and Michel Bruneau, September 1, 2017.

MCEER-17-0003 "Response of Steel-plate Concrete (SC) Wall Piers to Combined In-plane and Out-of-plane Seismic Loadings," by Brian Terranova, Andrew S. Whittaker, Siamak Epackachi and Nebojsa Orbovic, July 17, 2017.

MCEER-17-0004 "Design of Reinforced Concrete Panels for Wind-borne Missile Impact," by Brian Terranova, Andrew S. Whittaker and Len Schwer, July 18, 2017.

MCEER-17-0005 "A Simple Strategy for Dynamic Substructuring and its Application to Soil-Foundation-Structure Interaction," by Aikaterini Stefanaki and Metttupalayam V. Sivaselvan, December 15, 2017.

MCEER-17-0006 "Dynamics of Cable Structures: Modeling and Applications," by Nicholas D. Oliveto and Mettupalayam V. Sivaselvan, December 1, 2017.

MCEER-17-0007 "Development and Validation of a Combined Horizontal-Vertical Seismic Isolation System for High-Voltage-Power Transformers," by Donghun Lee and Michael C. Constantinou, November 3, 2017.

MCEER-18-0001 "Reduction of Seismic Acceleration Parameters for Temporary Bridge Design," by Conor Stucki and Michel Bruneau, March 22, 2018.

MCEER-18-0002 "Seismic Response of Low Aspect Ratio Reinforced Concrete Walls," by Bismarck N. Luna, Jonathan P. Rivera, Siamak Epackachi and Andrew S. Whittaker, April 21, 2018.

MCEER-18-0003 "Seismic Damage Assessment of Low Aspect Ratio Reinforced Concrete Shear Walls," by Jonathan P. Rivera, Bismarck N. Luna and Andrew S. Whittaker, April 16, 2018.

MCEER-18-0004 "Seismic Performance Assessment of Seismically Isolated Buildings Designed by the Procedures of ASCE/ SEI 7," by Shoma Kitayama and Michael C. Constantinou, April 14, 2018.

MCEER-19-0001 MCEER-19-0001 "Development and Validation of a Seismic Isolation System for Lightweight Residential Construction," by Huseyin Cisalar and Michael C. Constantinou, March 24, 2019.

MCEER-20-0001 "A Multiscale Study of Reinforced Concrete Shear Walls Subjected to Elevated Temperatures," by Alok Deshpande and Andrew S. Whittaker, June 26, 2020.

MCEER-20-0002 "Further Results on the Assessment of Performance of Seismically Isolated Electrical Transformers," by Shoma Kitayama and Michael C. Constantinou, June 30, 2020.

MCEER-20-0003 "Analytical and Numerical Studies of Seismic Fluid-Structure Interaction in Liquid-Filled Vessels," by Ching-Ching Yu and Andrew S. Whittaker, August 1, 2020.

MCEER-22-0001 "Modeling Triple Friction Pendulum Bearings in Program OpenSees Including Frictional Heating Effects," by Hyun-Myung Kim and Michael C. Constantinou, April 18, 2022.

MCEER-22-0002 "Physical and Numerical Simulations of Seismic Fluid-Structure Interaction in Advanced Nuclear Reactors," by Faizan Ul Haq Mir, Ching-Ching Yu, Andrew S. Whittaker and Michael C. Constantinou, July 8, 2022.

MCEER-22-0003 "Impedance-Matching Control Design for Shake-Table Testing and Model-in-the-Loop Simulations," by Sai Sharath Parsi, Mettupalayam V. Sivaselvan and Andrew S. Whittaker, September 30, 2022.

MCEER-22-0004 "Earthquake-Simulator Experiments of a Model of a Seismically-Isolated, Fluoride-Salt Cooled High-Temperature Reactor," by Faizan Ul Haq Mir, Kaivalya M. Lal, Benjamin D. Kosbab, Nam Nguyen, Brian Song, Matthew Clavelli, Kaniel Z. Tilow and Andrew S. Whittaker, October 24, 2022.

MCEER: Earthquake Engineering to Extreme Events

University at Buffalo, The State University of New York
133A Ketter Hall | Buffalo, NY 14260
mceer@buffalo.edu; buffalo.edu/mceer

ISSN 1520-295X